CAVE-TO-MILL: MINE AND MILL INTEGRATION FOR BLOCK CAVE MINES

by

Stefan Nadolski

B.Eng., The University of Sydney, 2005
M.A.Sc., The University of British Columbia, 2012

A THESIS SUBMITTED IN PARTIAL FULFILLMENT OF
THE REQUIREMENTS FOR THE DEGREE OF
DOCTOR OF PHILOSOPHY

in

THE FACULTY OF GRADUATE AND POSTDOCTORAL STUDIES
(Mining Engineering)

THE UNIVERSITY OF BRITISH COLUMBIA
(Vancouver)

November 2018

The following individuals certify that they have read, and recommend to the Faculty of Graduate and Postdoctoral Studies for acceptance, the dissertation entitled:

CAVE-TO-MILL: MINE AND MILL INTEGRATION FOR BLOCK CAVE MINES

submitted by Stefan Nadolski in partial fulfillment of the requirements for

the degree of Doctor of Philosophy

in Mining Engineering

Examining Committee:

Professor Bern Klein
Supervisor

Dr. Davide Elmo
Co-supervisor

Dr. Craig Hart
Supervisory Committee Member

Professor Scott Dunbar
University Examiner

Professor David Dreisinger
University Examiner

Additional Supervisory Committee Members:

Allan Moss
Supervisory Committee Member

Abstract

Population growth and economic development are expected to increase future global copper demand. The depletion of significant near-surface deposits and advances in detecting deeply buried ore has led to the mining industry progressively exploring further below the surface to discover new copper deposits. Accordingly, block and panel cave mining methods are being increasingly proposed as they allow massive, deeply situated ore-bodies to be mined economically. To improve the productivity of a mining method that will be used to excavate a growing proportion of global copper supply, an integrated mine and mill approach for planning and operating block cave mines, termed Cave-to-Mill, was developed.

Key distinguishing features of cave mining, in comparison to other mining methods, are the uncertainty in the size of rock being fed to the mill and the lack of selectivity. As part of the Cave-to-Mill framework, fragmentation and sensor-based sorting studies were carried out at the New Afton block cave mine to investigate opportunities to improve overall productivity.

Cave fragmentation is a key cave-to-mill parameter as it has implications on the productivity of both mining and milling processes. Fragmentation measurements of drawpoint muck, comminution tests and calibrated mill models were used to assess the impact of variations in feed size and hardness on New Afton mill performance. Analysis of historical mine and mill data showed that mill feed size and subsequently mill throughput are sensitive to the areas being mucked within the cave.

A sensor-based ore sorting study, incorporating bulk and particle sorting systems, showed that rock from the New Afton copper-gold porphyry deposit is amenable to prompt gamma neutron activation analysis, and to X-Ray fluorescence sensors. A conceptual flowsheet, where both technologies are used as separate unit operations, was evaluated. It was found that the sorting concept demonstrated an improvement in the net smelter return of excavated material. Results from the study were used to develop a method to design and evaluate a block cave for the case where sensor-based sorting systems are included in the flowsheet.

Lay Summary

An integrated mine and mill approach, termed Cave-to-Mill, was developed to improve the productivity of cave mines, which will be important contributors to future copper supply. In comparison to other mining methods, key distinguishing features of cave mining are the uncertainty in the size of rock being fed to crushing processes and the lack of selectivity between ore and waste within cave excavations.

Research with the New Afton block cave mine showed that implementation of grade sensors provides significant opportunity to address the lack of selectivity and improve project value. Analysis of caved rock size and mill throughput indicated that cave mine productivity can be improved by including rock size and hardness data in the decision making that goes into planning underground production schedules. Overall, results showed that the proposed cave-to-mill approach stands to improve the productivity of a mining method that will be increasingly applied.

Preface

This dissertation is ultimately based on outcomes of the Cave-to-Mill research project with New Gold Inc.

A version of Section 2.9 has been published in Mining Technology [Nadolski, S., Klein, B., Elmo, D., Scoble, M. Cave-to-Mill: a Mine-to-Mill approach for block cave mines, Transactions of the Institutions of Mining & Metallurgy, Section A, 2015. Vol 124, Issue 1, Pages 47-55, DOI: 10.1179/1743286315Y.0000000001]. I was the lead researcher, responsible for concept development, literature review, data collection, analysis and manuscript composition. Elmo D. and Klein B. were involved in development of the Cave-to-Mill flowchart, Figure 2.9. All authors contributed with manuscript edits.

A version of Chapter 4 has been published in Mining Technology [Nadolski, S., Munkhchuluun, M., Klein, B., Elmo, D., Hart, C. Cave fragmentation in a Cave-to-Mill context at the New Afton Mine part I: fragmentation and hang-up frequency prediction, Transactions of the Institutions of Mining & Metallurgy, 2017. Vol 127, Issue 2, Pages 75-83, DOI: 10.1080/14749009.2017.1351115]. I was the lead researcher, responsible for the literature review, sample collection, test work, data collection, analysis and manuscript composition. Munkhchuluun, M. assisted with image-based size analysis of drawpoint photos and review of data. Hart C. assisted with the geological description of the New Afton deposit. All authors contributed with manuscript edits.

A version of Chapter 5 has been published in Mining Technology [Nadolski, S., O'Hara, C., Klein, B., Elmo, D., Hart, C. Cave fragmentation in a Cave-to-Mill context at the New Afton Mine part II: implications to mill performance, Transactions of the Institutions of Mining & Metallurgy, 2018. Vol 127, Issue 3, Pages 155-166, DOI: 10.1080/25726668.2018.1437334]. I was the lead researcher, responsible for the literature review, sample collection, test work, data collection, analysis and manuscript composition. O'Hara, C. assisted with data collection and review. All authors contributed with manuscript edits.

A version of Section 6.1 has been published in the proceedings of MassMin2016 [Nadolski, S., Liu, Y., Klein, B., Elmo, D., Scoble, M. and Scholar, J. Investigation into the implementation of sensor-based ore sorting systems at a block caving operation, Seventh International Conference and Exhibition on Mass Mining, May 2016, Pages 393 - 399]. I was the lead researcher, responsible for the literature review, sample collection, test work, data collection, analysis and manuscript composition. Scholar, J. assisted with test work and review. All authors contributed with manuscript edits.

A version of Sections 6.2 to 6.3 has been published in the proceedings of the Canadian Mineral Processors Conference [Nadolski, S., Klein, B., Elmo, D., Samuels, M., Hart. C. Evaluation of cave-to-mill opportunities at the New Afton Mine. The 50th Annual Canadian Mineral Processors Conference, Ottawa, Canada. January 2018]. I was the lead researcher, responsible for the literature review, sample collection, test work, data collection, analysis and manuscript composition. All authors contributed with manuscript edits.

A version of Chapter 7 has been published in Minerals Engineering [Nadolski, S., Samuels, M. Klein, B., Elmo, D., Hart, C. J. Evaluation of bulk and particle sensor-based sorting systems for the New Afton block caving operation. Minerals Engineering, Volume 121, 2018, Pages 169-179, ISSN 0892-6875, DOI: 10.1016/j.mineng.2018.02.004]. I was the lead researcher, responsible for the literature review, sample collection, test work, data collection, analysis and manuscript composition. All authors contributed with manuscript edits.

A version of Chapter 8 has been accepted for publication in the proceedings of Caving2018 [Nadolski, S., Klein, B., Hart, C. J., Moss, A., Elmo, D. An approach to evaluating block and panel cave projects for sensor-based sorting applications. Fourth International Symposium on Block and Sublevel Caving, Australian Centre for Geomechanics, October 2018]. I was the lead researcher, responsible for the literature review, modelling, production simulations, analysis and manuscript composition. All authors contributed with manuscript edits.

Table of Contents

Abstract ..... **iii**
Lay Summary ..... **iv**
Preface ..... **v**
Table of Contents ..... **vii**
List of Tables ..... **xi**
List of Figures ..... **xiv**
List of Symbols ..... **xviii**
List of Abbreviations ..... **xxi**
Acknowledgements ..... **xxiii**
Dedication ..... **xxix**
Chapter 1: Introduction **1**
1.1 Problem Statement 1
1.2 Research Objectives 2
1.3 Cave-to-Mill Project Overview 3
1.4 Thesis Outline 4
Chapter 2: Literature Review **6**
2.1 Block and Panel Caving Methods 6
2.2 Mine-to-Mill 9
2.3 Cave Evaluation and Production scheduling 12
2.4 Rock Mass Characterization 14
2.5 Cave Fragmentation 16
2.6 Gravity Flow of Caved Material 21
2.7 Sensor-based Sorting 24
2.8 Cave-to-Mill Concept 28
2.9 Summary of Literature Review 31
Chapter 3: Site Description and Methodology **33**
3.1 Introduction 33
3.2 Site Description: New Afton Mine 33
3.3 Fragmentation Measurements 35

3.4 Drawpoint Sampling and Test Regimen 37
3.5 Mill Sampling and Surveying 40
3.6 Primary Crusher and Mill Modelling 42
3.7 Rock Type Specification and Characterization 44
3.8 Sensor-based Sorting 46
3.9 Cave and Mill Comminution Testing 49
3.10 Block Cave Planning and Scheduling 52
Chapter 4: Predicting Cave Fragmentation and Hang-Up Frequency 54
4.1 Introduction 54
4.2 Fragmentation Measurements 55
4.3 Comparisons with Block Cave Fragmentation (BCF) Predictions 57
4.4 Back-calculation of Gyratory Crusher Feed 59
4.5 Fragmentation Size and Rock Type 61
4.6 Comparison of Hang-Up Frequency to Fragmentation Results 63
4.7 Relating Fracture Intensity from DFN Models to Fragmentation Size 65
4.8 Influence of Veining on Fragmentation Size at New Afton 69
4.9 Discussion and Conclusions 71
Chapter 5: Relating Fragmentation Size to Mill Performance 74
5.1 Introduction 74
5.2 Analysis of Mine and Mill Data 74
5.3 Cave-to-Mill Modelling and Simulation Methodology 78
5.4 Size Analysis of Drawpoint Samples 79
5.5 Material Hardness Characterisation 81
5.6 Mill Surveys, Model Calibration and Validation 82
5.7 Mill Model Validation 84
5.8 Influence of Feed Size on Simulated Mill Performance 88
5.9 Relationships Between Point Load Index, Impact Breakage and Abrasion 89
5.10 Discussion 92
5.11 Conclusions 93
Chapter 6: Heterogeneity Analysis for Assessment of Sorting Potential 94
6.1 Introduction 94

6.2 Evaluation of Distributional Heterogeneity and Implications on Bulk Sorting 96
6.3 Analysis of Heterogeneity at the Extraction Level 97
6.4 Variation of Grade with Size 99
6.5 Discussion and Conclusions 101
Chapter 7: Bulk and Particle Sorting System Evaluation 102
7.1 Introduction 102
7.2 PGNAA Bulk Sensor Evaluation 103
7.3 XRF Particle Sensor Evaluation 106
7.4 Sorting System Evaluation 110
7.5 XRF Particle-Sorting Models 111
7.6 Process and Cost Assumptions 114
7.7 Application of Sorter Models to Grade Block Models 118
7.8 Discussion and Conclusions 120
Chapter 8: A Methodology for Cave Evaluation with Sensor-Based Sorting 123
8.1 Introduction 123
8.2 Description of the Cave Evaluation Method 123
8.3 Relating Sorting Performance to Head Grade 124
8.4 Nominating Footprint Geometry, Orientation and Elevation 125
8.5 Applying Models to Mixed Material in Draw Cones 127
8.6 Production Scheduling and Evaluation 128
8.7 Discussion and Conclusions 129
Chapter 9: Conclusions and Recommendations 131
9.1 Main Outcomes 131
9.2 Recommendations for Future Work 134
Chapter 10: Claims of Original Contributions 136
References 138
Appendices 153
Appendix A Vertimill Operational Data 153
Appendix B An Abbreviated DropWeight Test Method for Lump Rock 155
B.1 Introduction 155
B.2 Background 155

B.3 Methodology 156
B.4 Comparison of Testing Methods 158
B.5 Conclusions and Recommendations 162
Appendix C PGNAA and XRF Test Results 164
Appendix D Point Load Test Results 168
Appendix E DropWeight Test Results 206
Appendix F Bond Ball Mill Index Results 222
Appendix G Drawpoint Logs 235
Appendix H Image-based Size Distributions 238
Appendix I Mill Survey Results for Survey Carried Out March 3rd, 2015 243
Appendix J Mill Survey Results for Survey Carried Out March 16th, 2016 247
Appendix K Sample Preparation Flowsheet for PGNAA Testing 257

List of Tables

Table 3.1 Guideline for macro-description of rocks 45
Table 3.2 Specific energy and size summary for DropWeight testing 51
Table 4.1 Summary of draw point muck images 56
Table 5.1 New Afton mill feed and geological unit characteristics 82
Table 5.2 Summary of New Afton mill surveys 83
Table 5.3 Comparison of measured and simulated mill performance 84
Table 5.4 Equipment and process constraints for simulations 85
Table 6.1 Chronological mixing / comminution events and their impact on heterogeneity 95
Table 7.1 Main lithology and alteration types and implications on the New Afton operation 103
Table 7.2 Measurement repeatability in relation to the material handling system 105
Table 7.3 Cost and process assumptions 115
Table 8.1 Cave design and costing parameters for the copper-gold case study 126
Table 8.2 Mass Balance for a conceptual cave 129
Table B.1 Abbreviated DropWeight Test Regimen 156
Table B.2 Comparison of Axb results 162
Table C.1 Bulk samples used for PGNAA testing. 165
Table D.1 Point load test results for mill feed sample taken in March 2016 169
Table D.2 Point load test results for drawpoint sample B13S taken Nov 2015 173
Table D.3 Point load test results for drawpoint sample D7S taken Nov 2015 176
Table D.4 Point load test results for drawpoint sample D11N taken Nov 2015 179
Table D.5 Point load test results for drawpoint sample D11S taken Nov 2015 182
Table D.6 Point load test results for drawpoint sample D38N taken Nov 2015 185
Table D.7 Point load test results for drawpoint sample E13S taken Nov 2015 188
Table D.8 Point load test results for drawpoint sample E15N taken Nov 2015 191
Table D.9 Point load test results for drawpoint sample E23N taken Nov 2015 194
Table D.10 Point load test results for drawpoint sample E30N taken Nov 2015 197
Table D.11 Point load test results for drawpoint sample F33S taken Nov 2015 200
Table D.12 Point load test results for drawpoint sample G40N taken Nov 2015 203

Table E.1 DropWeight test results for mill feed sample collected March, 2016 206
Table E.2 DropWeight test results for 2015 mill feed sample, SMC method 210
Table E.3 DropWeight test results for drawpoint sample B13S (collected Nov, 2015) 211
Table E.4 DropWeight test results for drawpoint sample D7S (collected Nov, 2015) 212
Table E.5 DropWeight test results for drawpoint sample D11N (collected Nov, 2015) 213
Table E.6 DropWeight test results for drawpoint sample D11S (collected Nov, 2015) 214
Table E.7 DropWeight test results for drawpoint sample D38N (collected Nov, 2015) 215
Table E.8 DropWeight test results for drawpoint sample E13S (collected Nov, 2015) 216
Table E.9 DropWeight test results for drawpoint sample E15N (collected Nov, 2015) 217
Table E.10 DropWeight test results for drawpoint sample E23N (collected Nov, 2015) 218
Table E.11 DropWeight test results for drawpoint sample E30N (collected Nov, 2015) 219
Table E.12 DropWeight test results for drawpoint sample F33S (collected Nov, 2015) 220
Table E.13 DropWeight test results for drawpoint sample G40N (collected Nov, 2015) 221
Table F.1 Bond ball mill work index test results for mill feed sample (2016) 222
Table F.2 Bond ball mill work index test results for mill feed sample (2015) 223
Table F.3 Bond ball mill work index test results for drawpoint sample B13S 224
Table F.4 Bond ball mill work index test results for drawpoint sample D7S 225
Table F.5 Bond ball mill work index test results for drawpoint sample D11N 226
Table F.6 Bond ball mill work index test results for drawpoint sample D11S 227
Table F.7 Bond ball mill work index test results for drawpoint sample D38N 228
Table F.8 Bond ball mill work index test results for drawpoint sample E13S 229
Table F.9 Bond ball mill work index test results for drawpoint sample E15N 230
Table F.10 Bond ball mill work index test results for drawpoint sample E23N 231
Table F.11 Bond ball mill work index test results for drawpoint sample E30N 232
Table F.12 Bond ball mill work index test results for drawpoint sample F33S 233
Table F.13 Bond ball mill work index test results for drawpoint sample G40N 234
Table G.1 Logs of rock types reporting to drawpoints 235
Table G.2 Logs of rock types reporting to drawpoints 236
Table G.3 Rock types identified in mill feed sample (collected March, 2016) 237

Table H.1 Drawpoint size distributions from image-based measurements and sieving 238
Table H.2 Drawpoint size distributions from image-based measurements 239
Table H.3 Drawpoint size distributions from image-based measurements 239
Table H.4 Drawpoint size distributions from image-based measurements 240
Table H.5 Drawpoint size distributions from image-based measurements 240
Table H.6 Drawpoint size distributions from image-based measurements 241
Table H.7 Drawpoint size distributions from image-based measurements 241
Table H.8 Drawpoint size distributions from image-based measurements 242
Table I.1 Summary of samples taken March 3rd, 2015 243
Table I.2 Summary of samples taken March 3rd, 2015 244
Table I.3 Size distributions for samples taken March 3rd, 2015 245
Table J.1 Summary of samples taken March 16th, 2016 247
Table J.2 Size distributions of samples taken March 16th, 2016 248
Table J.3 Size distributions of samples taken March 16th, 2016 249
Table J.4 Size distributions of samples taken March 16th, 2016 250
Table J.5 Outline of measured and calculated streams 253

List of Figures

Figure 1.1 Cave-to-Mill project team and scope 3
Figure 2.1 Cross-sectional draw zone for different cut-off grades at the Northparkes Mine 8
Figure 2.2 Examples of caving project schedules..... 12
Figure 2.3 Schematic of block model to slice file conversion in PC-BC 14
Figure 2.4 Relation of tonnes drawn per secondary breakage event and percentage extracted.... 18
Figure 2.5 Sequence to implement intensive pre-conditioning at Cadia East 20
Figure 2.6 Conceptual flow of material in a cross-section of the cave..... 22
Figure 2.7 Cave Tracker detectors and beacons within fragmented muck pile 24
Figure 2.8 Sortability of ores 27
Figure 2.9 Cave-to-Mill Concept..... 30
Figure 3.1 Geological and fault structures at the extraction level 34
Figure 3.2 Simplified New Afton flowsheet..... 35
Figure 3.3 Fragmentation analysis of drawpoint F10N 36
Figure 3.4 PortaMetricsTM Tablet 37
Figure 3.5 Test regimen for the core of the test program 39
Figure 3.6 Simplified New Afton flowsheet and sampling points..... 40
Figure 3.7 Diverted mill feed sample (2.2 tonnes) from the underground to surface conveyor... 41
Figure 3.8 Collected +50 mm samples from drawpoint D11N..... 45
Figure 3.9 Sample being loaded into Geoscan-M with conveyor belt cut-off..... 48
Figure 3.10 JK DropWeight test unit at the NBK Institute of Mining Engineering..... 50
Figure 4.1 Size distribution curves for secondary fragmentation at New Afton 57
Figure 4.2 Size distribution curves for secondary fragmentation at New Afton, B2 cave 59
Figure 4.3 Modelled crusher product and feed sizes 61
Figure 4.4 Secondary fragmentation size in relation to carbonate and fault rock content..... 62
Figure 4.5 Hang-Up Frequency for East and West Caves 63
Figure 4.6 100% passing sizes of drawpoint muck..... 64
Figure 4.7 80% passing sizes of drawpoint muck..... 64
Figure 4.8 Hang-up frequency for HOD of 60 to 100 metres..... 65
Figure 4.9 In situ fragmentation based on DFN analysis..... 66

Figure 4.10 Geostatistical P_{32} block model 67
Figure 4.11 Hang-up frequency and fracture intensity P_{32} 68
Figure 4.12 Hang-up frequency and fracture intensity P_{32} for three HOD ranges 69
Figure 4.13 Drawpoint sample E13S (West Cave) taken November, 2015 (+50 mm) 70
Figure 5.1 New Afton drawpoint layout 75
Figure 5.2 Mill feed size and throughput 76
Figure 5.3 Mill feed size and proportion of material from drawpoints within B1 Cave 77
Figure 5.4 Mill throughput and the proportion of material from B1 Cave drawpoints 78
Figure 5.5 Example of estimated gyratory crusher feed size for sample D7S 81
Figure 5.6 Simulated mill throughput rates and mill feed size 86
Figure 5.7 Simulated mill throughput rates and DropWeight Index parameters 87
Figure 5.8 DropWeight Index and measured F80 size of sample drawpoint muckpiles 87
Figure 5.9 Pearson correlation coefficient for material sizes and simulated mill throughput. 89
Figure 5.10 Point Load Index IS(50) and DropWeight Index results 90
Figure 5.11 Point Load Index IS(50) and Abrasion, ta, results for twelve samples 90
Figure 5.12 Abrasion Index, ta, and measured F80 size of drawpoint muck 91
Figure 5.13 Point Load Index IS(50) and measured F80 size of drawpoint muck 91
Figure 6.1 Distribution heterogeneity of caved muck and bulk sorter performance 97
Figure 6.2 Distribution heterogeneity of caved muck 98
Figure 6.3 Distribution heterogeneity and average draw point grade 99
Figure 6.4 Copper grade of different size fractions in hypogene drawpoint samples 100
Figure 6.5 Copper grade of different size fractions in drawpoint samples 100
Figure 7.1 Predicted copper grades of bulk samples using PGNAA sensors 104
Figure 7.2 Predicted gold grades of bulk samples using PGNAA sensors 106
Figure 7.3 Predicted copper grades from surface readings 107
Figure 7.4 Particle sorting performance based on pXRF testing of 291 particles 108
Figure 7.5 Predicted copper grades from surface readings taken under dynamic conditions 109
Figure 7.6 Particle sorting performance from testing under dynamic conditions 110
Figure 7.7 Simplified flowsheet of the mine and sorting systems 111
Figure 7.8 Constitution heterogeneity based on surface readings of rocks 113
Figure 7.9 Constitution heterogeneity and Cu grade of underground samples 113

Figure 7.10 NSR and copper recovery in relation to mass pull 117
Figure 7.11 Economic mass pull and corresponding copper recovery 118
Figure 7.12 NSR in relation to head grade and sorting option 120
Figure 8.1 Summary of approach to cave-sorting evaluation 124
Figure 8.2 Conceptual cave footprint for a proposed extraction level elevation 127
Figure 8.3 Example production schedule runs for a conceptual cave 128
Figure A.1 Vertimill operating performance and ball mill main motor requirements 154
Figure B.1 Distribution of particle mass for sample #1 158
Figure B.2 Distribution of specific energies for 11 samples 159
Figure B.3 Distribution of specific energies for 11 samples, ... 160
Figure B.4 Mean squared error using a typical DropWeight approach 161
Figure B.5 Mean squared error using the proposed DropWeight method 162
Figure C.1 Rock type and pXRF measurement for Ni 164
Figure C.2 Rock type pXRF surface measurement for Cr. 164
Figure C.3 PGNAA and ICP measurements for Ni 165
Figure C.4 PGNAA and ICP measurements for Cr 166
Figure C.5 Ratio of copper to sulfur from PGNAA measurements 166
Figure C.6 Copper grade of drawpoint sampleand copper grade of fines (-2 mm) 167
Figure C.7 Fe content in fines (-2 mm), and the proportion of carbonate rock 167
Figure D.1 Point load test results for Mill Feed (sample collected March 2016) 172
Figure D.2 Point load test results for drawpoint sample B13S taken Nov 2015 175
Figure D.3 Point load test results for drawpoint sample D7S taken Nov 2015 178
Figure D.4 Point load test results for drawpoint sample D11N taken Nov 2015 181
Figure D.5 Point load test results for drawpoint sample D11S taken Nov 2015 184
Figure D.6 Point load test results for drawpoint sample D38N taken Nov 2015 187
Figure D.7 Point load test results for drawpoint sample E13S taken Nov 2015 190
Figure D.8 Point load test results for drawpoint sample E15N taken Nov 2015 193
Figure D.9 Point load test results for drawpoint sample E23N taken Nov 2015 196
Figure D.10 Point load test results for drawpoint sample E30N taken Nov 2015 199
Figure D.11 Point load test results for drawpoint sample F33S taken Nov 2015 202
Figure D.12 Point load test results for drawpoint sample G40N taken Nov 2015 205

Figure E.1 Breakage index t10 and input energy with the standard A & b model 208
Figure E.2 Breakage index t10 and input energy and fitted M and fmat model..... 208
Figure E.3 Breakage index t10 and tn for mill feed..... 209
Figure E.4 Breakage index t10 and energy for drawpoint sample B13S..... 211
Figure E.5 Breakage index t10 and energy for drawpoint sample D7S..... 212
Figure E.6 Breakage index t10 and energy for drawpoint sample D11N..... 213
Figure E.7 Breakage index t10 and energy for drawpoint sample D11S..... 214
Figure E.8 Breakage index t10 and energy for drawpoint sample D38N..... 215
Figure E.9 Breakage index t10 and energy for drawpoint sample E13S..... 216
Figure E.10 Breakage index t10 and energy for drawpoint sample E15N 217
Figure E.11 Breakage index t10 and energy for drawpoint sample E23N 218
Figure E.12 Breakage index t10 and energy for drawpoint sample E30N 219
Figure E.13 Breakage index t10 and energy for drawpoint sample F33S 220
Figure E.14 Breakage index t10 and energy for drawpoint sample G40N..... 221
Figure G.1 Mill feed sample (~2 tonnes) and example of rock type groupings (+50 mm)..... 237
Figure I.1 Size distributions for samples taken March 3rd, 2015..... 246
Figure J.1 Size distributions for the SAG mill circuit (March, 2016) 251
Figure J.2 Size distributions for the SAG mill circuit (March, 2016) 251
Figure J.3 Mass balances relating to SAG mill screen undersize calculation 252
Figure J.4 Mass balance calculation #1 for SAG mill screen undersize..... 254
Figure J.5 Mass balance calculation #2 for SAG mill screen undersize..... 255
Figure J.6 Size distributions SAG mill screen undersize..... 256
Figure K.1 Sample preparation procedure for sulfide samples..... 257
Figure K.2 Sample preparation procedure for oxide sample 258

List of Symbols

Υ_{sorter}	Proportion of sorter feed mass, or mass yield, that reports to sorter concentrate
A	Parameter in energy-breakage equation describing used in application to DropWeight testing. Represents the maximum breakage for infinite energy input
a_i	Grade of an individual particle within a lot in Constitutional Heterogeneity
a_L	Weighted-average grade of an entire lot of material in Constitutional or Distributional Heterogeneity equations
a_n	Grade of an individual group in a Distribution Heterogeneity equation
b	Parameter in energy-breakage equation describing used in application to DropWeight testing. Represents the maximum breakage for infinite energy input
$\widehat{Cu}$	Predicted copper content of a fragment based on a sensor measurement
Cu_{avg}	Average XRF copper measurement for a fragment where multiple faces are measured
Cu_{max}	Maximum XRF copper measurement for a fragment where multiple faces are measured
eff_{sort}	Efficiency of particle sorting systems downstream of grade sensors
f	Head grade of material
F80	80 % passing size of feed material
F50	50 % passing size of feed material
fines dilution	Grade of fines (-12.5 mm) as a percentage of head grade
$f_{mill\ feed}$	Copper feed grade in %

$I_{S(50)}$	Size-corrected point load strength index. The original point load strength index value multiplied by a factor to normalize the value that would have been obtained with a diametral test of diameter 50 mm (ASTM, 2013)
K	Size modulus in the Gaudin-Schuhmann equation
L	A Lot of particles or groups of material in Constitutional and Distributional Heterogeneity equations
m	Slope parameter in the Gaudin-Schuhmann equation
M_i	Mass of an individual particle within a lot in Constitutional Heterogeneity
M_L	Weighted-average mass of an entire lot of material in Distribution Heterogeneity equations
M_n	Mass of an individual group in Distributional Heterogeneity equations
M(x)	Weight of undersize in the Gaudin-Schuhmann equation
n	Number of groups in Distributional Heterogeneity equations
N_g	Number of groups in a lot in Distributional Heterogeneity equations
N_F	Number of fragments (particles) in a lot in Constitution Heterogeneity equations
$P_{12.5mm}$	Mass proportion of material that passes a 12.5 mm aperture screen
P_{32}	Fracture area divided by unit volume (m^2/m^3). A 3D measure of fracture intensity
P_{10}	Number of fractures per unit length of borehole (1/m). A 1D measure of fracture intensity
R	Metal recovery
$R_{flotation}$	Metal recovery by flotation

R_R	Reduction Ratio
R_{sort}	Proportion of metal in sorter feed that is recovered by a sorter
t10	Abrasion parameter determined from abrasion testing
Wio	Operating work index.

List of Abbreviations

BBWI	Bond Ball Mill Work Index
BCF	Block Cave Fragmentation (software)
BPC	Blast Pre-Conditioning
CH	Constitutional Heterogeneity
DE	Discrete Element
DFN	Discrete Fracture Network
DH	Distributional Heterogeneity
DWI	DropWeight Index
DWT	DropWeight
FE	Finite Element
HF	Hydraulic Fracturing
HFEMS	High Frequency Electro Magnetic Susceptibility
HOD	Height of Draw
HPGR	High Pressure Grinding Rolls
HR	Hydraulic Radius
ICP	Inductively Coupled Plasma
LHD	Load Haul Dump
MRMR	Mine Rock Mass Rating

NMR	Nuclear Magnetic Resonance
NPV	Net Present Value
NSR	Net Smelter Return
PCBC	Personal Computer Block Cave (software)
PGNAA	Prompt Gamma Neutron Activation Analysis
PLI	Point Load Index
pXRF	Portable X-Ray Fluorescence
QEMSCAN	Quantitative Evaluation of Minerals by SCANning
RMR	Rock Mass Rating
ROM	Run-Of-Mine
RQD	Rock Quality Designation
SAG	Semi-Autogenous Grinding
SRM	Synthetic Rock Mass
SWIR	Short Wave InfraRed
XRF	X-Ray Fluorescence
UCS	Unconfined Compressive Strength

Glossary

This glossary defines the main technical terms as they are used in this thesis. Where practical, the definitions follow “Caving Terminology & Glossary” by Van As (2010).

Alteration: The change in the mineralogic composition of a rock due to various natural processes, especially by the action of hydrothermal solutions

Apex Level: The level in a cave mine which provides access to the apex of a crinkle-cut (chevron shaped) undercut. Usually developed to ensure the continuity of undercut blasts

Aspect Ratio (caveability): The ratio of cave footprint length to width when considered in plan view

Aspect Ratio (fragment): A parameter used in Block Cave Fragmentation software that relates cave fragment volume, surface area and length

Best Height of Draw: The column height above a drawpoint that provides the highest dollar value for a given set of mining and processing costs, and factors for product revenue and metal recovery

Block Model: A set of specifically sized blocks used to describe the characteristics of a rock mass. Although the size of the blocks is usually the same, each block has unique characteristics such as grade, density, rock type and any other features that are known and relevant to mining and/or processing

Caveability: The ability of a rock mass to cave for a designated layout

Cave Back: The under-surface of the in situ, but possibly disturbed, rock above a cave or muckpile of caved ore (located above the extraction level)

Caving: The gravitational collapse of in situ rock from the cave back

Caving Rate: The average rate at which the cave naturally propagates upwards

Dilution Entry: The percentage of the ore column that has been drawn before dilution appears at the drawpoint (Laubscher, 2000)

Drawbell: An excavated structure, ideally having the shape of an inverted bell, which channels caved or broken rock to a drawpoint

Draw Control: The process of controlling the amounts of rock drawn from individual drawpoints in order to achieve a number of mining objectives

Drawpoint: The excavated structure on the extraction or production level through which caved or broken rock is loaded and moved to underground material handling systems

Drawpoint Spacing: The spacing in plan view between like points in adjacent drawpoints. Usually defined by two distances: the distance between drawpoints that are separated by the major apex and the distance between drawpoints that are separated by the minor apex

Drift: A horizontal excavation in or near an orebody driven from one working place to another. It is usually of a relatively small cross section compared with larger sections which are usually referred to as tunnels

Extraction Level: The level in a caving mine through which caved or broken rock is extracted and transported away from the cave

Fault: A fracture or a fracture zone in crustal rocks along which there has been displacement of the two sides relative to one another parallel to the fracture. The displacement may be a few millimetres or many kilometres long

Footprint Finder: An application within Gems Geovia PCBC software which works off geological block models and determines a block cave layout's elevation, footprint shape and size for a given set of inputs

Froth Flotation: The separation of ore and waste minerals made possible by the selective adhesion of air bubbles to mineral or gangue surfaces in a slurry

Fragmentation: The process, or the result, of blasting, caving and draw of initially in situ rock

Geometallurgy: The combination of geological, metallurgical and other information relating to mine and mill production for use in spatial or geology-based models

Hang-up: The wedging of one or more large blocks of rock in or above the drawpoint or drawbell such that they will not move further by gravity

Haulage Level: The level in an underground mine through which caved or broken rock is transported away from the production area to crushers or material handling systems (for transport to surface)

Height of Draw (HOD): The vertical distance travelled by material reporting to a drawpoint from its original location in the in situ rock mass

Hydraulic Radius: In the context of underground mining, the ratio of the surface area to the perimeter of an excavated surface, such as the back of an undercut

Hypogene (Rock): Rock formed beneath the surface of the Earth by ascending solutions

In Situ: In the natural or original position. Applied to a rock, soil, or stress etc., occurring in the original, unaltered state prior to mining

In Situ Fragmentation: The size of naturally occurring blocks within the rock mass prior to being disturbed by caving, pre-conditioning or undercutting

Isolated Draw Zone (IDZ): A draw zone isolated from other draw zones as a consequence of being spaced too far away for any interaction to occur with its neighboring drawpoints

LHD (Load-Haul-Dump): A mechanical shovel or other machine for loading ore or rock

Lithology: A description of the physical characteristics of lump rock or core samples, such as colour, texture, grain size, or composition. Referred to as a summary of the gross physical character of a rock

Major Apex: The shaped structure or pillar above the extraction level formed between two adjacent drawpoints that are separated by an extraction (production) drift

Minor Apex: The shaped structure or pillar formed between two adjacent drawbells that are located on the same side of an extraction (production) drift. Generally oriented normal to the major apex

Monzonite (Rock): Coarse grained plutonic rock containing approximately equal amounts of orthoclase and plagioclase (Mindat, 2018)

Orepass: A vertical or inclined passage for the downward transfer of ore. An orepass is driven in ore or country rock and connects a level with a lower level

Picrite (Rock): A dark basaltic rock which is rich in olivine

Pre-conditioning: A process, or well-defined group of processes, implemented before the initiation of caving to alter the inherent characteristics of the target rock mass to enhance its caving and fragmentation characteristics

Primary Fragmentation: The size reduction that occurs as blocks separate from the cave back at the onset of caving

Production Schedule (Draw Schedule): The planned allocation of draw tonnes for each drawpoint over the life of the mine

Rilling: The downward movement of material along the surface slope of caved muck located above the extraction level

Rock Mass: The rock as it occurs in situ, including all its discontinuities

Secondary Fragmentation: The breakage of caved rocks as they fall onto caved (or blasted muck) and move through a draw column to the exit point of drawpoints

Supergene (Rock): Rock formed or altered by processes, such as the circulation of meteoric waters, occurring relatively near the surface of the Earth

Undercut: A horizontal slot mined to initiate caving of a block or panel

Acknowledgements

I would like to express my deepest appreciation to my supervisor Bern Klein for providing a platform to investigate new concepts with mining operations at the beginning of the PhD program. In addition to the support received while carrying out the Cave-to-Mill research, I'd also like to express my gratitude to Bern for providing me with a wide range of opportunities to develop as an engineer since the beginning of my studies with UBC Mining.

I am very grateful to my supervising committee, Davide Elmo, Craig Hart and Allan Moss, for providing valuable insight during the research project. Paper writing was thoroughly enjoyable thanks to the timely support received. Davide Elmo's direction for the geotechnical scope was critical to linking the doctoral work to that of other students within the Cave-to-Mill project group. The research benefited considerably from Craig Hart's guidance on defining and relating geology to research outcomes. Allan Moss' input kept the work grounded and was key to assessing the applicability of the research to practical implementation.

I would like to extend my sincere thanks to personnel at New Afton and New Gold for supporting the Cave-to-Mill project and for providing access to samples and data from the New Afton block cave operation. Special thanks to Mike Samuels, who had belief in the project and provided guidance throughout. Thanks also to Marty Henning who provided considerable assistance with sampling, data collection and facilitated most of the site work.

I gratefully acknowledge the assistance from industry sponsors who provided in-kind support. ALS Metallurgy in Kamloops, BC carried out Bond ball mill work indices, froth flotation tests and assays. MineSense Technologies provided access to an Olympus pXRF and a ConductOre test unit. MotionMetrics provided access to a PortaMetrics^{TM} tablet for on-site work.

I would also like to thank the Natural Sciences and Engineering Research Council of Canada for the financial support provided to this research through a Collaborative Research Development grant (Grant No. 11R74149; Mine-to-Mill Integration for Block Cave Mines).

Many thanks to fellow research students of the Cave-to-Mill research project. Munkhtsolmon Munkhchuluun's and Yubo Liu's assistance with on-site work and fragmentation analysis was invaluable to the project. Their efforts for ensuring that Discrete Fracture Network research outcomes dovetailed with the scope of the Cave-to-Mill research project are greatly appreciated. I would also like to acknowledge the sensor test work and data analyses carried out by Elberel Erdenebat.

I very much appreciate the assistance with sampling, mill surveys and laboratory testing provided by Tugba Cebeci, Daozhen Gong and Ding Zhang. Additionally, I'd like to thank the following students for helping with the geotechnical, metallurgical and sensor-based sorting test programs: Emilio Adriano, Monong Huang, Huaizhe (Harvey) Li, Joshua Scholar, Hiten Sulakh, and Nawoong Yoon. Santiago Seiler and Amit Kumar provided valuable input during the research.

I am very grateful to my wife, Yuri Nadolski, for her patience over the course of the research, dealing with moving timelines, and for being an amazing mother to our two daughters, Anika and Mia.

I would like to thank my mother, Eva Nadolski, for carefully proofreading manuscripts and providing valuable editorial feedback.

To Anika and Mia

Chapter 1: Introduction

The problem statement and research objectives are presented in this section. An overview of the Cave-to-Mill research team and an outline of the thesis is included at the end of this chapter.

1.1 Problem Statement

Population growth and economic development are expected to increase copper demand by 213 to 341% by the year 2050 (Elshkaki et al., 2016). Meeting future copper demand will require a combination of primary raw materials from mining operations and recycled materials (ICA, 2017). Due to the depletion of significant near-surface deposits and advances in detecting deeply buried ore, the mining industry is progressively exploring further below the surface to discover new copper deposits. Approximately 69% of known copper is contained in copper-porphyry deposits (Singer, 2018) and exploration trends indicate that they will continue to account for the majority of copper reserves as discoveries of deeply-situated copper deposits continue. Block and panel caves, which have the lowest mining costs of all underground mining methods, can achieve ore excavation rates which are comparable to that of open pit operations. The solution to supplying future copper demands lies in the discovery of deeply-situated deposits and their excavation through block and panel caving.

The productivity of operating and future cave mines, defined as the real dollar output from pay metals in concentrate per unit of capital and operational dollar input, will play a large role in addressing copper demand. Furthermore, the mining method will be pushed to its extremes as deeper and larger deposits will be discovered with advances in exploration methods. Caving of more heterogeneous and competent rock masses will bring about risks associated with, among others, caveability, dilution, ore recovery, ground support and variability in mill feed. The variable and relatively uncontrollable nature of cave fragmentation and lack of selectivity are key distinguishing features of block cave mining when compared to other mining methods. Innovative approaches to planning and operating cave mines will be required to mitigate risks and drive productivity. Operational strategies that have an end-to-end view and avoid silos by taking an integrated approach have been recognized as being conducive to productivity within

the mining industry (EY, 2017). The development of an integrated operational approach for block cave mines stands to play an important role in the mining industry's efforts to meet future copper production needs.

1.2 Research Objectives

The goal of this doctoral thesis is to develop an integrated mine and mill approach for planning and operating block cave mines, termed Cave-to-Mill, to improve productivity. Copper-porphyry applications are of primary focus, as they account for the majority of copper reserves and the deposit types where block caving is applied.

To develop Cave-to-Mill, the following research objectives were defined for completion with involvement of an operating block cave mine:

- Identify key linkages between areas of cave planning and operation, and define opportunities for their coordination to improve cave productivity (Section 2.9)
- Relate geology, geotechnical properties, footprint location and operational parameters to cave fragmentation size, which affects productivity at the cave mine and mill (Chapter 4)
- Determine the influence of underground production scheduling on mill productivity (Section 5.2)
- Identify the size fractions within caved muck that are critical to mill performance (Section 5.8)
- Identify relationships between geology, geotechnical data, fragmentation and geometallurgical data for more efficient rock characterization and improved valuation of blocks contained within block models (Section 5.9 and Table 7.1)
- Addressing the non-selectivity of the cave mining method, evaluate grade heterogeneity on a bulk scale to identify suitable locations for separate handling of ore and waste underground (Section 6.3)
- Evaluate bulk and particle sensor-based sorting systems as a means to add selectivity to the mining method and improve productivity (Chapter 7)

- Develop a method to incorporate sensor-based sorting parameters in cave planning and production scheduling software to assess the change in reserve size and cave value (Chapter 8)

1.3 Cave-to-Mill Project Overview

At the onset of the Cave-to-Mill project it was recognized that a research team would be required to properly address the broad scope of the project. Three master's level students were recruited to focus on objectives relating to fragmentation and grade heterogeneity, as described in Figure 1.1. A multi-disciplinary committee from the University of British Columbia covering the fields of geology, geotechnical engineering, mining and mineral processing oversaw the research group. Similarly, a multi-disciplinary group from the sponsoring block cave mine, New Afton, provided input and direction over the course of the project.

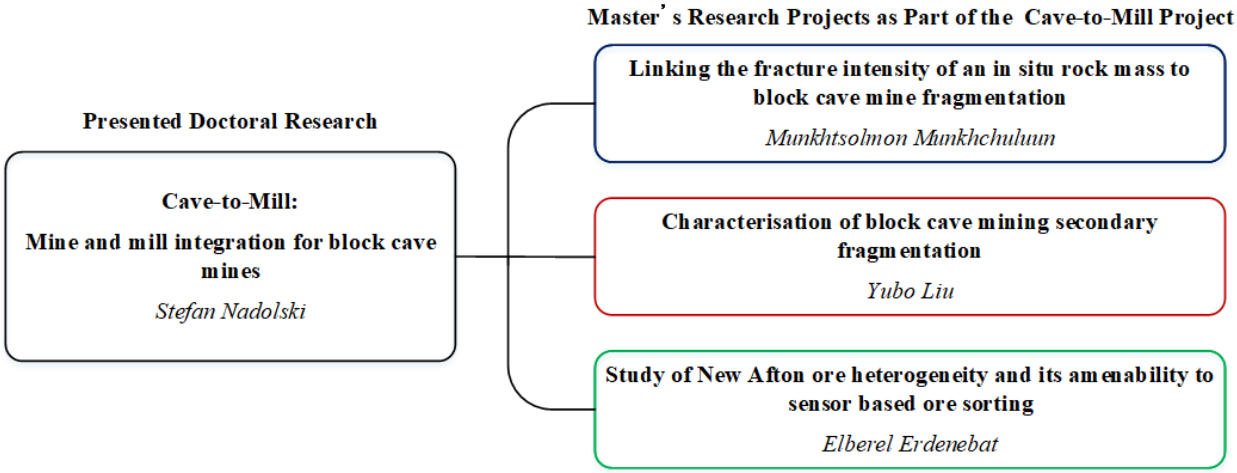

Figure 1.1 Cave-to-Mill project team and scope

Each of the three master's theses generated valuable outcomes as individual research projects and as contributions to development of the Cave-to-Mill approach. Key contributions from each thesis are shown below.

Linking the fracture intensity of an in situ rock mass to block cave mine fragmentation
Munkhtsolmon Munkhchuluun

- Developed a Discrete Fracture Network (DFN) model of the New Afton rock mass and related fracture intensity to cave fragmentation size (Section 4.7)

Characterisation of block cave mining secondary fragmentation
Yubo Liu

- Compared the outputs of PortaMetrics™ and WipFrag™ methods for size measurement of drawpoint muck (Section 3.3)

Study of New Afton ore heterogeneity and its amenability to sensor-based ore sorting
Elberel Erdenebat

- Related bulk scale grade heterogeneity (distribution heterogeneity) to the average grade of material reporting to individual drawpoints (Figure 6.3)

1.4 Thesis Outline

Chapter 2 includes a review of literature pertaining to the development of a Cave-to-Mill approach for improved productivity. The Cave-to-Mill concept was developed as an outcome of the literature review and is presented in the same chapter.

Chapter 3 describes the New Afton block cave mine, which served as the basis of the research. The methodology used to address focus areas of Cave-to-Mill, such as assessing the impact of cave fragmentation on mill performance and evaluating sensor-based sorting systems, is included in this chapter.

Chapter 4 presents findings from a fragmentation study, which relates cave fragmentation and hang-up frequency to geology, geotechnical properties, footprint location and the vertical distance travelled by ore blocks.

Chapter 5 identifies drawpoints at the New Afton mine that provide finer mill feed and are associated with increased mill throughput. Results from mill simulations show how mill throughput varies due to changes in mill feed size and hardness.

Chapter 6 describes New Afton grade heterogeneity on a bulk scale as an initial step towards evaluation of sensor-based sorting opportunities. Grade data for different size fractions within drawpoint muck is also presented.

Chapter 7 describes the results of a bulk and particle sensor-based sorting evaluation. A flowsheet which combines both bulk and particle sorting technologies is proposed. The increase in the net smelter return (NSR) as a result of implementing the flowsheet is presented. The chapter includes a summary of key rock types and their implications on mine and mill productivity.

Chapter 8 presents a method to include sensor-based sorting parameters in the outputs of cave planning and production scheduling software. Results from the sorting study, which was carried out at the New Afton block cave mine, are used to demonstrate the method for a conceptual cave in a copper-porphyry deposit.

Chapter 9 describes the conclusions drawn from the research. Recommendations for further development of Cave-to-Mill are presented in the same chapter.

Chapter 10 outlines the original claims that resulted from this Cave-to-Mill doctoral thesis.

Chapter 2: Literature Review

This chapter presents a review of literature from seven broad areas of research that are relevant to the development of an integrated mine and mill approach for cave mines. An outcome of the literature was the development of the cave-to-mill concept, which integrates different areas of research with a systems engineering approach. A review of the block and panel caving mining methods is presented in Section 2.1. Mine and mill strategies, based on fragmentation size and geometallurgical information, are presented in Section 2.2. Cave evaluation and production scheduling methods are reviewed in Section 2.3. A review of relevant rock mass characterisation methods is presented in Section 2.4. Models and measurement methods for cave fragmentation size are discussed in Section 2.5. Models for predicting gravity flow and the use of markers for tracking caved ore are reviewed in Section 2.6. An overview of sensor-based sorting, for bulk and particle applications, is shown in Section 2.7. From review of literature, a cave-to-mill concept is put forward in Section 2.8. Reviewed literature is summarized in Section 2.9.

2.1 Block and Panel Caving Methods

Block and panel caving are low-cost underground mass mining methods that are suitable for excavating weak, massive and steeply-dipping orebodies. Accordingly, cave mining methods have predominantly been used to mine copper porphyry and diamond bearing deposits. Due to the depletion of near-surface orebodies, it is expected that block and panel caving methods will be increasingly used in the copper-gold industry. Typical production rates for caving operations in massive deposits range from 17,500 tpd at the New Afton mine to 160,000 tpd at the Grasberg complex. Examples of cave mines proposed for British Columbia include the Kwanika Mine, Red Chris underground, Kemess Underground project, and the Iron Cap and Mitchell cave mines of the Kerr-Sulphurets and Mitchell (KSM) project (Moose Mountain Technical Services, 2017; Imperial Metals, 2017; Golder Associates, 2017; Tetra Tech, 2016). Significant future caves proposed worldwide include the Grasberg Block Cave, Oyu Tolgoi's Hugo North Cave, Resolution Mine and Chuquicamata.

In both panel and block cave mines, an excavation is blasted below the base of the ore body, referred to as an undercut, inducing gravity-assisted fragmentation known as caving. Subsequently, caved material flows through a number of funnel like drawbells and is subjected to a series of hauling, crushing, grinding and beneficiation processes. As ore is removed from drawbells by load haul dumps (LHD), the cave back (roof) progresses vertically towards the surface. Although block and panel caving are recognized as being the most cost-efficient underground mining methods, approximately 70 percent of capital costs are consumed before any revenue is generated (Oancea, 2013).

In panel caving operations, the orebody is not undercut completely, rather, a number of panels or strips of the orebody are undercut and caved individually until the planned footprint is excavated (Brown, 2003). Generally, variations of panel and block caving methods are implemented at caving operations. For clarity, further use of the term ‘block caving’ will generally refer to both panel and block caving methods.

Both block and panel caving methods are associated with low selectivity in terms of the capability of selecting grades within a spatial distribution. The limitation of the method is illustrated in Figure 2.1, which shows the cross-sectional draw zone for different cut-off grades at the E48 Northparkes Mine. The illustration shows that the selectivity of the mining method for material located above the extraction level is practically limited to providing control over the height of each draw column. Underground mining methods that provide greater selectivity, while being applied at lower production rates, include sub-level caving, long-hole stoping, cut-and-fill stoping, and vein mining.

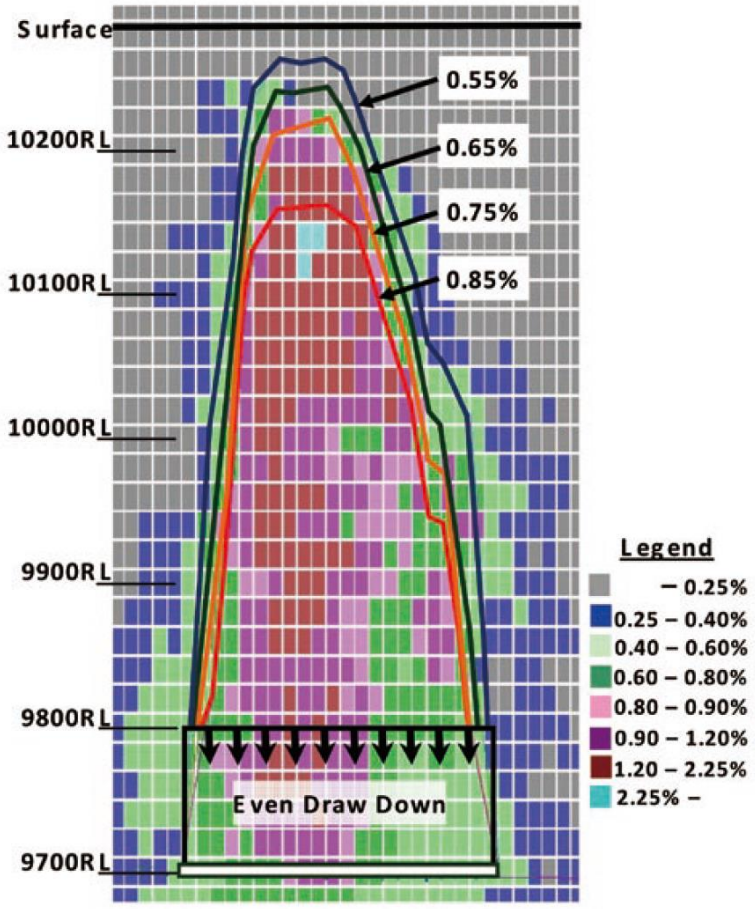

Figure 2.1 Cross-sectional draw zone for different cut-off grades at the E48 Northparkes Mine, looking North (Sagawa & Yamatomi, 2009)

Significant developments in the caving method have occurred since its first reported implementation in 1895 at iron mines in Michigan (Woo et al., 2013). Over the last 20 years, the following major technological changes, relating to the proposed Cave-to-Mill approach, have been observed from review of literature:

- Automation/Semi-automation of LHDs by implementing tele-remote systems (Sandvik, 2012)
- Installation of electronic markers to monitor the vertical and horizontal flow of caved ore in real-time (Whiteman et al., 2016)
- Development of single-shot drawbell blasting solutions (Lovitt & Degay, 2004, and Dunstan & Popa, 2012)

- Development of independent block caves, called macro blocks, to excavate larger footprints and reduce interference between development and production (de Wolfe & Ross, 2016, Fuentes, 2014 and Manca, 2013)
- Improvements in conveying systems leading to decline access being a favorable option over shaft access for extraction levels located at greater depths (de Wolfe & Ross, 2016)
- Installation of sizers as a more compact alternative to jaw crushers or gyratory crushers (Paredes et al., 2016 and Orozco, 2010)

As a result of operational block caving experience and development of technologies, the method is being pushed to new extremes in terms of its application. In particular, increasing draw heights from 550 to over 1000 meters, caving of more heterogeneous ore bodies, and caving of deeper and more competent rock masses (Manca, 2013, Orozco, 2010, Chitombo, 2010 and Flores 2014).

From review of trends in the block caving industry, it is envisaged that Cave-to-Mill will be increasingly relevant. Developments in mine automation are conducive to implementation of broader operational strategies, as the installation of extensive monitoring and control equipment allows operational silos to be broken down and systematic approaches to be adopted. Furthermore, caving of more heterogeneous ore bodies will result in a greater variation of ore types, in terms of milling properties, being fed to process plants.

2.2 Mine-to-Mill

Mine-to-Mill spans (at a minimum) the domains of geology, geotechnical/rock mechanics, mining and processing (Mckee, 2013). The benefits of Mine-to-Mill approaches in open-pit mines have been well documented over the last 20 years by industry. Historically, the term has been used to define two operational approaches: 1) Optimization of blasting and crushing/grinding processes with the aim of increasing overall productivity, also referred to as a drill-to-mill strategy; 2) Characterisation of the ore body in terms of process performance and using this information within the mine plan and milling approach to improve productivity,

widely referred to as geometallurgy. Both operational approaches are relevant to the proposed Cave-to-Mill approach.

Mine-to-Mill, Fragmentation and Comminution

The productivity of concentrators, that use semi-autogenous (SAG) mills, is known to be sensitive to the competency and size of mill feed; lower throughput rates are associated with coarser and more competent mill feed (Morrell & Valery, 2001). For open-pit operations, studies have shown how improvements in productivity were achieved by adjusting blast designs to reduce the size of mill feed. At the Paddington Gold Operations, implementation of a higher intensity blast design resulted in a 36% improvement in mill throughput and a slight coarsening of the final product size of the ball mill grinding circuit (Kanchibotla et al., 2015). Improvements in throughput were also attributed to changes in ore hardness and process equipment. At the Cerro Corona copper-gold mine, which is an open-pit mine and uses a SAG mill based comminution circuit, a 19.4% increase in mill throughput was achieved primarily by modifying the blast pattern to increase the powder factor (La Rosa et al., 2015). In block and panel cave mines, fluctuations in caved ore hardness and fragment size will also impact the performance of downstream crushing and grinding circuits. Significant challenges in mill operation were experienced as the Palabora mill transitioned from treating material from the open-pit to that of the block cave mine (Condori et al., 2012). A greater variation in material hardness, due to non-selectivity of the mining method, and variation in the size distribution of feed to the autogenous mills prevented Palabora mill operators from achieving design throughput rates.

Dance (2016) modelled SAG and ball mill throughput performance for a range of cave fragmentation sizes which were predicted based on fragmentation modelling. Mill throughput performance was estimated to increase by up to 44% as drawpoints within the planned cave (of an anonymous operation) matured. The variable and relatively uncontrollable nature of cave fragmentation necessitates a different approach for mine and mill integration to those used for open-pit operations. Addressing this need, the Cave-to-Mill concept is proposed to give existing and future block cave operations an opportunity to improve production performance.

Mine-to-Mill, Geometallurgy

The field of geometallurgy includes aspects of geotechnical engineering, process mineralogy, geology, metallurgy, resource modelling, geostatistics and mine planning (Bye, 2010). Typically, geometallurgical characterizations are carried out using core samples and the results are used to quantify the value associated with including an individual block in the mining footprint.

The majority of reviewed geometallurgical studies involved the process of defining geometallurgical domains or units. Lotter (2011), describes a geometallurgical unit as an individual or group of ore types that possess a unique set of textural or compositional properties from which it can be predicted that a similar metallurgical performance will result.

Bye (2010) mentions that in order to define the inherent variability of an orebody, coordinating smaller volume tests, rather than compositing of core samples, is a dominant trend in the field of geometallurgy. A challenge associated with handling geometallurgical data is the fact that not all geometallurgical characteristics are additive. For example, Bond ball mill work indices are not additive and need to be converted into alternative units through simulation if they are to be used with kriging or inverse distance methods to populate a block model (Barratt et al., 2008). Alternatively, blend-response models, as proposed by Bye (2011), have been identified as a solution to modelling mill performance for a variety of ore types.

Many geometallurgical studies have shown strong correlations between geotechnical test data and crushing/grinding indices. Burger et al. (2006) found good correlations between the Point Load Index $I_{s(50)}$ and DropWeight Indices for certain ore types. Advantages of the Point Load Index (PLI) test are the relatively low test costs and short turn-around time in comparison to DropWeight type breakage tests. Proper geotechnical characterization of ore bodies is critical for caving projects, resulting in an abundance of geotechnical data that is available for consideration in a Cave-to-Mill approach.

2.3 Cave Evaluation and Production Scheduling

Cave evaluation involves the use of planning and scheduling software to determine the associated value of a caving lift for an ore body. Geological block models, which include revenue factors such as mining cost and mill recovery, can be input by users along with the planned extents of the extraction level to determine the best Height of Draw (HOD) for each draw-point and the associated project value (Diering et al., 2010). Examples of cave production schedules are shown in Figure 2.2 for a number of potential caving projects.

Evaluation of an ore body requires consideration of a multitude of production scenarios which account for, among others, variations in footprint geometry, orientation, sequence, elevation and height of draw. Gantumur et al. (2016) assessed nearly 54,000 production scenarios when evaluating the Resolution Copper Project; initial evaluation was carried out using the Footprint Finder tool in PCBC production scheduling software (Dassault Systèmes, 2018) to identify high value scenarios, these were evaluated further with detailed production schedule runs in PCBC.

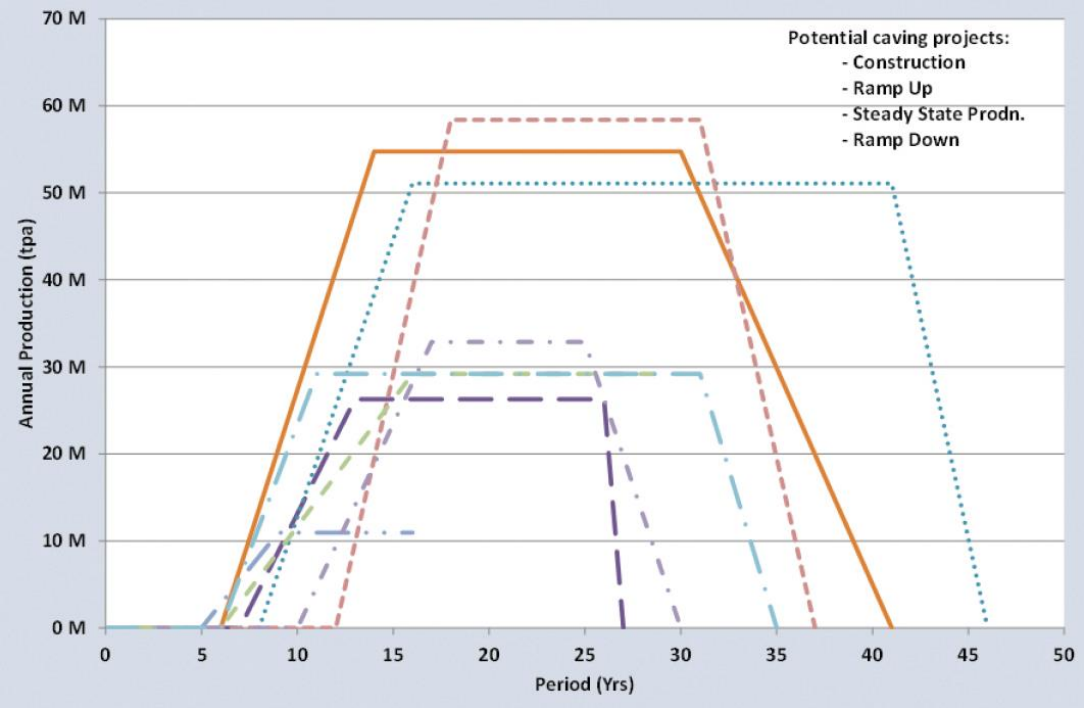

Figure 2.2 Examples of caving project schedules – construction, ramp-up, steady stage and ramp-down (Stewart & Butcher, 2016)

To date, a number of software applications have been developed to address the need for scheduling underground processes at caving operations. Examples include Linear Programming (LP), Mixed-Integer Linear Programming (MILP), Mixed-Integer Programming (MIP) and Quadratic Programming (QP) based methods (Khodayari et al., 2014). Scheduling programs generally consider ore grade, mine and mill production capacity, and the sequence of draw-point development as primary inputs. In addition to their respective mathematical methods, programs also differ according to the degree to which they consider mining/processing costs, penalty elements, horizontal and vertical mixing, geotechnical constraints and interference between construction and production activities. In direct contrast to the many scheduling programs that are based on directly optimizing cave mine net present value (NPV), Diering (2012) describes a method, available in the PCBC scheduling program, where the cave geometry is set as the objective function while ore grades are set as constraints. Figure 2.3 shows a schematic of the general steps involved in setting up a PC-BC project. Rahal (2003) proposes an MILP-based method which sets the panel profile as the goal of the objective function. The suitability of cave geometry has implications on geotechnical factors, such as subsidence profiles and air gaps, which can lead to critical mining disruptions if they are not appropriately considered within the production schedule.

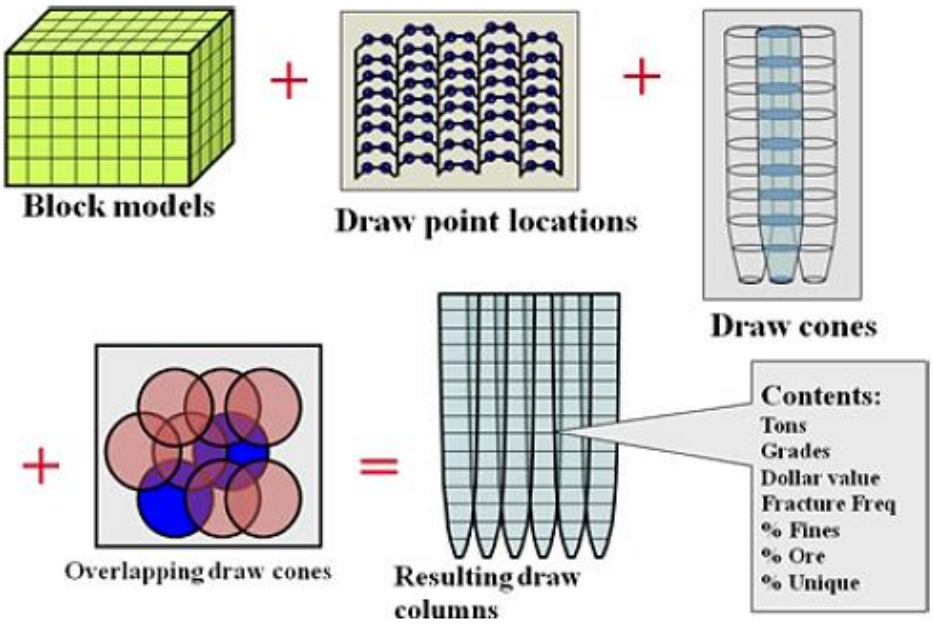

Figure 2.3 Schematic of block model to slice file conversion in PC-BC (Diering, 2010)

Production scheduling software offer significant potential for incorporating geometallurgical and sensor-based sorting data for use in the proposed Cave-to-Mill approach. Although schedules are constrained by cave stresses, flow geometry and cave geometry, they do provide the possibility to control properties of the plant feed that affect mill performance when considered as a means to blend ore types in a fashion that increases mill productivity. An example showing that sufficient flexibility exists within production schedules is the practice of blending drawpoint muck according to moisture at the Grasberg block caving operation. The fines content observed at different areas of the extraction level is one of the inputs that is considered when setting the production schedule. The fines are blended such that the moisture in the material handling system is below levels that cause problems at the haulage level (Moss, 2017).

2.4 Rock Mass Characterization

Rock mass characterization methods are essential to block cave design. Empirical approaches that are typically referenced for block cave applications include the Mining Rock Mass Rating (MRMR), Barton's Tunneling Quality Index (Q) and the Mathews stability number, N.

The MRMR classification method was introduced for cave mining applications and has been related to estimations for caveability, subsidence angles, failure zone, fragmentation, undercutting sequence and support design (Laubscher, 2011). The method relies on a variation of the Rock Mass Rating (RMR) value, as defined by Bieniawski, and adjusts it to account for in situ and induced stresses, join orientations, stress changes and the effects of blasting, water and weathering (Hoek, 2007). A limitation of empirical rock mass characterization methods, such as MRMR, is the sensitivity of their application to the judgement of the practitioner. Additionally, the relevance of MRMR for cave design is limited to the range of applications that are included in the empirical dataset. Future caving projects are pushing the mining method to new extremes in terms of its application, thereby prompting industry to supplement empirical methods with modelling tools.

Discrete Fracture Network (DFN) methods are one example of the modelling tools that are used for rock mass characterization. DFN uses statistical distributions to characterize each discontinuity set within a structural domain; variables included in the characterization include orientation, persistence and spatial location of discontinuities (Elmo et al., 2010). A major outcome of DFN modeling is the spatial distribution of fracture intensity, referred to as P_{32} and expressed in units of m^2/m^3 (fracture area/unit volume). DFN-based methods are considered to be particularly advantageous as they rely on quantifiable fracture data that is collected from field analysis of the rock mass. Since these fracture properties are preserved during the modeling process, the heterogeneity of the fracture system is better defined, resulting in an appropriate method to describing local scale problems (Rogers et al., 2010).

The three main parameters that are used to validate DFN models are: 1) fracture frequency along a borehole or scanline, commonly referred to as P_{10}; 2) orientation of fractures intersected by a borehole; and 3) comparison of trace length distributions in the case where considerable mapping data is available (Elmo et al., 2014).

In the context of the proposed Cave-to-Mill research, DFN models also provide considerable value as a means to predict cave fragmentation; a critical input parameter for predicting flow geometry, draw-point availability and crushing/grinding requirements. Rogers et al. (2010)

developed a method to predict all three stages of cave fragmentation (in situ, primary and secondary) using DFN and 2D Finite Element/Discrete Element (FE/DE) methods coupled with field data and cave stress predictions.

Synthetic Rock Mass (SRM) modeling is a method for characterising the strength of rock masses and, integrated within geomechanical models, can be used to predict cave fragmentation and caving rates. Key inputs include the previously described DFN model, as well as stress conditions, and the strength of joints and individual rock blocks (Chitombo, 2010 and Pierce, 2010). An advantage of Synthetic Rock Mass (SRM) methods is that the response of rock masses to caving conditions can be evaluated numerically at a scale that is significantly larger than the limit of geotechnical test equipment.

2.5 Cave Fragmentation

In the context of the proposed Cave-to-Mill approach, fragmentation size is a critical input parameter for predicting flow geometry, draw-point availability, sorting potential and crushing/grinding requirements. The variable and relatively uncontrollable nature of cave fragmentation is a key distinguishing feature of block cave mines when compared to other mining methods. Three different stages of fragmentation are generally defined in the field of the study: 1) In situ fragmentation, which is represented by naturally occurring blocks within the rock mass 2) Primary fragmentation, representing the size reduction that occurs as blocks separate from the cave back at the onset of caving 3) Secondary fragmentation, which refers to the breakage of blocks as they fall onto caved muck and move through a draw column to drawpoints (Brown, 2003).

Several commercial software packages have been developed or adapted to address the different stages of cave fragmentation, including: Discrete Fracture Network (DFN) based methods (Rogers et al., 2010) and BCF, a rules-based software program (Laubscher, 2000). The BCF program is based on analytical and empirical rules describing the processes and factors that play a role in cave fragmentation. Input data to the software includes jointing, fracture frequency, stresses in the cave face, and the strength of the rock mass, and intact rocks (Esterhuizen, 2005).

To quantify the fragmentation occurring in a draw column (secondary fragmentation), Gómez et al. (2017) conducted experiments on gravity flow under confinement and adopted modelling approaches used to describe comminution occurring in crushers and grinding mills. Their experiments, using a 700 mm diameter piston press with an outlet representing a drawbell, showed that the extraction of material affected the size reduction of finer material through abrasion. Dorador (2016) carried out 1-D compression tests to evaluate secondary fragmentation on broken ore within the plug flow zone in a draw column. Findings showed that hang-up potential was more sensitive to block strength than to block shape and block size distributions (primary fragmentation).

Comparisons of measured and predicted fragmentation results at Cadia East Panel Cave 1 (CEPC1), located at the Cadia Valley Operations, showed that DFN-based predictions of secondary fragmentation were significantly coarser than that measured using image-based methods (Brunton et al., 2016). The same study also found that BCF predictions of secondary fragmentation corresponded relatively well to coarser fractions of measured size distributions, however, for finer fractions it was found that the content of fines was considerably underestimated. Similarly, the content of fines was underpredicted by Core2Frag software for Forsterite and Forsterite-Magnetite skarn rock at the Grasberg Deep Ore Zone (DOZ) operation (Srikant et al., 2004). Although the importance of predicting cave fragmentation is well addressed by mining literature, there is a general lack of published results from cave fragmentation studies.

Image-based size analysis of caved material at drawpoints has been reported by Brown (2003) to be feasible, should there be sufficient lighting and minimum airborne dust. The quantification of fines is a known limitation of the method (Narendrula, 2004). Many operations, including the Grasberg mine in Indonesia, assess fragmentation based on human observations of certain size fractions (Srikant, 2006). Campbell and Thurley (2017) demonstrated a 3D laser scanning technique for size measurement of drawpoint muck at the Ernest Henry sub-level caving operation. Operational factors that serve as an indication of fragmentation include hang-up frequency, drawpoint availability and secondary blasting efforts (Tollenaar, 2008). Viera et al. (2014) propose a metric for secondary fragmentation, which is defined by the tonnage drawn

divided by the number of recorded secondary breakage events. Figure 2.4 shows a comparison of the tonnes drawn per secondary breakage event and the proportion of ore extracted from the draw column, directly related to height of draw (HOD), at the Esmerelda Sur Mine. From the graph it can be seen that less secondary breakage is required as draw columns are depleted due to the greater degree of secondary fragmentation taking place.

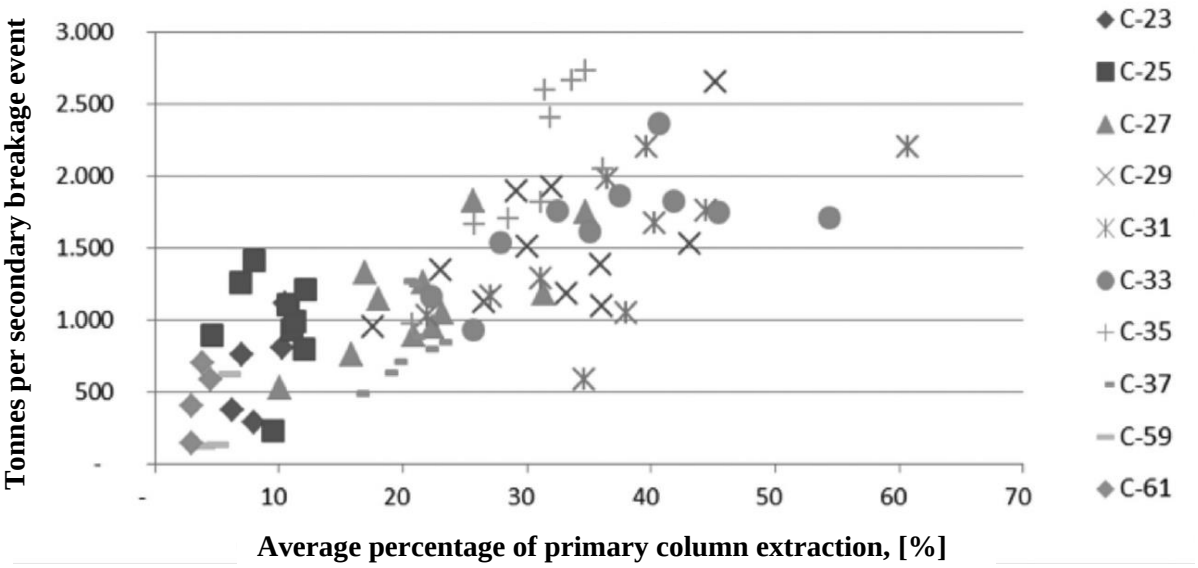

Figure 2.4 Relation of tonnes drawn per secondary breakage event and percentage extracted (Viera et al., 2014)

Comparing the outlined methods for assessing cave fragmentation, 3D laser scanning and digital image-based fragmentation programs are a solution to producing a size distribution curve that is relatively free from operator bias. The size distribution of blasted material is typically referred to as a critical parameter of Mine-to-Mill studies for open-pit operations (Burger et al., 2006 and Esen et al., 2007). Similarly, quantifying the size distribution of caved material is a key element of the proposed research, as it serves to verify the output of fragmentation models and is an important input to comminution models for downstream crushing and grinding equipment.

Pre-conditioning Methods

The ability of an ore body to cave is related to characteristics of the rock mass such as the nature of inherent discontinuities. Fracturing of the rock mass, using pre-conditioning methods (PC) is

typically carried out before undercutting competent rock masses to ensure that caving will initiate and continue at an acceptable rate. Since the production rate for a certain footprint is directly linked to the caving rate, the success of pre-conditioning methods has a significant impact on project economics. Early records of attempts at pre-conditioning date back to 1968 where hydraulic fracturing was carried out at the Shabanie Mine (Laubscher, 2000).

Chitombo (2010) states that pre-conditioning has proven to be a cost-effective means for cave inducement, improving caving rates and fragmentation, and will become an important part of cave mining in the future. The industry trend of applying intensive pre-conditioning is a marked changed from original applications of the block caving method where naturally fragmented ore was caved.

The Cadia East Mine is the first major panel caving operation to use both hydraulic fracturing (HF) and blast pre-conditioning (BPC), referred to as intensive pre-conditioning (Catalan et al., 2017). Figure 2.5 shows the sequence used for implementing pre-conditioning at Cadia East. The rock mass has a Mine Rock Mass Rating (MRMR) of 57 to 62, which is relatively high when plotted on Laubscher's (2000) graph of MRMR for historical cave mines. The blast design for ore located up to 130 meters above the undercut equates to a powder factor of 0.04 kg per tonne, which is approximately $1/10^{th}$ of the powder factor that is usually used for production blasts in open-pit mines. Similar to Mine-to-Mill practices at open-pit mines, intensive pre-conditioning was recognized by Newcrest Mining Ltd, the owner of the Cadia East Mine, as having the potential to improve mill performance (Newcrest Panel Session, 2012).

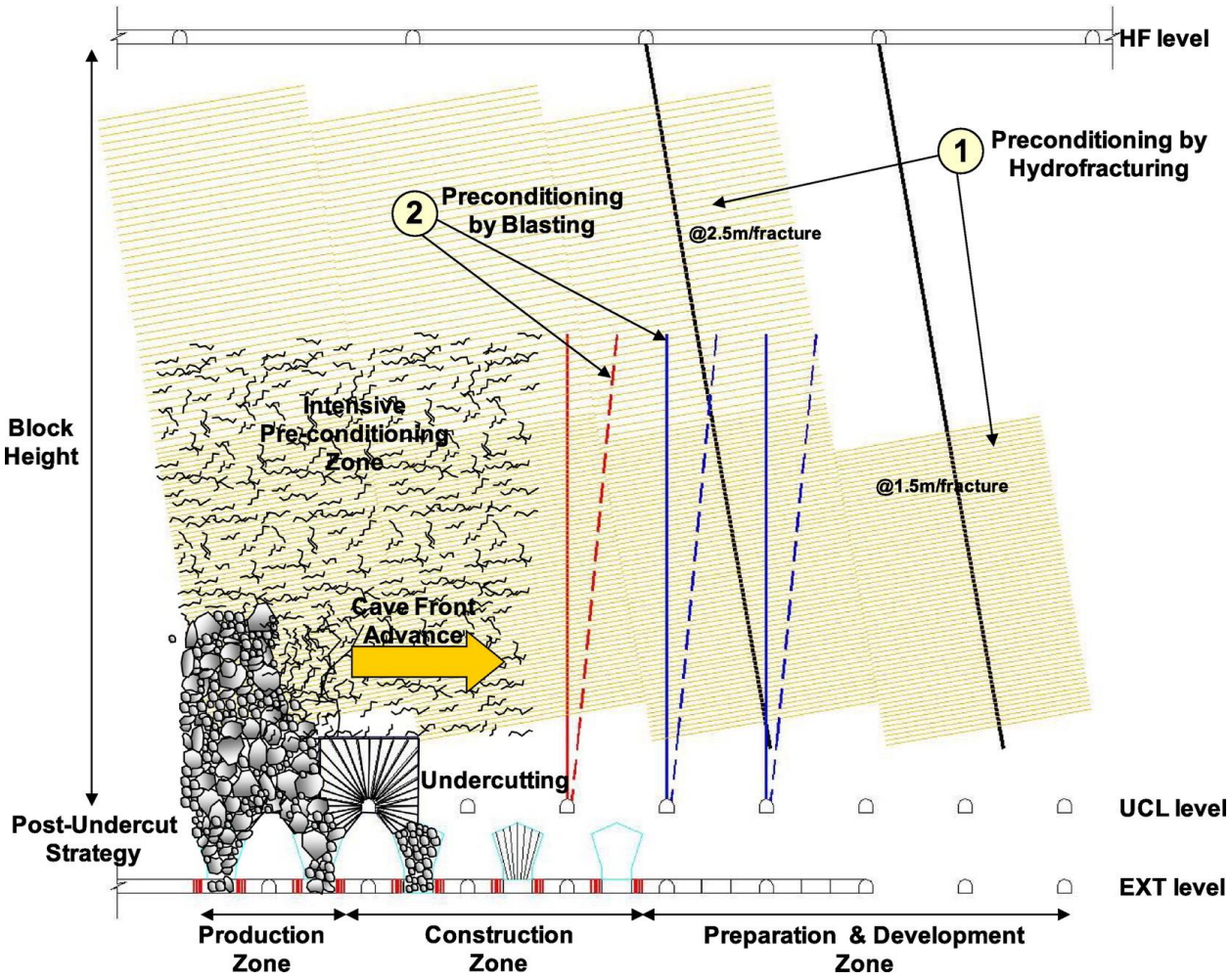

Figure 2.5 Sequence to implement intensive pre-conditioning at Cadia East (Catalan et al., 2017)

Catalan et al. (2017) found that hydraulic fracturing does not affect intact rock strength, while noticeable reductions in intact rock strength were attributed to blast pre-conditioning. Results of the study indicate that implementation of blast pre-conditioning has the potential to reduce crushing and grinding requirements. Hydraulic fracturing is considered by Catalan et al. (2017) to have a greater impact on enlarging existing discontinuities and creating macro scale discontinuities, thereby its influence is more noticeable on a rock mass scale. Pre-conditioning is considerably relevant to Cave-to-Mill, as it is an opportunity to coordinate confined blasting and/or hydraulic fracturing methods with cave productivity and mill operation.

2.6 Gravity Flow of Caved Material

As a rock mass fragments due to stresses in the cave back, individual rock fragments fall onto a pile of caved material and follow a flow path that is influenced by inter alia draw strategy, size distribution of the caved muckpile and undercutting rate and direction. Understanding the flow of broken ore is critical to be able to link the grade and properties of the in situ rock mass, which are characterized using samples from exploration drilling, to the quality of ore reporting to drawpoints during production.

A simplified representation of the flow regions of interest in a cross-section of the cave is presented in Figure 2.6. Interactive flow, as shown in the figure, is achieved when drawpoints are spaced close enough such that volumes of mobilized material overlap and an appropriate draw schedule is implemented. Isolated draw zones occur when drawpoint spacing is excessive or a drawpoint is drawn exclusively within a cluster of drawpoints.

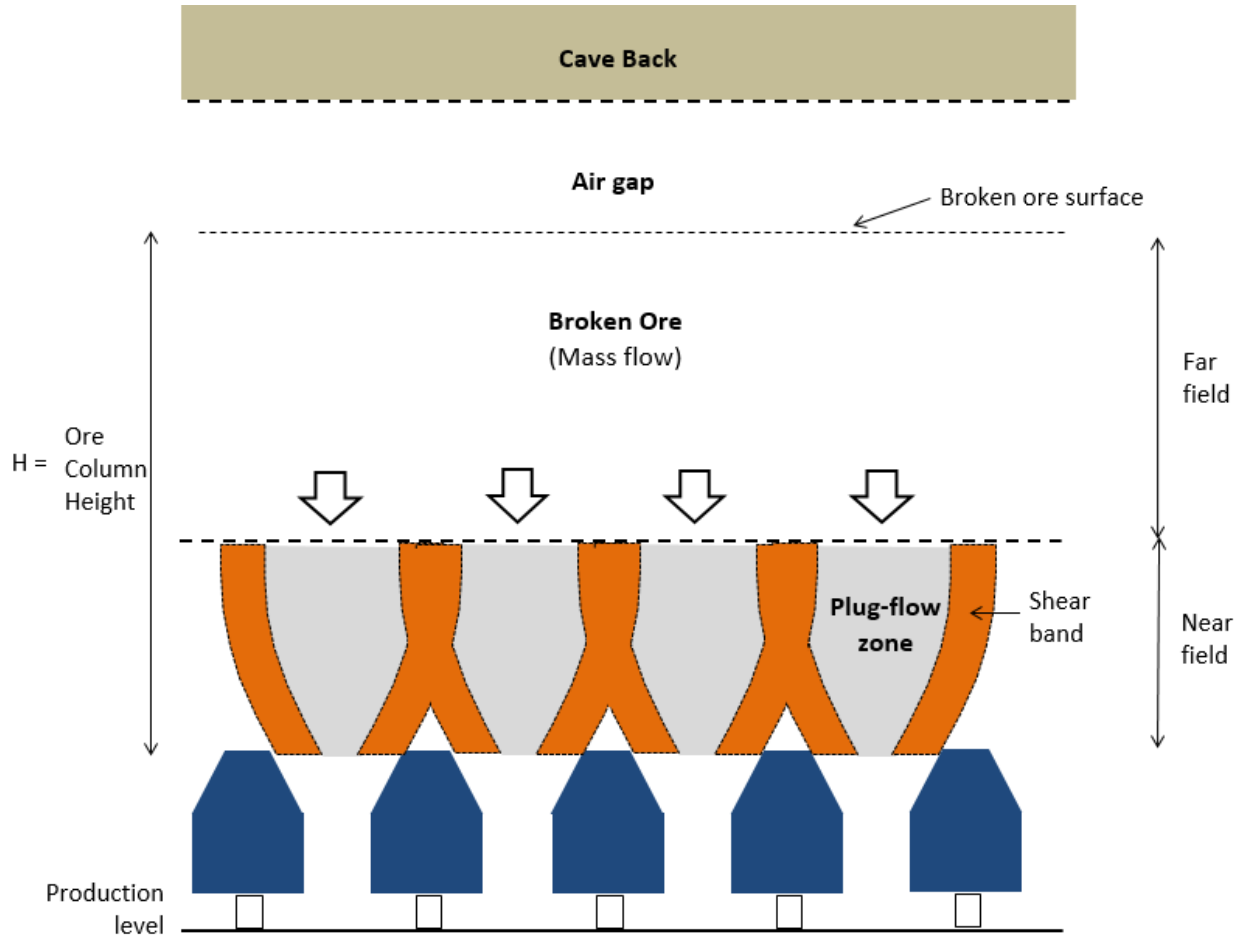

Figure 2.6 Conceptual flow of material in a cross-section of the cave (Dorador, 2016)

When drawpoints are drawn in isolation, rat holes occur with rapid introduction of dilution from waste overlying the ore body (Laubscher, 2000). Dilution entry is also known to occur due to horizontal movement of material. Paredes et al. (2014) state that lateral dilution entry occurs due to: 1) horizontal migration of waste from a laterally located waste boundary by rilling over the pile of caved ore, 2) lateral movement of waste due to inclination of the Isolated Movement Zone (IMZ) towards the waste boundary.

Various models for explaining the gravity flow of fragmented ore have been developed for application to block cave mines. Pierce (2010) developed a model for flow of fragmented rock for use in REBOP (rapid emulator based on particle flow code), a code originally developed by Cundall et al. (2000) that emulates particle flow interactions using observations from other models (physical and numerical). The Cellular Automata model, a stochastic model, uses

probability distributions to estimate the movement of blocks within the fragmented ore column (Alfaro & Saavedra, 2004). A 3D version of the model has been adopted for use in the PCBC scheduling package (Villa & Farías, 2016).

Recent developments in marker technology have significantly improved the quality of information available to track the flow of broken ore. Early efforts involved the use of tire markers such as old loader tyres and various steel tube designs (Talu et al., 2010). Markers were assigned unique IDs, placed in exploration shafts or left on undercut or extraction levels (in the case where a lift is planned below an existing cave). The use of Smart Markers, fitted with Radio-frequency identification (RFID) tags, was trialled at the Northparkes block cave mine and the Telfer sub-level cave mine. Scanners located in ore cross cuts, perimeter drives or orepasses, were used to link original Smart Marker locations to the drawpoints from which they were extracted (Whiteman 2010). Real-time monitoring of cave flow was presented by Whiteman et al. (2016), where Cave Tracker markers and detectors were placed in the in situ rock mass, as shown in Figure 2.7. The system was used to monitor the movement of markers in 3D at a time resolution of two days (Whiteman et al., 2016). Real-time monitoring of cave material allows production schedules to be refined daily so that favourable draw conditions are achieved. The technology has direct implications to cave management and the proposed Cave-to-Mill research.

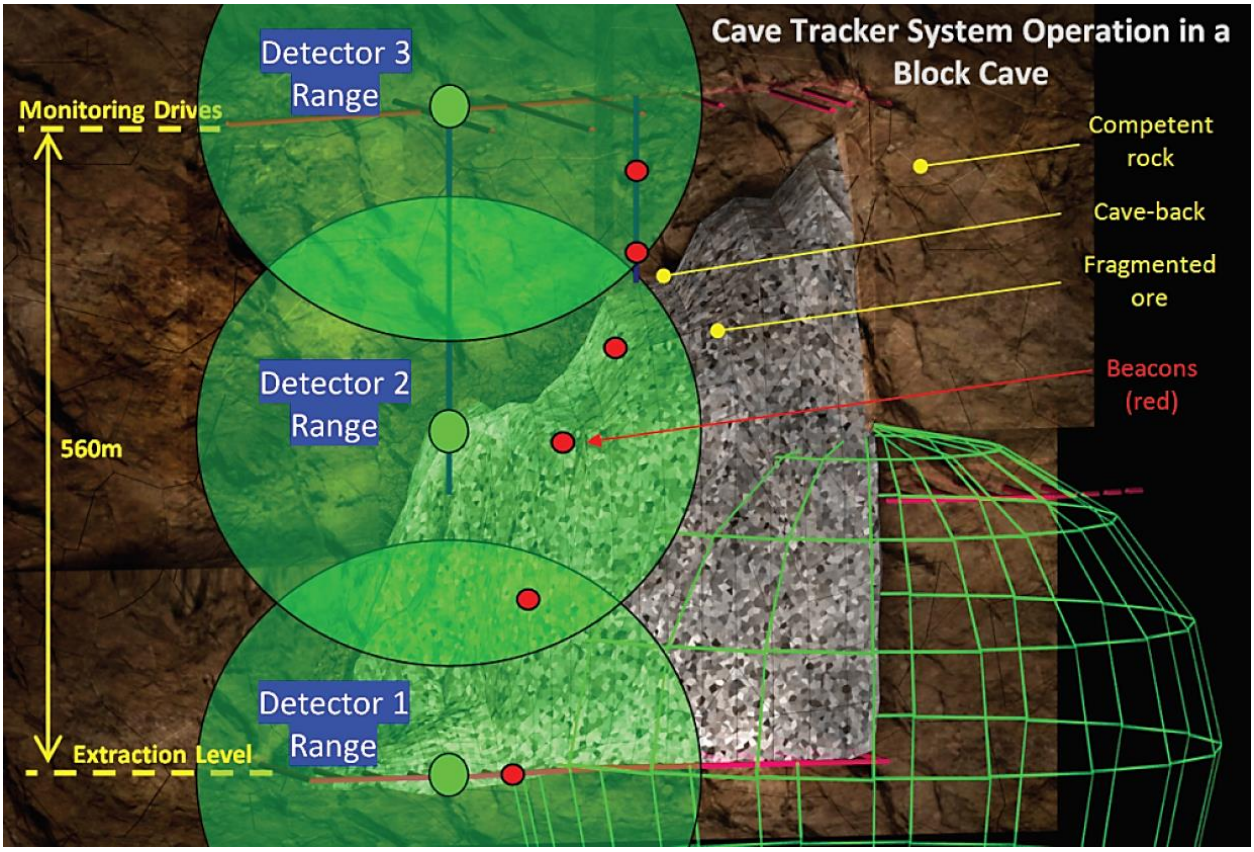

Figure 2.7 Cave Tracker detectors and beacons within fragmented muck pile (Whiteman et al., 2016)

2.7 Sensor-based Sorting

A growing number of mining operations are implementing sensor-based sorting technologies to pre-concentrate excavated material. Sensor technologies can be mounted on shovels, hoppers and conveyors, and sorted as bulk lots of material or on a particle-by-particle basis. Wyman (1966) presented a list of the necessary elements for successful mechanical sorting, they include: 1) a means of presenting the mineral pieces for examination; a sensing device for selecting the pieces to be removed; 3) an electronic system to act upon the information provided by the sensing device; and 4) a means of removing the selected pieces.

Sensor types for mineral applications include prompt gamma neutron activation analysis (PGNAA), optical, X-Ray transmission (XRT), X-Ray Luminescence (XRL), near-infra red, X-

ray fluorescence (XRF), electro-magnetic and radiometric sensors (Klein & Bamber, 2018 and Kobzev, 2014).

At Newcrest's Ridgeway Deeps mine, trials of a nuclear magnetic resonance (NMR) sensor for rapid (20 second) bulk sensing of chalcopyrite, the main copper-bearing mineral, showed that the technology has potential for use in a bulk sorting system through integration with a diverter (Coghill et al., 2018). Teck trialled shovel-mounted XRF sensors at their Highland Valley Copper operations to measure grade information in real time and instruct operators whether loads are to be sent to ore or waste stockpiles (Teck, 2018). Sensor technologies can be mounted on shovels, hoppers, conveyors and slurry systems (Van Haarlem, 2017), and sorted as bulk lots of material or on a particle-by-particle basis.

At the Priargunsky Mine in Russia, both bulk and particle sorting systems are used for beneficiation of uranium ore. On a bulk scale, the grade of material inside rail cars or dump trucks is measured using XRF sensors; material that is above cut-off grade is fed to XRF-based particle sorters for further beneficiation while low grade material is directed to a heap leaching site (Kobzev, 2014).

Ore sorting at the Khumani Iron ore operation is another example where both bulk and particle sorting technologies are combined. At Khumani, the grade of run-of-mine (ROM) material is measured with a PGNAA online analyser. Low grade ROM material is sent to waste stockpiles, intermediate grade material is sent to washing, screening and jig beneficiation circuits, and product grade material bypasses treatment and is sent directly to product stockpiles (Matthews & du Toit, 2011). An advantage of this arrangement is the reduction in capacity requirements of the beneficiation plant. Furthermore, the bulk sorting system reduces fluctuations in the grade of material being sent to the beneficiation plant, allowing the jig beneficiation circuit to be operated more effectively.

PGNAA grade sensors are also used at the Sepon copper-gold operations in Laos. Kurth (2017) describes the technology used at both Sepon and Khumani as having a source of neutrons, Californium-252 located under the conveyor belt, and the emitted neutrons are absorbed by

elemental nuclei in the material being transported on the conveyor belt. Each excited nucleus generates a gamma ray having an energy level related to the element from which it has been emitted; detector arrays positioned above the conveyor belt measure the energy of received gamma rays (Kurth, 2017). The measured elemental content of transported material is output to the plant control system that operates diverter gates within the material handling system.

The effectiveness of particle sorting systems relies on the use of grade sensing technologies that are suitable for the feed material (Rule et al., 2015 and Tong et al., 2015). In particle sorting applications, XRF sensors use the interaction of x-rays with rock surface material to determine its elemental composition. Sensor data is used in algorithms to infer the grade of the rock. A sorting decision is made based on the relation between the inferred grade and the setpoint cut-off grade. Sorting is typically carried out through use of blasts of compressed air, or mechanical paddles. XRF-based sorters have been used in precious metal, base metal, ferrous metal, industrial and rare earth ore applications (Tong et al., 2015). The capacity constraints of XRF-based particle sorters support the use of bulk sorting to reduce the quantity of material requiring beneficiation and thereby decrease the number of sorter modules operating in parallel.

Bamber et al. (2008) describe four key components of evaluating the feasibility of sensor-based sorting: ore heterogeneity, sensor response evaluation, sorting analysis and feasibility, as presented in Figure 2.8.

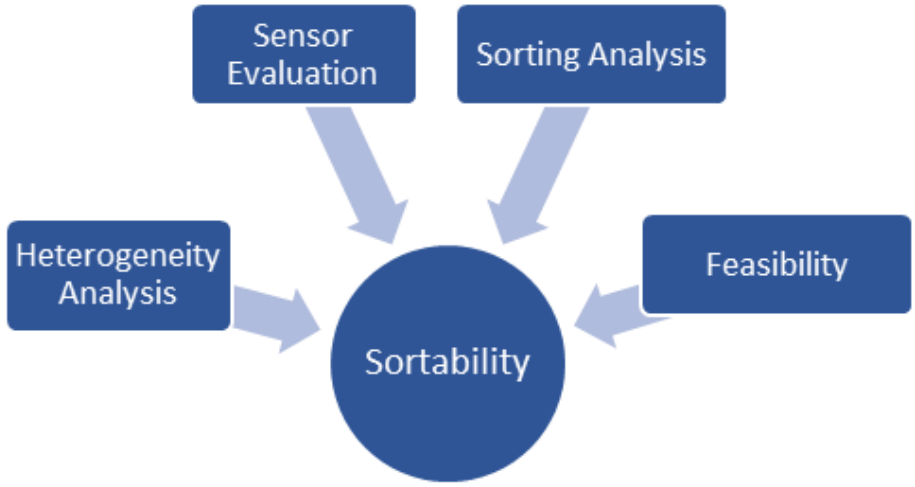

Figure 2.8 Sortability of ores (Klein & Bamber, 2018)

The natural grade heterogeneity of the material being assessed for sorting controls the limit of sorting potential (Duncan, 2016, Kobzev 2018 and Mazhary & Klein, 2015). Gy (2004) defines heterogeneity as occurring in two main forms:

Constitutional Heterogeneity (CH): The variation in the content of a certain component, for example copper or elements related to gangue minerals within individual rock fragments which make up an ore domain. Blending does not affect CH; however, CH increases with comminution.

Distributional Heterogeneity (DH): The variation in the content of a certain component, such as copper, within individual groups of ore (which report to draw-points or surface in a caving application). The sum of all of the groups makes up a lot. The DH parameter is considered to represent the potential to sort ore types at a bulk scale. DH can be reduced by blending ores but is not affected by comminution stages.

CH has been used as an indicator of particle sortability by Robben (2014), and Mazhary and Klein (2015), while DH shows potential for assessment of bulk sorting systems.

As a cave matures, it is expected that the large number of mixing events that have occurred within caved ore results in a lower variation in grade on a bulk scale, represented by a lower DH value, thereby reducing the potential for bulk sorting.

The nature of cave operations makes them ideal for incorporation of sensor-based systems to reject rock and allow the operation to become more dynamic. An integrated mine and mill approach will be necessary to coordinate mine schedules and beneficiation processes so that a satisfactory level of throughput and recovery can be achieved.

2.8 Cave-to-Mill Concept

Addressing the objective of improving block cave productivity, reviewed literature formed the basis of a proposed systems engineering approach for cave mine operations, termed Cave-to-Mill. Both mine and mill models are set up at the beginning of a project and continuously refined as the project progresses. Figure 2.9 shows how key aspects of a caving operation are linked so that a coordinated effort can be made to maximize Net Present Value (NPV). The presented Cave-to-Mill strategy focuses on its application to copper porphyry deposits, as the majority of present and future caving operations are based on excavating copper ores.

Focus areas and enabling technologies, highlighted in blue and green respectively, represent significant opportunities to improve the productivity of block caving operations by implementing these technologies in Cave-to-Mill.

The major objective of adjusting design and operational parameters within Cave-to-Mill is to maximize project value. A central component is the ore block model, which is continuously refined during project development and operation through input of geotechnical, geological and metallurgical information. At the exploration stage, initial access to an orebody is generally provided through exploratory drilling, allowing block models and design parameters to be established through analysis of core samples. As projects progress towards development, excavations and boreholes provide access to additional sample and data, which can be used to repopulate block models. Following plant commissioning, logs of mine and mill performance,

such as fragment size measurements and specific energy consumption of mill processes, can serve to calibrate predictive models and to refine block models.

The cave-to-mill approach is proposed for trial at a caving operation to quantify the benefits associated with its implementation.

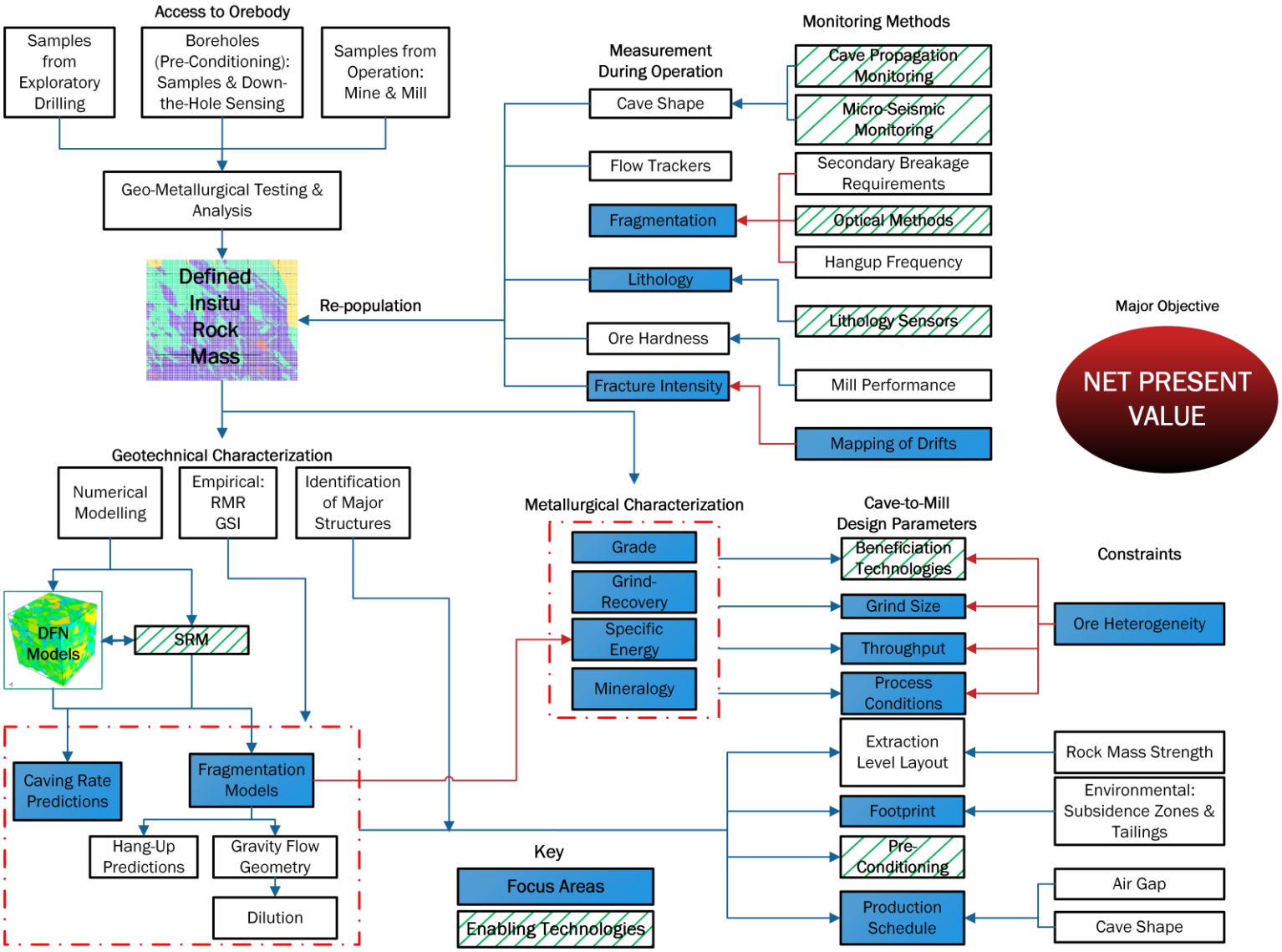

Figure 2.9 Cave-to-Mill Concept

2.9 Summary of Literature Review

Review of literature from seven areas of research was carried out with respect to the objective of developing Cave-to-Mill. A summary of key findings is included in this section.

Block and panel caving methods will be increasingly used in the copper-gold industry. Future caving projects will push the limits of applicability of the mining method in terms of increasing cave heights, caving of more heterogeneous ore bodies, and caving of deeper and more competent rock masses.

Significant benefits in the productivity of open-pit mines have been attributed to implementation of mine-to-mill strategies, where blast fragmentation and/or geometallurgical information were used for coordination of mining and processing activities. Many geometallurgical studies have shown strong correlations between geotechnical test data, which are in abundance in cave mines, and crushing/grinding indices.

Cave planning and scheduling software can be used together with geological block models, which include revenue factors such as mining cost and mill recovery to determine the associated value of a caving lift for an ore body. Conceptually sorting and geometallurgical models can be included in the block model as a Cave-to-Mill approach. Existing caving operations show that flexibility in production schedules exist, providing the possibility to control properties of the plant feed that affect mill performance.

Rock mass characterization methods are critical to block cave design and planning. Empirical and numerical approaches are required to confirm the suitability of cave mining for a proposed footprint and estimate caveability, subsidence angles, failure zone, fragmentation, undercutting sequences and support design.

Cave fragmentation size is a critical parameter that affects flow geometry, draw-point availability, sorting potential and crushing/grinding requirements. Application of caving methods

to competent rock masses necessitates the use of pre-conditioning methods, which present an opportunity to influence the size of feed to sorters and milling equipment.

Systems for tracking of fragmented ore in real-time have recently become available. In addition to reducing uncertainty in muckpile shape (above the extraction level), this development provides opportunity to track grade and geometallurgical properties of material through the cave, material handling system and up to the mill. For caving project evaluation, cave planning is still reliant on gravity flow models.

Grade heterogeneity is a key material characteristic that governs the opportunity to sort material. The capacity constraints of particle sorters supports the use of bulk sorting to reduce the quantity of material requiring beneficiation and thereby decrease the number of sorter modules operating in parallel.

Literature was reviewed with a focus on finding a means to improve block cave productivity. An outcome of the review was the development of a Cave-to-Mill concept that was put forward for trial at a block caving operation.

Chapter 3: Site Description and Methodology

3.1 Introduction

This chapter describes the methodology used to develop a Cave-to-Mill approach which targets improvements in cave mine productivity. Access to samples and data from an operating block caving operation was identified as a key requirement at the onset of the research. The New Afton block cave mine, located in British Columbia, Canada, was engaged for the research project and served as the main source of operational data and sample. Site visits were carried out by the research group to measure drawpoint muckpiles with image-based systems, collect samples and carry out mill surveys. Further detail of the New Afton mine and methodology used is provided in the following sections of this chapter.

3.2 Site Description: New Afton Mine

The New Afton Mine is a 17,500 tonne per day copper-gold operation. The mine officially commenced production in July, 2012. The B1 and B2 caves, which were in production at the time of this study, are located 615 metres below surface and their combined mining footprint is approximately 800 metres in length and 150 metres in width. The majority of the deposit occurs within crystalline and polylithic fragmental volcanics belonging to the Triassic Nicola Group and lesser monolithic intrusive breccias consolidated into a single-host package, which is informally referred to as BXF (Davies, 2015). A plan view of geological and structural features at the extraction level is shown in Figure 3.1.

The footwall and hanging-wall faults bound the deposit to the North and South respectively. Numerous faults, which in many cases are carbonate-healed, transect the deposit. The concentration of faults is significantly greater in the in situ rock mass of the B1 cave. Hypogene zones, where copper primarily exists in the form of copper sulphide minerals, and supergene zones, where copper primarily exists in the form of native copper, both occur within the BXF unit. A large picrite unit lies at the southwestern edge of the deposit, adjacent to the hanging-wall. The picrite is distinctly less competent than other rock types within the cave footprint. A

monzonite stock intrudes the south-central part of the deposit and represents the most competent rock type. In the eastern half of the deposit, the BXF is intruded by the diorite phase of the iron mask complex. The supergene is also hosted within the diorite intrusive.

The rock mass rating (RMR) of the economically viable portion of the deposit is in the order of 35 – 55 $RMR_{(1976)}$. Due to the presence of several fault structures, a lower mining rock mass rating (MRMR) of 40 is associated with the B1 cave while an MRMR of 45 has been reported for the B2 cave (Bergen et al., 2015).

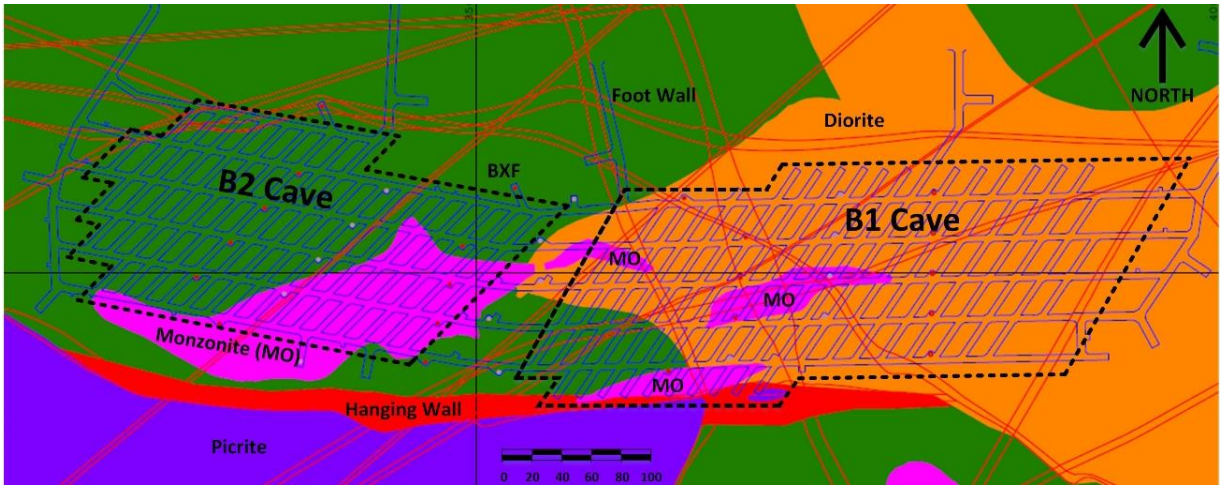

Figure 3.1 Geological and fault structures at the extraction level

A simplified flowsheet for the New Afton mine is shown in Figure 3.2. The mill feed consists of material that has been caved and mucked from drawpoints, dropped into orepasses, which are 25 m in length and 2.4 m in diameter, and fed to a gyratory crusher located at the haulage level. To generate finer mill feed, the gyratory crusher is operated at its smallest close-side setting of 90 mm. Crusher product is conveyed to a surface stockpile and fed by two interdependently controlled reclaim feeders to a SAG mill, which operates in closed circuit with a screen and a pebble crusher for treating screen oversize. Material segregation within the bed of material on the underground-to-surface conveyor results in coarser material being thrown further past the head pulley towards the northern reclaim feeder, while finer material discharges closer to the southern reclaim feeder. An expert control system is used to adjust the throughput rate of each of the two feeders, effectively blending coarser and finer material within the stockpile, to maximize

mill throughput performance. The feeder that handles coarser material is slowed down when the SAG mill circuit is throughput constrained and it is sped up when SAG mill throughput capacity is available; the feeder handling finer material is operated in the opposite manner.

SAG mill screen undersize is fed to a ball mill circuit. In 2015, a VTM3000 VertiMill was installed in a tertiary grinding role as part of a mill expansion. The target P80 size of the Vertimill cyclone overflow, which is the feed to rougher flotation cells, is approximately 145 microns.

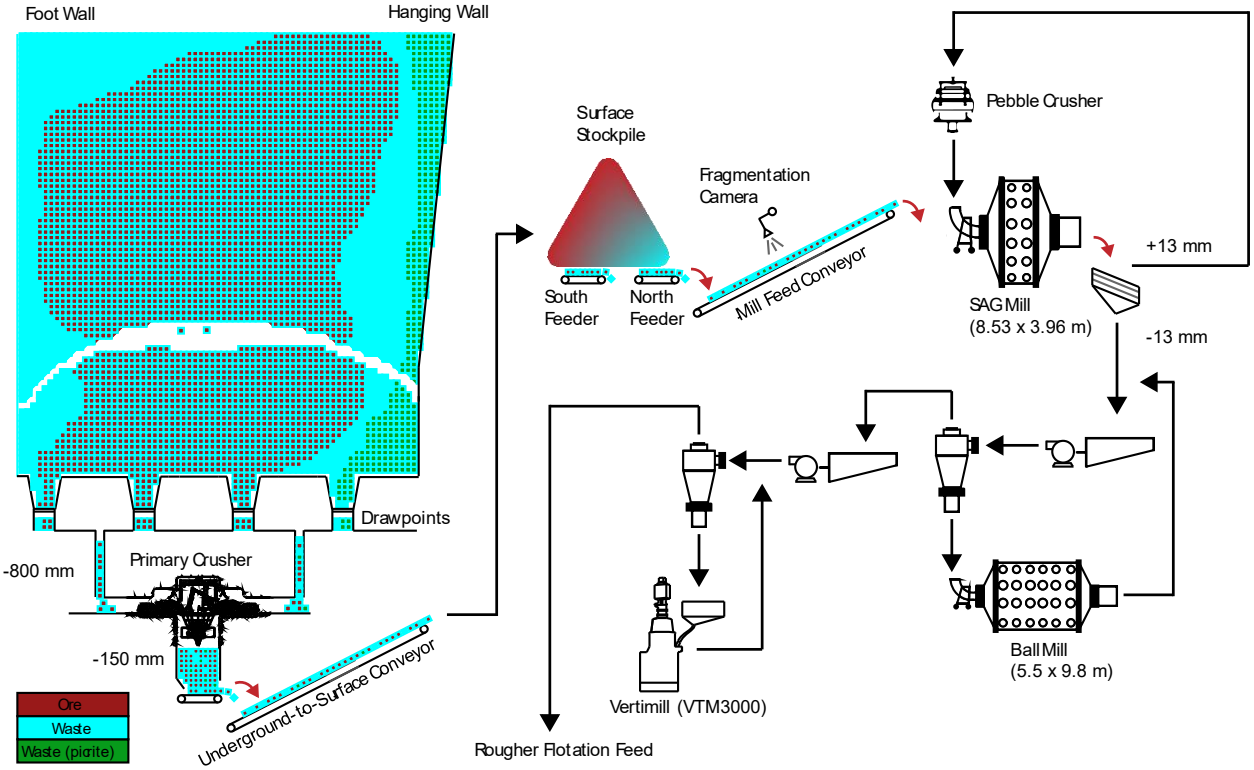

Figure 3.2 Simplified New Afton flowsheet

3.3 Fragmentation Measurements

Cave fragmentation is a key parameter within cave-to-mill that affects the extraction level layout (Laubscher, 2000), mixing within the cave, hang-up frequency (Tollenaar, 2008), mill performance (Condori et al., 2012) and the quantity of material available for particle sorting. To measure the size distribution of drawpoint muck at the New Afton B1 and B2 caves, image-

based methods, as used by Brunton et al. (2016) at the Cadia Mine, were used. Prior to taking photographs, scale reference markers were placed on muckpiles and portable lighting equipment was arranged to minimize shadow effects. The majority of images taken were processed with WipFrag^{TM} software. Edge delineation was carried out manually within the software for particles that were coarser than approximately 80 mm, amounting to approximately one hour of manual correction per image. Analysis of finer sizer fractions significantly extended the amount of time required for image delineation. An example of a muckpile photo and edge-delineation is shown in Figure 3.3.

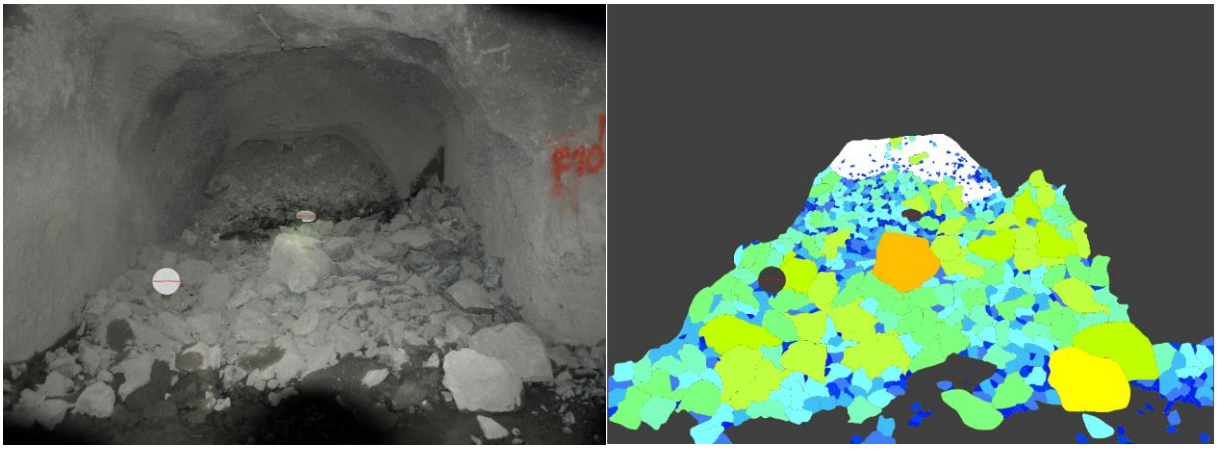

Figure 3.3 Fragmentation analysis of drawpoint F10N (taken on November 4th, 2013)

Overall, 79 photos were taken such that a range of lithologies, alterations and height of draws (HOD) were captured. The quantity of photos that could be taken and analyzed was limited by the amount of time required for manual correction of particle delineations generated by WipFrag^{TM}. Comparisons of fragmentation size and hang-up frequency, outlined in Section 4.6, showed similar trends with height of draw, supporting the approach used for image-based size analysis. PortaMetrics^{TM}, a portable fragmentation analysis tablet, which includes three high-resolution cameras, was used to analyse ten muckpiles. Figure 3.4 shows the model that was used for the study. In a previous study, good agreement between the outputs of PortaMetrics^{TM} and WipFrag^{TM} was found when manual delineation was used with the software package (Liu et al., 2015). Particle delineation was found to be improved with the PortaMetrics^{TM} tablet resulting in less time being spent on manual correction. Additionally, automatic scaling functions within the tablet meant that scale reference markers did not need to be placed on muckpiles.

Figure 3.4 PortaMetricsTM Tablet

The quantification of fines is a known limitation of image-based size measurement (Narendrula, 2004). To characterise the fines content of drawpoint muck, the -25 mm fractions from each drawpoint were sieved using a sieve shaker to a final screen size of 0.5 mm. Sieving methods were also used for three primary crusher product samples.

3.4 Drawpoint Sampling and Test Regimen

Over the course of the research, twenty-five drawpoints were sampled after photos had been taken for size distribution analysis using WipFrag software. Samples weighing approximately 50 kg for each drawpoint were shovelled from along the width of the base and mid-section of each drawpoint muckpile. Care was taken to collect samples from the full width of the muckpile. The sample quantities collected from each drawpoint and fragment size were limited by the practical constraints associated with shovelling samples into pails and transporting them with personnel/service vehicles. The top size of collected samples was approximately 150 mm.

Ross (2012) mentions that one of the sources of error associated with drawpoint sampling is the tendency for fines to flow around coarser fragments that are hang-up within a drawbell. Effectively, the coarse fragments behave like a sieve, resulting in size classification within the draw column. When sampling at New Afton, drawpoints that contained noticeably hung fragments were avoided to reduce the effect of size segregation on sampling.

Material from eleven drawpoints was used for a comprehensive test program, shown in Figure 3.5. Drawpoints were chosen such that each of the critical lithology and alteration types, in terms of impact on mine and mill operations, were collected. Surface samples were also taken during mill surveys so that mill models could be calibrated based on feed size and hardness, and mill performance. The results of two mill surveys were used to validate the mill models. The program included geotechnical, metallurgical and sensor-based sorting tests to characterize the ores for cave-to-mill modelling.

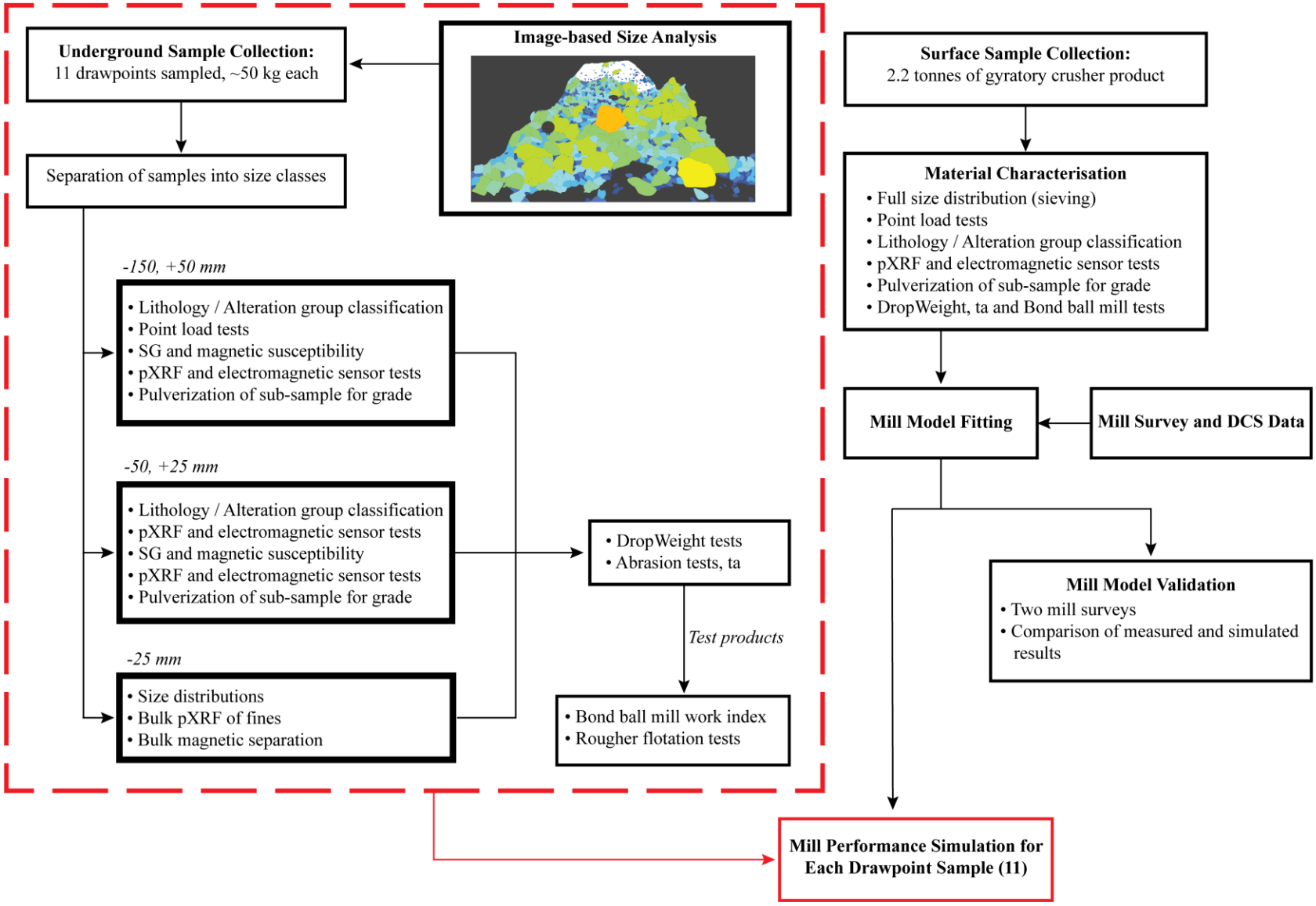

Figure 3.5 Test regimen for the core of the test program

3.5 Mill Sampling and Surveying

To estimate the change in mill performance due to variations in cave fragmentation size and material hardness, mill models were calibrated with New Afton mill survey data. The outputs of calibrated mill models could then be validated and used to characterize each drawpoint sample in terms of mill performance for use in the Cave-to-Mill approach. Sieving of collected mill feed samples also provided an indication of the quantity of fines in caved material, which could be linked to the cave fragmentation component of the study.

Two mill surveys were carried out in 2015 and 2016 for the cave-to-mill research program. Results from a later survey, carried out by Cebeci et al. (2017), were also made available for the study. Figure 3.6 shows the sampling points for the mill surveys that were used for this study.

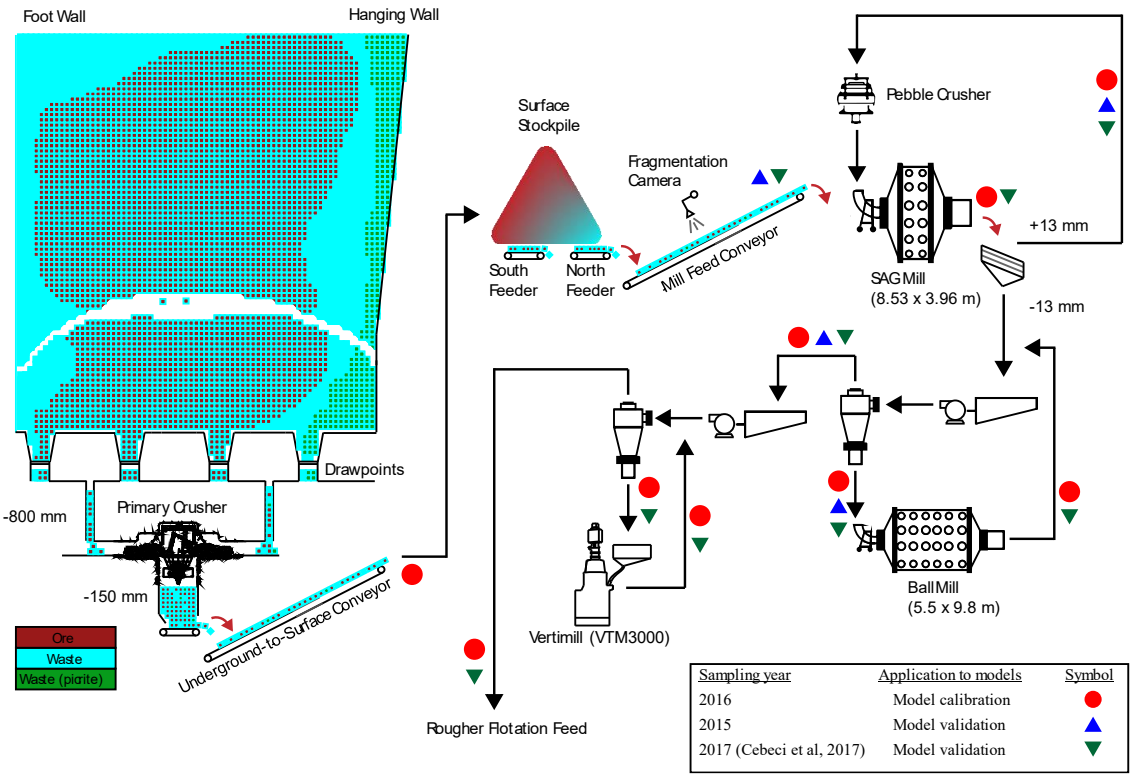

Figure 3.6 Simplified New Afton flowsheet and sampling points

For the 2015 survey, 0.7 tonnes of mill feed was sampled from the SAG mill feed conveyor, which is located below the mill feed stockpile. To avoid the effect of size segregation occurring

in the mill feed stockpile, the second mill survey (2016) involved sampling of 2.2 tonnes of rock that was diverted from the underground-to-surface conveyor, shown in Figure 3.7. Cebeci et al. (2017) collected 1.1 tonnes of mill feed from the mill feed conveyor and sieved the sample as part of a New Afton mill survey. Guidelines for surveying and sampling grinding circuits recommend that mill feed sample quantities be in the range of 500 to 1,500 kg (Global Mining Standards and Guidelines Group, 2016), which was met or exceeded by all three surveys. Data from the mill survey of 2016 was nominated for mill calibration, due to the large quantity of mill feed collected and number of sampling points sampled from within the grinding circuit.

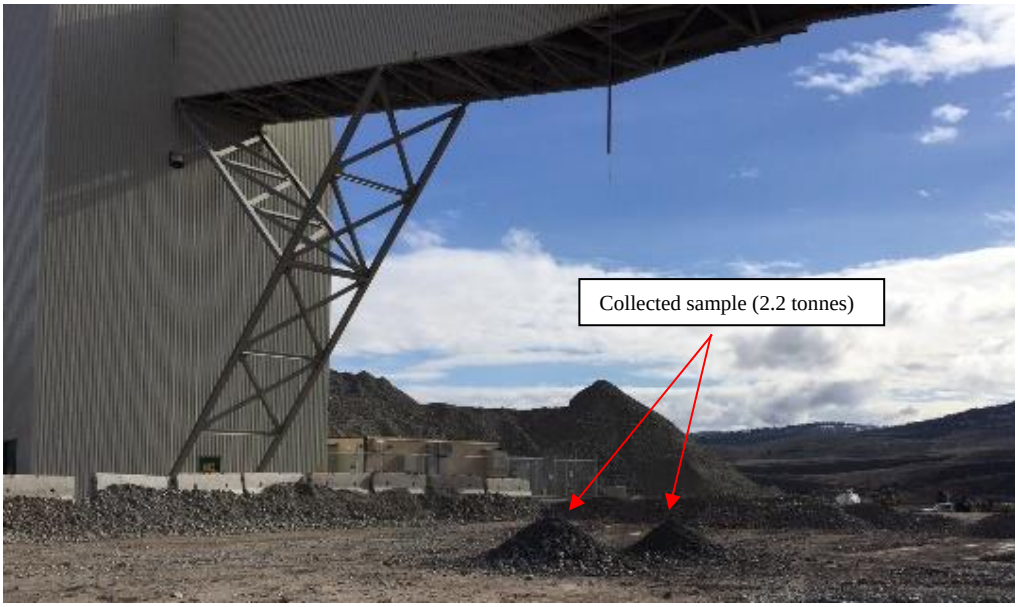

Figure 3.7 Diverted mill feed sample (2.2 tonnes) from the underground to surface conveyor. Sample collection for 2016 mill survey

For the 2016 survey, which was used for model calibration, the stockpile live capacity was estimated as being two-hours at the time of sampling. Approximately two hours after mill feed collection, samples from within the grinding circuit were taken at 15-minute intervals over the course of one hour; an exception was the pebble crusher feed, for which approximately 200 kg was taken just after the survey. Procedures for carrying out the survey were in line with guidelines for surveying and sampling grinding circuits (Global Mining Standards and

Guidelines Group, 2016). Collected samples were weighed, dried/filtered, sieved and used for the test program shown in Figure 3.5.

3.6 Primary Crusher and Mill Modelling

Calibrated crusher and mill models were used to estimate mill productivity for samples collected from drawpoints. The boundary limits for comminution modelling were defined as starting at the feed to the primary crusher and ending at the cyclone overflow of the Vertimill operating in a tertiary grinding role. A significant number of mine-to-mill studies have successfully made use of JKSimMet, a software package for simulation of comminution circuits, including that of Burger et al. (2006) and Kanchibotla et al. (2015). For the presented cave-to-mill research, JKSimMet was used to model the primary and pebble crushers, and the SAG mill within the New Afton circuit. The Anderson-Arachie-Whiten crusher model and the variable rates SAG mill model, included in JKSimMet, are based on population balance principles and separate equations are used for predicting power requirements (Foggiatto, 2017).

Crusher modelling

The primary inputs for crusher modelling included measured parameters:

- Feed size from image analyses and sieving of samples
- Appearance functions from DropWeight testing of samples, which define the product size distribution of a particle following crushing

and parameters that were fitted based on results from mill surveys, and crusher closed and open-side settings:

- Breakage parameter t10, which represents the proportion of product passing $1/10^{th}$ of the original feed size
- Classification parameters $K_{1\text{-}3}$, which define the size of material that is selected for breakage

SAG mill modelling

To apply the JKSimMet Variable Rates model to the New Afton fully-ported SAG mill, the guidelines of Bailey et al. (2009) were followed. Stark et al. (2008) found that experimental error in the DropWeight test method resulted in a coefficient of variation, which is the standard deviation divided by the mean, of 3.8% for JKSimMet throughput predictions in a SAG mill circuit. Two validation surveys were included in the test program to verify the accuracy of the calibrated model. Similar to the approach used for crusher modelling, measured ore parameters from sieving, DropWeight and abrasion testing were used along with SAG mill operational parameters as inputs to the variable rates SAG mill model.

Ball mill modelling

For the ball mill circuit, a Bond efficiency method, as published by the Global Mining Standards and Guidelines Group (2015) was used to calculate the Bond Standard Circuit Energy Factor, which is the ratio of the operating work index to the Bond ball mill work index of sampled mill feed. The efficiency factor could then be used for different material types.

$$Ball\ Mill\ Power\ (kW) = Bond\ Eff\ Factor\ x\ 10\ x\ tph\ \ x\ BBWI\ \left(\frac{kWh}{t}\right) x\ \left(\frac{1}{\sqrt{P80}} - \frac{1}{\sqrt{F80}}\right) \quad \textbf{(3.1)}$$

Where Ball mill power includes drivetrain inefficiencies, F80 and P80 are the 80% passing sizes of SAG mill screen undersize ball mill cyclone overflow respectively in microns. BBWI is the Bond ball mill work index determined for sampled material and tph is the rate of fresh feed to the circuit.

Vertimill modelling

To model the Vertimill, operating in a tertiary role in the New Afton grinding circuit, operational data and Bond ball mill work indices for sampled ore were reviewed. Results showed that the Vertimill main motor power draw is approximately 62% of the power draw of a ball mill that is carrying out the same comminution duty, shown in Figure A1 of the appendix. Efficiency factors from Rowland (1982) were applied to account for the low reduction ratio (< 2) associated with the tertiary grinding duty and the use of modern larger diameter mills (> 3.81 m diameter). Ball

mill drivetrain efficiencies of 97% for the gear reducer and 96% for a wound rotor induction motor were assumed based on Doll and Barratt (2010). The following is the resulting equation for relating Vertimill power draw, as measured at the DCS, feed F_{80} and product P_{80} sizes:

$$Vertimill\ power\ (kW) = \text{0.62 x Ball mill power (kW)} \quad \textbf{(3.2)}$$

$$= 0.62\ x\ 10\ x\ tph\ x\ Eff_3\ x\ Eff_7\ x\ BBWI\ \left(\frac{kWh}{t}\right) x\ \left(\frac{1}{\sqrt{P80}} - \frac{1}{\sqrt{F80}}\right) x\ \frac{1}{0.96\ x\ 0.97} \quad \textbf{(3.3)}$$

Where F_{80} and P_{80} are the 80% passing sizes of ball mill cyclone overflow and Vertimill cyclone overflow respectively. Eff3, equal to 0.914, corrects calculated power draw to account for improved energy performance of modern larger diameter mills (> 3.81 m). Eff. 7 is applied to correct power draw for low-reduction ratios (< 6), determined by:

$$Eff_7 = \frac{\mathbf{2\ (R_R - 1.35) + 0.26}}{\mathbf{2(R_r - 1.35)}} \quad \text{(Rowland, 1982)} \quad \textbf{(3.4)}$$

Where Rr is the reduction ratio, F_{80} divided by P_{80}.

For each feed size and material type, the calibrated comminution models were able to be used to determine associated mill throughput and energy performance. Thereby, changes in the quality of caved ore could be related to fluctuations in mill productivity, an aim of cave-to-mill.

3.7 Rock Type Specification and Characterization

At the beginning of the test program, collected drawpoint samples were sieved into three size fractions (+50, – 25, and -50, +25 mm). Rocks coarser than 25 mm were washed, individually marked with a unique ID number and subjected to the test program with the objective of compiling a large database of information that could be referenced for the cave-to-mill program. An example of rock classification is presented in Figure 3.8. Following washing and inspection of the collected samples, a rock classification system was developed to group rocks according to their lithology or type of alteration. For rocks between 12.5 and 25 mm in size, the mass

proportions of each rock type were measured. Table 3.1 shows the criteria established to define each rock type.

Table 3.1 Guideline for macro-description of rocks

Rock Group #	Lithology / Alteration Code	Characteristics	Ore / Dilution
1	Hypogene	Biotite dominant. K-Spar*< 20%	Ore (high grade)
2	Picrite	Talc (soapy texture). Serpentinised.	Dilution
3	Hypogene	50 > K-Spar > 20%	Ore (medium grade)
5	KK	K-Spar > 50%	Ore / Waste (monzonite)
6	Fault Rock	Round. Very soft. Alteration obscured	Dilution
7	Carbonates	White or clear carbonate minerals	Dilution
8	Supergene	Visible iron oxides (red)	Ore

*K-Spar: Observable potassium feldspar

Figure 3.8 Collected +50 mm samples from drawpoint D11N

The specific gravity of each (+25 mm) rock was recorded using the buoyancy method and a rare earth magnet was used to identify magnetic rocks.

3.8 Sensor-based Sorting

The lack of selectivity and potential for dilution entry associated with the block cave mining methods results in both ore and waste being caved and transported through material handling systems to the surface for processing. Sensor-based sorting systems provide an opportunity to automate the discrimination between ore grades and rock types, providing an enhanced level of selectivity for ore control and thereby improving mine productivity, an objective of cave-to-mill.

A combination of bulk and particle sorting systems was considered for trial at New Afton based on a similar approach used at the Priargunsky Mine in Russia. For the bulk sensing application, PGNAA technology was trialled as a solution to measuring the grade of material being conveyed from underground to surface and diverting bulk lots according to copper grade. An advantage of PGNAA technology over other sensor technologies is its ability to measure the grade of material within the bed of rock on a conveyor, while a disadvantage is the long sensing time (typically 0.5 to 2 minutes) required to record a suitably accurate grade measurement.

For the particle sorting application, the amenability of XRF technology to New Afton ore was tested. The XRF test method relies on surface grade measurements for estimations of whole rock grade. Potential alternatives to XRF technology includes XRT sensors, however Mazhary (2017) found that the presence of iron minerals decreases the grade-sensing efficiency of XRT sorters when the metal of interest is of a similar atomic density. At New Afton, iron oxides in the form of hematite and magnetite occur in abundance and do not have a reliable association with either copper grade or waste. An XRF sorting study by Tong et al. (2015) on copper porphyry material from the Spence Mine in Chile indicated that XRF surface measurements could be used for effective pre-concentration.

Bulk Sorting

As a separate test component, PGNAA bulk sensing test work was carried out using sample from drawpoints, mill feed and waste stockpiles. Each sample weighed approximately 220 kg. Overall, a wide range of copper grades and rock types were prepared.

The grade of each bulk sample was determined by crushing and screening to 100% passing 9.5 mm, homogenizing, sub-sampling, and assaying sub-samples with inductively coupled plasma (ICP) spectrometry and fire assays. The nine samples were sent to Scantech testing facilities in South Australia for testing with a Geoscan-M unit, shown in Figure 3.9, which was fitted with four detectors. Assay results were provided for six of the nine samples, while the remaining three were treated as blind samples. During testing, samples were placed on a section of New Afton conveyor belt provided by the mine to account for any influence of belt material on sensor response. Since the accuracy of the PGNAA sensor system is not affected by particle size (Kurth, 2017), results for the -9.5 mm test samples could be used to evaluate application of the technology with New Afton ROM material.

A sub-sampling and crushing procedure was established referencing François-Bongarçon and Gy's (2002) sampling method. The maximum error associated with sub-sampling was recorded for both copper and gold using the following formula from François-Bongarçon and Gy (2002):

$$S_{FSE}{}^2 = \left(\frac{1}{M_s} - \frac{1}{M_L}\right) fgcld^3 \quad \textbf{(3.5)}$$

where $SFSE^2$ is the sampling relative variance, M_s and M_l are masses of the sample and lot respectively. Constants f and g, which are usually set to 0.5 and 0.25 respectively, are 'convenience' constants, c is the mineralogical factor, d is the nominal size of the rock fragments (95% passing size), and l is the liberation factor.

From grind-recovery performance in the regrind circuit of the process plant, the liberation size, used to determine the liberation factor in equation 3.5, was assumed to be 35 microns for copper-sulphides and gold. Quantitative Evaluation of Minerals by SCANning (QEMSCAN) analyses indicated a copper-sulphide liberation size of approximately 20 microns. A gold deportment

study indicated that the majority of liberated gold is in the size range of 10 to 75 microns (AMTEL, 2006). An analysis of native copper deportment showed that approximately 50% of native copper was in the sub-10 microns size fraction while 40% was coarser than 200 microns (AMTEL, 2006). A conservative liberation factor of 500 microns was assumed for supergene ore. The sub-sampling procedure provided relative standard deviations of less than 1% for copper and less than 25% for gold.

Figure 3.9 Sample being loaded into Geoscan-M with conveyor belt cut-off (Balzan, 2016)

Each sample was measured for a period of at least three hours. During the three-hour measurement time, individual instantaneous analysis periods were varied throughout the test work to achieve a number of results for different measurement periods. The expected accuracy of a Geoscan-M unit when installed on a conveyor could then be estimated for different measuring times (which are directly related to the quantity of conveyed material).

Sensor-based Particle Sorting

An Olympus model 500316 XRF unit, mounted in a tripod stand, was used to measure the elemental content of surface rocks. Samples were separate from those used for PGNAA testing and consisted of material taken from drawpoints and mill feed stockpiles.

XRF measurements were carried out on the surfaces of 1,226 rocks in the (-150, +25 mm) size range using a measuring time of 10 seconds. For each individual reading, the pXRF unit measured the elemental content of material located on the surface of the rock within a circle having a diameter of 1 cm. Four readings were taken per rock. From the master set of 1,226 rocks, 291 rocks were selected based on rock type and subjected to crushing and pulverizing. A representative sub-sample of the finely pulverized material was measured with the same pXRF unit to determine the grade of each rock.

To calibrate the pXRF unit, ICP measurements and pXRF measurements were carried out on 20 pulverized New Afton rocks. A coefficient of determination, R-squared, of 0.999 resulted from comparison of ICP and pXRF results for copper.

3.9 Cave and Mill Comminution Testing

Comminution processes occurring within the cave and the mill were relevant to the research program, and thus accounted for in the test regimen. Eleven drawpoint samples and one mill feed sample were characterized with the whole comminution program which included Point load, DropWeight (JK Tech, 2016), low-energy abrasion tests (JK Tech, 2016) and Bond ball mill work index testing.

Due to the importance of proper geotechnical characterization of rock masses being considered for caving, an abundance of point load strength data is typically available for caving projects. In the case that point load data correlates to milling parameters, such as DropWeight Indices, a database of point load variation within the orebody is very relevant to the proposed Cave-to-Mill approach. Published work by Burger et al. (2006) showed that useful correlations between the Point Load Index $I_{s(50)}$ and DropWeight Indices can be found for some deposits. Advantages of the Point Load Index (PLI) test are the relatively low test costs and short turn-around time in comparison to DropWeight type breakage tests. The test program provided opportunity to investigate for correlations between point load strength, muckpile size distributions and metallurgical performance.

Point Load Tests

Following sensor-based testing, point load tests were carried out according to ASTM standards for lump rock (ASTM, 2013). Tested rock samples were generally in the size range of -100, +50 mm. Overall, samples from twenty-four drawponts were tested (of which eleven were used for the full metallurgical program). Approximately 30 rocks were tested per drawpoint sample.

DropWeight Testing

Following point load testing, sub-samples were sieved at 63 mm, which is the coarsest size of material used in a standard JK Drop Weight test (JKTech Pty Ltd, 2016). Results were used for crusher and SAG mill modelling within JKSimMet. For drawpoint samples, an abbreviated form of the DropWeight test was used to conserve sample for the sensor-based sorting scope of work. The abbreviated dropweight test was based on the SMC method, where five energy levels are tested using one feed particle size range (SMC Testing, 2018). Testing with mill feed sample was used to determine the relationship between feed size, energy and product size, t10.

Figure 3.10 JK DropWeight test unit at the NBK Institute of Mining Engineering

For each drawpoint sample, 150 particles were selected in the size range of -31.5, +26.5 mm and their individual weights were recorded. Based on the weight distribution of particles, rocks were grouped into heavy, medium and light groupings. The standard JKDropWeight test regimen involves random selection of a group of similarly sized rocks for breakage at an equivalent impact energy. To generate product for one energy-size combination, the height of the drop weight is selected so that a target specific energy input kWh/t is achieved based on the mean particle mass (typically 10 or more particles are used per energy-size combination). Due to variations in particle mass, this method results in particles experiencing specific energy inputs that are above and below the setpoint. To reduce the variation in specific energy input to test sample, particles were grouped into high, medium and light masses such that the overall error in specific energy input would be minimized. An example is shown in Table 3.2. A detailed description of the abbreviated DropWeight test method is described in Appendix B.

Table 3.2 Specific energy and size summary for DropWeight testing

Target specific energy level, kWh/t	Size range, mm	Particle weight grouping
2.5	-31.5, + 26.5	Heavy Medium Light
1.8	-31.5, + 26.5	Heavy Medium Light
1	-31.5, + 26.5	Heavy Medium Light
0.5	-31.5, + 26.5	Heavy Medium Light
0.25	-31.5, + 26.5	Heavy Medium Light

Abrasion Tests

Standard ta abrasion tests were carried out using a JK abrasion mill having approximate dimensions of 1 ft diameter and width. Tests were carried out according to the test procedure (JKTech Pty Ltd, 2016), which was as follows:

Three kilograms of -53, + 37.5 mm sample was processed in the mill for ten minutes at a speed which is equivalent to 70% of critical speed for the internal mill dimensions. Products were sieved to find the percentage passing $1/10^{th}$ of the feed size. The abrasion parameter ta, was reported as the product t10 divided by 10. An energy meter connected to the unit indicated an approximate specific energy input of 1 kWh/t per test run. Results from abrasion testing were used within JKSimMet for SAG mill modelling.

Bond Ball Mill Work Index Tests

Ball mill and Vertimill models relied on outcomes from the Bond ball mill test method. Drawpoint and mill feed sub-samples were crushed to -3.35 mm and subjected to the standard Bond ball mill test method (Bond, 1962). Care was taken to ensure that mass-weighted proportions from each size fraction were taken for Bond ball mill testing. ALS Metallurgy in Kamloops, BC carried out twelve Bond ball mill work index tests as an in-kind contribution to the study. Approximately 7 kg of sample was required per test.

Separate from the presented cave-to-mill research, New Afton mine had regularly conducted Bond ball mill tests using a closing screen size of 106 microns. The same closing screen size was nominated for the test program to be able to compare results to historical grindability data.

3.10 Block Cave Planning and Scheduling

The PCBC^{TM} module within GEMS GEOVIA software, version 6.8.1 package (Dassault Systèmes, 2018) was used for cave planning and production scheduling. Block models provided by New Afton were used in combination with outcomes from fragmentation and sensor-based sorting studies. For each block of ore, Net Smelter Return (NSR) calculations were carried out

using the block manipulation editor which is available within GEMS GEOVIA. Scripts were written in Cypress Enable Language (CEL), as accepted by the software.

For the case where sorting systems were investigated, block attributes were created to represent:

- Proportion of each block accepted to high grade, intermediate grade or waste stockpiles
- Recovery of contained copper and gold within each block to its designated stockpile
- Resulting grade of material sourced from a block following sorting
- Flotation recovery of copper and gold as a function of block grade following sorting

Addition of the above attributes allowed sensor-based sorting and flotation recovery parameters to be included in the cave planning and production scheduling solution. A mass balance was carried out at the end of each production scheduling run. Further information on the steps taken is included in Chapter 8.

Chapter 4: Predicting Cave Fragmentation and Hang-Up Frequency

4.1 Introduction

The size of caved rock fragments has significant implications to the profitability of caving operations. Predictions of secondary cave fragmentation, representing the size of material reporting to drawpoints, are a key input to extraction level design and cave evaluation at the project development stage. Furthermore, knowledge of the size of mill feed is critical for accurate equipment sizing. Even though a significant amount of effort may be directed towards estimating cave fragmentation at the beginning of a block cave project, these models tend not to be reliably calibrated and referenced for ongoing mine planning and scheduling activities. Advances in the prediction of cave fragmentation stand to significantly reduce the risk associated with caving projects.

With the objectives of Cave-to-Mill in mind, drawpoint samples, measurements and operational data from two caves at the New Afton operation were analysed to gain a better understanding of the fragmentation associated with the footprint. Results of the analysis could then be applied at the project design and evaluation stages for future caves being considered within the New Afton deposit.

The differences in fragmentation size at the New Afton Mine can be attributed to variation in the geological composition of caved rock. A method to identify rock types relevant to fragmentation size, using data available in the ore block model, was established. Consistent with other reported studies on the topic, finer drawpoint muckpile size distributions were measured for material that had travelled a greater height through the ore column, referred to as Height of Draw (HOD). *Block Cave Fragmentation (BCF)* software (Esterhuizen, 2005), version 3.05, predictions were found to be in-line with measurements for aperture sizes coarser than 0.5 m. However, significant deviations were apparent for the cumulative percentage passing of sizes finer than 0.3 m.

A comprehensive fragmentation study involving two image-based measurement methods, WipFrag™ (WipWare Inc., 2017) and PortaMetrics™ (Motion Metrics International Corp., 2017), as well as sieving of muck was carried out as a component of the cave-to-mill research program being conducted at New Afton. A cave-to-mill project team member, Mukhtsolmon Munkhchuluun, developed a Discrete Fracture Network (DFN) model for the in situ rock mass of the B2 (West) Cave. Correlations between fracture intensity and hang-up frequency were apparent.

A distinguishing feature of the fragmentation study is the abundance of sample characterization data available for drawpoint muck samples that had been measured using image-based techniques, inter alia, X-ray Fluorescence (XRF) measurement for sensor-based sorting evaluation, comminution test work for mill performance prediction and point load testing.

4.2 Fragmentation Measurements

Measurements of the size of caved rock fragments located at drawpoints of the B1 and B2 caves were taken using an image-based approach. Prior to taking photographs, scale reference markers were placed on muckpiles and portable lighting equipment was arranged to minimize shadow effects. Overall, 79 photos were taken such that a range of lithologies, alterations and height of draws (HOD) were captured. Table 4.1 shows the number of images that were analysed for different ranges of HOD.

Table 4.1 Summary of draw point muck images

B2 Cave (West Cave)			B1 Cave (East Cave)		
Height of Draw Range [m]	**Average Height of Draw [m]**	**Number of Images [#]**	**Height of Draw Range [m]**	**Average Height of Draw [m]**	**Number of Images [#]**
9 - 14	12	8	23 - 35	29	6
14 - 40	24	8	35 - 62	52	7
40 - 62	52	9	62 - 90	72	6
62 - 98	74	8	90 - 140	112	7
98 - 120	107	5	140 - 180	164	4
120 - 190	151	12			
190 - 289	239	9			

In order to determine the content of fines (-10 mm material) within caved muck, two bulk samples of gyratory crusher product were collected and sieved. In 2015, 0.7 tonnes were sampled from a mill feed conveyor, which is located below the mill feed stockpile. To avoid the effect of size segregation occurring in the mill feed stockpile, in 2016 a second sample of 2.2 tonnes of rock was diverted from the underground-to-surface conveyor, collected and sieved. Huang et al. (2017) collected 1.1 tonnes of mill feed from the mill feed conveyor and sieved the sample as part of a New Afton mill survey. Figure 4.1 shows size distributions for measured secondary fragmentation and sieving results for gyratory crusher products. Secondary fragmentation for picrite, reporting to drawpoints located near the southern boundary of the cave, was generally found to be finer, while coarser fragmentation was associated with monzonite rock. The remaining rock types, hypogene and phyllic-altered rock, were grouped based on similarities in fragmentation size.

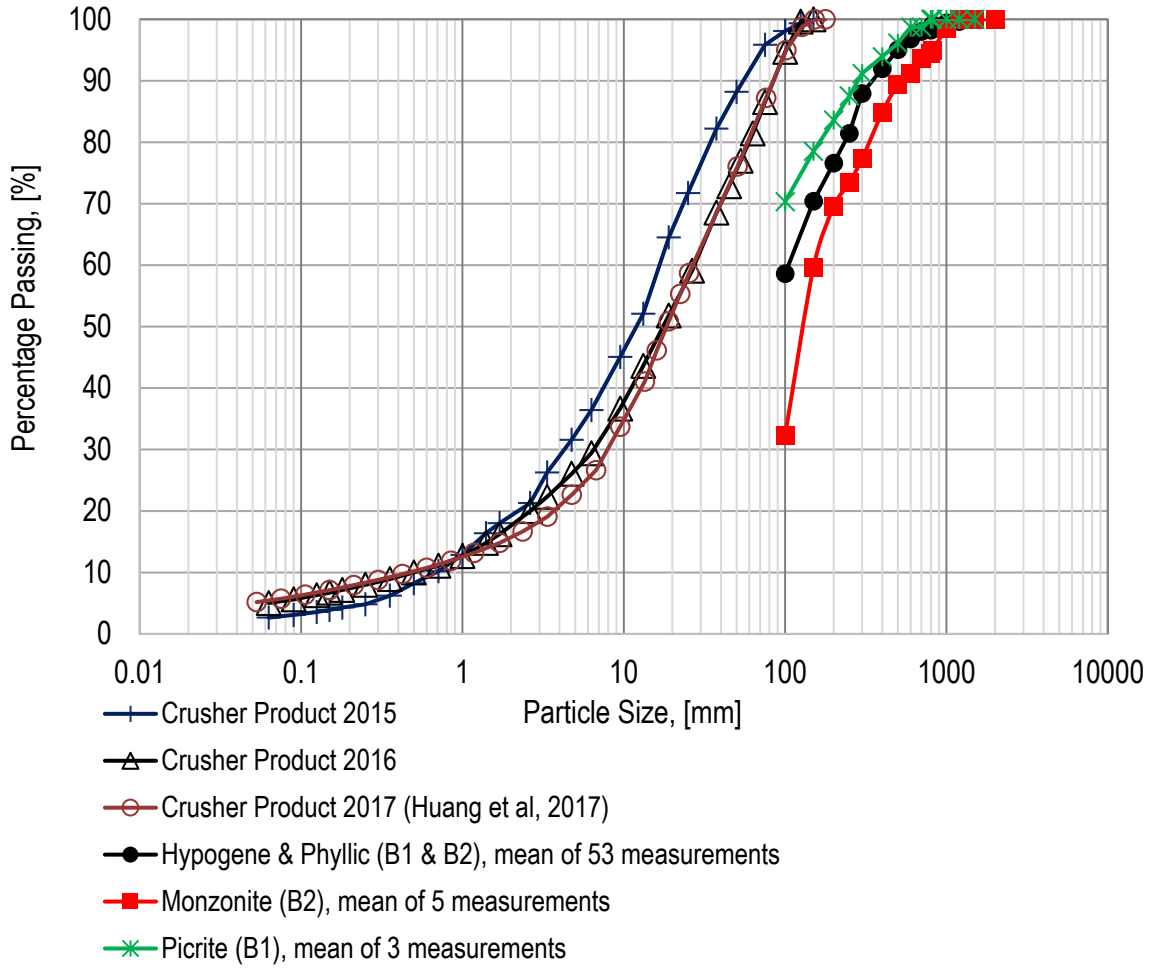

Figure 4.1 Size distribution curves for secondary fragmentation at New Afton

4.3 Comparisons with Block Cave Fragmentation (BCF) Predictions

Comparisons of predictions from BCF software and measurements are shown in Figure 4.2. The program does not account for the influence of undercut blasting on fragment size. For this reason, outputs of the program for material that was taken below the back of the undercut were not compared to measurements of drawpoint muck.

The presented data is relevant to the central area of the B2 cave where hypogene material is predominantly collected. Size distributions for measurements taken underground were grouped with respect to their corresponding HOD, which was estimated using the PCBC^{TM} production scheduling module in the GEMS GEOVIA, version 6.7.4, software package (Dassault Systèmes,

2017). Within PCBC^{TM}, HOD is calculated based on drawpoint spacing, tonnage drawn from a drawpoint, bulking factors and an assumed geometry of the drawcone. A constant bulking factor and drawcone shape was used within the software for all drawpoints. The results for approximately eight images were averaged for each HOD value shown in Figure 4.2. BCF predictions were converted from a block volume size, in units of m^3, as output by the software, to a screen aperture size that could be compared to the output of WipFrag^{TM} software. Size conversion was carried out under the assumption that blocks are in the shape of a square prism, where the screen aperture size is equal to the side-length of the square. The assumption that blocks output by the BCF program be treated as square prisms was recommended by the developer of BCF, GS Esterhuizen (2017 email from GS Esterhuizen to the author, unreferenced). Block aspect ratios were provided by the BCF software for each block and used in the calculation process.

BCF-based predictions were generally in line with measurements for aperture sizes coarser than 0.5 m. However, the software was found to under predict the content of material in the finer size fractions.

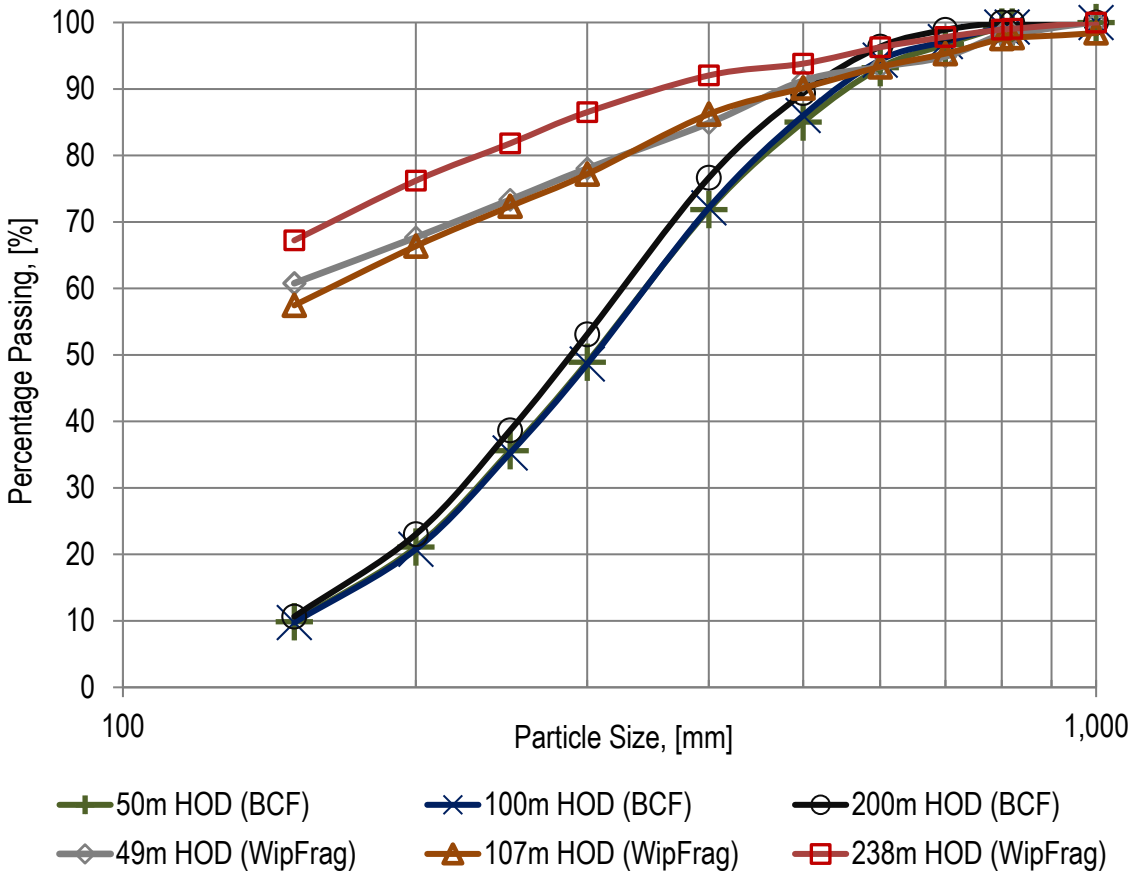

Figure 4.2 Size distribution curves for secondary fragmentation at New Afton, B2 cave

4.4 Back-calculation of Gyratory Crusher Feed

Feed to the gyratory crusher, located on the haulage level, consists of drawpoint muck that has passed through orepasses and been hauled to the crusher surge pocket. In order to estimate the size of crusher feed, sieving results for the 2.2 tonne sample of crusher product were used in combination with Anderson-Arachie-Whiten crusher models (JKTech Pty Ltd, 2015) that are available in the JKSimMet software package, version 6.1 (JKTech Pty Ltd, 2015). At the time of sampling, the crusher was operating with a closed-side setting of 80 mm.

Following sieving, standard JK Drop Weight tests (JKTech Pty Ltd, 2016) were carried out on samples of crusher product to determine their hardness and appearance functions. Analysis of

individual rocks and assays of representative sub-samples showed that the bulk sample was composed of high grade hypogene ore.

To model the crusher feed, WipFrag^{TM} measurements for drawpoints that were similar to the collected crusher product sample in terms of rock lithology and alteration were averaged. The average size distribution was treated as initial feed to the crusher model within the JKSimMet package. Following comparison of modelled product sizes and sieving results, the percentage content of each size fraction in the feed to the crusher model was manually adjusted and the crusher model was run again. The approach was repeated until reasonable alignment between modelled and measured product was achieved, shown in Figure 4.3. Included in the graph is the average size distribution of secondary fragmentation, 61 image-based measurements in total, taken up to the time of mill feed sampling. A similar approach was used by Esen et al. (2007) to estimate the size of blasted material being fed to a primary crusher.

The modelling exercise matches the results of image analysis for sizes coarser than 125 mm. For size fractions below 3 mm, the feed and product curves overlap. An explanation for this is that the gyratory crusher does not influence the content within these size fractions. Alternative methods are required to estimate the percentage content of the finer fractions.

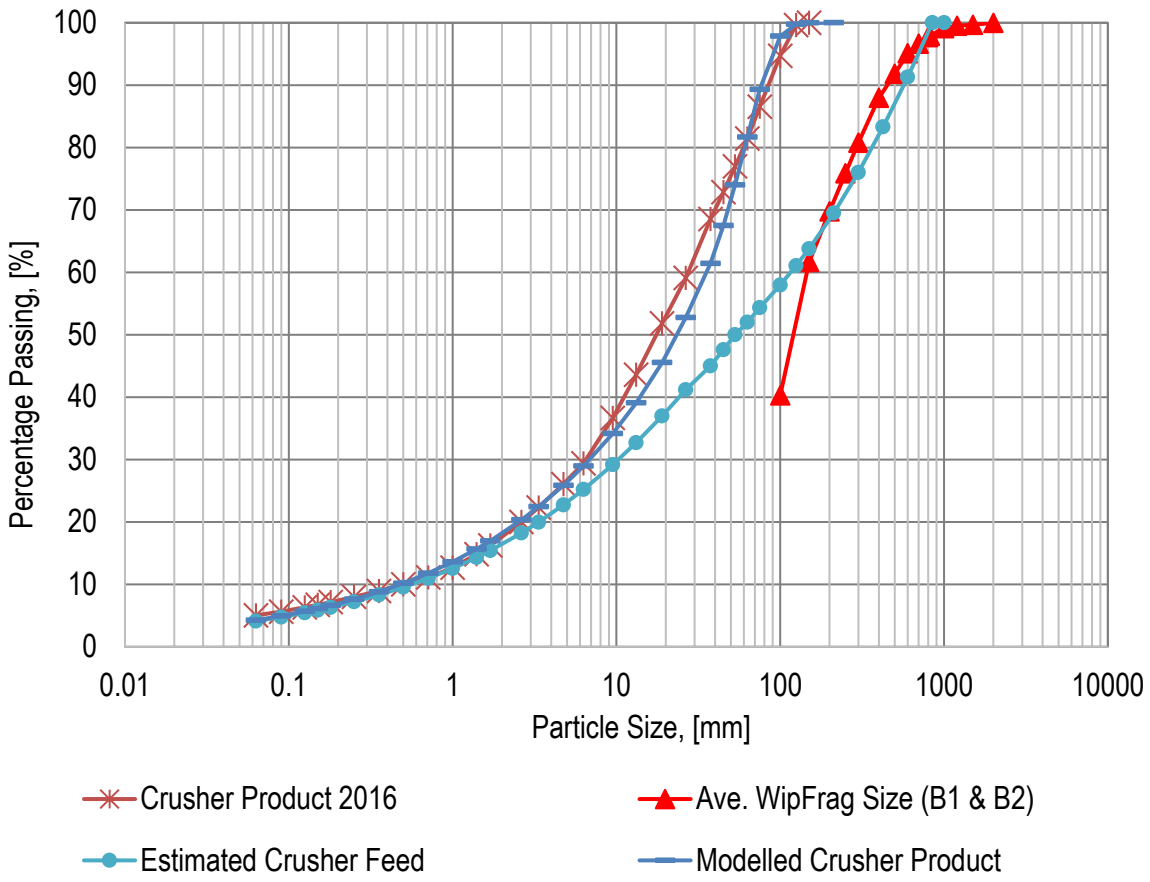

Figure 4.3 Modelled crusher product and feed sizes

4.5 Fragmentation Size and Rock Type

For the eleven drawpoints that had been sampled, size distributions from image-based measurements were compared to the content of each rock type at the time of sampling. It was found that finer muckpiles, as measured with WipFrag^{TM}, contained larger proportions, on a mass basis, of both fault and carbonate rock. Since carbonate rocks at New Afton originate from fault-related alteration, observations indicated that the secondary fragmentation size at New Afton is strongly related to the degree of faulting. Figure 4.4 shows a comparison of fragmentation size and the quantity of carbonate and fault rock. The HOD for all samples was at least 28 metres higher than the undercut, meaning that fragment sizes of these rocks would be unaffected by blasting.

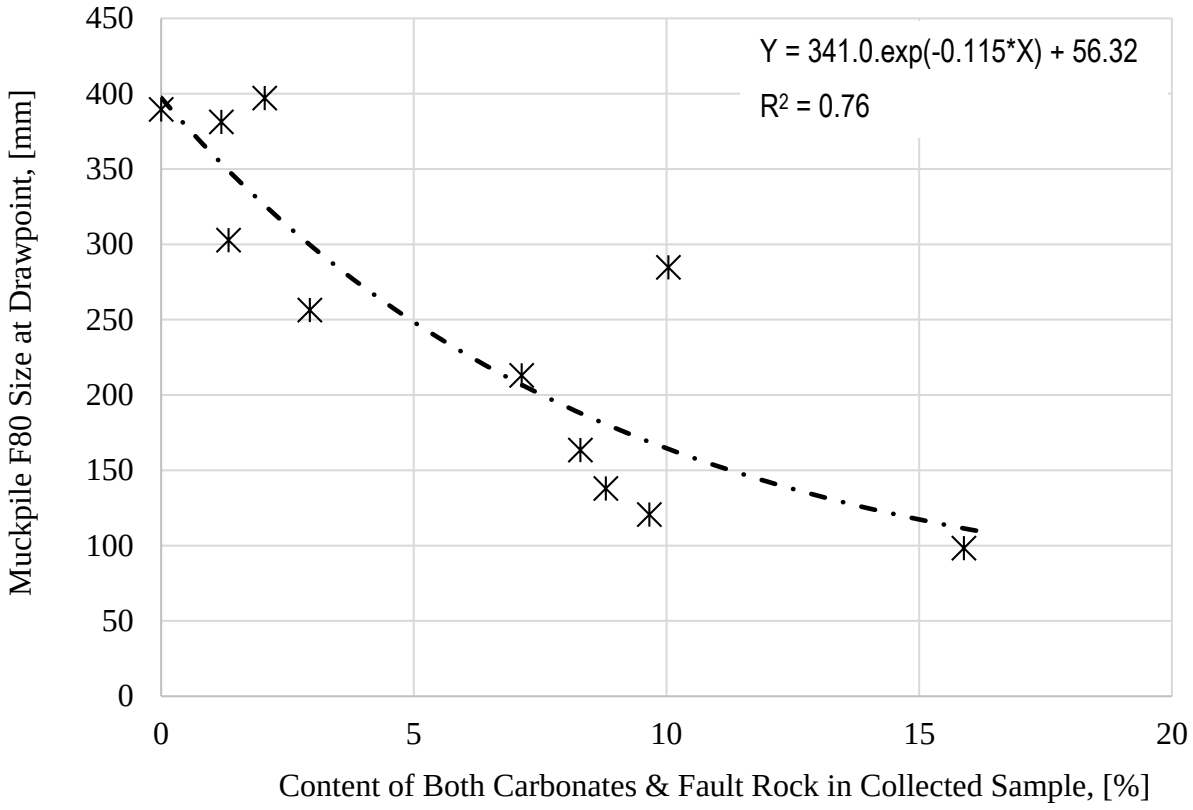

Figure 4.4 Secondary fragmentation size in relation to the content of carbonate and fault rock

Through analysis of test data, it was found that fault and carbonate rocks can be distinguished from other rocks within the New Afton deposit by referencing their respective XRF, magnetic susceptibility and point load index measurements. In comparison to other rock types reporting to drawpoints, carbonates were found to have high specific gravity, high concentrations of calcium and manganese, and low magnetic susceptibility. Fault rocks were distinguishable due to their low point load strength and high sulphur content. Magnetic susceptibility, point load strength and assay data are included in the New Afton block model. Therefore, fragmentation predictions can be carried out for future lifts by estimating the content of carbonate and fault rocks in future cave footprints and combining the results with historical fragmentation logs for existing caves, as shown in Figure 4.4.

4.6 Comparison of Hang-Up Frequency to Fragmentation Results

Hang-up and production logs from the period of September, 2011 to November, 2016 were used to determine the hang-up frequency for each month, shown in Figure 4.5. The figure represents 8,430 datapoints for both B1 and B2 caves. Figure 4.6 and Figure 4.7 show how the top-size and 80% passing sizes changed with increasing HOD**.** Intervals for 90% confidence, assuming data follows a normal distribution, have been included in all three figures.

In the case of the B2 cave, for which 59 size measurements were available, a distinct peak in both hang-up frequency and fragmentation size is apparent for an HOD of approximately 30 metres. This trend is expected because material originating from an HOD that is less than this height has been fragmented by drawbell and undercut blasting. Therefore, material above the undercut level has broken from the cave back, representing primary fragmentation, and experienced minimal breakage through secondary fragmentation. As more material is drawn, it can be noticed that both hang-up frequency and fragment size reduce. For the B1 cave, a total of 30 fragmentation measurements were available. Hang-up logs and fragmentation measurements indicated that fragmentation at the B1 cave is significantly finer.

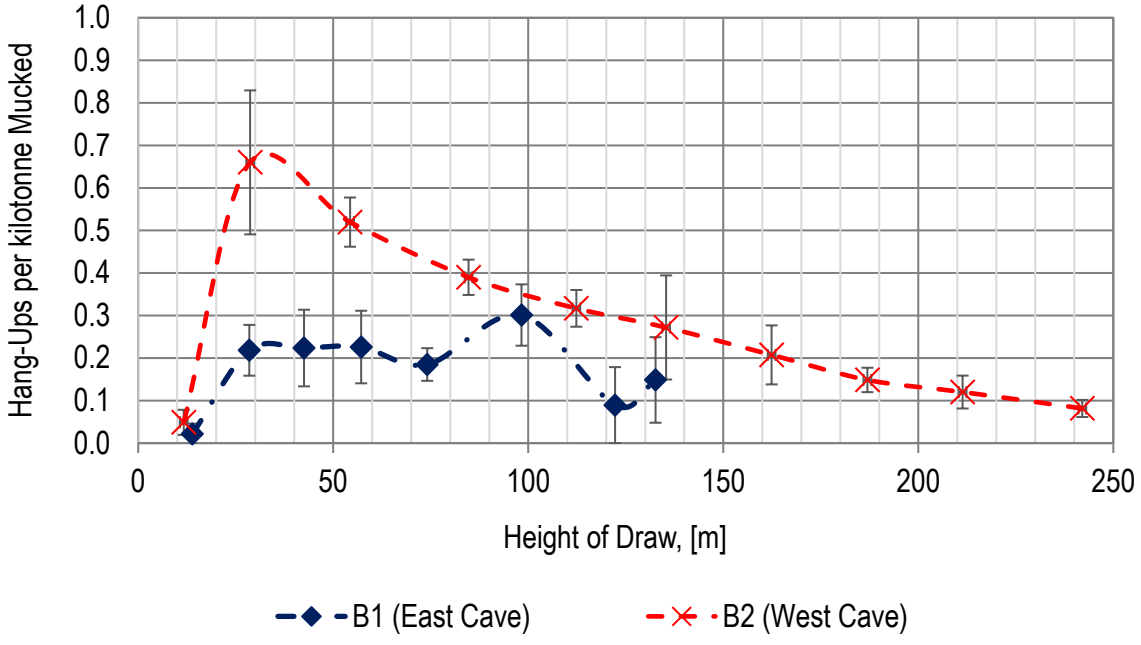

Figure 4.5 Hang-Up Frequency for East and West Caves (including 90% confidence intervals)

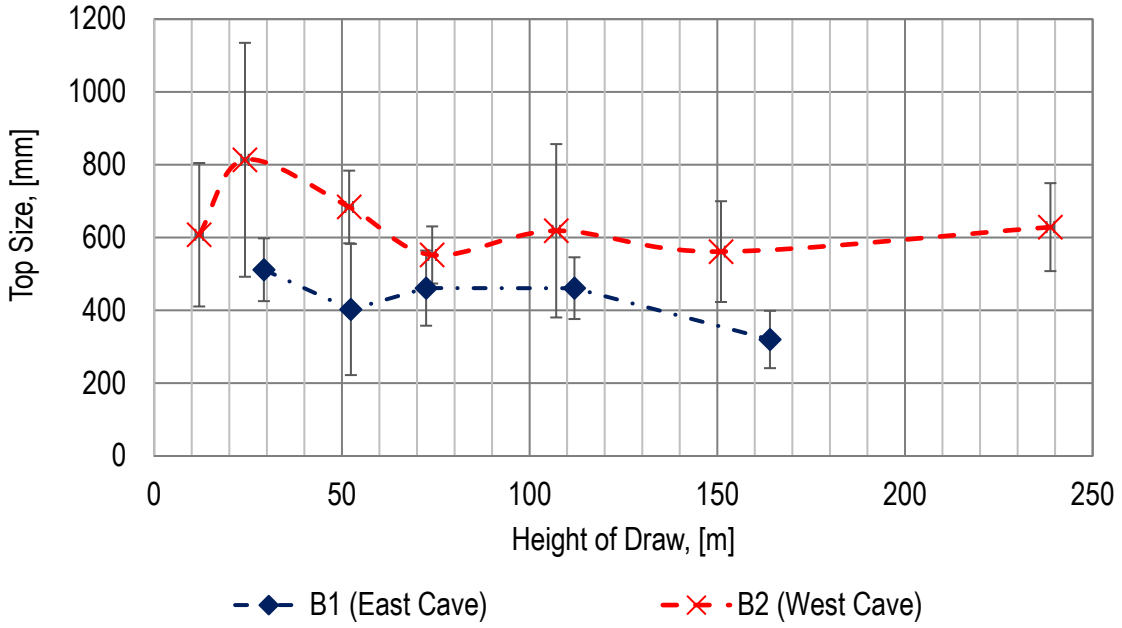

Figure 4.6 100% passing sizes of drawpoint muck (including 90% confidence intervals)

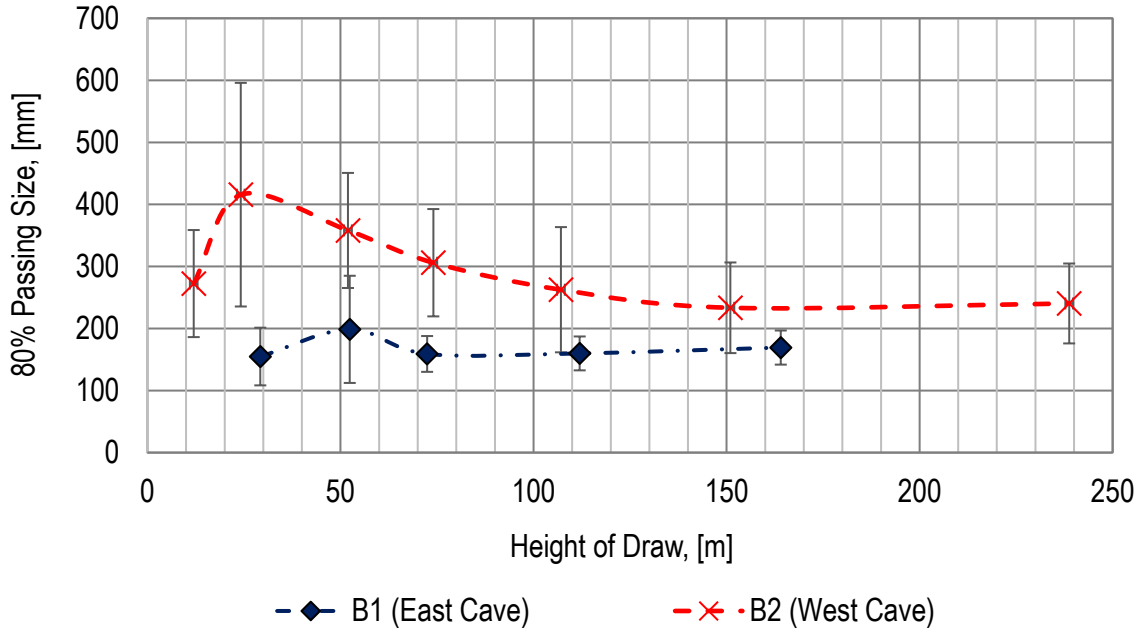

Figure 4.7 80% passing sizes of drawpoint muck (including 90% confidence intervals)

Higher hang-up frequencies are observed at drawpoints that are located at the perimeters of the B1 and B2 caves, as shown in Figure 4.8. This is particularly apparent at the western edge of the B2 cave, where coarser fragmentation was also measured.

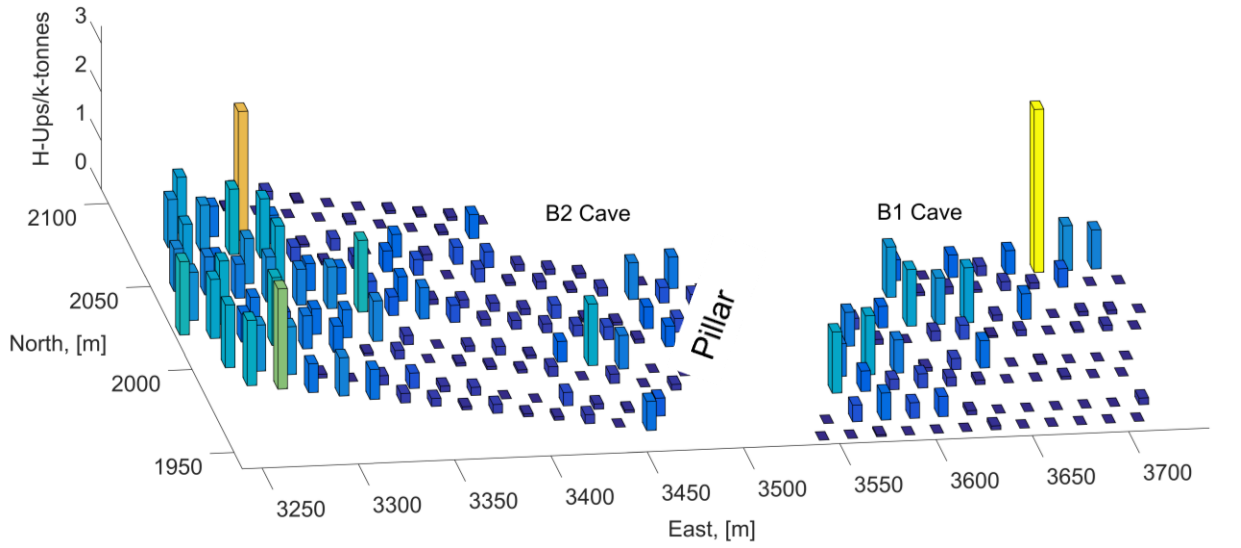

Figure 4.8 Hang-up frequency for HOD of 60 to 100 metres

4.7 Relating Fracture Intensity from DFN Models to Fragmentation Size

A DFN model was developed for the New Afton B2 Cave footprint by Munkhtsolmon Munkhchuluun, as part of his Master's research in the Cave-to-Mill project. The following is a summary of the methodology used to build a DFN model and relate fracture intensity to cave fragmentation. More detail can be found in Munkhchuluun (2017). P_{10} values, which represent the number of fractures per unit length, were referenced from provided geotechnical drill core data. Information from drift mapping at the apex level provided data for fracture orientations and length. Through iterative DFN modelling, this information could be used to relate P_{10} for a drill core interval to the equivalent P_{32} value, which represents fracture area for a unit of volume. The relationship between the volumetric size distribution of the in situ rock mass and fracture intensity is presented in Figure 4.9.

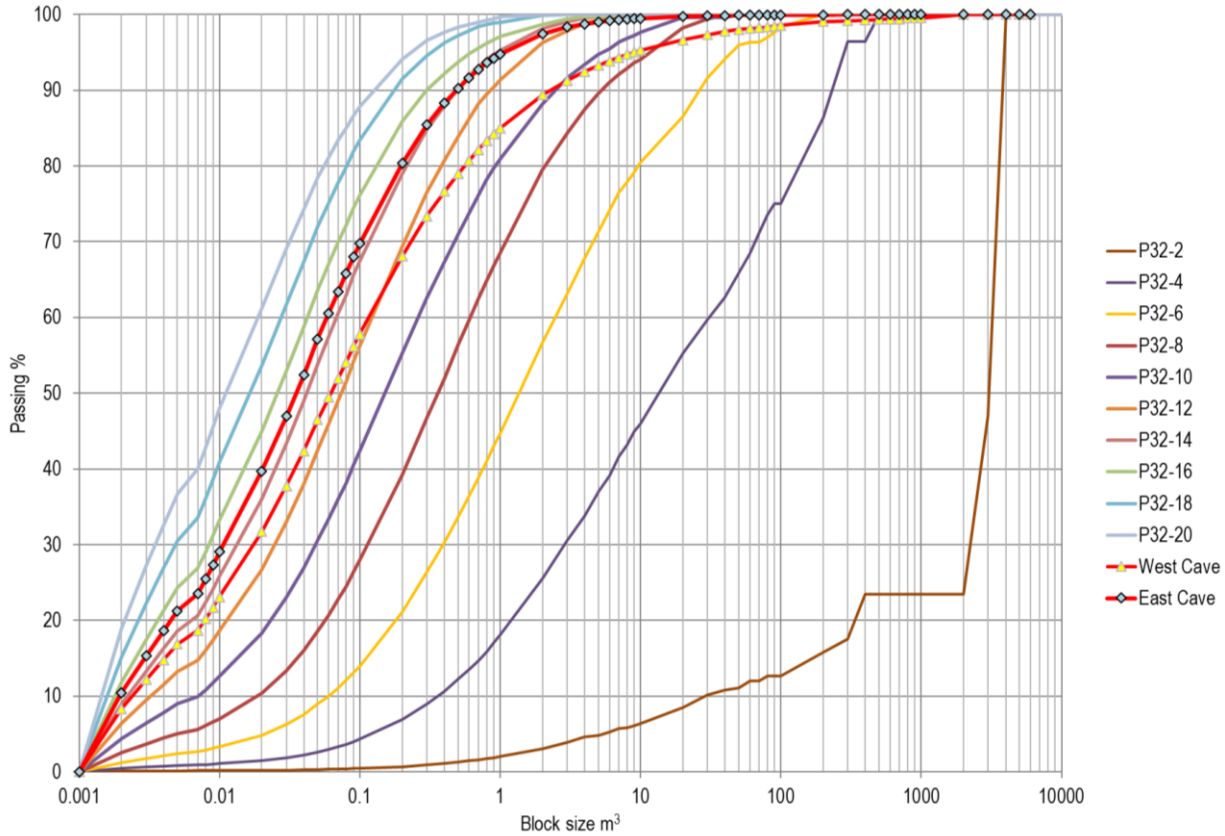

Figure 4.9 In situ fragmentation based on DFN analysis for varying P_{32} intensities, and weighted averages for B2 (West) and B1 (East) Caves (Munkhchuluun, 2017)

Ordinary kriging was used to build a P_{32} block model with 10 m cubic blocks for the B2 Cave. Major structures were deterministically located in the block model and assigned a P_{32} value of 20 (high fracture intensity), which accounted for 8% of block model volume.

Figure 4.10 shows the resulting P_{32} block model.

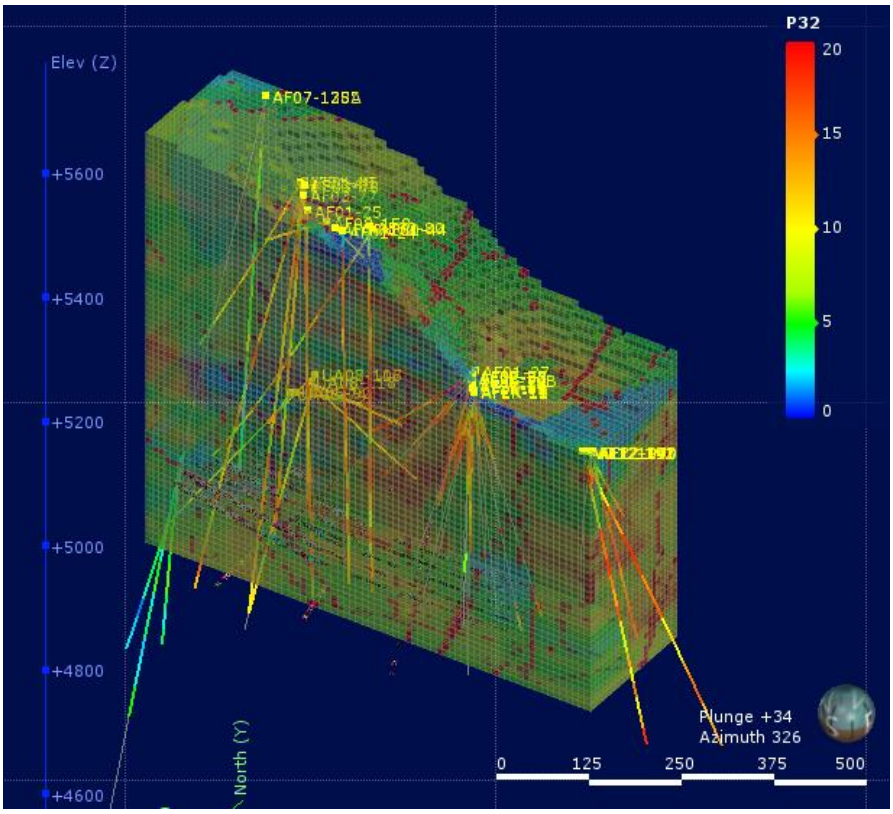

Figure 4.10 Geostatistical P_{32} block model (Munkhchuluun, 2017)

The P_{32} block model was used with New Afton Mine's PCBC parameters, including the profile of draw columns and historic production schedules, to determine the P_{32} values reporting to individual drawpoints for each month of production. The corresponding HOD of drawpoint muck could be estimated from knowledge of the cumulative tonnage drawn from each drawpoint. Essentially, fracture intensity P_{32} was treated as a grade parameter within PCBC.

In order to relate in situ fracture intensity to hang-up frequency, hang-up frequency data was grouped into 10 m ranges of height of draw to reduce the influence of secondary fragmentation. An example is presented in Figure 4.11, where hang-up frequency and fracture intensity data for a height of draw of 80 to 90 metres within the B2 Cave is included. The graph shows that hang-ups were less frequent when material originating from more highly fractured rock mass (higher P_{32}) was drawn. As a comparison, Brzovic et al. (2016) reported P_{32} values ranging from 2 to 15 m^2/m^3 for the El Teniente Mine.

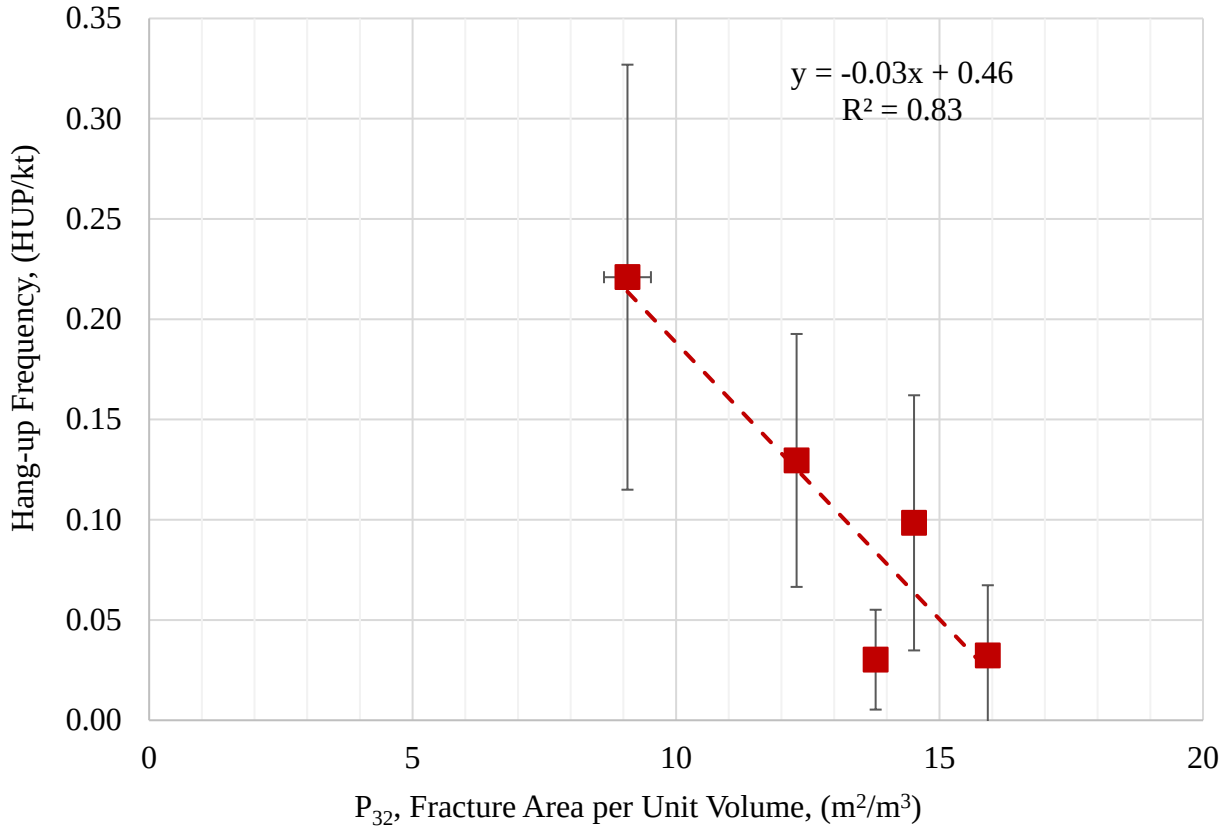

Figure 4.11 Hang-up frequency and fracture intensity P_{32} for material with a HOD of 80-90m with 90% confidence intervals. From data generated by Munkhchuluun, (2017)

A relationship between hang-up frequency and fracture intensity was also apparent for other HOD ranges, as shown in Figure 4.12. Based on the results, Munkhchuluun (2017) concluded that the fragmentation of material at low HOD values (affected by undercut blasting) is strongly influenced by fracture intensity while the fragmentation of more mature draw columns (high HOD) is more reliant on breakage through secondary fragmentation. Therefore, the proposed method is particularly relevant for predicting fragmentation size and by extension, mine productivity, for earlier stages of drawpoint production.

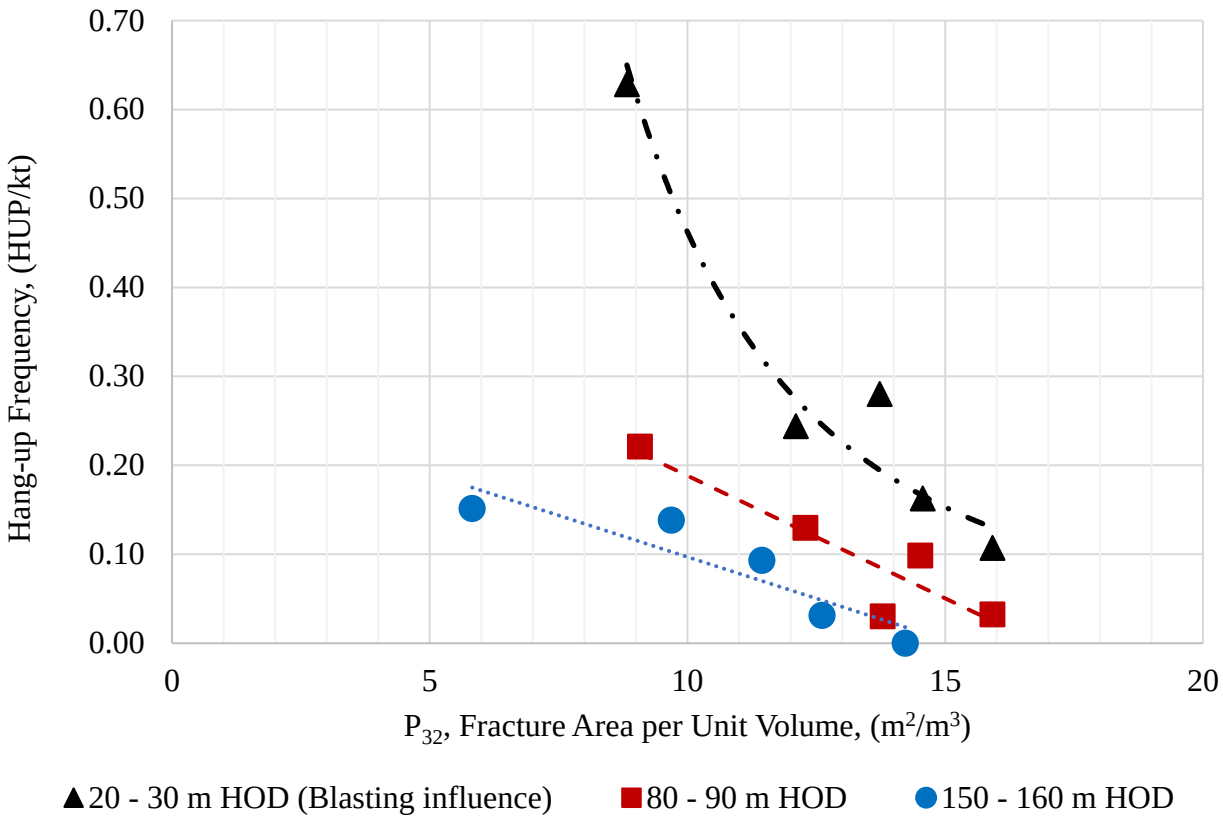

Figure 4.12 Hang-up frequency and fracture intensity P_{32} for three HOD ranges. From DFN data generated by Munkhchuluun (2017)

4.8 Influence of Veining on Fragmentation Size at New Afton

Veining has been identified as a contributing factor to the cave fragmentation process by a number of publications, including Bewick and Keiser (2016) and Brzovic et al. (2014). Quantitative data describing the quantity and type of veinlets in drill core pertaining to the East and West caves was not available. During inspection of collected drawpoint muck, rocks with calcite-coated faces were present in most samples. Since calcite is a common in-fill material at New Afton, it is assumed that the presence of calcite-coating is due to preferential breakage having taken place along calcite veins. Many rocks were also found with intact veins, similar to that shown in Figure 4.13.

The presence of vein in-fill material on rock faces indicates that veining does play a role in the fragmentation process at New Afton. However, the extent of its influence on muck size is unclear.

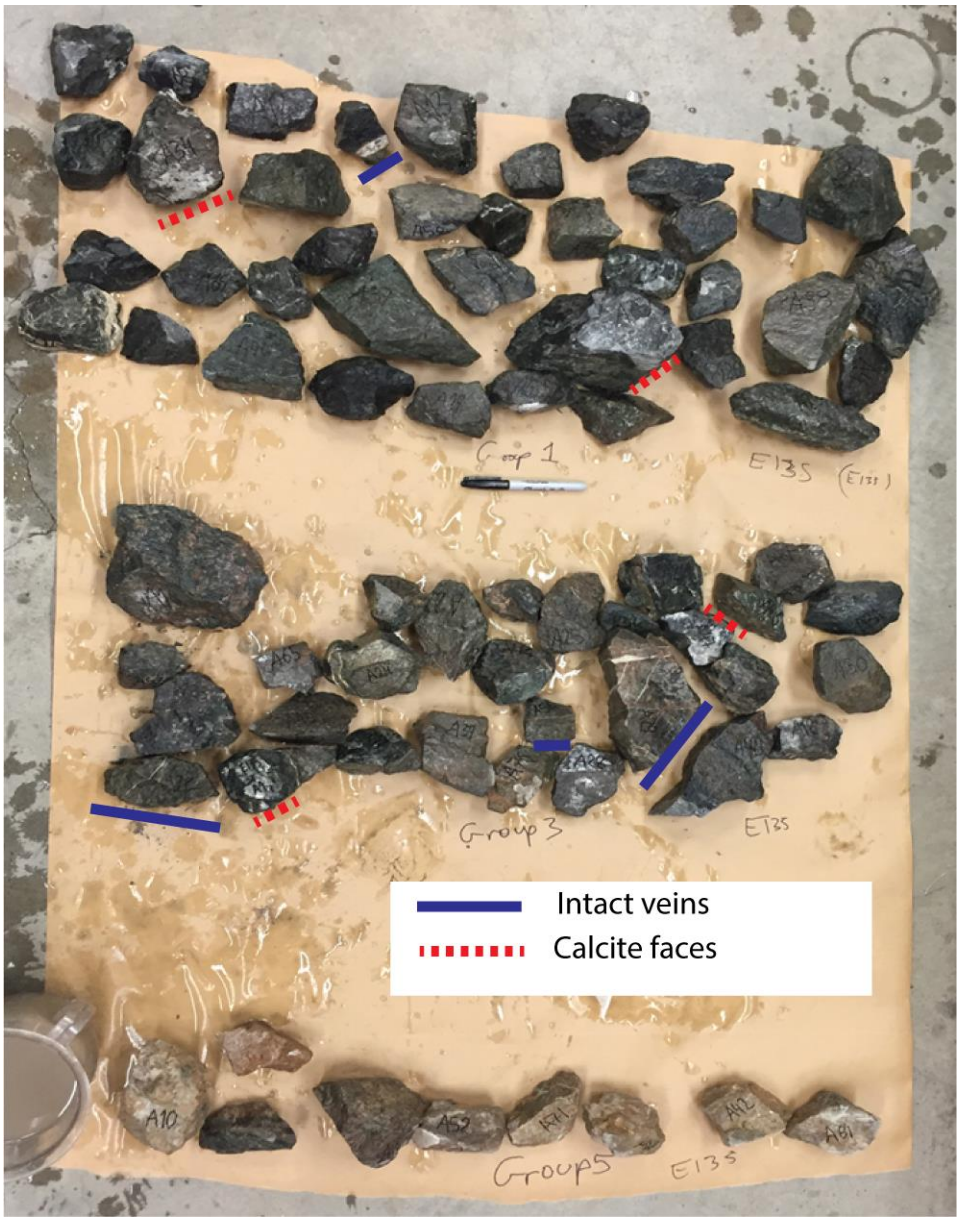

Figure 4.13 Drawpoint sample E13S (West Cave) taken November, 2015 (+50 mm)

4.9 Discussion and Conclusions

Results indicated that fragmentation at New Afton is primarily controlled by faulting, as shown by Figure 4.4. The wide range in 80 percent passing size, from approximately 100 to 400 mm, for the eleven drawpoint muckpiles, was found to be strongly related to the abundance of carbonate and softer fault rock where the alteration has been obscured. Furthermore, this hypothesis is supported by the lower hang-up frequencies and finer fragmentation sizes that were recorded for the B1 cave, which had a significantly larger number of fault structures intersecting the in situ rock mass.

Although a sizeable quantity of fragmentation size measurements and point load strength data was available, there was no evidence of a strong correlation between the two parameters. Prior to this study, it was expected that coarser muckpiles would be associated with higher point load strengths. The lack of correlation is attributed to the fact that competent carbonate rocks, for which an average $I_{s(50)}$ value of 5.3 MPa was measured, are also present in faults that have a direct bearing on fragmentation size.

The impact of HOD on fineness, shown by fragmentation measurements and hang-up logs, was found to be lower for the B1 cave. At the El Teniente mine, the influence of HOD on fragment size was not significant for rock masses that had high volumetric fracture intensity, defined by P_{32} (Brzovic et al., 2016). This is inline with findings from the work done by Munkchuluun (2017) for this Cave-to-Mill research program, where fracture intensity was linked to hang-up frequency. The phenomenon may explain the lower degree of size degradation with HOD that was observed for the B1 cave. For the B2 cave, the relationship between fragmentation size and HOD was similar to results presented by Moss (2004) for the Palabora cave, where the coarsest fragmentation was measured for samples originating at the zone of primary fragmentation followed by a reduction in size with increasing HOD.

The DFN component of the fragmentation study by Munkhchuluun (2017) showed that fracture intensity P_{32} is relevant to fragmentation size and hang-up frequency. Similar to the findings of Brzovic et al. (2016) at the El Teniente Mine, the largest reduction in hang-ups was found during

the earlier stages of drawpoint extraction. For future application of DFN-based fragmentation models, two refinement stages are proposed: 1) repopulation of DFN models as access to exposed ore increases during project development 2) calibration with size measurements of caved ore and hang-up logs when the project moves towards production. In the case that macro blocks are planned for a deposit, calibrated fragmentation models for an initial macro block can be treated as valuable design and planning tools for future lifts.

For the New Afton B2 cave, BCF-based percentage passing predictions for size fractions coarser than 0.5 m were within 5% of image-based measurements, where the average of approximately eight image-based size distributions was compared to corresponding BCF predictions. Similar to the findings published by Brunton et al. (2016), BCF software was found to under predict the content of fines. This may be due to the proportion of faulting assumed in the B2 cave when running the BCF simulations.

Since fault and carbonate rocks can be identified on the basis of point load strength, XRF response and Magnetic Susceptibility readings, information which is contained in the New Afton block model, fragmentation predictions can be made for future caves at the New Afton deposit. The effect of HOD on fragmentation size for future lifts can likely be inferred from the data shown for the B1 and B2 caves. However, more analysis on the influence of the cave boundary on hang-up frequency and fragmentation size is required.

Image-based size analysis was found to be practical for particle sizes coarser than 100 mm. The percentage passing of aperture sizes below 100 mm is of relevance to material handling systems, production potential of the mill and the potential of sensor-based sorting systems to upgrade ore. The full-size distribution of gyratory crusher feed was back-calculated using the results of sieving and a crusher model in the JKSimMet simulation package. The method assumed that significant breakage does not occur in the orepasses, which are approximately 25 metres in length.

Overall, secondary fragmentation at New Afton was found to be sensitive to faulting, fracture intensity, HOD and boundary effects. In small caves, such as the B1 and B2 caves, a large

proportion of the drawpoints is influenced by boundary effects, making fragmentation predictions particularly challenging.

Chapter 5: Relating Fragmentation Size to Mill Performance

5.1 Introduction

Cave fragmentation is a key cave-to-mill parameter as it has implications on the productivity of both mining and milling processes. Chapter 4 showed that hang-up frequency and caved ore size at the New Afton Mine can be related to the geology, fracture intensity, proximity of drawpoints to the cave boundary and the amount of material drawn through a drawpoint. The focus of this chapter is to determine the impact of fluctuations in caved material size on mill performance.

Fragmentation measurements of drawpoint muck, comminution tests and calibrated mill models were used to assess the impact of variations in feed size and hardness on New Afton mill performance. Image-based size analyses of drawpoint muck and comminution tests showed that coarser material generally contained harder rock.

5.2 Analysis of Mine and Mill Data

Four months of production data, September to December 2016, were analysed to identify relationships between the location of the ore being mucked, mill feed size and mill throughput. The extraction level layout and the drawpoints that were active during the operating period are shown in Figure 5.1.

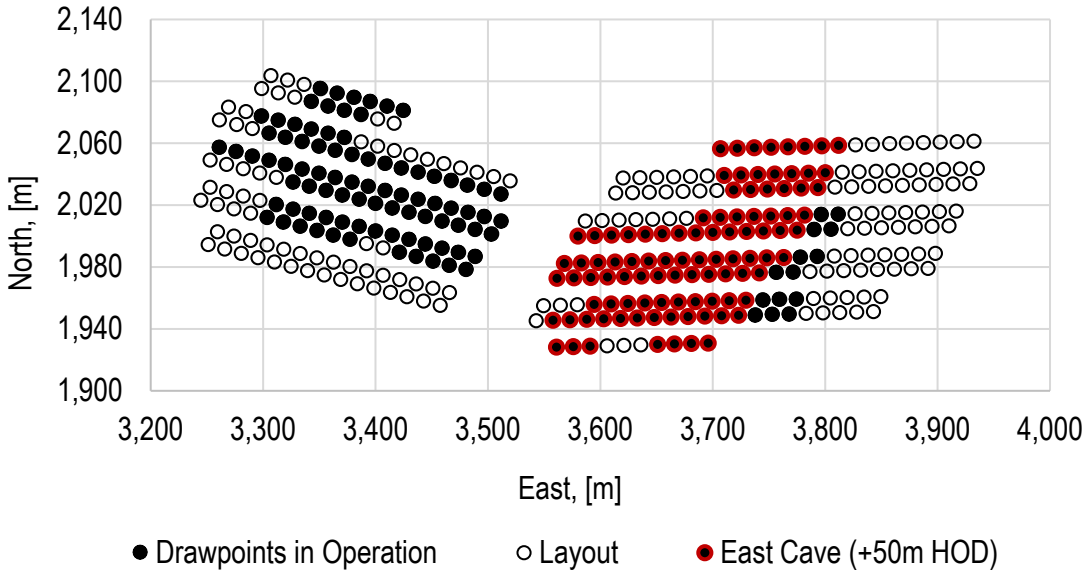

Figure 5.1 New Afton drawpoint layout including drawpoints in operation during the four-month period analysed for this study. B1 Cave drawpoints that had reached over 50 m in height of draw by the end of the 4-month operating period are shown in red.

Mill feed size, as measured online by a camera mounted on the mill feed conveyor, was compared to mill throughput during periods of operation when the mill was throughput constrained. These periods were defined as one-hour intervals of operation when the mill did not achieve the throughput set by the mill operator due to control system interlocks engaging to maintain product size fineness, reduce pebble recirculating load and/or adhere to other control system criteria. Throughput data for mill-constrained operation were selected from the four-month operating period as they represented the maximum potential of the mill for the size and hardness of feed material being processed.

Comparisons indicated that productivity of the New Afton mill is sensitive to the size of mill feed, as shown in Figure 5.2. Decreases in the 80% passing size of SAG mill feed (F_{80}) from 90 mm to 70 mm result in improvements in throughput rate from approximately 570 to 660 tph. A

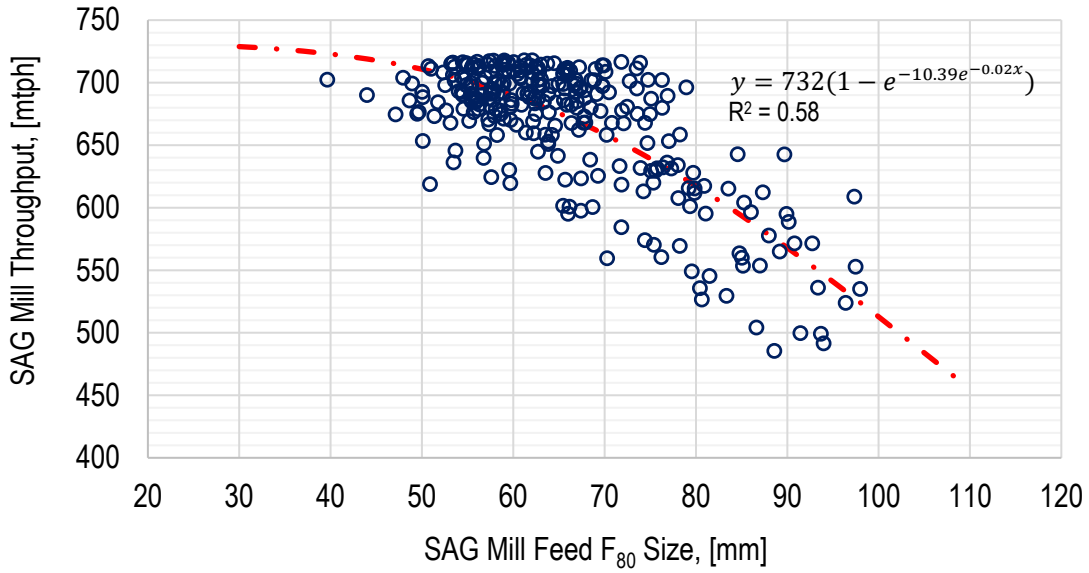

Figure 5.2 Mill feed size and throughput when circuit is constrained by grinding circuits for operation during Sep to Dec, 2016

To relate the source of mill feed to mill feed size and throughput, the amount of material mucked from each drawpoint for each 12-hour shift was compared to mill feed conveyor camera data and logs for mill throughput; camera and throughput data were available as one-hour averages. Based on the size of orepasses, bins and stockpiles, a six-hour offset was applied to camera and mill data to account for the time taken for material to travel from drawpoints to the mill.

An analysis of underground production data showed that mill feed size and throughput was sensitive to the proportion of run of mine material that was taken from drawpoints that have reached over 50 metres height of draw (HOD), located in the B1 Cave. Their locations are also indicated in Figure 5.1. This is in line with results from Chapter 4 of this thesis, which showed that: 1) B1 Cave drawpoint muck was significantly finer than B2 Cave drawpoint muck, and 2) for material originating from HOD heights above the undercut level (approximately 30 m), fragmentation size reduces as more material is drawn.

The change in feed F_{80} size due to increases in the proportion of material taken from drawpoints with HOD greater than 50 m within the B1 Cave is presented in Figure 5.3. The size of the confidence intervals is attributed to fluctuations in material residence time and size segregation

occurring within the material handling system, and instrument errors. In comparison to the throughput and feed size data presented in Figure 5.2, the range of mill feed F_{80} sizes shown in Figure 5.3 is significantly lower. Each datapoint represents an average of approximately 23 days of operation; averaging over extended periods dampens the extreme variations observed over shorter time periods.

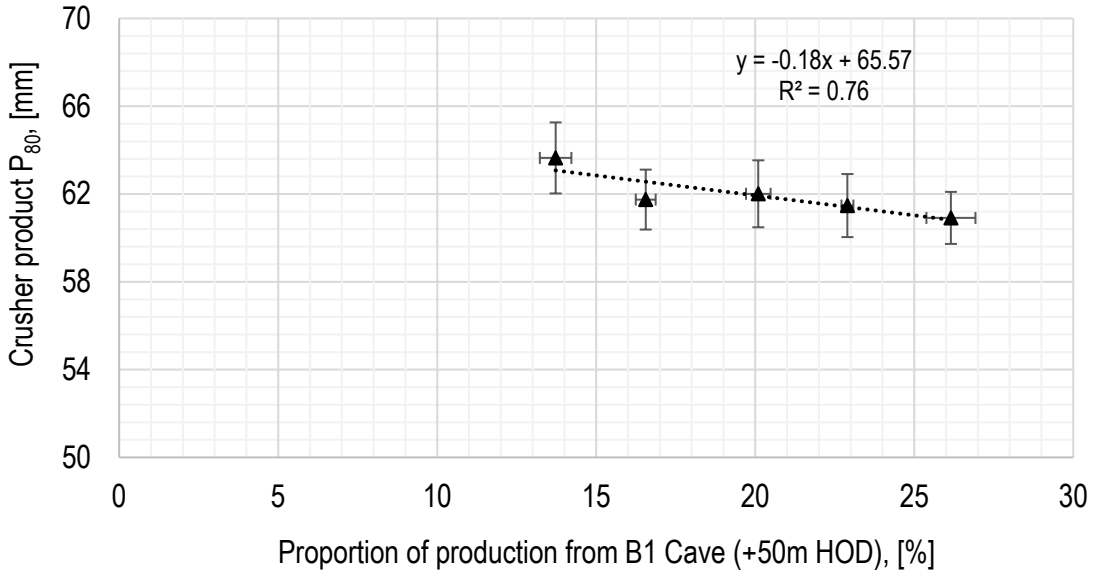

Figure 5.3 Mill feed size measured by an online camera on the mill feed conveyor and proportion of material from drawpoints within B1 Cave where HOD is greater than 50 m (including 90% confidence intervals). Each datapoint represents the average of 22 to 23 operating days (24 hours)

The analysis of production data also showed an increase in mill throughput when a larger proportion of material was sourced from B1 Cave drawpoints with HOD greater than 50 m, shown in Figure 5.4. The average mill throughput increased from 670 to 700 tph when material drawn from these B1 Cave drawpoints increased from 14 to 26 % of overall mill feed.

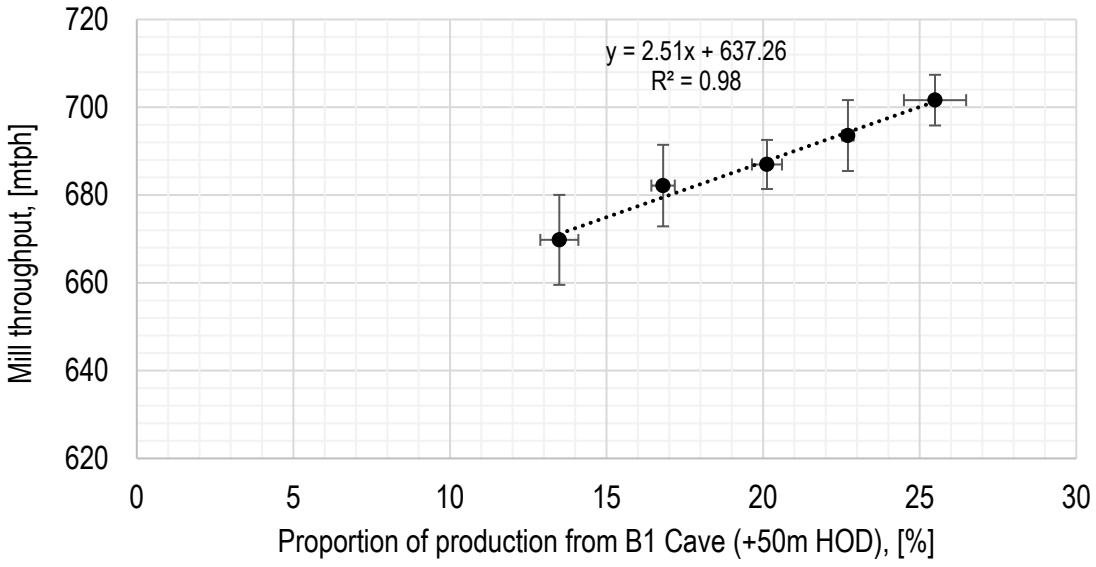

Figure 5.4 Mill throughput when the mill is throughput constrained and the proportion of material from drawpoints within the B1 Cave where HOD is greater than 50 m (including 90% confidence intervals). Each datapoint represents the average of 15 to 16 operating days (24 hours)

The analysis of mine and mill data did support the hypothesis that the mine production schedule has an impact on the size of mill feed and subsequently affects mill throughput performance. It is important to note that during periods of mine production where larger proportions of material were taken from B1 Cave drawpoints with HOD greater than 50 m, less material was being taken from other areas of the mine, such as the B2 Cave which was found to have significantly coarser material (as presented in Chapter 4).

5.3 Cave-to-Mill Modelling and Simulation Methodology

Mine and mill data analysis in the previous section was linked to the F_{80} size of mill feed, as measured online by conveyor-mounted cameras. To better understand the role of the hardness and size of caved material on mill throughput performance, the New Afton mill was modelled with calibrated crushing and grinding models using inputs from a comprehensive test program. The flowchart presented in Figure 3.5 shows the steps taken to calibrate mill models and collect feed size and hardness data for use as model inputs for simulation. The results of two mill surveys were used to validate the mill models.

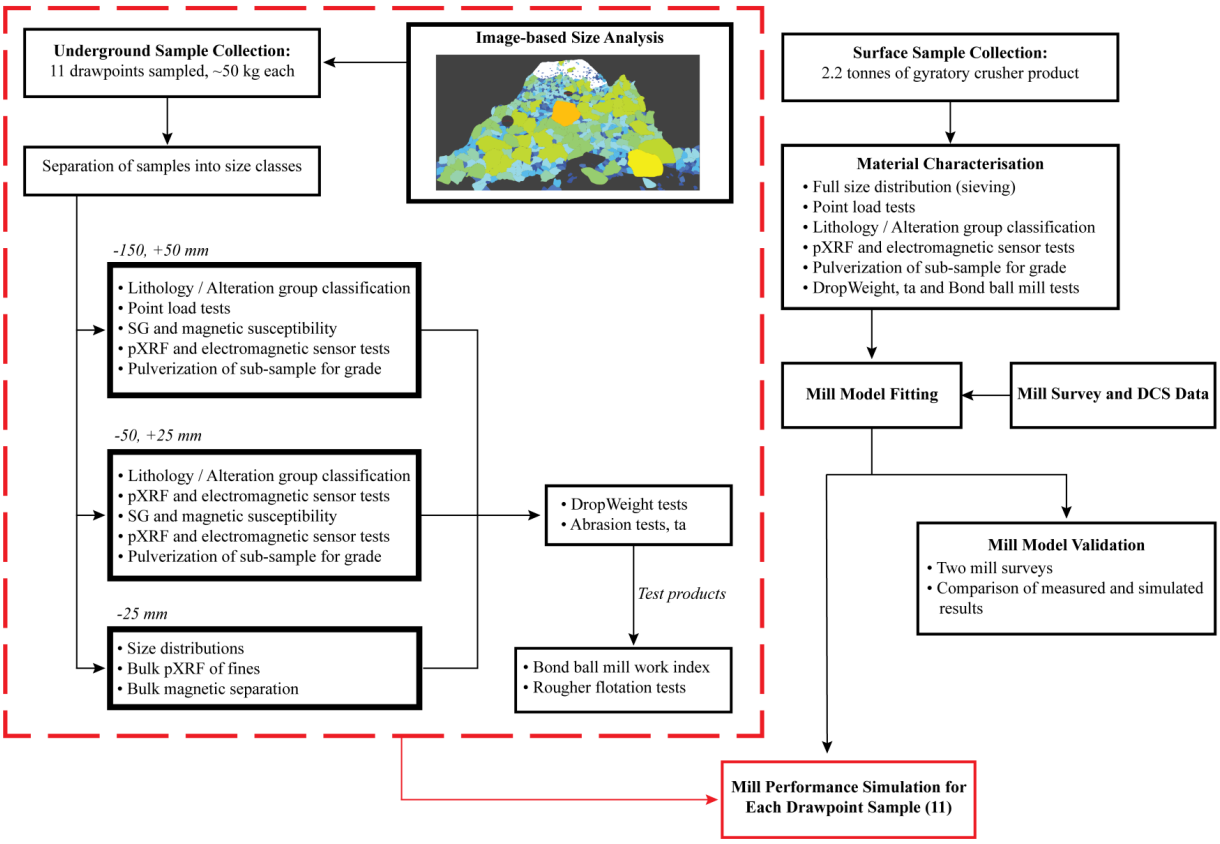

Figure 3.5 Test regimen for the core of the test program (repeated for convenience)

5.4 Size Analysis of Drawpoint Samples

Over the course of two days, eleven drawpoints were sampled after photos had been taken for size distribution analysis using WipFrag software. The drawpoints were chosen to ensure that the major ore types and end-members of the New Afton deposit were included. Further detail on the image-based size analyses is included in Section 3.3. Samples weighing approximately 50 kg for each drawpoint were shovelled from along the width of the base and mid-section of each drawpoint muckpile, described in greater detail in Section 3.4.

To characterise the fines content of drawpoint muck, the -25 mm fractions from each drawpoint were sieved using a sieve shaker to a final screen size of 0.5 mm. The goodness of fit achieved with several mathematical models was compared and it was found that the Gaudin-Schuhmann equation, shown in equation 5.1, provided the best fit.

$$\frac{M(x)}{M_0} = (\frac{x}{K})^m \quad \textbf{(5.1)}$$

where x is the particle size, M(x) is the weight of undersize, K is the size modulus and m is the slope parameter (Gaudin et al., 1962).

As presented in Chapter 4, image-based size measurements of muckpiles at drawpoints were found to be reliable for particle sizes coarser than approximately 100 mm. Since sieving results of muckpile samples were only available for -25 mm material, an approach for estimating the percentage passing aperture sizes from 25 to 100 mm was developed.

The Gaudin-Schuhmann equation was fitted to WipFrag measurements for size fractions of 125 mm and above. The fitted model was then used to estimate the percentage passing for size fractions between 100 and 25 mm. Similarly, a Gaudin-Schuhmann model was fitted to sieving results for collected -25 mm drawpoint muck samples using a size modulus, K, value of 25 mm. The determined slope, m, was then applied to determine the percentage passing for size fractions below 25 mm. An example of the approach is shown in Figure 5.5 for drawpoint D7S. The method was carried out for eleven drawpoint muckpiles to estimate the size of gyratory crusher feed that would result for each case.

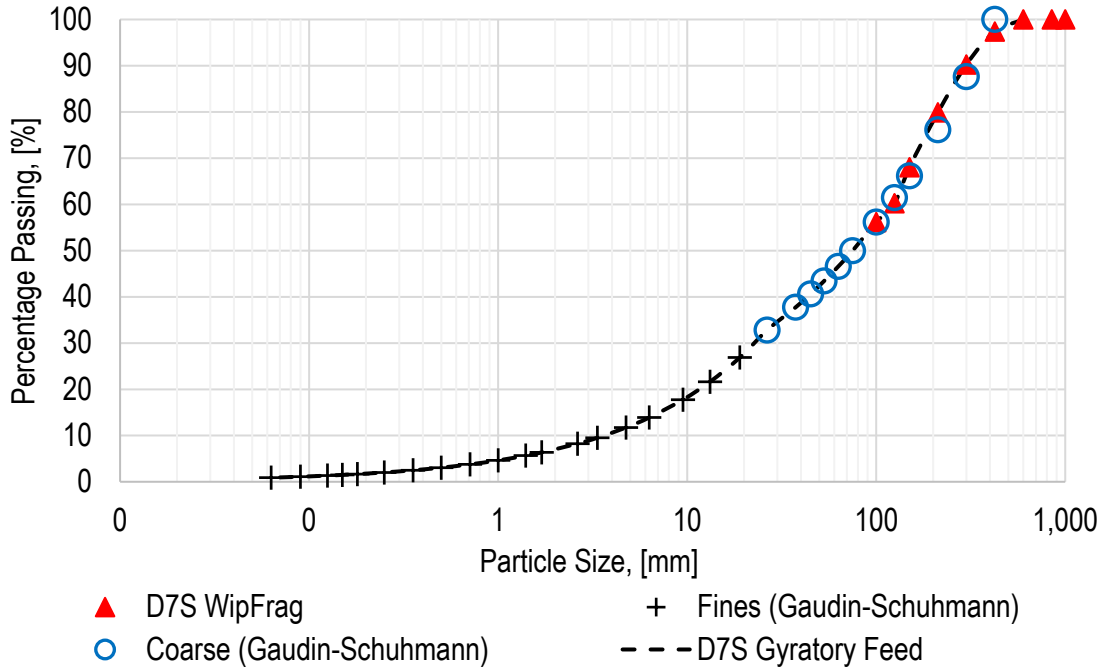

Figure 5.5 Example of estimated gyratory crusher feed size for sample D7S

5.5 Material Hardness Characterisation

Point load, DropWeight (JK Tech, 2016), low-energy abrasion tests (JK Tech, 2016) and Bond ball mill work index tests were carried out for the eleven drawpoint samples and a mill feed sample, which was taken for model fitting. Table 5.1 shows a summary of the material properties and measured F_{80} muckpile sizes.

Table 5.1 New Afton mill feed and geological unit characteristics

Sample & Cave (B1/B2)	Specific Gravity [-]	F_{80} Size of Muck [mm]	DropWeight Index , kWh/m^{3**} [-]	ta [-]	BBWI [kWh/mt]
SAG Mill Feed 2016	2.75	370*	6.98	0.29	18.4
#1, Hypogene B2	2.70	394	8.31	0.41	19.3
#2, Hypogene B2	2.67	99	6.91	0.39	18.4
#3, Hypogene B2	2.72	213	6.86	0.40	18.0
#4, Hypogene B2	2.72	117	8.08	0.27	19.4
#5, Hypogene B2	2.73	137	7.79	0.36	19.3
#6, Monzonite B2	2.72	263	6.91	0.28	17.9
#7, Phyllic-Altered B2	2.69	303	5.82	0.44	18.8
#8, Hypogene B1	2.76	276	7.08	0.38	20.8
#9, Secondary Hyp. B1	2.66	411	6.47	0.50	20.1
#10, Picrite B1	2.64	386	3.91	0.66	17.9
#11, Supergene B1	2.72	166	4.45	0.92	18.6

** Estimated from crusher modelling and sieving of crusher product*

*** Calculated using method of Doll (2016) to convert density and Axb values, from DropWeight testing, to DropWeight Index (kWh/m^3)*

5.6 Mill Surveys, Model Calibration and Validation

A mill survey, for which 2.2 tonnes of mill feed was collected, was carried out in March, 2016 to generate data to fit established comminution models. Sampling points are shown in the mine and mill flowsheet (Figure 3.6). A summary of the operating performance of the mill during the survey is shown in Table 5.2. Data from two additional mill surveys which were used to validate fitted mill models have also been included. For the 2015 and 2017 surveys, approximately 700 and 1,100 kg of mill feed sample was collected from the SAG mill fresh feed conveyor, respectively. Further detail regarding the mill surveys is presented in Section 3.5.

Table 5.2 Summary of New Afton mill surveys

Area	Parameter	Units	Survey (2016), Model Fitting	Survey (2015), Validation #1	Survey (2017), Validation #2**
Feed Properties	Fresh feed rate, dry	[mtph]	700	651	728
	Specific gravity	[-]	2.75	2.72	2.72
	Feed size, F_{80}	[mm]	60	35	59
	Feed size, F_{50}	[mm]	18	12	18
	Feed size, F_{20}	[mm]	3	2	4
	DropWeight, A	[-]	61	70.3	58
	DropWeight, b	[-]	0.64	0.51	0.70
	Abrasion parameter, ta	[-]	0.29	0.34	0.29
	Bond ball mill work index	[kWh/mt]	18.4	18.9	19.4
SAG Mill Circuit	SAG mill speed, % of critical	[%]	64.0	63.8	63.8
	SAG mill diameter, inside liners	[m]	8.36	8.39	8.32
	SAG mill ball load	[%]	15	15	17
	SAG mill power draw	[kW]	4,766	4,324	4,914
	Effective screen aperture size	[mm]	13.2	9.5	9.5
	Pebble crusher bypass	[%]	0	19***	0
	Pebble port size (width)	[mm]	114.3	88.9	114.3
	Media diameter	[mm]	158.8	152.4	158.8
	Pebble crusher closed side-set	[mm]	20	12	20
	SAG mill screen undersize F_{80}*	[mm]	3.31	NA	2.59
Ball Mill Circuit	Ball mill power draw	[kW]	5,255	5,446	5,415
	Media diameter	[mm]	63.5	50	63.5
	Medial load	[%]	38	38	37
	Circulating load	[%]	255	372	307
	Ball mill cyclone overflow, P_{80}	[µm]	289	226	287
	Operating Work Index, Wio	[kWh/mt]	16.5	NA	17.2
	Bond Energy Factor, Wio/ BBWI	[-]	0.99	NA	0.97
Vertimill Circuit	Vertimill power draw	[kW]	2,090	Not Installed	2,165
	Media diameter	[mm]			
	Circulating load	[%]	143		165
	Vertimill cyclone overflow, P_{80}	[µm]	150		152

** Not directly sampled. Determined by mass balances around SAG screen and ball mill cyclone feed sump*

*** From Cebeci et al. (2017)*

**** Bypass observed during survey due to magnetite or tramp metal in pebble stream triggering metal detectors prior to pebble crusher*

5.7 Mill Model Validation

To model the SAG mill circuit, the variable rates SAG mill model within JKSimMet (JK Tech, 2015a), a software package for simulation of comminution circuits, was used. Recommendations by Bailey et al. (2009) for application of the model for fully-ported SAG mills, such as the New Afton mill, were followed. Anderson-Arachie-Whiten crusher models (JK Tech, 2015b), were used for pebble crusher simulation. For estimation of ball mill and Vertimill performance, Bond efficiency methods, which are based on the ratio of the operating work index to the Bond ball mill work index of sampled mill feed, were applied. The modelling method is described in more detail in Section 3.6.

The model fitted to 2016 survey data was used to simulate the operating conditions of two separate mill surveys. Comparisons of simulated and measured data showed that predictions were within +/-10% for product size, throughput performance and power draw, as presented in Table 5.3. Performance predictions were more accurate for the 2017 survey, during which mill operating conditions were similar to the base case (2016) used to fit the models.

Table 5.3 Comparison of measured and simulated mill performance

	Parameter	Units	Measured	Simulated	Percent Error, %	Simulation Method
Survey 2015	SAG mill power	[kW]	4,324	4,710	8.9	JKSimMet
	Pebble recycle	[mtph]	149	159	6.7	
	SAG screen under size F_{80}	[µm]	NA	2,792	-	
	Ball mill power	[kW]	5,446	-	-	Input into Eq. 3.1
	Ball mill cyclone overflow P_{80}	[µm]	226	247	9.3	Eq. 3.1
Survey 2017	SAG mill power	[kW]	4,914	4,955	0.8	JKSimMet
	Pebble recycle	[mtph]	196	208	5.7	
	SAG screen under size F_{80}	[µm]	2,587	2,736	5.8	
	Ball mill power	[kW]	5,415	5,419	0.1	Eq. 3.1
	Ball mill cyclone overflow P_{80}	[µm]	287	299	4.3	Eq. 3.1
	Vertimill power	[kW]	2,165	-	-	Input into Eq. 3.3
	Vertimilll cyclone overflow P_{80}	[µm]	152	153	0.3	Eq. 3.3

Simulation of Mill Performance

Fitted models were used to determine the mill throughput potential associated with the eleven drawpoint samples, each having a unique size distribution and competency. The boundary limits for modelling were defined as starting at the feed to the primary crusher and ending at the cyclone overflow of the Vertimill operating in a tertiary grinding role. Product from the Vertimill is fed to a rougher flotation circuit. Table 5.4 shows the equipment and process constraints that were adhered to when calculating maximum throughput performance.

Table 5.4 Equipment and process constraints for simulations

Equipment	Units	Value	Constraint Type
Max SAG mill motor power draw	[kW]	5,000	Drivetrain
Max Vertimill motor power draw	[kW]	2,200	Drivetrain
Max Ball mill motor power draw	[kW]	5,450	Drivetrain
Max pebble crusher tph	[mtph]	250	Material handling
Max SAG volume load	[%]	30	Operational
Fixed product size, Vertimill cyclone overflow	[µm]	150	Flotation Recovery

A comparison of SAG mill feed size and mill throughput potential is shown in Figure 5.6. Simulated throughputs varied from 561 to 735 tph for F80 feed sizes of 73 to 44 mm. For feed F80 sizes coarser than 64 mm, simulations indicated that throughput was SAG mill constrained. For finer feed sizes, the bottleneck would shift to the ball and Vertimill circuits, at which point ball and Vertimill power draws were at their operational maximums.

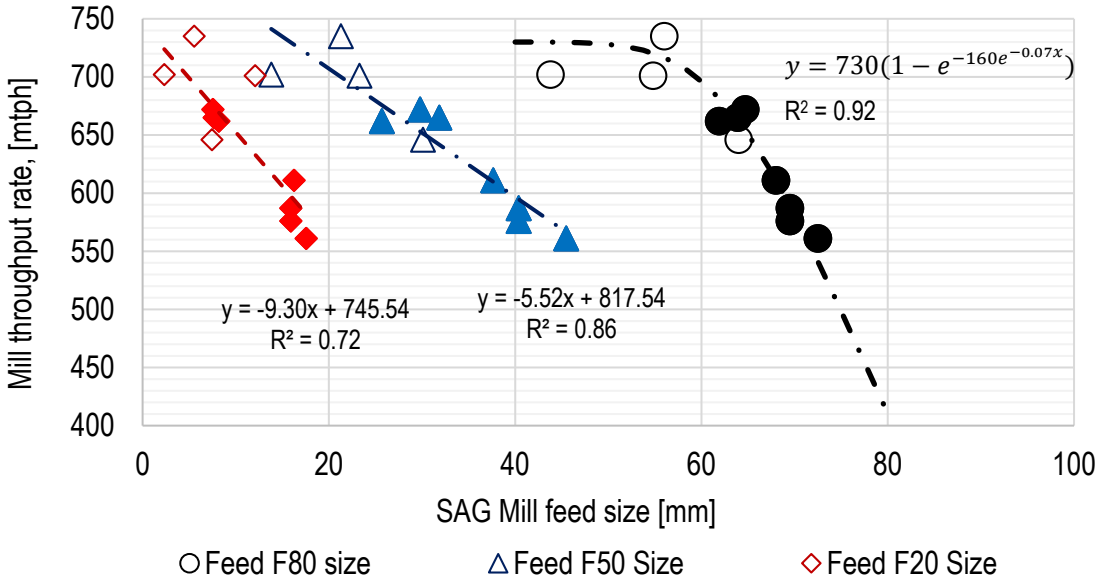

Figure 5.6 Simulated mill throughput rates and mill feed size for 11 drawpoint samples. Filled markers indicate SAG mill limited operation. Empty markers indicate ball and Vertimill limited operation.

For the range of available hardness parameters that were determined, the DropWeight index most closely correlated to the simulated throughput rates, shown in Figure 5.7. Simulations showed that throughput performance was constrained by the SAG mill for more competent ore types having DropWeight Index values greater than approximately 6.6 kWh/m^3.

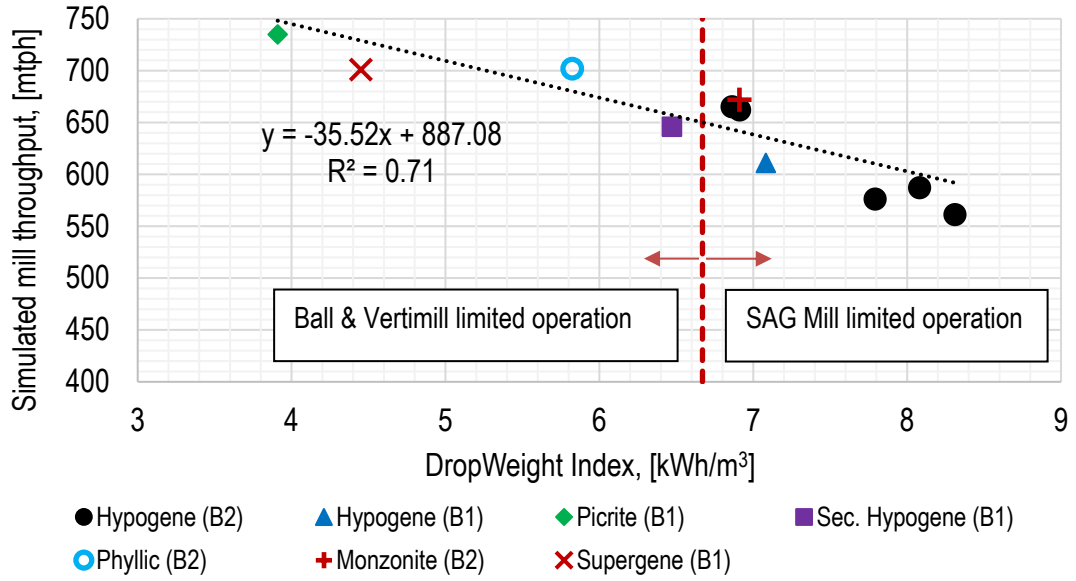

Figure 5.7 Simulated mill throughput rates and DropWeight Index parameters

Simulations provided an understanding of the sensitivity of mill throughput to changes in ore hardness and feed size. Figure 5.8, which shows the relationship between impact hardness and the size distribution of the muckpile, indicates that hardness and feed size are not independent of each other. Coarser sample is generally harder. Therefore, drawpoint muck size, which directly relates to mill feed size, and ore hardness are considered to be material specific parameters that affect mill throughput and the location of bottlenecks.

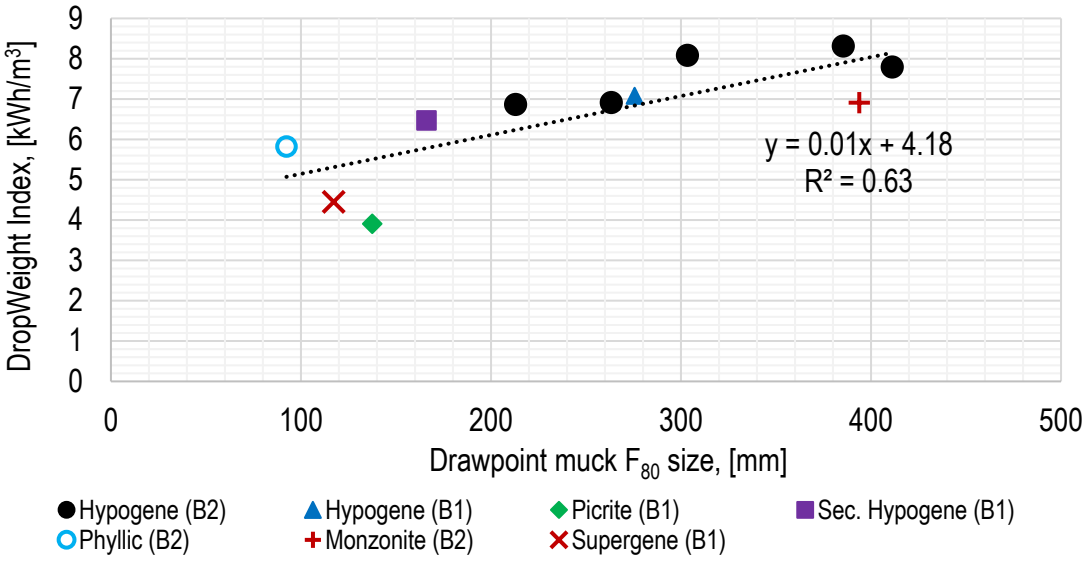

Figure 5.8 DropWeight Index and measured F80 size of sample drawpoint muckpiles

5.8 Influence of Feed Size on Simulated Mill Performance

In many power-based comminution models (Bond, 1962, Morrell, 2014 and Doll, 2015) mill feed size and throughput comparisons rely on the F_{80} as the main indicator of feed size. Esen et al. (2007) mention that in addition to mill feed top size and F_{80}, the proportion of -10 mm material in mill feed affects SAG mill throughput performance (higher proportions improve throughput). An analysis of feed size distributions and simulated mill throughput provided results that are in line with this statement. Using the set of eleven mill simulations, the Pearson correlation coefficient for the relationship between throughput and the proportion of feed material retained on each sieve was calculated. A correlation coefficient of 1 implies that a linear equation perfectly describes the relationship between simulated mill throughput and the proportion retained on sieve size x. While a value of -1 indicates a perfectly inverse relationship.

Figure 5.9 shows that the coarser (+27 mm) size fractions of mill feed negatively correlated with simulated mill throughput, while the proportion of material retained on sieves smaller than the SAG screen aperture size (13.2 mm) positively correlated with simulated throughput. Essentially, these fine sizes exit the SAG mill circuit in one pass with minimal contribution to the volume load (and power draw) of the SAG mill.

The primary crusher at New Afton, which operates at a closed-side setting of 90 mm, does not noticeably increase the content of -13.2 mm material. Mill throughput forecasting stands to improve should better methods for predicting the content of fines (-10 mm) in drawpoint muck be developed.

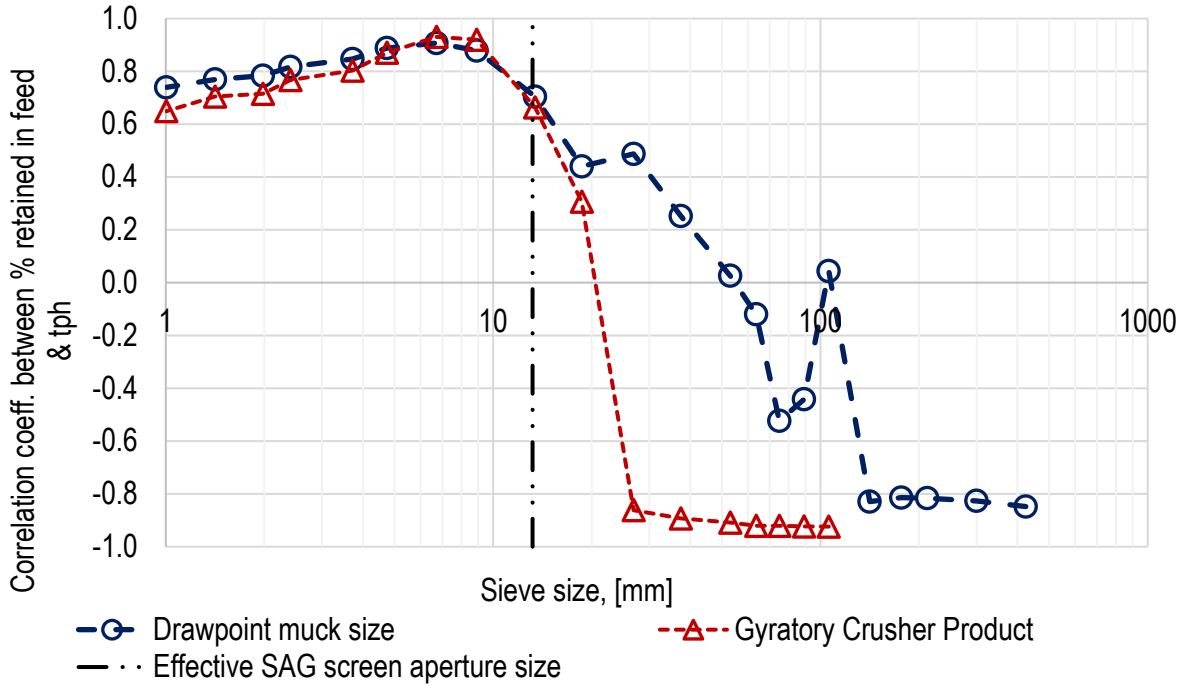

Figure 5.9 Pearson correlation coefficient between proportion of material retained on each sieve and simulated mill throughput.

5.9 Relationships Between Point Load Index, Impact Breakage and Abrasion

Results from the geotechnical and metallurgical test program showed that correlations exist between the results from New Afton Point Load Index $I_{S(50)}$ testing and milling parameters describing the resistance of material to breakage by impact and abrasion, represented by the DropWeight Index and ta abrasion parameter, respectively. Figure 5.10 and Figure 5.11 show a comparison of Point Load Index $I_{S(50)}$ results and the DropWeight Index and ta abrasion parameters. The graphs indicate that there is potential for use of the New Afton database of drill core point load strength results to forecast mill performance. Similarly, Burger et al. (2006) found useful correlations between Point Load Index and DropWeight strength.

Figure 5.12 shows a minor correlation between muckpile 80% passing size and the resistance of the samples to abrasion, as determined by an abrasion test, ta. A weak correlation between muckpile 80% passing size and point load strength was apparent, presented in Figure 5.13.

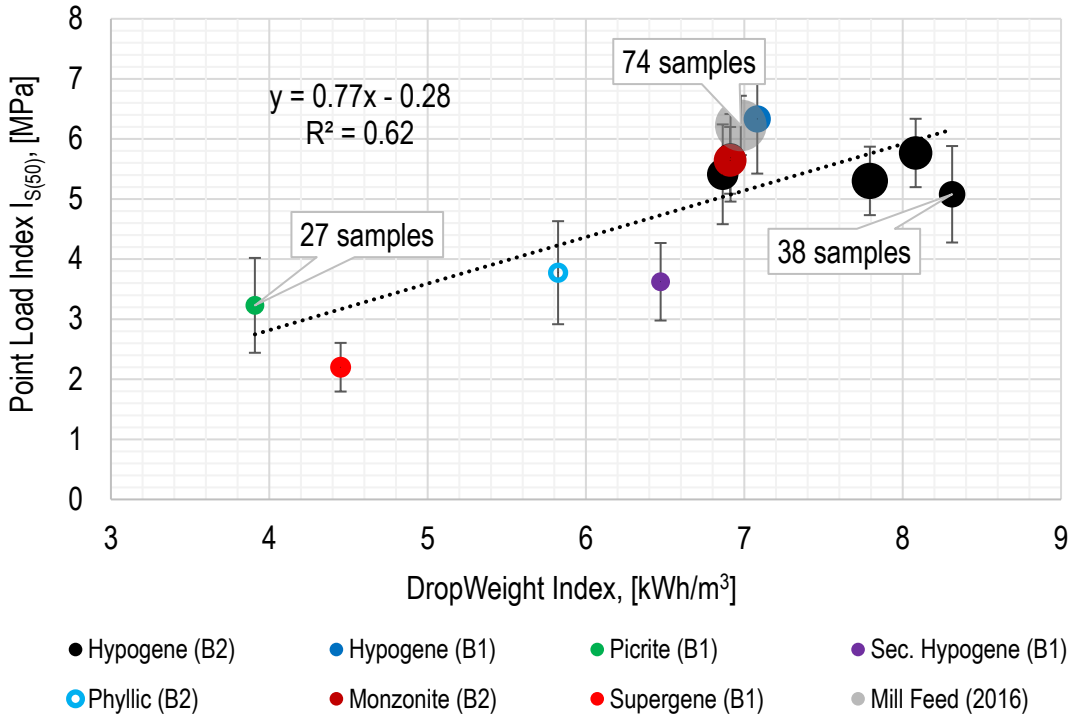

Figure 5.10 Point Load Index IS(50), including 90% confidence intervals, and DropWeight Index results for twelve samples

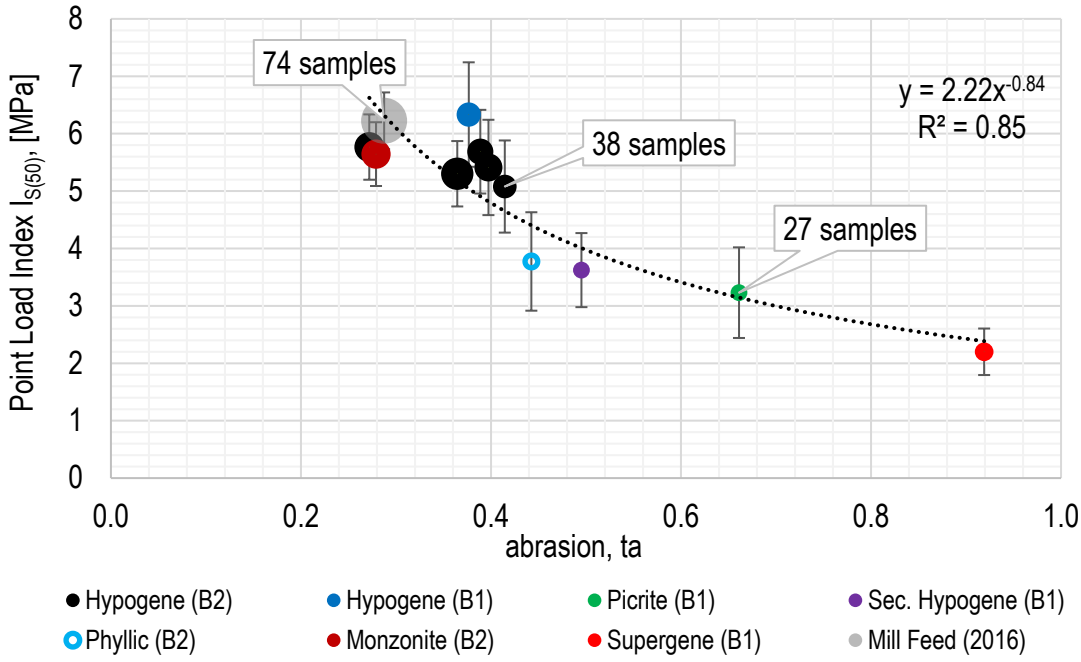

Figure 5.11 Point Load Index IS(50), including 90% confidence intervals, and Abrasion, ta, results for twelve samples

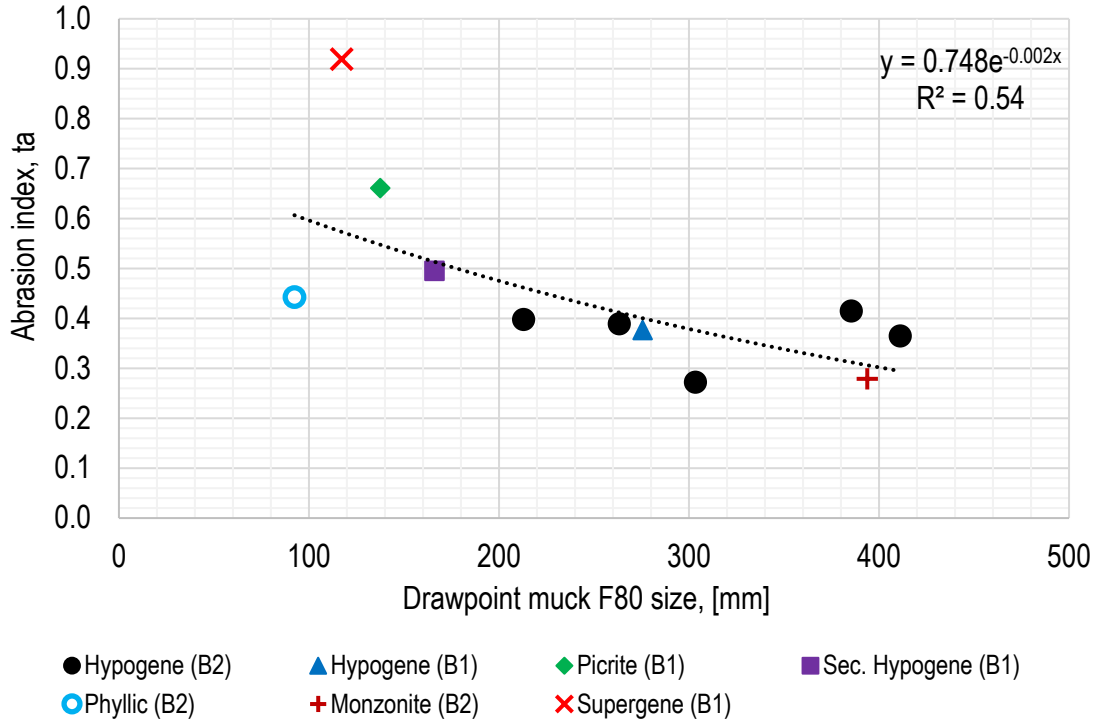

Figure 5.12 Abrasion Index, ta, and measured F80 size of drawpoint muck

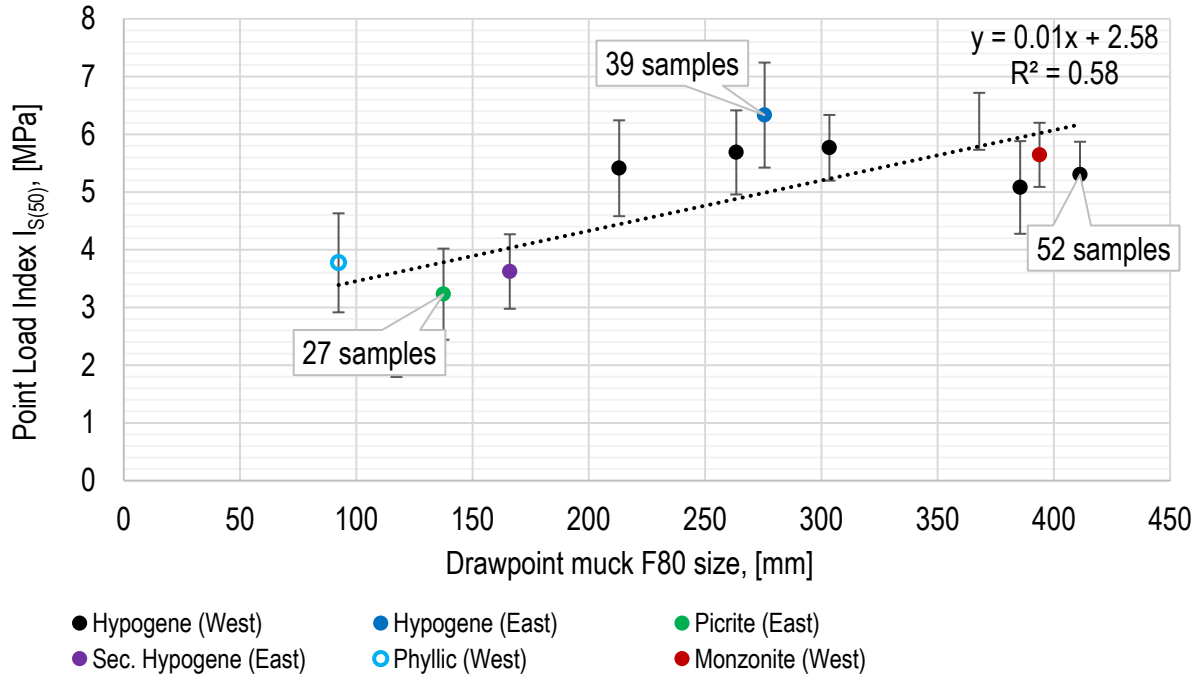

Figure 5.13 Point Load Index IS(50), including 90% confidence intervals, and measured F80 size of drawpoint muck

5.10 Discussion

Analysis of mine and mill data indicated that finer mill feed and increased mill throughput was achieved when higher proportions of mucked material were sourced from B1 Cave drawpoints that had an HOD greater than 50 metres. Simulations showed how mill throughput varies due to changes in mill feed size and hardness. The question then arises: what levers are available to mining engineers to generate finer mill feed? Aside from preconditioning methods, one lever is the adjustment of the closed-side setting of primary crushers to an operational minimum, as carried out at New Afton. A second lever is the inclusion of fragmentation data in the decision making that goes into planning underground production schedules.

An example of the second lever being put into practice is the blending of material at the Grasberg block cave operation to ensure that the fines content in the material handling system is below levels that cause problems at the haulage level. The fines content observed at different areas of the extraction level is one of the inputs that is considered when setting the production schedule. Although blending practices at Grasberg are not directed at improving mill performance, the example does show that sufficient flexibility exists within production schedules, even though they are usually nominated to meet grade targets and constrained by the requirement to maintain similar draw rates between neighbouring drawpoints.

Installation of secondary crushers ahead of existing SAG mill circuits also provides opportunity to improve mill throughput productivity at existing operations and reduce fluctuations in performance. High Pressure Grinding Roll (HPGR) based circuits are increasingly popular alternatives to SAG mill-based circuits due to their improved energy performance. HPGR-based circuits are known to be less sensitive to variations in ore size and hardness (Klymowsky, 2011) and their implementation would substantially offset the impact of variation in caved ore size on throughput performance.

The collection of fragmentation data was limited due to the time-consuming process of manually correcting images of drawpoint muckpiles. Placement of cameras at draw-points, orepasses or crusher excavations is a solution to continuously measuring the size of caved ore. At the LKAB

Kiruna sub-level caving operation, Thurley et al. (2015) used a 3D-imaging system to produce automated size estimates of material in LHD buckets. The technology to monitor fragmentation using 3D imaging already exists; a critical step forward is its implementation to provide online measurements of cave fragmentation (Nadolski et al., 2015).

5.11 Conclusions

Block and panel caving methods are being pushed to their extremes. Caving of deeply situated deposits, more competent rock masses and heterogeneous ore bodies presents greater challenges to predicting cave fragmentation size accurately. The initial lifts of block caving projects provide a valuable opportunity to gather cave-to-mill information to improve evaluation, design and operation of future lifts.

Chapter 4 showed how fragmentation size and hang-up frequency relate to geology, fracture intensity, proximity to the cave boundary and the height of draw at the New Afton mine. The second part showed how variation in fragmentation size affects mill performance and the location of mill bottlenecks. The sensitivity of mill throughput to the content of fines (-10 mm) warrants more research on developing practical methods to measure fines content in muckpiles to inform approaches to improve fragmentation and flow models.

Further work on defining the relationship between muckpile 80% passing size and DropWeight Index would help characterise ore domains in terms of mine and mill productivity. For the eleven samples tested in this study, there was an apparent correlation between muckpile 80% passing size and the resistance of the samples to abrasion, as determined by an abrasion test, ta.

The study made use of results from the initial New Afton lift, comprising of the B1 and B2 caves. It is envisaged that mill feed will continue to decrease in size as the B2 cave, a source of coarser ore, depletes and finer material from maturing drawpoints of the B1 cave is sent to the mill. The improvement in mill size fineness may warrant changes to be made to equipment in the mill to increase throughput, such as increasing the duty of the SAG mill by reducing the aperture size of the SAG mill screen or changing the size of steel media used in the SAG and ball mills.

Chapter 6: Heterogeneity Analysis for Assessment of Sorting Potential

6.1 Introduction

Sensor-based sorting was identified earlier as a key focus area of the proposed Cave-to-Mill approach as it address the lack of selectivity and potential for dilution associated with the block cave mining method. Online monitoring and bulk-sorting systems hold the potential to alleviate this problem and improve the productivity of caving operations while reducing energy and water requirements for each tonne of concentrate produced. The potential to sort is limited by the natural grade heterogeneity of the material being assessed. Where heterogeneity exists, there is an opportunity to use sensors to discriminate between ore and waste. For this reason, heterogeneity assessment is typically the initial component of a sorting study.

The definitions for Constitutional (CH) and Distributional (DH) heterogeneity, presented by Gy (2004), have been adopted to assess particle and bulk sorting, respectively. CH was used to represent grade variation within particle sorter feed sized particles (-100, + 10 mm) that make up an ore domain. While DH was used to represent grade variation within individual groups of ore reporting to drawpoints; the sum of the groups represents a *lot*. The *lot* is a special domain that can represent an entire draw column, in the case that heterogeneity within an individual drawpoint is being assessed, or a horizontal slice of caved ore, in the case that heterogeneity during a period of mine production is being determined.

Both Constitutional and Distributional Heterogeneity are affected by the various comminution and blending stages that take place from the onset of caving through to delivery of ore to the mill, as shown in Table 6.1. From the table it can be seen that as ore blocks travel away from their original in situ locations towards the surface stockpile, CH increases and DH decreases. In other words, the opportunity to sort particles increases and, conversely, the opportunity to bulk sort material decreases. It is important to note that the limitations of state-of-the-art particle sorting machines relate to throughput rate and particle size, approximately 10 mm being the finest particle size that can be economically sorted. Therefore, comminution steps that result in sub 10 mm particles being generated do not aid in increasing the sortability of ore.

The decrease in DH suggests that bulk sorting of material reporting to drawpoints would be most effective in the case that extraction and haulage levels are designed for separate handling of ore and waste.

Table 6.1 Chronological mixing / comminution events and their impact on heterogeneity

Chronology	Blending / Comminution Event	Blending or Comminution Event	Impact on heterogeneity	
			Constitutional Heterogeneity	Distributional Heterogeneity
1	Fragmentation at cave back	Fragmentation (primary)	⬆	-
2	Collapse onto caved ore muckpile	Blending & minor fragmentation	⇧	⬇
3	Waste entering draw cones	Blending (new ore type generated)	-	⬍
4	Flow through draw cones	Blending & secondary fragmentation	⬆	⬇
5	Haulage to orepass (through grizzly)	Blending & minor fragmentation	⇧	⬇
6	Mixing in orepass	Blending	-	⬇
7	Primary crushing	Mechanical comminution	⬆	-
8	Material flow through crusher product silo	Blending	-	⬇
9	Material transport to surface stockpile	Minor blending	-	⇩
10	Flow through stockpile	Blending	-	⬇

⇕ Minor Change ⬍ Significant Change

6.2 Evaluation of Distributional Heterogeneity and Implications on Bulk Sorting

An analysis of caved material heterogeneity was carried out to evaluate the potential to bulk sort at the New Afton mine. Mine personnel regularly sample drawpoints to support production scheduling decisions and carry out mine and mill reconciliation. As part of the regular sampling campaign, a grab sample of approximately 5 kg is collected for every ~350 tonnes of material that is excavated from drawpoints. Although the sampling procedure is biased by the size of rock that can be collected by samplers (+100 mm rocks not being collected), assays from collected samples provide valuable grade trends. Ross (2012) states that collecting 10 kg of drawpoint sample for every 2,500 tonnes of production yielded statistically relevant grade data at the Palabora block cave mine.

New Afton grade data for underground drawpoint samples were analyzed to predict the potential to bulk sort using a grade sensor and diverter system mounted on the underground-to-surface conveyor. For two months of operation, 2,478 copper grade results were analyzed. A cut-off grade of 0.3% Cu was nominated when calculating the proportion of run of mine (ROM) material that would have been diverted by the bulk sorting system prior to the mill. The Distribution Heterogeneity of the mill feed was calculated using Equation 6.1, from Gy (1995), for every day of production.

$$DH_L = N_G \sum_n \left[\frac{(a_n - a_L)M_n}{a_L M_L}\right]^2 \quad \textbf{(6.1)}$$

where N_g is the number of groups in a lot (equivalent to the number of drawpoints mucked during a day of production), L, a_n and M_n are the grade and mass of an individual group (equivalent to the muck from an individual drawpoint), n, and a_L and M_L are the weighted-average grade and mass of the entire lot of material (equivalent to the total mill feed for one day of operation).

Figure 6.1 shows simulated sorter performance for varying ROM grade and heterogeneity; the figure shows an inverse relationship between DH and ROM grade. Over the two months of

operation, 9.7% of material was below the cut-off grade of 0.30 % Cu. Efficient operation of a bulk sorter that is able to divert lots of 300 tonnes and greater, would yield an improvement in mill feed grade from 1.09 to 1.18 % Cu at a copper recovery of 98.5%.

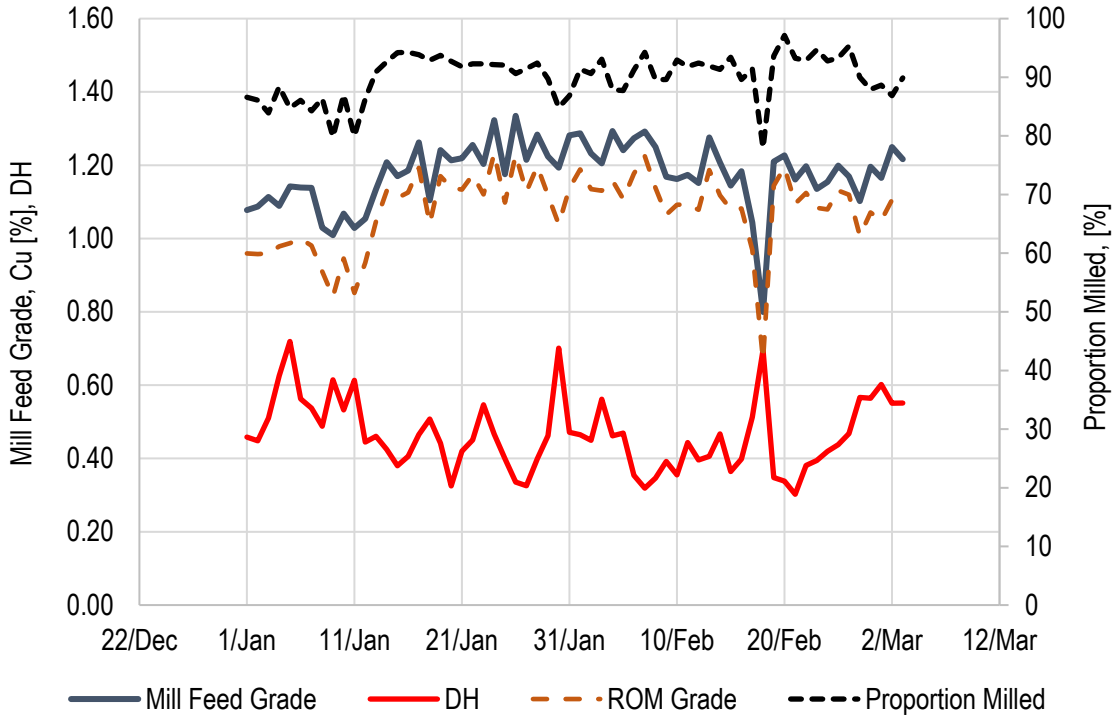

Figure 6.1 Distribution heterogeneity of caved muck during two months of operation in 2014 and theoretical bulk sorter performance for a cut-off grade of 0.3% Cu

6.3 Analysis of Heterogeneity at the Extraction Level

The extraction level of a cave mine refers to the network of drifts that provide access to drawpoints. Developments in bucket-mounted grade sensors for loaders prompted the analysis of grade heterogeneity within the columns of ore above individual drawpoints. To take full advantage of grade sensors mounted on load haul dumps (LHD), which transport material from drawpoints to orepasses, dedicated ore and waste material handling systems would be required; ideally these would be located in close proximity to drawpoints that experience high variability in ore grade. Figure 6.2 shows the grade heterogeneity calculated using Equation 6.1 for the 176

drawpoints that were in production during the period of January 1st to March 3rd, 2014. The figure shows that a greater degree of heterogeneity occurs at the boundary of the cave.

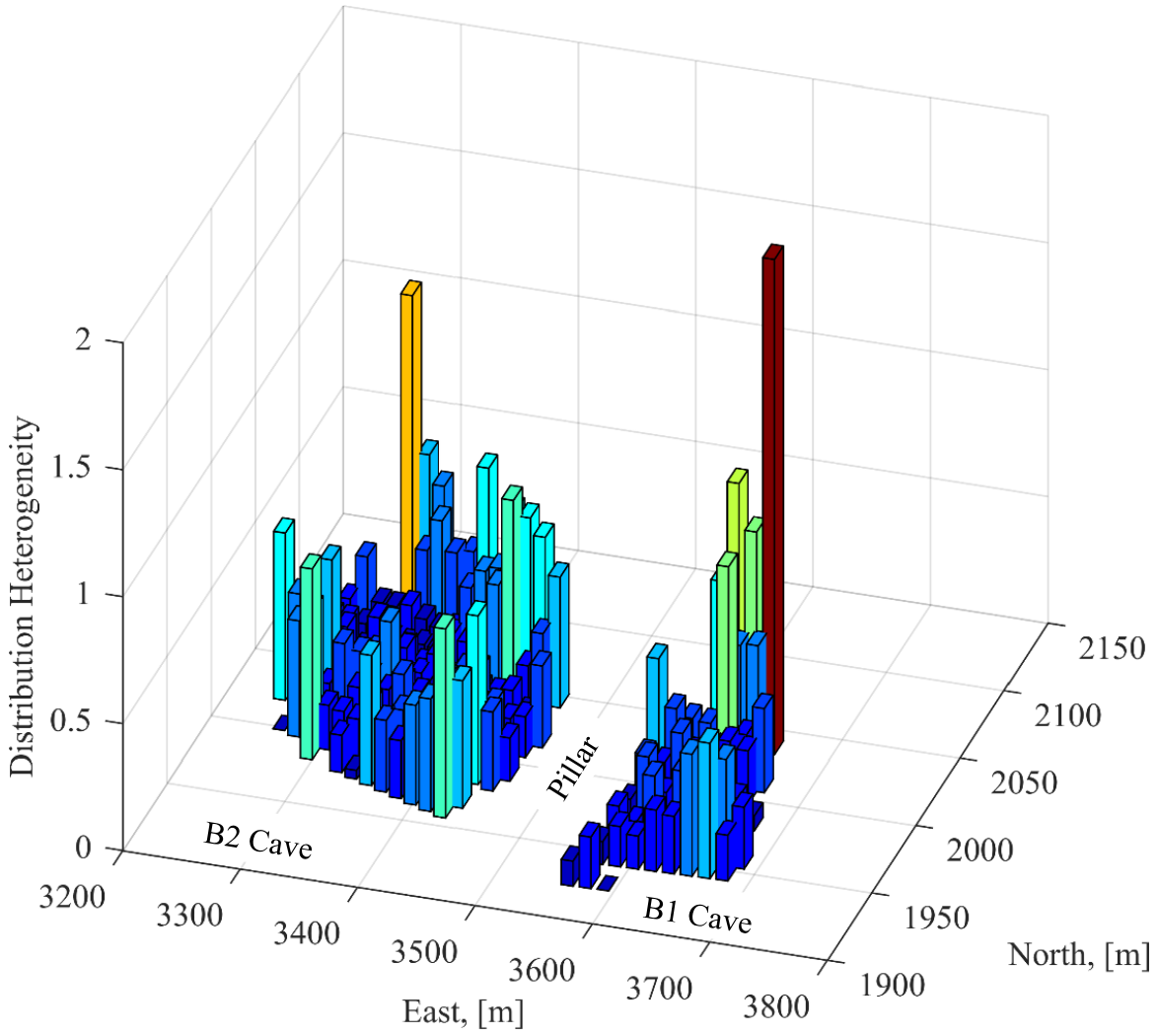

Figure 6.2 Distribution heterogeneity of caved muck during two months of operation in 2014

Erdenebat (2017) evaluated bulk material heterogeneity at the New Afton mine as part of his Master's research within the Cave-to-Mill research project. Grade data from regular drawpoint sampling was compared to the average grade of drawpoints during their life of production (effectively a grade estimate for the draw column), presented in Figure 6.3. The graph shows that bulk-scale heterogeneity generally decreased with grade.

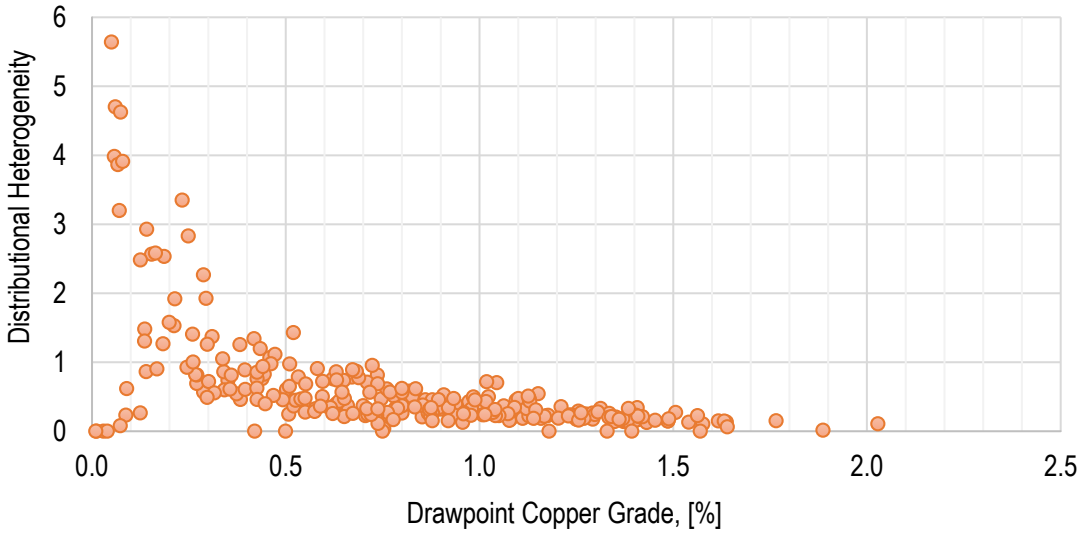

Figure 6.3 Distribution heterogeneity and average draw point grade (Erdenebat, 2017)

6.4 Variation of Grade with Size

The deportment of gold to different size fractions has a strong influence on the performance of particle sorting systems. In the case that copper-gold mineralization significantly reports to fine fractions, economic upgrading of mill feed could be carried out through size classification alone. Analysis using drawpoint samples showed that the fines (-2 mm) were generally lower in grade than the coarser fractions of (-50, +25 mm) and (-150, + 50 mm). Primary and secondary hypogene samples showed that grade increased with rock size, shown in Figure 6.4. Samples that were diluted with phyllic, picrite and/or monzonite material, presented in Figure 6.5, were found to have higher grades in the middling fraction of -50, +25 mm.

From the graphs it can be seen that the variation in copper grade was lower for sub 2 mm material. Since fines are known to flow preferentially within caves, it is expected that they are well mixed in comparison to other size fractions and therefore more homogenous in terms of grade.

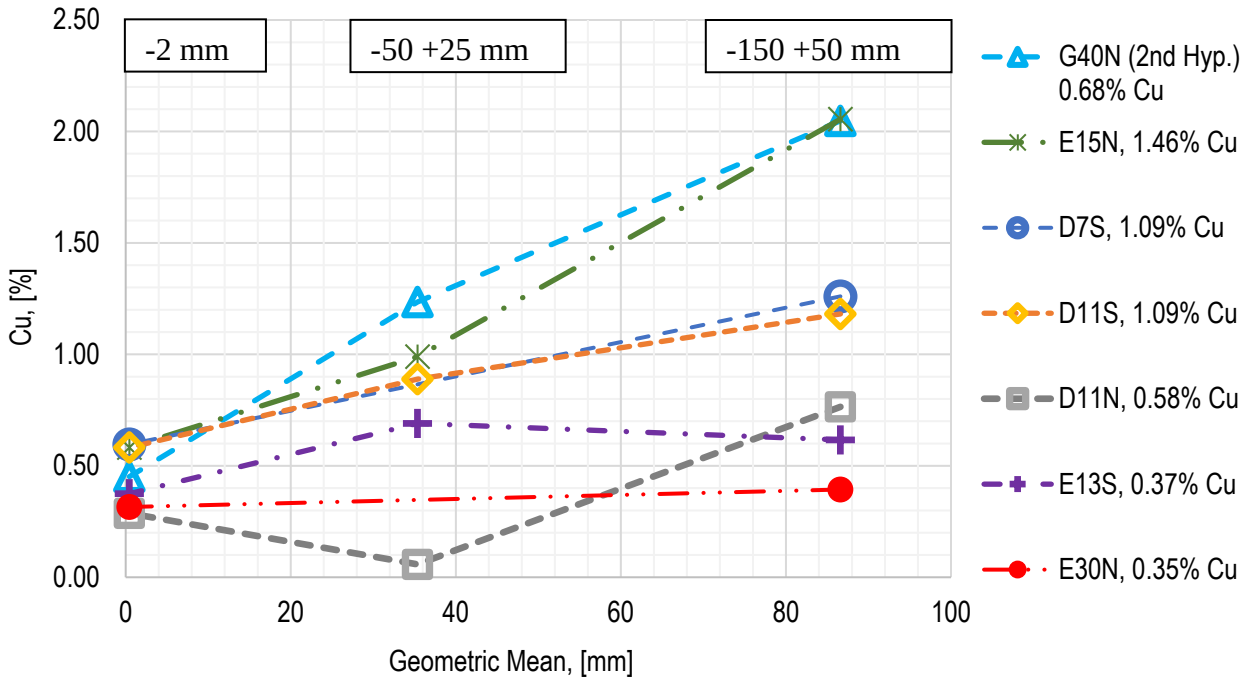

Figure 6.4 Copper grade of different size fractions in hypogene drawpoint samples. Grades of overall drawpoint samples from ICP analysis of representative sub-samples are shown in the legend

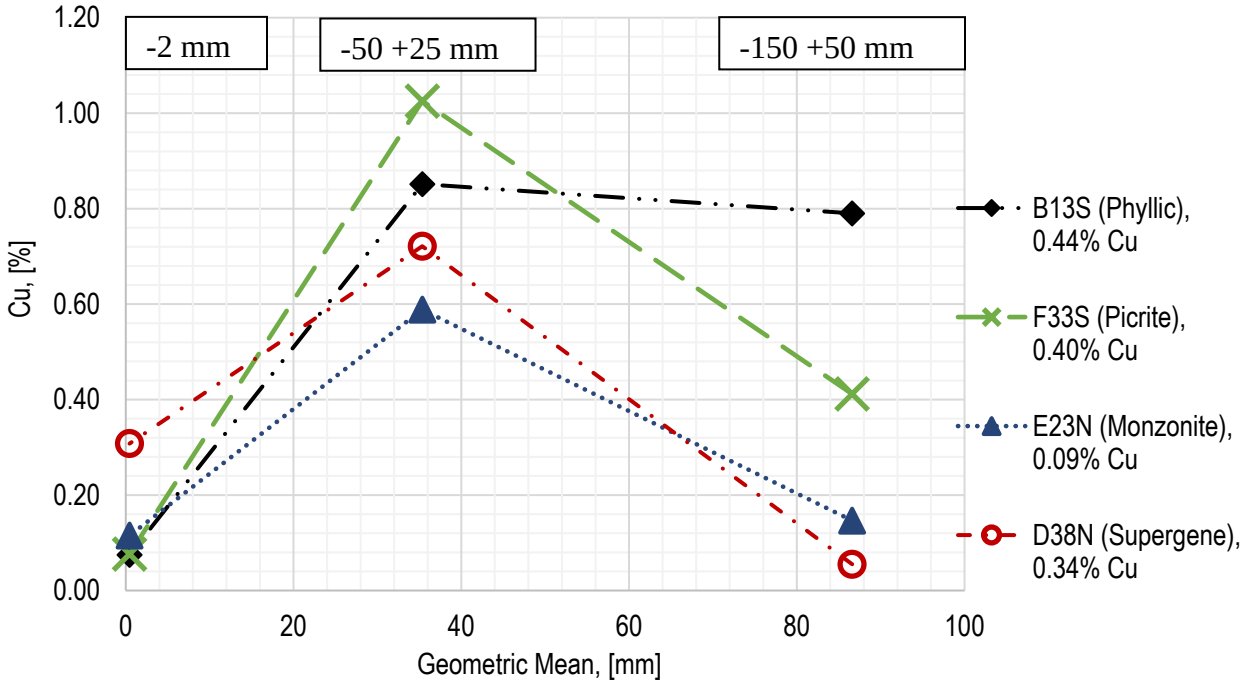

Figure 6.5 Copper grade of different size fractions in drawpoint samples with identified dilution/mineralization type. Grades of overall drawpoint samples from ICP analysis of representative sub-samples are shown in the legend

6.5 Discussion and Conclusions

The heterogeneity analysis supported the use of bulk sorting in the proposed Cave-to-Mill approach. When comparing the grade of material reporting to individual drawpoints, higher variations in grade were found to occur at the perimeter of the cave. At New Afton and most cave mines, orepasses are used to handle both ore and waste. This results in ore dilution occurring when material is transported from drawpoints and through the material handling system to surface. The results suggest that bulk sorting systems, such as the use of bucket-mounted grade sensors with production LHDs, should be focused on areas near the perimeter of the cave. Designing extraction and haulage levels to include dedicated ‘waste’ passes may also hold value to future cave operations.

Grade data for different size fractions indicates that screening of ROM material prior to particle sorters will generate a lower grade fines stream and a higher grade coarse stream for particle sorting or direct processing. The grade distribution in different size fractions shows that the size bias associated with collecting samples for grade monitoring of drawpoints will affect the accuracy of grade estimates.

.

Chapter 7: Bulk and Particle Sorting System Evaluation

7.1 Introduction

Successful implementation of sensor-based sorting systems stands to reduce milling requirements, improve the quality of mill feed and increase the size of the economic footprint. Following the heterogeneity analysis, presented in Chapter 6, an evaluation of bulk and particle sorting technologies was carried out at the New Afton block caving operation. It is envisaged that implementation of sensor-based sorting as part of the proposed Cave-to-Mill approach has considerable potential to improve the productivity of existing and future block cave operations.

From outcomes of the cave fragmentation (Chapter 4) and mill performance (Chapter 5) evaluations, a summary of key rock types and their implications on productivity is shown in Table 7.1 Identification of unique sensor responses for these rock types provides an opportunity to apply sorting strategies according to grade, and mill comminution and recovery performance.

Table 7.1 Main lithology and alteration types and implications on the New Afton operation

Lithology / Alteration	Ore / Dilution	Implications on Mine	Implications on Mill
Hypogene	Ore (high grade)	Competent rock	Highest value mill feed
Secondary Hypogene	Ore (high grade)		Increasing tennantite concentration
Supergene	Ore	Present geotechnical challenges due to low competence. Fine cave fragmentation	Lower copper recovery when treated by flotation. Increasing copper recovery by applying gravity concentration.
Picrite	Dilution		Negatively affects froth flotation performance
Fault Rock	Dilution		Low work index
Monzonite	Waste (monzonite)	Competent rock associated with coarse fragmentation	Difficult to grind due to high work index
Carbonates	Dilution	Competent rock on a lump scale. Associated with faults	

7.2 PGNAA Bulk Sensor Evaluation

As discussed in the Methodology Section (3.8), nine samples of approximately 220 kg each were prepared for PGNAA testing. Samples were collected from drawpoints, mill feed and waste

stockpiles. Overall, a wide range of copper grades and rock types, as outlined in Table 7.1, were prepared.

The nine samples were sent to Scantech testing facilities in South Australia for testing with a Geoscan-M unit, which was fitted with four detectors. Each sample was measured for a period of at least three hours, during which individual instantaneous analysis periods were varied throughout the test work to achieve a number of results for different measurement periods. The expected accuracy of a Geoscan-M unit when installed on a conveyor could then be estimated for different measuring times (which are directly related to the quantity of conveyed material). Figure 7.1 shows a comparison of copper grades measured by the Geoscan-M test unit and ICP analysis of representative sub-samples. The relative standard deviation associated with sampling and ICP analysis for copper content was less than 5% of the mean copper grade of each sample. Included in the figure are 95% confidence intervals based on the sub-sampling and assaying procedures used.

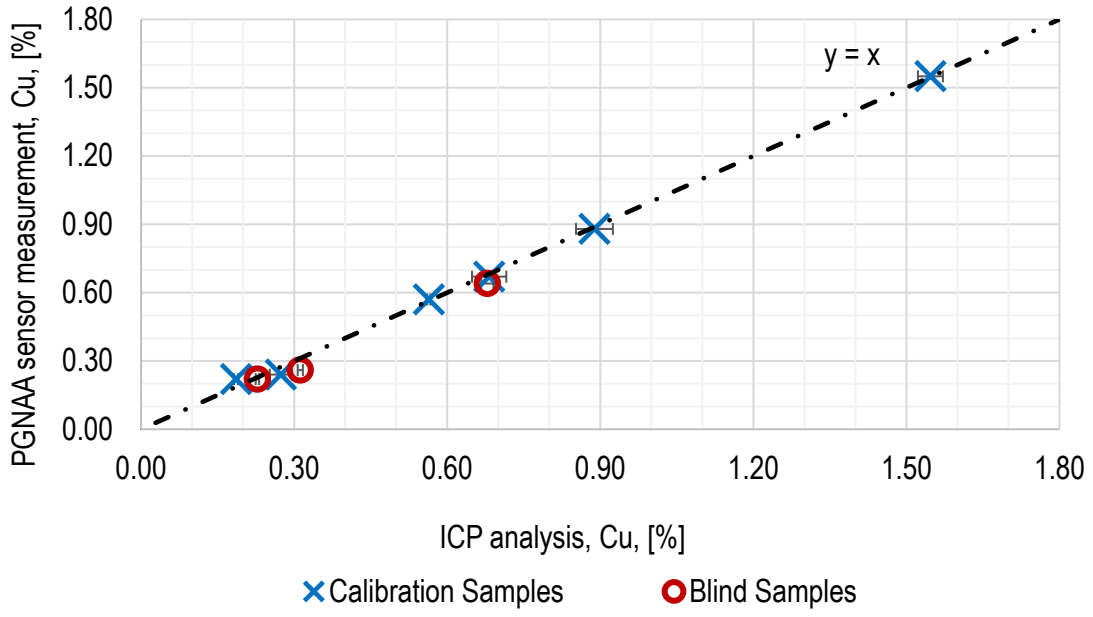

Figure 7.1 Predicted copper grades of bulk samples using PGNAA sensors and results from ICP analyses for copper including 95% confidence intervals for sub-sampling and ICP analysis

The repeatability of copper grade measurements in relation to analysis time and number of detectors, reported by Balzan (2016), is shown in Table 7.2. At New Afton, an underground-to-surface conveyor transports ore and waste at approximately 1,000 tonnes per hour. Based on this conveying rate, the quantity of material transported during each analysis interval has been estimated and included in the table. Selection of an analysis interval represents a trade-off between grade measurement accuracy and sorting lot size, assuming that the conveyor is fitted with a means to segregate the increment. Essentially, the sorting lot size should be nominated with consideration of the heterogeneity of conveyed material. The measurement accuracy of a PGNAA sensor unit can be improved up to a certain limit by increasing the number of detectors at the expense of additional sensor cost.

Table 7.2 Measurement repeatability in relation to the material handling system

Analysis Period [minutes]	Tonnes Scanned [tonnes]	Equivalent Material Handling Lots	Number of Detectors [#]	Copper Measurement, Standard Deviation [%]
2	33	One haul truck load	4	0.035
2	33		6	0.029
2	33		8	0.025
2	33		12	0.020
0.5	8	One LHD bucket	4	0.070
0.5	8		6	0.057
0.5	8		8	0.050
0.5	8		12	0.041

The gold grades associated with New Afton ROM material are below the threshold measurement value of 500 ppm, equivalent to 500 grams per tonne, of the Geoscan-M unit. Applications of the technology for gold grade measurement typically rely on proxy elements being used in a regression equation to estimate gold content. For the case of New Afton, drill core data and

grades from regular drawpoint samples show that the average ratio of gold (g/t) grade to copper (%) grade is approximately 0.8.

Figure 7.2 shows how gold grade predictions and fire assay results compared. An R-squared value of 0.76 resulted. The 95 % confidence intervals representing sampling and fire assay error ranged from 0.11 to 0.39 g/t.

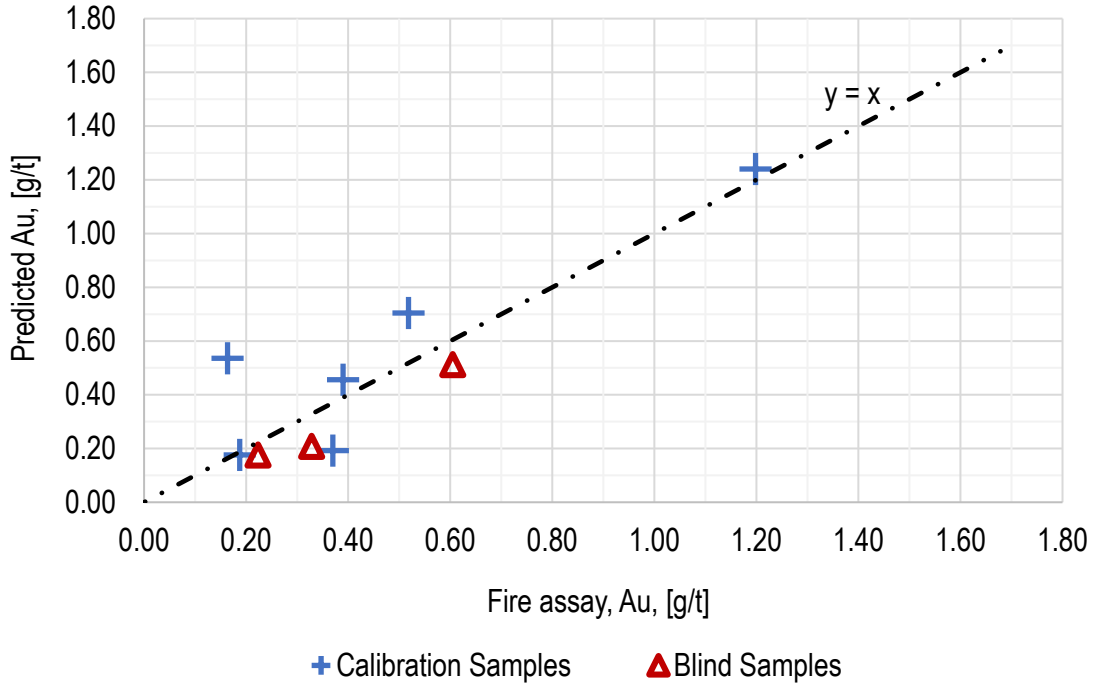

Figure 7.2 Predicted gold grades of bulk samples using PGNAA sensors and results of fire assays

7.3 XRF Particle Sensor Evaluation

XRF measurements were carried out on the surfaces of 1,226 rocks in the (-150, +25 mm) size range using a measuring time of 10 seconds for samples taken from drawpoints and mill feed stockpiles. Four surface readings were taken per rock. From the master set of 1,226 rocks, 291 rocks were selected based on rock type and subjected to crushing and pulverizing to determine the grade. More information is provided in the Methodology Section (3.8) and the test work flow is shown in Figure 3.5.

Matlab R2016b was used to carry out stepwise regression analysis of pXRF readings for rock surfaces and powder material after pulverizing. Model terms with an entrance tolerance less than a p-value of 0.05 and an exit tolerance less than a p-value of 0.10 were accepted into the model. Equation 7.1 shows the resulting model for copper. Figure 7.3 shows a plot of predicted and observed copper grades, where an R-squared of 0.79 was achieved.

$$\widehat{Cu} = 2.41Cu_{avg} - 0.46Cu_{max} - 0.15{Cu_{avg}}^2 \quad \textbf{(7.1)}$$

where $\widehat{Cu}$ is the predicted copper content, Cu_{avg} and Cu_{max} are the average and maximum Cu grades of four pXRF surface readings. The root mean squared error for each rock was weighted by the copper grade from readings of pulverized material. The coefficients in Equation 7.1 were fitted by minimising the sum of the weighted root mean squared error.

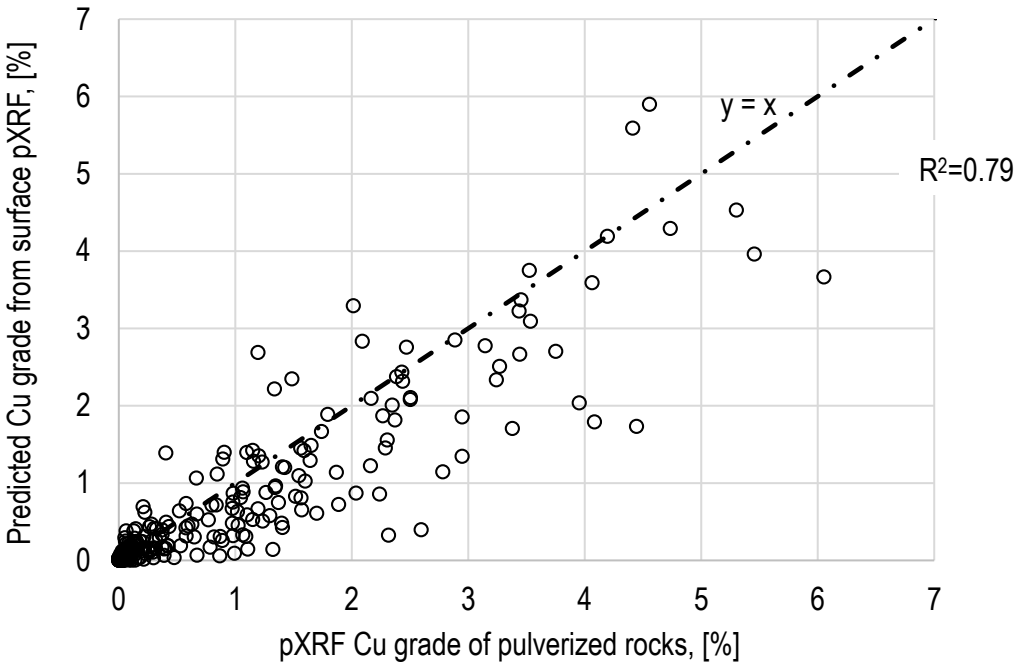

Figure 7.3 Predicted copper grades from surface readings and observed copper grades for 291 particles

Results from the dataset of 291 particles, having a weighted average grade of 0.86% Cu, were used to simulate the sorting performance of a sorter. Grade and recovery curves in relation to sorter mass pull are presented in Figure 7.4. The figure shows that surface XRF readings can be

used to recover 90% of the copper in 40 % of the material, which has a resulting grade of almost 2% Cu. Ideal grade-recovery data, determined using the copper content of each rock, shows that a recovery of approximately 92% is theoretically achievable for the same mass pull. Results from PGNAA and XRF test work confirmed that New Afton material is amenable to these technologies for sensor-based sorting.

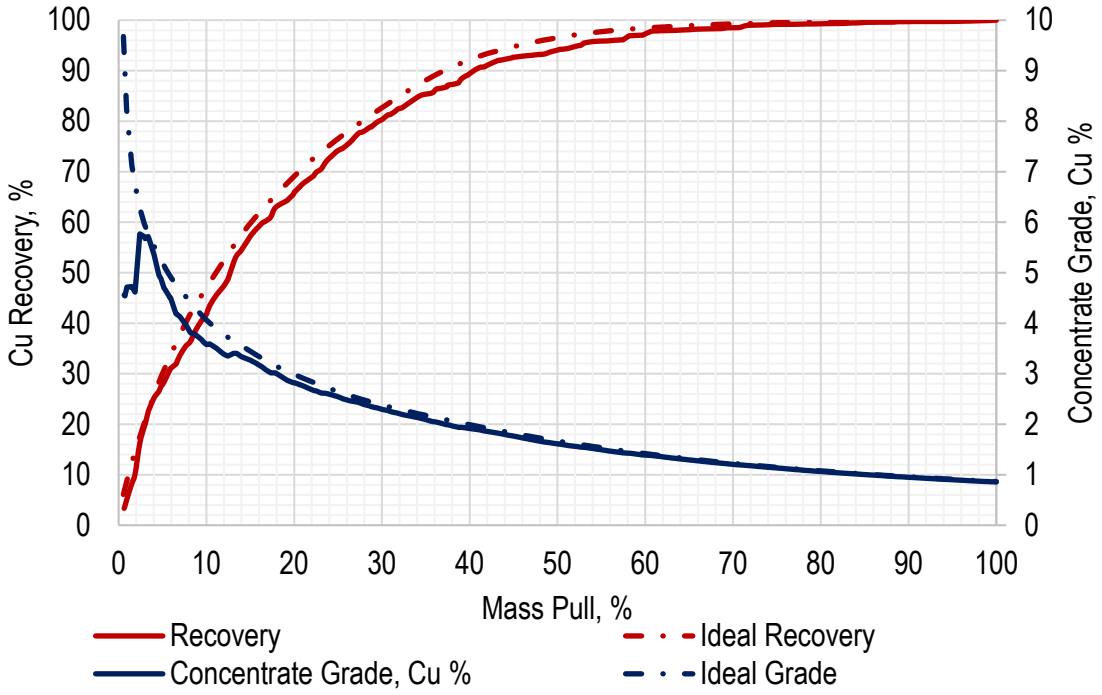

Figure 7.4 Particle sorting performance based on pXRF testing of 291 particles

The XRF measurement time that is achievable during sorter operation is shorter than the 10 second measuring time that was used for portable XRF testing. Test data for a Steinert pXRF sorting unit from an independent study by Mazhary (2018) were analysed to observe the difference in sensing performance. The sorter tests were carried out on 94 particles that were conveyed individually past the XRF sensor and measured in millisecond time-scales. Following testing, each particle was pulverised and sub-sampled for copper grade measurement by ICP analysis. Equation 7.2 shows the resulting model for copper.

$$\widehat{Cu} = \beta_0 . \mathrm{Cu} - \beta_1 . Cu^2 \qquad \textbf{(7.2)}$$

Where β_0 and β_1 are fitted constants and Cu is the measured copper under dynamic conditions. Figure 7.5 shows a plot of predicted copper grades under dynamic conditions and observed copper grades. An R-squared of 0.76 was achieved, which is slightly lower than the R-squared value of 0.79 achieved with the portable XRF unit using longer measurement times for multiple surfaces.

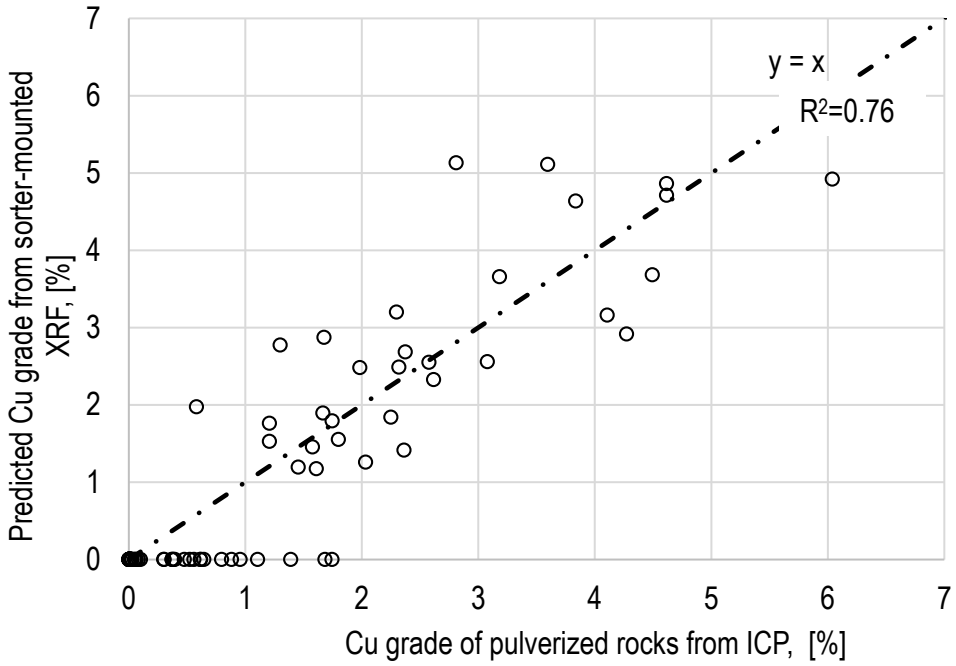

Figure 7.5 Predicted copper grades from surface readings taken under dynamic conditions using a sorter-mounted XRF and observed copper grades for 94 particles

Grade and recovery curves in relation to sorter mass pull were calculated for sorter operation and are presented in Figure 7.6. Sorting performance estimates based on portable XRF testing and dynamic testing from Mazhary (2018) were similar. For example, at a mass pull of 30%, dynamic sorting tests showed a recovery of 81.5 % while using portable XRF test results a recovery of 80.3% was determined.

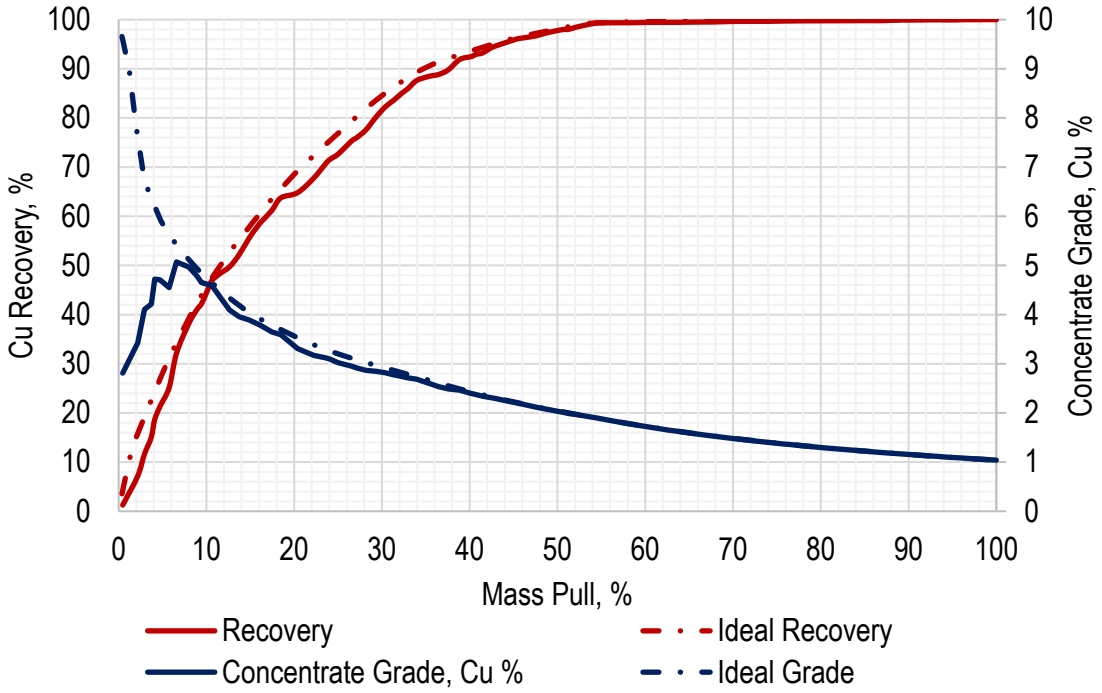

Figure 7.6 Particle sorting performance from testing under dynamic conditions using a sorter-mounted XRF with 94 particles

7.4 Sorting System Evaluation

The envisaged combination of bulk and particle sorting systems at the New Afton block cave mine is presented in Figure 7.7. All caved material, irrespective of grade, is conveyed to surface past a PGNAA bulk sensor. Based on the grade measurement, a mechanized diverter separates the material into high grade, intermediate grade and waste stockpiles.

Low grade material that is transported on the underground-to-surface conveyor is dumped to a waste stockpile and high-grade material is sent directly to the mill.

Intermediate grade material is fed to a double-deck screen with aperture sizes of 100 and 37.5 mm. Oversize (+100 mm) is crushed in closed-circuit with the screen and the middlings are sent to a coarse (-100, +37.5 mm) particle sorting unit. Screen undersize is conveyed to a single-deck screen with a cut-point of 12.5 mm. The oversize is processed by a fine (-37.5, +12.5 mm) particle sorting unit and the fines are either milled or dumped to a waste stockpile depending on

the head grade measured by the bulk sensor at the time when it was conveyed from underground or depending on the measured grade should an additional PGNAA sensor be installed. Screening is carried out with wet sprayers to clean the surfaces of the rocks. Both coarse and fine particle sorting units are equipped with (1) XRF sensors that determine copper grades from surface readings, and (2) pneumatic ejectors, that send above cut-off grade material to a mill feed stockpile. The ratios of the maximum and minimum particle sizes for the coarse and fine units are within the guideline range of 3:1 for particle sorting; a guideline suggested by Salter and Wyatt (1991).

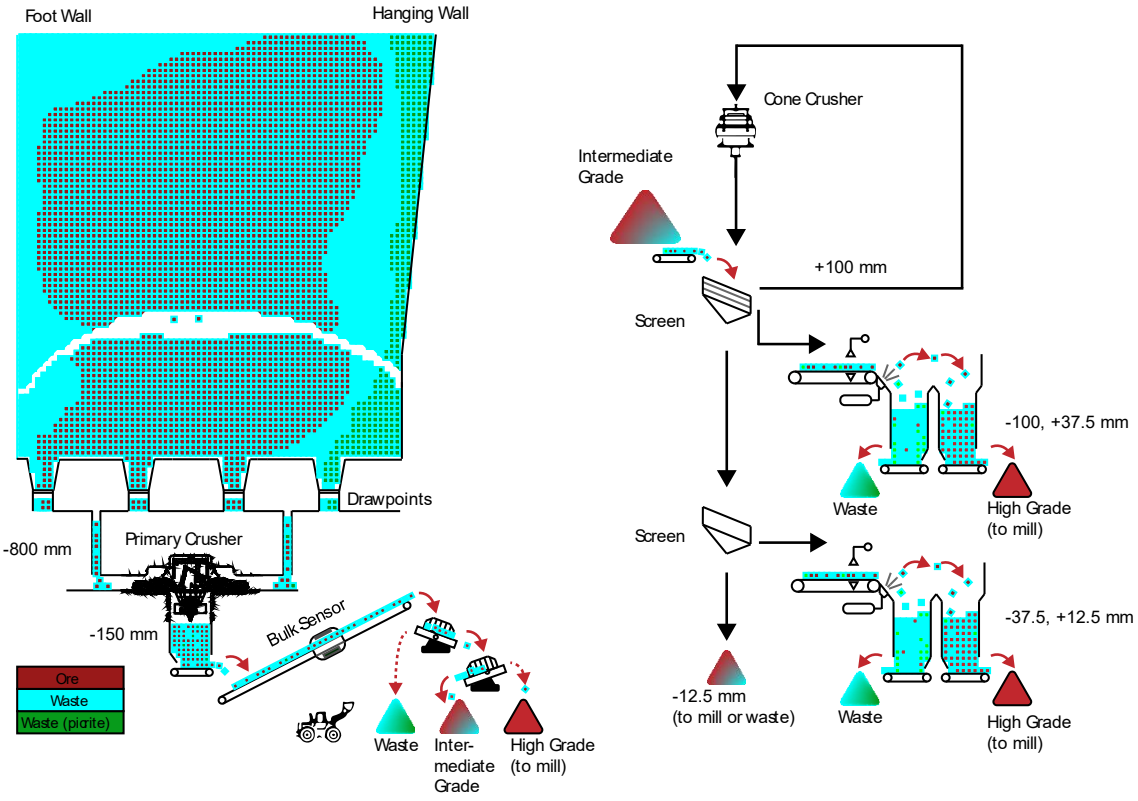

Figure 7.7 Simplified flowsheet of the mine and sorting systems

7.5 XRF Particle-Sorting Models

The amount of ore available for particle sorting depends on the proportion of fines (-12.5 mm) contained in the primary crushed ore. Sieving of primary crushed material was carried out as part of the fragmentation study described in Chapters 4 and 5. Results showed that approximately

34% of primary crushed material would pass a 12.5 mm screen. The proportion of fines was found to increase as the cave matures. Analysis of copper grades within different size fractions, presented in Section 6.4, showed that the grade of finer size fractions (-2 mm) was lower than the coarser size fractions of (-50, + 25 mm) and (-150, +50 mm). Based on the results it was assumed that within primary crushed material, the grade of the -12.5 mm size fraction was 75% of the head grade. Based on the assumptions for caved ore size and grade variation with size, the grade of ore sorter feed (+12.5 mm), is calculated by the following equation:

$$f_{sorter\ feed}\ (\%) = \frac{f.(1-fines\ dilution.P_{12.5mm})}{(1-P_{12.5mm})} \quad \textbf{(7.3)}$$

where f is the copper grade of caved material, $P_{12.5\ mm}$ is the proportion of feed that passes a 12.5 mm screen and *fines dilution* is the grade of fines (-12.5 mm) as a percentage of head grade.

The Constitutional Heterogeneity (CH) of underground drawpoint samples and a surface sample, which is a blend of material from underground drawpoints, were calculated based on pXRF surface readings for copper and pXRF readings of the same rocks after pulverizing using equation 7.4.

$$CH_L = N_F \sum_i \left[\frac{(a_i - a_L)M_i}{a_L M_L}\right]^2 \quad \textbf{(7.4)}$$

where N_F is the number of particles in a lot, L, a_i and M_i are the grade and mass of an individual particle within the lot, and a_L and M_L are the weighted-average grade and mass of the entire lot of particles.

Figure 7.8 shows that the degree of grade heterogeneity, represented by CH, determined from surface readings is in-line with the grade heterogeneity determined from pulverized rocks. Therefore, pXRF surface measurements and rock masses could be used to determine the CH of each muckpile. The head grade of each muckpile sample was determined by crushing all collected rocks and fines, sub-sampling and carrying out ICP analysis. A comparison of CH and

muckpile grade is shown in Figure 7.9. Variations in copper grade were found to be higher for lower grade samples.

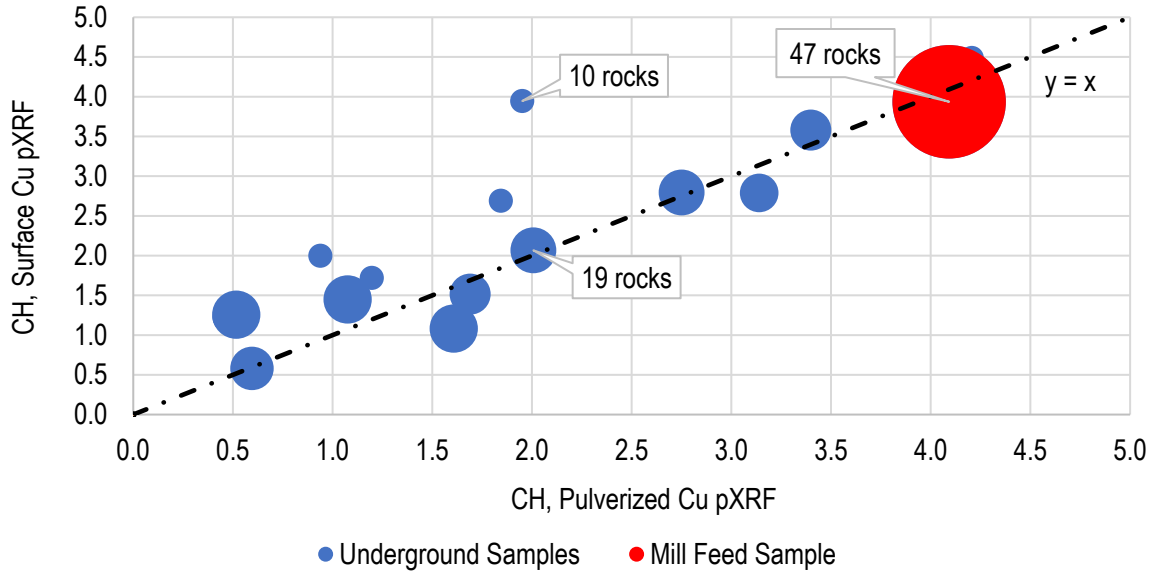

Figure 7.8 Constitution heterogeneity based on surface readings of rocks and pulverized samples. Bubble widths are based on the number of rocks in each sample.

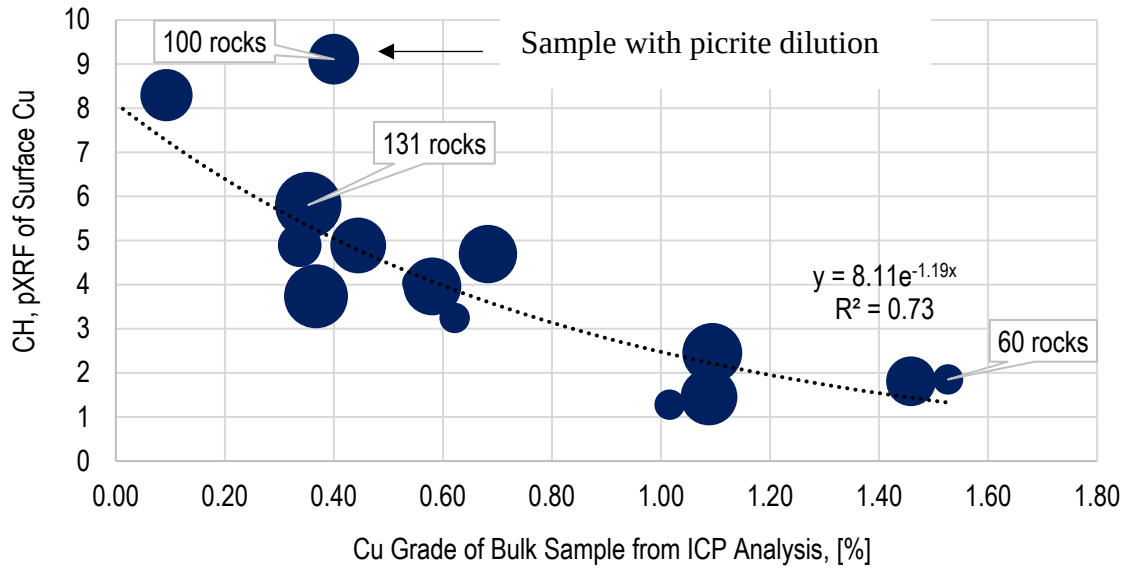

Figure 7.9 Constitution heterogeneity from surface pXRF measurements and Cu grade of underground samples (determined from ICP analysis of all collected sample including fines). Bubble widths are based on the number of rocks in each sample

To simulate the performance of an XRF particle sorter operating with different head grades, the master data set for 291 rocks that had surface and pulverized sample measurements taken was separated into data sub-sets representing head grades ranging from 0.02 to 1.4 % Cu. When selecting rocks for a target heard grade, a grade-weighted random selection function was used in Excel. Objectives of the selection function were to select rocks such that (1) the weighted average grade of the rocks corresponded to the target head grade and (2) the head grade and CH were within 15% of the trend line included in Figure 7.9. Equation 7.3 was used to determine the head grade based on the weighted average grade of rocks and the fines dilution. For example, for a head grade of 0.22% Cu, surface and powder pXRF measurements for 218 rocks were randomly selected and the resulting CH was 6.8. The weighted average grade of all 218 rocks was 0.25% Cu. Equation 7.1 was then applied to determine the sorting performance achievable with the surface pXRF measurements.

Particle sorting performance could then be simulated for a range of head grades while accounting for the heterogeneity occurring within lots of New Afton caved material.

7.6 Process and Cost Assumptions

Table 7.3 shows the assumptions used to evaluate the sorting system. The mechanical sorting efficiency, which is defined as the efficiency of the ejection system to recover above-grade material that had been correctly identified by the XRF sensors, was assumed to be 95%. Milling and material handling costs were determined from demonstrated site cost data. The cost for screening, crushing and sorting was nominated to be $0.80 per tonne of screen feed. Lessard et al. (2016) assumed a cost of $0.10 to $0.13 for XRT particle sorting of pebbles from a semi-autogenous mill circuit.

Table 7.3 Cost and process assumptions

Process	Units	Value
Copper price	$/lb	2.90
Gold price	$/oz	1,290
Silver price	$/oz	17
Ratio of Cu (%) to Au (g/t)	-	0.81
Loading (screening plant cost)	$/t	0.65
Milling cost	$/t of mill feed	9
Waste disposal cost	$/t	2.48
Screening, crushing & sorting cost	$/per tonne of screen feed	0.80
Percentage passing 12.5 mm	%	34
Mechanical sorting efficiency, eff_{sort}	%	95
Grade of -12.5 mm material (fines dilution)	% of head grade	75

The following flotation recovery model for copper in B1 and B2 hypogene ores was determined by New Afton metallurgists from site data and applies for mill process rates of 15,500 tonnes per day:

$$Cu\ Flotation\ Recovery\ (\%) = 89.1(-0.37 f_{mill\ feed}^{2} + 0.80 f_{\text{mill feed}} + 0.57) \quad \textbf{(7.5)}$$

where $f_{\text{mill feed}}$ is the copper feed grade in %.

Recovery models based on historical mill data were also used for gold and silver recovery calculations. All cost and mill recovery assumptions were combined with the particle sorting model to determine the mass pull that provides the highest value for each head grade. For the case where material is screened, the oversize is processed by a particle sorter and the fines are processed by the mill, recovery of copper contained in screen feed is calculated by the following equation:

$$Copper\ Recovery, R\ (\%) = R_{sort}.eff_{sort}.(1 - fines\ dilution.P_{12.5mm}) + P_{12.5mm}.fines\ dilution \quad \textbf{(7.6)}$$

where R_{sort} is the proportion of copper in sorter feed that is recovered by the sorter and eff_{sort} is the efficiency of particle sorting systems downstream of the sensors.

The proportion of ROM material that is directed to the mill is given by:

$$\Upsilon\ (\%) = \Upsilon_{sorter}\ .(1 - P_{12.5mm}) + P_{12.5mm} \quad \textbf{(7.7)}$$

where Υ_{sorter} is the proportion of sorter feed mass, or mass yield, that reports to sorter concentrate.

The grade of mill feed is calculated as:

$$f_{mill\ feed}\ (\%) = \frac{R.f}{\Upsilon} \quad \textbf{(7.8)}$$

where f is the head grade of caved material.

Similar calculations are used for the case where caved material is screened and the oversize is processed by a particle sorter while the fines are dumped to waste stockpiles.

$$R_{without\ fines}\ (\%) = R_{sort}.eff_{sort}.(1 - fines\ dilution.P_{12.5mm}) \quad \textbf{(7.9)}$$

The mass pull, Υ, of caved material that reports to sorter concentrate is:

$$\Upsilon\ (\%) = \Upsilon_{sorter}.(1 - P_{12.5mm}) \quad \textbf{(7.10)}$$

For both particle sorting scenarios, the value of recovered copper in copper concentrate is determined by the following equation:

$$Cu\ value\ \left(\frac{\$}{t}\right) = f.R.R_{flotation}(\%).Cu\_price\left(\frac{\$}{t}\right) \quad \textbf{(7.11)}$$

where R is the copper recovery of the screening and sorting circuit which is determined from either Equation 7.6 or 7.9 (depending on whether fines are milled or dumped to waste), and $R_{flotation}$ is the flotation copper recovery. Similarly, the gold and silver values are determined by applying their respective flotation recoveries and market values.

The overall value per tonne of ore is:

$$NSR\ \left(\frac{\$}{t}\right) = Cu\ value + Au\ value + Ag\ value - \ Milling\ cost\left(\frac{\$}{t}\right).\Upsilon(\%) - Sorting\ cost\left(\frac{\$}{t}\right) \quad \textbf{(7.12)}$$

An example of how the two sorting options compare for a feed grade of 0.22% Cu is shown in Figure 7.10. A mass pull of 31% provides the best value for both sorting options. The highest value of $6.52 per tonne was calculated for the option of particle sorting and processing of fines. This result represents an improvement over the value of $6.12 per tonne associated with direct milling.

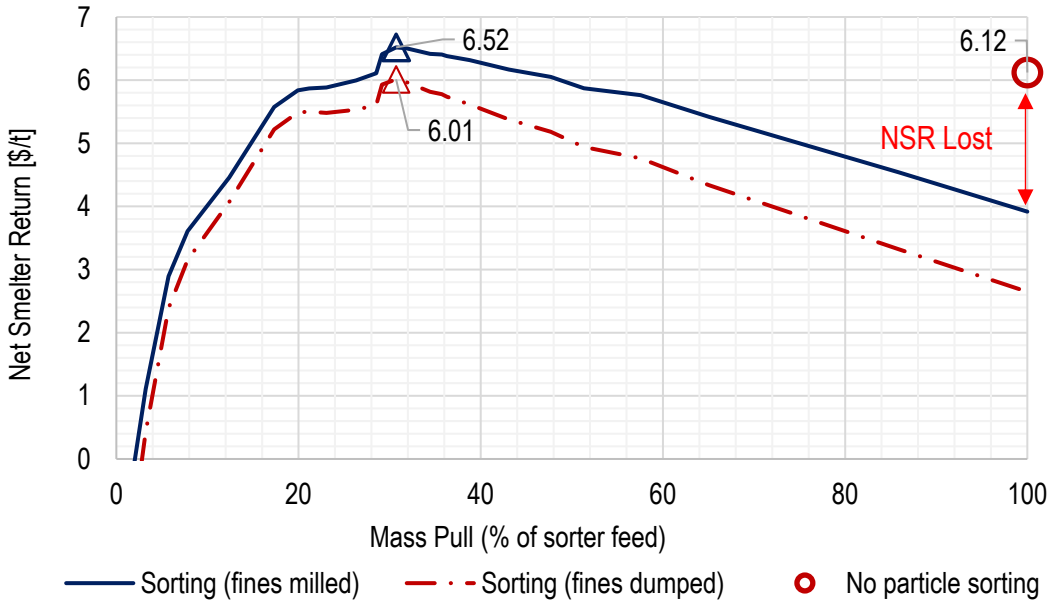

Figure 7.10 NSR and copper recovery in relation to mass pull for a material copper grade of 0.22%

The modelling process was repeated for all sub-sets so that the optimum mass pull target (maximum sorting NSR) for a range of copper grades could be determined, which is shown in Figure 7.11. The corresponding sorter recoveries are included in the graph.

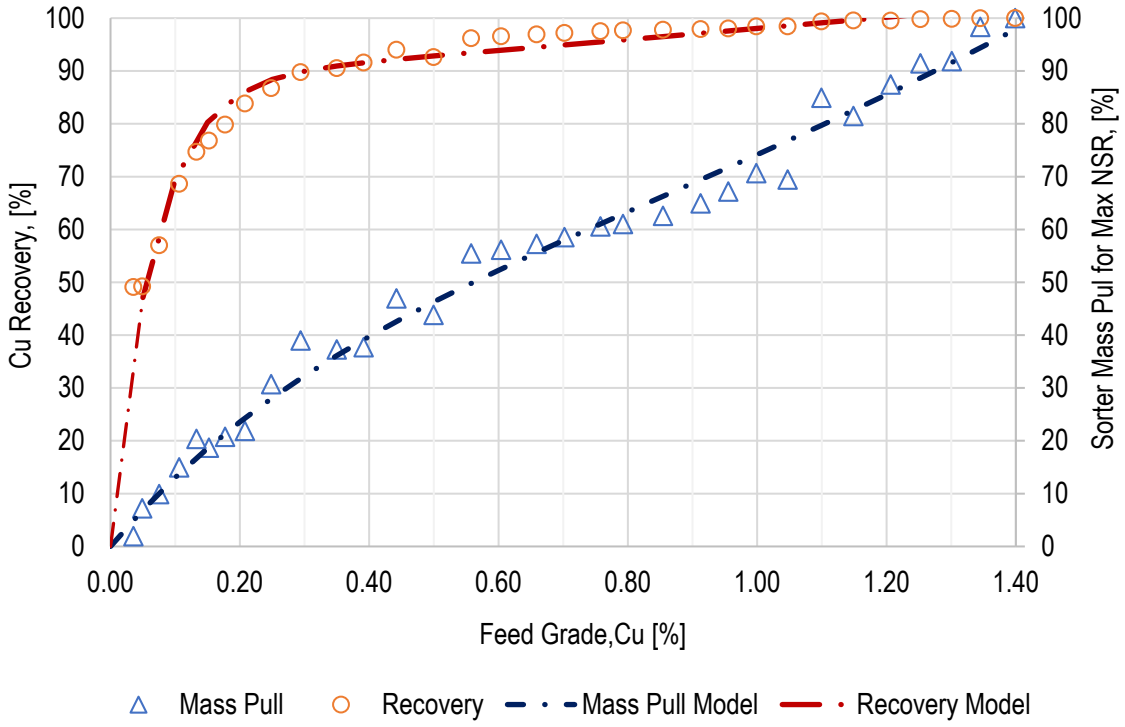

Figure 7.11 Economic mass pull and corresponding copper recovery in relation to material grade

Models for economic sorter mass pull and the corresponding metal recovery were fitted to results using the following equations:

$$Economic\ Sorter\ Mass\ Pull = 40.04e^{0.64 f_{sorter\ feed}} - 40.04e^{-3.00 f_{sorter\ feed}} \quad \textbf{(7.13)}$$

$$Economic\ R_{Sorter} = 88e^{0.11 f_{sorter\ feed}} - 88e^{-15.09 f_{sorter\ feed}} \quad \textbf{(7.14)}$$

By combining Equations 7.13 and 7.14 with equation 7.3, which relates the grade of caved material to the grade of sorter feed, sorting performance can be applied to a grade block model to determine the value associated with each processing option.

7.7 Application of Sorter Models to Grade Block Models

For each block of ore within a grade block model, the value associated with direct milling (contained NSR), particle sorting with and without fines dumping (ore sorting NSR), versus

disposal as waste can be determined and compared using the calculations presented. Running production schedules for a nominated footprint allows the capacity requirements of sorting equipment to be estimated.

Incorporating assumptions for contained gold and silver ratios, a comparison of ore value and feed grade is presented in Figure 7.12, which shows that for grades from 0.10 to 0.20% Cu, the highest value is achieved by particle sorting +12.5mm particles and sending -12.5 mm material to waste dumps. For ore grades of 0.20 to 0.36% Cu, the most economic option is to sort +12.5 mm material and process -12.5 mm in the mill. For grades above 0.36% Cu, the highest value is achieved by sending all material to the mill. At these grades, reductions in milling cost due to sorting are outweighed by the value of copper lost due to particle sorting inefficiencies.

In caving operations, there are periods of operation where waste is caved and transported to surface due to: the requirement of achieving a suitably large footprint to ensure that the cave initiates and propagates, to access ore that is separated from the extraction level by blocks of waste and due to unplanned dilution. Once sub-economic material has been brought to surface, the value added by particle sorting may make it a preferable option to moving material to a waste dump. For this reason, mining costs have not been included in the value calculation in Figure 7.12. The graph shows that the cut-off grade for on-surface material is 0.11% Cu.

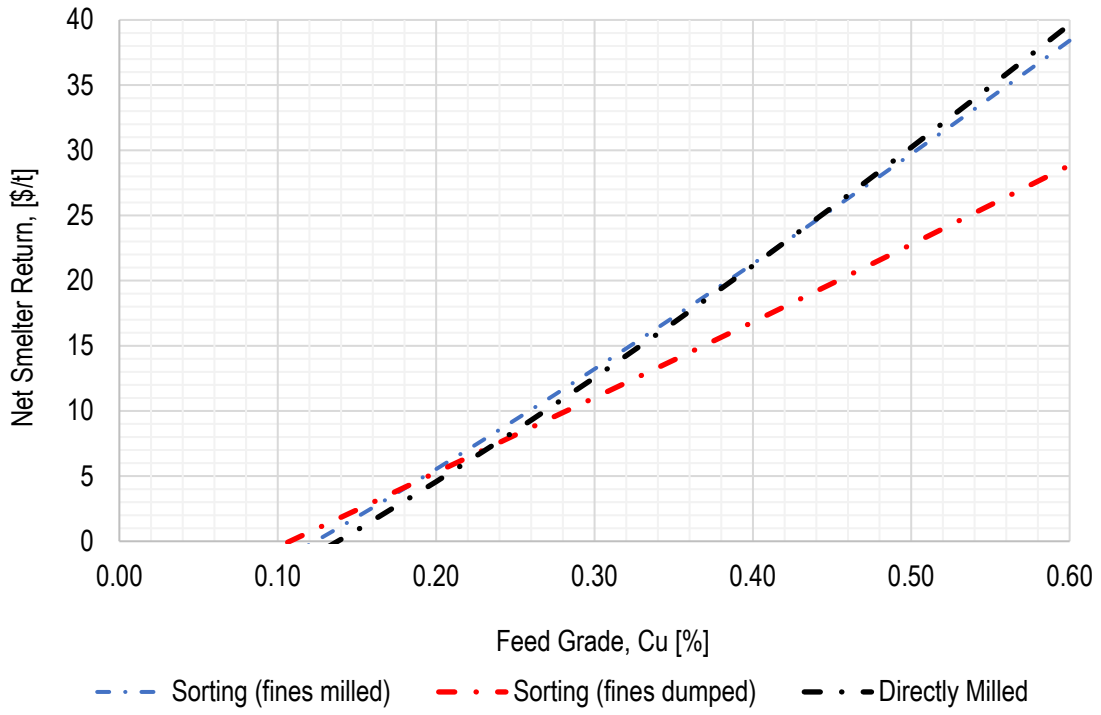

Figure 7.12 Net smelter return in relation to material grade for three sorting options. Grade ratios of Au (g/t): Cu (%) and Ag (g/t):Cu (%) of 0.82 and 2.6 assumed based on grade data

7.8 Discussion and Conclusions

The sorting evaluation relied on key outcomes from the fragmentation and heterogeneity studies, and mill recovery models. An integrated approach, as proposed with Cave-to-Mill, is required for proper assessment of the potential to add value through implementation of sorting systems.

The presented method for assessing the value of bulk and particle sorting systems was developed using material from an operating block cave mine. For block cave mines that are in the project development stage, drill core samples could be used in place of drawpoint samples. Grade-recovery results from alternative particle sorting systems, such as XRT-based sorters, can be modelled using similar calculation methods. Capacity requirements of particle sorting units, irrespective of sensing technology, would stand to be significantly reduced by the presence of the proposed bulk sorting system.

The value of sensing systems extends beyond the opportunity to sort ore according to grade. Both pXRF and PGNAA test results showed that picrite, a waste rock that negatively affects copper recovery in the flotation circuit, can be identified by elevated concentrations of nickel and chromium, shown in Appendix C. Additionally, PGNAA could be used to identify ore with native copper mineralization due to its distinct high copper to sulfur ratio, shown in Figure C.5. There is an opportunity to use information from the sensors in a feed-forward system to trigger adjustments to grinding and reagent addition for flotation or to direct material to alternative processing circuits.

The installation of bulk sorting systems prompts reconsideration of the approach to nominating underground production schedules. Although production schedules are constrained by cave stresses, flow geometry and cave geometry, they do provide the possibility to blend ore types in a fashion that increases mill productivity. At many block cave mines, production schedules are nominated to provide a consistent grade of mill feed. This approach encourages mixing of grades in the crushing and material handling systems. However, in the case where a bulk sorting system is in place, production schedules should be nominated to minimize mixing so that high-grade and waste material can be campaigned to surface. This provides more opportunity to beneficiate the ore prior to the mill.

When calculating the cost performance of the sorting systems, it was apparent that a significant cost benefit was the improvement in flotation recovery due to increases in mill feed grade. For a feed grade of 0.20% Cu, an improvement in ore value of $0.97 per tonne was calculated for the case where bulk and particle sorting systems are installed. Further evolutions of the approach involve implementation of bucket mounted grade sensors and tracking of load haul dump (scooptram) movements along the extraction level. Such an approach would provide opportunity to take advantage of the heterogeneity of caved material and improve mill productivity.

To strengthen the assessment of XRF-based particle sorting, more test work is required to increase the database of 291 characterised particles for use in Net Smelter Return calculations. Bulk particle testing will provide opportunity to update the model to allow for sorting

inefficiencies that are associated with material presentation to the sorters and fluctuations in throughput.

Chapter 8: A Methodology for Cave Evaluation with Sensor-Based Sorting

8.1 Introduction

The addition of sensor-based sorting to caving projects is envisaged to affect the size of the footprint and overall project value. This chapter presents a method for including sensor-based sorting parameters in the outputs of the PCBC cave planning and production scheduling software. Results from the sorting study carried out at the New Afton block cave mine were used to demonstrate the method for a conceptual cave in a copper-porphyry deposit. The method highlights the importance of integrating mine and mill parameters in the form of Cave-to-Mill, as inputs ranging from geotechnical to mill recovery parameters are referenced to carry out the cave evaluation.

8.2 Description of the Cave Evaluation Method

Sensor-based sorting parameters, described in Chapter 7, were combined with the outputs of the PCBC cave planning and production scheduling module within the GEMS GEOVIA, version 6.8.1 package (Dassault Systèmes, 2018). A summary of the proposed method for determining the economic cave footprint and associated value for a grade block model is shown in Figure 8.1. The key steps of the proposed method include:

- Assessing the applicability of bulk and/or particle grade sensors to material from the deposit, described in Chapters 6 and 7.
- Relating sorting models to material head grade, presented in Chapter 7.
- Populating the block model with sorting parameters for integration with the PCBC production scheduling module
- Nominating the footprint geometry, orientation and elevation using Footprint Finder
- Generating a mixed slice file. Updating the grade block model with mixed slice data using inverse distance weighting
- Populating the updated grade block model with sorting parameters

- Calculating the Best Height of Draw (HOD) for each drawpoint and running production schedules to estimate project value, waste rejection and throughput rates for sorting and milling equipment

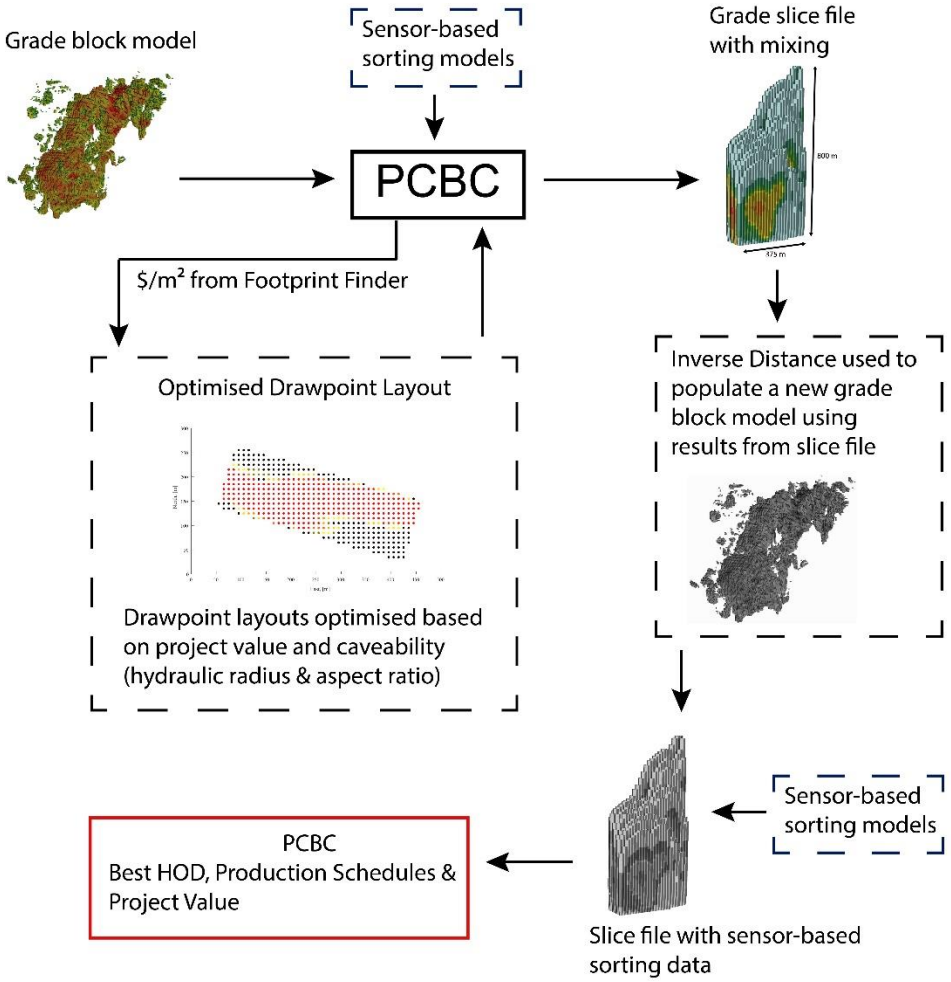

Figure 8.1 Summary of approach to cave-sorting evaluation

8.3 Relating Sorting Performance to Head Grade

To predict the properties of ore above a proposed extraction level layout, PCBC applies cave mixing models to generate a slice file, where rock mass data is arranged according to draw cones, representing the flow geometry of ore above drawpoints. Each draw cone is split into slices that contain grade and other additive information for the caved rock. The size of each slice is related to drawpoint spacing and the height of blocks within the grade block model. Therefore,

nominating block size is an important parameter that will affect the quality of sorting predictions. The block size should be nominated with careful consideration to geostatistical implications, which are outside the scope of this thesis, and the sorting unit size of the bulk sorting technology being assessed.

In the case of establishing linkages between particle sorting performance and head grade, various drill core or drawpoint materials from existing caves within the deposit should be collected to cover a range of grades and lithology/oxidation types including waste rock. Sensor-based sorting tests for the relevant technology can then provide critical parameters, such as metal recovery and mass pull, to relate to head grade.

During sorter operation, the mass pull of the sorting system can be controlled by modifying the cut-off grade (by way of changing a sensor threshold) for accepting and rejecting particles. The optimum mass pull for a sorting unit is a function of several parameters including metal value and costs for processing and material handling. The same cost and process assumptions as used for the sensor-based sorting study, presented in Table 7.3, were used for the case study.

8.4 Nominating Footprint Geometry, Orientation and Elevation

Once sorter models are available as a function of head grade, they can be applied to the grade block model to define the block NSR, and the sorter mass pull and recovery for each block. To run a high-level comparison of extraction level sizes and elevations, the Footprint Finder function in the PCBC module provides the value of each unit area ($/m^2) for a range of elevations. The outputs can be exported in spreadsheet form so that a footprint area, horizontal location and elevation that represents a high project NPV can be identified in external packages (e.g. Matlab or Excel). Practically, the footprint geometry is constrained by the caveability of the rock mass and the nominated drawpoint spacing and drift dimensions. An example of costing, caveability and design inputs is shown in Table 8.1.

Table 8.1 Cave design and costing parameters for the copper-gold case study

Item	Units	Value
Mining cost	$/t	11
Development cost per footprint area	$/m^2	5,800
Drawpoint spacing, minor	m	15
Drawpoint spacing, major	m	20.9
Drift, width x height	m	4.2 x 4.2
Vertical caving rate	m/year	40
Minimum aspect ratio (length to width)	[-]	3
Minimum hydraulic radius	[m]	30
Development rate	Drawpoints per month	8
Discount rate	%	8

Based on sorting data and conceptual cave data, Figure 8.2 shows the footprint area and elevation that provides maximum project value while adhering to the constraints shown in Table 8.1. Footprints for various sorting flowsheets can be compared to the nominal footprint that has been solved assuming sorting systems are not implemented. From the figure it can be seen that a proportion of the footprint has lower value (black) and is only developed to adhere to geometric constraints for hydraulic radius and aspect ratio. To reduce the risk of cave stall, a minimum height of draw of 50 metres was assigned to all drawpoints within the footprint. The cost of processing material from marginal drawpoints is reduced by rejecting low grade material prior to the mill.

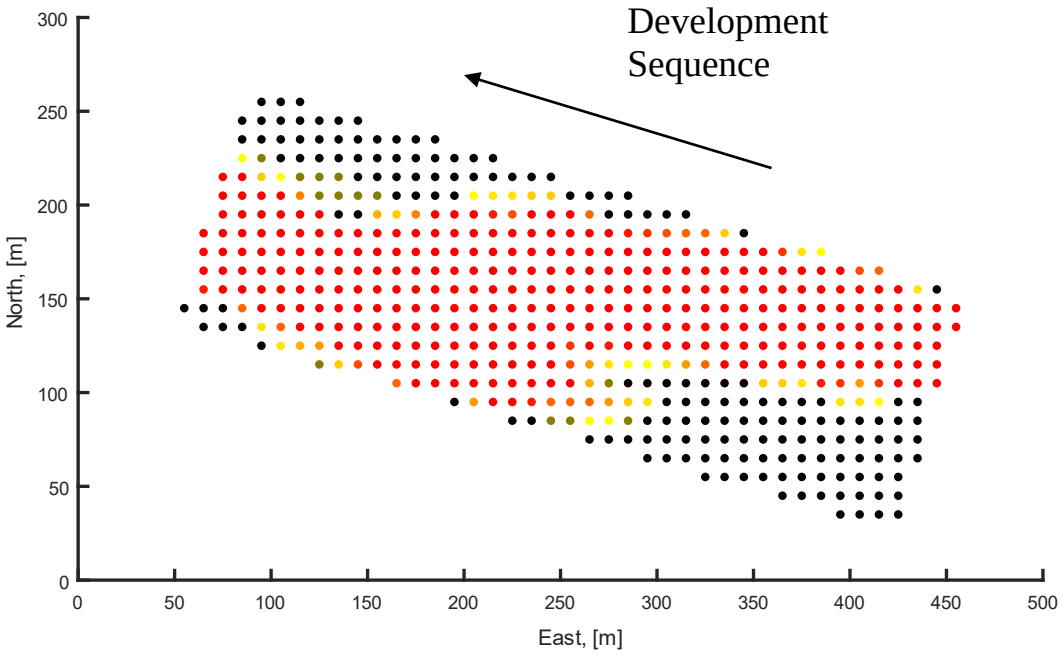

Figure 8.2 Plan view of a conceptual cave footprint for a proposed extraction level elevation and sorting scenario. Red datapoints refer to high-value areas of the footprint

8.5 Applying Models to Mixed Material in Draw Cones

Since PCBC scheduling software, in its current form, does not allow for input of sorter models within the production scheduling routine, sorter models are applied in a three-step approach.

1. A slice file is generated for all drawpoints in the proposed layout. During slice file creation, mixing models are applied based on estimates for the height of the mixing horizon and draw cone diameter, both of which relate to fragmentation size
2. The grade block model is updated using inverse distance weighting of data from the mixed slice file
3. Sorter models and NPV calculations are applied to blocks within the updated grade block model, which now includes a more accurate representation of material that will report to drawpoints

To prepare for production scheduling, a final slice file is generated with no mixing applied.

8.6 Production Scheduling and Evaluation

The best height of draw, acting as a limit for drawpoint tonnage, is calculated for each drawpoint based on the final slice data, the draw strategy using the production rate curve (PRC) and draw cone profiles. Figure 8.3 shows an example of a production schedule for the case study. Typical run of mine production would follow the blue 'Actual' curve, whereas mill feed production rates following sorting would follow the 'Mill Feed' curve. Results show that approximately 21% of low grade material could be rejected by bulk and particle sorters prior to the mill, while achieving a metal recovery of 97%. Table 8.2 shows the corresponding mass balance, where it can be seen that the use of bulk sorting significantly reduces the capacity requirements of screening and particle sorting equipment.

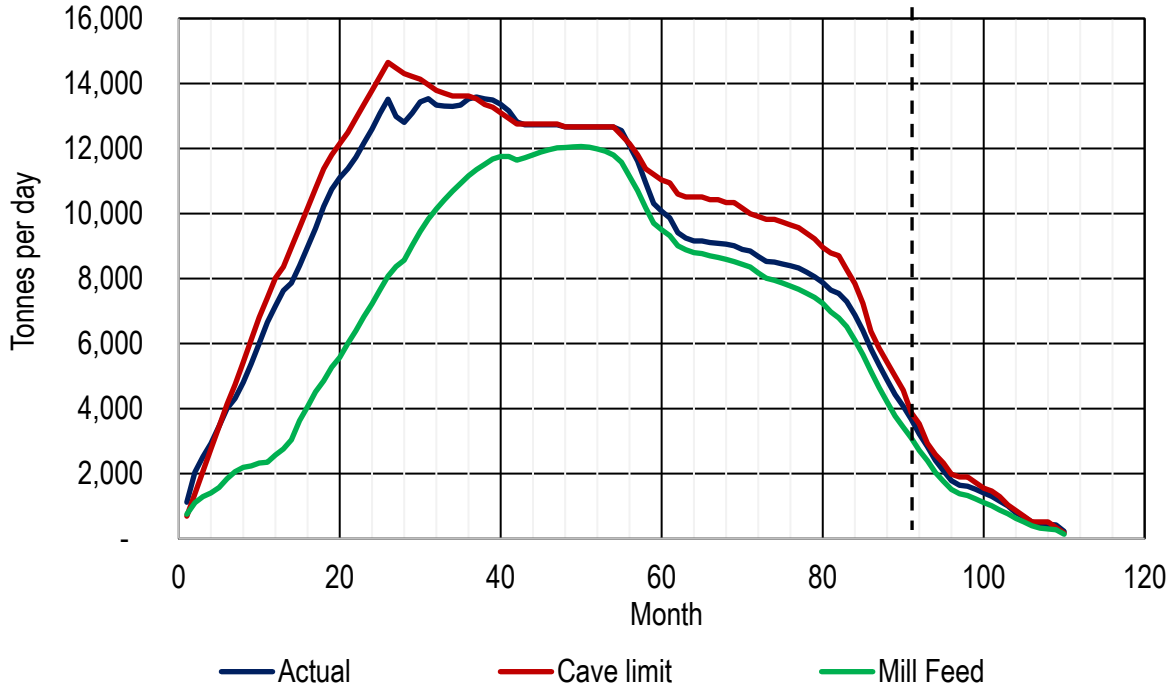

Figure 8.3 Example production schedule runs for a conceptual cave

The mass balance shown in Table 8.2 provides valuable input for sizing of screens, sorters and mill equipment.

Table 8.2 Mass Balance for a conceptual cave

Stream	Mass Proportion, %	Metal Proportion, %
Bulk Sorter Feed (ROM)	100	100
Bulk Sorter, High Grade Stream (to mill)	66.7	92.2
Particle Sorter Concentrate	4.1	4.6
Particle Sorting Plant, Fines (to mill)	8.4	0.8
Particle Sorter Waste	12.1	2.1
Bulk Sorter, Waste	8.7	0.3
Total Mill Feed	**79.2**	**97.6**

8.7 Discussion and Conclusions

The nature of cave operations makes them ideal for incorporation of sensor-based systems to reject rock and allow the operation to become more dynamic. The presented method, which relies on Cave-to-Mill parameters ranging from geotechnical rock mass characterization to mill performance, provides a means to design and evaluate a block or panel cave for the case where sensor-based sorting systems are included in the flowsheet. The resulting mass balance can be used for stockpile estimation and equipment sizing to estimate the capital cost savings associated with lower mill throughput requirements. Using the method, changes in footprint size, project value and life of mine metal production can be compared to alternative scenarios where sorting systems are not in place.

The implementation of bulk sorting systems on underground-to-surface conveyors or integrated with production shafts prompts reconsideration of underground production scheduling. For example, campaigning of low-grade and high-grade ore from drawpoints will reduce blending within orepasses and downstream material handling systems, and improve sorting performance.

The value opportunity associated with sensor-based particle sorting is strongly related to fragmentation size. For proper evaluation of particle sorting systems at cave mines, the variable

nature of cave fragmentation and the deportment of mineralization to different size fractions within caved ore need to be considered.

Chapter 9: Conclusions and Recommendations

9.1 Main Outcomes

An initial outcome of the research was the definition of a Cave-to-Mill approach targeting block cave productivity. Key aspects of cave planning and operation were identified in the form of a Cave-to-Mill flowchart, Figure 2.9, which showed how a coordinated effort can be made to maximize productivity in the form of Net Present Value (NPV). A central component is the ore block model, which is continuously refined during project development and mine operation through input of geotechnical, geological and metallurgical information. It is envisaged that the flowchart will be a valuable reference for cave project planning and operations.

Bulk and Particle Sorting

To address the lack of selectivity of the block cave mining method and improve productivity, bulk and particle sensor-based sorting systems were evaluated using New Afton ore. A configuration where bulk and particle systems are used in series was found to improve the Net Smelter Return (NSR) of caved material and reduce the number of particle sorters required.

To assess the change in reserve size and cave value associated with sorting of caved ore, a method was developed to incorporate sensor-based sorting parameters in cave planning and production scheduling software (Chapter 8). This methodology can now be used to assess the value of future cave mines and caving lifts. Variations of bulk and particle sorting configurations can be incorporated with the method. The resulting mass balance can be used for stockpile estimation and equipment sizing to estimate the capital cost savings associated with lower mill throughput requirements.

Evaluation of XRF-based particle sorters led to development of a method to relate feed grade to particle sorting performance based on grade heterogeneity (Section 7.5). The method is applicable to all mining methods and allows sorting parameters to be included in block models to assess the size of reserve and mine value when sorting systems are included in the flowsheet.

The research assessed the use of a PGNAA sensor for online grade measurement of New Afton caved material. Based on results of the work, New Afton mine installed a PGNAA sensor on the underground-to-surface conveyor in late 2017. In mid-2018, an upgraded diverter was installed on the conveyor to divert caved material at intervals of 30 seconds or more based on outputs of the PGNAA sensor. The installation is the first of its kind in the caving industry. Bulk sensing and sorting is expected to become an industry standard in caving operations. In mid-2018, a PGNAA sensor was installed at Newcrest's Cadia East Block Cave Mine.

An analysis of grade heterogeneity on a bulk scale showed that drawpoints located at the New Afton cave boundary were more suitable for separate handling of ore and waste underground (Section 6.3). To take full advantage of grade sensors mounted on load haul dumps (LHD), which transport material from drawpoints to orepasses, dedicated ore and waste material handling systems would be required. Ideally these would be located in close proximity to drawpoints that experience high variability in ore grade. The outcomes are of value for designing alternative extraction and haulage level designs which facilitate bulk sorting with mobile equipment.

Cave Fragmentation and Mill Productivity

Analysis of underground production scheduling and mill productivity (Section 5.2) identified drawpoints that provided finer mill feed and are associated with increased mill throughput. Coarser (+27 mm) size fractions of mill feed negatively correlated with simulated SAG mill throughput, while the proportion of material retained on sieves smaller than the SAG screen aperture size (13.2 mm) positively correlated with simulated throughput.

Opportunities for improving cave productivity by providing finer feed to the mill were identified as being (1) adjustment of the closed-side setting of primary crushers to an operational minimum and (2) inclusion of fragmentation and hardness data in the decision making that goes into planning underground production schedules. Installation of secondary crushers ahead of existing SAG mill circuits also provides opportunity to improve mill throughput productivity at existing operations and reduce fluctuations in performance.

For future caving projects, High Pressure Grinding Rolls (HPGR), which are increasingly popular alternatives to SAG mill-based circuits and are known to be less sensitive to variations in

ore size and hardness, were identified as a solution to reducing the impact of cave size fluctuations on mill throughput performance.

The cave fragmentation study showed that secondary fragmentation at New Afton is sensitive to faulting, fracture intensity, height of draw (HOD) and boundary effects. Similar to the findings published by Brunton et al. (2016), BCF software was found to under predict the content of fines within caved ore.

The DFN component of the fragmentation study by Munkhchuluun (2017) showed that fracture intensity P_{32} is relevant to fragmentation size and hang-up frequency. As found by Brzovic et al. (2016) at the El Teniente Mine, the largest reduction in hang-ups due to increases in height of draw was found during the earlier stages of drawpoint extraction. Based on outcomes of the fragmentation study, the following two-stage method for application of DFN-based fragmentation models was proposed: 1) repopulation of DFN models as access to exposed ore increases during project development 2) calibration with size measurements of caved ore and hang-up logs when the project moves towards production. In the case that macro blocks are planned for a deposit, calibrated fragmentation models for an initial macro block can be treated as valuable design and planning tools for future lifts.

Rock Characterization

The main test regimen characterized rocks in terms of the terminal limits of the study, starting at the in situ rock mass and terminating at the rougher flotation cells of the mill. Lithology and alteration types were described in terms of their impact on mine and mill performance. For New Afton material, relationships were found between geotechnical and metallurgical test results, and cave fragmentation size. Carrying out a similarly structured test regimen at the cave planning stage should allow for more efficient rock characterization and improved valuation of blocks within block models (Section 5.9 and Table 7.1).

9.2 Recommendations for Future Work

Size Analysis

Image-based size analysis was found to be practical for particle sizes coarser than 100 mm. The percentage passing of aperture sizes below 100 mm is of relevance to material handling systems, production potential of the mill and the performance of sensor-based sorting systems. It is recommended that further research be focused on developing practical methods to measure fines content in muckpiles to inform approaches to improve fragmentation and flow models.

Fragmentation Models

BCF software was found to under predict the content of -0.5 m material within caved ore. Similar findings were found at the Cadia Mine by Brunton et al. (2016). Improved methods for measuring -100 mm material, as described in the previous recommendation, would provide data for developing fragmentation models that more accurately describe fines fragmentation.

Linking Sensor Responses to Cave-to-Mill Characteristics

At New Afton, finer cave fragmentation size was associated with the content of fault and carbonate rocks within muckpiles. Since fault and carbonate rocks can be identified on the basis of point load strength, XRF response and Magnetic Susceptibility readings, information which is contained in the New Afton block model, fragmentation predictions can be made for future caves at the New Afton deposit. It is recommended that further research be focused on core characterization in terms of cave and mill performance. Efforts to recognize relationships between geotechnical and metallurgical parameters would help streamline core analyses.

Design of Underground Bulk Sorting Systems

Results from the heterogeneity study prompts further research in the area of extraction and haulage level design for underground bulk sorting. Configurations where grade sensors are used on mobile equipment, orepasses and conveyors could be explored. Trials of bucket-mounted grade sensors with a participating cave mine would confirm readiness of available sensor technologies to underground conditions. In addition to sorting, grade sensors on mobile equipment could be used for drawpoint grade control, as suggested by Ross (2012).

Relating In Situ Fracture Intensity to Secondary Fragmentation Size

The DFN component of the fragmentation study by Munkhchuluun (2017) showed that fracture intensity P_{32} is relevant to fragmentation size and hang-up frequency. It is posited that fragmentation predictions would improve should DFN approaches be combined with secondary fragmentation models, similar to those proposed by Dorador (2016).

Production Scheduling with Sensor-Based Sorting Parameters

To refine the proposed approach for evaluation of cave mines working with sensor-based sorting systems, it is recommended that work be carried out to update algorithms within the PCBC module of GEMS Geovia software. The presented method did not allow sensor-based sorting equations to be applied to the results of more advanced mixing and flow algorithms, such as Cellular Automaton, contained within the software. An update of the software where block parameters relating to head grade are accepted, would allow sensor-based sorting performance to be calculated with the results of more advanced mixing models.

Chapter 10: Claims of Original Contributions

A novel approach for planning and operating block cave mines, termed Cave-to-Mill, was developed with data and samples from an operating cave mine and presented in this thesis. The proposed integration of cave mine and mill systems is the first published work of its kind. The following are outcomes of the research that are original and significant to the field.

Cave-to-Mill Flowchart

A comprehensive flowchart, which focuses on cave mine productivity, is novel due to the emphasis on block model definition and progressive refinement with geological, caving and milling parameters as a caving project progresses from planning to cave maturation stages.

Cave Planning and Evaluation with Sensor-Based Sorting

A method was developed to incorporate sensor-based sorting parameters in cave planning and production scheduling software. This methodology can now be used to assess the value of future cave mines and caving lifts. Variations of bulk and particle sorting configurations can be incorporated with the method. The resulting mass balance can be used for stockpile estimation and equipment sizing to estimate the capital cost savings associated with lower mill throughput requirements.

Particle Sorting Assessment

Evaluation of XRF-based particle sorters led to development of a method to relate feed grade to particle sorting performance. The method uses grade heterogeneity determined from surface measurements to simulate sorter performance for a range of head grades. The method is applicable to all mining methods and allows sorting parameters to be included in block models to assess the size of the reserve and mine value when sorting systems are included in the flowsheet.

Evaluation of Bulk and Particle Sorting Systems for a Cave Mine

The assessment of bulk and particle sorting systems to determine the upgrade to Net Smelter Return (NSR) value, was the first published sorting study for a block cave mine, where bulk and particle sorting systems are included in the flowsheet. The study considered the impacts of cave

fragmentation size and the grade distribution of copper minerals within different size fractions on particle sorting performance. Improvements in flotation performance, as a result of higher mill feed grades, were also included in the value calculation.

Cave-to-Mill Rock Characterization

The characterization of New Afton rock samples in terms of grade, mine and mill performance, including cave fragmentation, is the first published work of its kind. Original contributions include determined relationships between cave fragmentation size, DropWeight strength, resistance to abrasion and point load strength.

Cave Fragmentation Size and Mill Performance

Analysis of mine and mill data showed that increased mill throughput was achieved when higher proportions of mucked material were sourced from one area of an extraction level at a cave mine. Simulations showed how the locations of mill throughput bottlenecks change according to the size and hardness of caved material being processed.

Grade Heterogeneity

The presented research on grade heterogeneity is the first published research showing grade heterogeneity at the extraction level of an operating cave mine. Results were shown with a focus on separation of ore and waste for separate material handling.

Abbreviated DropWeight Test Method

The author is aware of one other abbreviated DropWeight testing method for energy-breakage characterization of rock sample, however, it relies on unpublished methodologies and calculation methods. To address the need for a public domain method, an abbreviated DropWeight test was developed and presented in Appendix B.

References

Alfaro, M., & Saavedra, J. (2004). Predictive models for gravitational flow. Proceedings of the Fourth International Conference and Exhibition on Mass Mining (MassMin 2004) Pg. 179 -184.

AMTEL (2006). Deportment of gold in in composites of ore styles from New Afton Mine. AMTEL Report 06/30. September 11, 2006.

Van As, A. (2010). Caving terminology and glossary. Rio Tinto Copper Projects. Vancouver, Canada.

ASTM D5731-08. (2013). Standard test method for determination of the point load strength index of rock and application to rock strength classifications. West Conshohocken, PA.

Bailey, C., Lane, G., Morrell, S., & Staples, P. (2009). What can go wrong in comminution circuit design. Tenth Mill Operator's Conference, October 12 – 14, 2009. Adelaide, South Australia

Balzan. L. (2016). New Afton copper porphyry ore test report. November 25, 2016. Scantech, South Australia.

Bamber, A.S., Klein, B., Pakalnis, R., & Scoble, M. J. (2008). Integrated Mining, Poressing and Waste Disposal Systems for Reduced Energy and Operating Costs at Xstrata Nickel's Sudbury Operations, Institute of Materials, Mining Technology 117, no. 3: 142-153

Barratt, D., & Doll, A. (2008). Testwork programs that deliver multiple data sets of comminution parameters for use in mine planning and project engineering

Bbosa, L. S., Mainza, A. N., & Powell M. (2014). Analysis of the Breakage Data of a Series of Devices. Proceedings of the XXVII International Mineral Processing Congress – IMPC 2014.

Bergen RD, Krutzelmann H., & Rennie DW. (2015). New Gold Inc. NI 43-101 Technical report on the New Afton Mine. RPA Inc. Toronto, Canada. March 23.

Bewick, R., P., & Kaiser, P. K. (2016). Characterisation and classification of veined rocks for rock mass behaviour assessment. Proceedings of the 7th International Conference and Exhibition on Mass Mining - MassMin 2016, Sydney, Australia, May 9 -11, 2016.

Bond, F. (1962). More accurate grinding calculations. Society of Mining Engineers. Annual Meeting of the American Institute of Mining, Metallurgical and Petroleum Engineers, Inc., New York February 18 to 22, 1962

Brown E.T. (2003). Block Caving Geomechanics. Indooroopilly, Queensland: Julius Kruttschnitt Mineral Research Centre.

Brunton I, Lett J.L., & Thornhill T. (2016). Fragmentation prediction and assessment at the Ridgeway Deeps and Cadia East Cave operations. Seventh International Conference and Exhibition on Mass Mining; May 9 – 11. Sydney, Australia. p. 151–159.

Brzovic A., Vallejos J., Arancibia E., Burgos L., Delonca A., Gaete M., & Barrera, V. (2016). Analysis and modelling of the fragmentation process – case studies at El Teniente Mine. Seventh International Conference and Exhibition on Mass Mining, May 9 – 11. Sydney, Australia. p. 305–310.

Brzovic A., Schachter, P., de los Santos, C., Vallejos, J. A., & Mas Ivars, D. (2014). Characterization and synthetic simulations to determine rock mass behaviour at the El Teniente Mine, Chile. Part I. Proceedings of the Third International Symposium on Block and Sublevel Caving 2014, Santiago, Chile.

Burger, B., McCafferey, K., Jankovic, A., Valery, W., & McGaffin, I. (2006). Batu Hijau model for throughput forecast, mining and milling optimisation and expansion studies, Advances in Comminution, S. K. Kawatra Ed, 461 – 479, SME 2006.

Bye, A. (2011). Case studies demonstrating value from geometallurgy initiatives, First AusIMM International Geometallurgy Conference, 9-30, Brisbane, The Australasian Institute of Mining and Metallurgy.

Campbell, D., & Thurley, M. J. (2017). Application of laser scanning to measure fragmentation in underground mines, Mining Technology, 126:4, 240-247

Catalan, A., Onederra, I., & Chitombo, G. (2017). Evaluation of intensive preconditioning in block and panel caving – Part I, quantifying the effect on intact rock, Mining Technology, 126:4, 209-220

Cebeci, T., Wang, C., Huang, M., & Liu, S. (2017). Study on variable speed drives for ball mills and vertimills at the New Afton Mine. UBC Mining report. November 28, 2017. Vancouver, BC.

Chitombo, G. P. (2010). Cave mining: 16 years after Laubscher's 1994 paper, 'Cave mining – state of the art', Transactions of the Institutions of Mining and Metallurgy Section A: Mining Technology, Vol. 119, Issue. 3, 132 – 141.

Coghill, P., Cutmore, N., Lehmann-Horn, J., Lovric, B., McEwen, A., Milinkovic, D., Miljak, D., Roberts, G., & Yong, R. (2018), 'Demonstration of a magnetic resonance analyser for bulk copper sorting', Proceedings of the Eighth Conference on Sensor-Based Sorting & Control, Aachen, pp. 152–160.

Condori, P., Fischer, D., Winnett, J., & Makgatho, J. (2011). From open cast to block cave and the effects on the autogenous milling circuit at Palabora Mining Copper. The Fifth International Conference on Autogenous Grinding, Semi-autogenous Grinding and High Pressure Grinding Roll Technology, September 25th - September 28th, 2011. Vancouver, Canada.

Cundall. P., Mukundakrishnan B., & Lorig. L. (2000). REBOP (Rapid Emulator Based on PFC3D) Formulation and User's Guide, Itasca Consulting Group, Inc., Report to the International Caving Study, ICG00-099-7-20

Dance, A. (2016). Downstream effects of block caving. Cave Mining Forum. Workshop Series II. October 14th, 2016. Vancouver, BC, Canada.

Dassault Systèmes. (2018). Geovia GEMS PCBCTM. Version 6.8.1. Dassault Systèmes. Vancouver, Canada. https://www.3ds.com/products-services/geovia/products/pcbc/

Davies A. G. L. (2015). Case study: Understanding the mechanics behind the rockmass deformation observed in an extraction strike drive at New Gold's New Afton Mine block cave operation, 49th US Rock Mechanics / Geomechanics Symposium. June 28 – July 1. San Francisco, CA, USA.

Diering, T., Richter, O., & Villa, D. (2010), 'Block cave production scheduling using PC-BC', SME Annual Meeting & Exhibit, Feb. 28 – Mar. 3, 2010, Phoenix.

Diering, T. (2012). Quadratic programming applications to block cave scheduling and cave management, Proceedings of the Sixth International Conference and Exhibition on Mass Mining (MassMin 2012), Sudbury, Canada.

Doll. A., & Barratt. D. (2010). Choosing the right motors for your mills. VII International Mineral Processing Seminar. December 8 – 10, 2010. Santiago, Chile.

Doll. A. (2016). Calculating DWi from a drop weight test result. SAGMilling.com. Accessed Nov, 29, 2017.

Doll. A. (2015). Technical Memorandum to the UBC Mine 331 (Unit Operations) Clas) on the subject of SAG mill + ball mill circuit sizing. February 16, 2015.

Dorador, L. (2016). “Experimental Investigation of the Effect of Broken Ore Properties on Secondary Fragmentation during Block Caving.” Electronic Theses and Dissertation

Duncan, G. (2016). Development of a protocol to determine the sorting potential of particulate ore material. Master’s dissertation. University of Johannesburg.

Dunstan, G., & Popa. L. (2012). Innovative cave establishment practices at Ridgeway Deeps. Proceedings of the Sixth International Conference and Exhibition on Mass Mining (MassMin 2012), Sudbury, Canada.

Elshkaki, A., Graedel, T.E., Ciacci, L., & Reck, B. (2016). Copper demand, supply, and associated energy use to 2050, Journal of Global Environmental Change, Vol. 39, 2016, Pages 305-315.

Encina, V., Méndez, D., Caballero, C., & Osorio, H. (2010). New approach for rapid preparation of block caving mines, Mining Technology, Volume 119

Erdenebat, E. (2017). Study of New Afton ore heterogeneity and its amenability to sensor based sorting. Master’s dissertation. August 2017. Vancouver, BC, Canada

Esen, S., Rosa, D. La, Dance, A., Valery, W., Jankovic, A. (2007). Integration and optimisation of blasting and comminution processes, EXPLO Conference, Wollongong, NSW, September 2007, 1 – 10, The Australasian Institute of Mining and Metallurgy.

Esterhuizen G. S. (2005). BCF Version 3.05. A program to predict block cave fragmentation. Technical reference and user’s guide. Venetia, PA.

Ernst & Young, (2017). Productivity in mining: now comes the hard part - a global survey. Ernst and Young Global Mining & Metals Network.

Flores, G. (2014). Future challenges and why cave mining must change, Proceedings of the 3rd International Symposium on Block and Sublevel Caving, Santiago Chile. Conference proceedings. June 5/6, 2014, Pg. 23 – 52.

Foggiatto, B. (2017). Modelling and simulation approaches for exploiting multi-component characteristics of ores in mineral processing circuits. Dissertation. University of Queensland. Sustainable Minerals Institute.

François-Bongarçon, D. and Gy, P. (2002). The most common error in applying 'Gy's Formula' in the theory of mineral sampling, and the history of the liberation factor. The Journal of the South African Institute of Mining and Metallurgy. November/December 2002. Pg. 475 – 480.

Frenzel, M. (2016). New continuous production system in block cave mining – the Rock Flow System. Seventh International Conference and Exhibition on Mass Mining; May 9 – 11. Sydney, Australia.

Fuentes, S., & Villegas, F. (2014). Block caving using macro blocks, Proceedings of the 3rd International Symposium on Block and Sublevel Caving, Santiago Chile. Conference proceedings. Pg. 211 – 216.

Gantumur, J., Godard, R., Prince, F., & Pascoe, C. (2016). Development and evaluation processes of cave production schedules for the Resolution Copper Project. Seventh International Conference and Exhibition on Mass Mining; May 9 – 11. Sydney, Australia.

Gaudin, A. M., Meloy, T. P. (1962). Model and a comminution distribution equation for single fracture. Society of Mining Engineers of AIME 223 (March 1962): 40.

Global Mining Standards and Guidelines Group. (2015). Determining the Bond efficiency of industrial grinding circuits. August 20, 2015.

Global Mining Standards and Guidelines Group. (2016). Methods to survey and sample grinding circuits for determining energy efficiency. April 28, 2016.

Golder Associates. (2017). Technical Report for the Kemess Underground Project and Kemess East Project, British Columbia, Canada. July 12, 2017. Vancouver, BC, Canada

Gómez, R., Castro, R.L., Casali, A. (2017). A Comminution Model for Secondary Fragmentation Assessment for Block Caving Rock Mech Rock Eng (2017) 03 July 2017, 50: 3073

Gy, P. (2004). Sampling of discrete materials – a new introduction to the theory of sampling I. Qualitative approach, Journal of Chemometrics and intelligent laboratory systems, 74 (2004) 7 – 24.

Gy. P. (1995). Introduction to the theory of sampling I. Heterogeneity of a population of uncorrelated units. Trends in Analytical Chemistry, Volume 14, Issue 2, 1995, Pages 67-76.

Van Haarlem, Y. (2017). Ultragold: Real-time gold-in slurry analysis with 100 PPB accuracy. Proceedings of the Conference of Metallurgists. Aug 27-30, 2017. Vancouver, Canada.

Hoek, E. (2007) Practical Rock Engineering. Chapter on Rock mass classification.

Imperial Metals. (2017). Annual Information Form for the Year Ended December 31, 2016. Dated March 29, 2017.

International Copper Association (ICA). (2017). The long-term availability of copper. NY, USA. October, 2017.

Ivars, D M, Pierce, M. E., Darcel, C., Reyes-Montes, J, Potyondy, D. O, Young, R. P., & Cundall, P. A. (2011). The synthetic rock mass approach for jointed rock mass modelling, International Journal of Rock Mechanics and Mining Sciences, Volume 48, Issue 2, 2011, Pages 219-244.

JKTech Pty Ltd. (2016). Procedure for the JK Drop Weight Test. Indooroopilly, Queensland.

JKTech Pty Ltd. (2015). JKSimMet, Version 6.1. User Manual. JKTech Pty Ltd. Indooroopilly, Queensland.

JKTech Pty Ltd. (2015). JKSimMet Version 6.1. Build 29. JKSimMet. Indooroopilly, Queensland. http://jktech.com.au/jksimmet

Kanchibotla, S. S., Vizcarra, T.G., Musunuri, S. A. R., Tello, S., Hayes, A., & Moylan, T. (2015). Mine to Mill optimisation at Paddington Gold Operations. The 6th International Conference on Semi-Autogenous and High Pressure Grinding Technology, September 20-23. Vancouver, Canada.

Khodayari F. & Pourrahimian, Y. (2014). Determination of the best height of draw in block cave sequence optimization, Proceedings of the 3rd International Symposium on Block and Sublevel Caving, Santiago Chile. Conference proceedings. June 5/6, 2014, Pg. 457 – 465.

Klein, B., & Bamber, A. S. (2018). Chapter on mineral sorting. SME Mineral Processing and Extractive Metallurgy Handbook. Editors: Dunne, R., Young, C., Kawatra, S. K. Society for Mining, Metallurgy and Exploration. CO, USA. Published date: 2018.

Klymowsky, R. (2009). HPGR – Accepted technology in mining. Mining Magazine Congress. Oct. 8 -9, 2009. Niagara-on-the-lake, Canada.

Kobzev, A. (2014). History of Sensor-Based Sorting in CIS, Proceedings of the Sixth Conference on Sensor-Based Sorting, Aachen, pp. 39–48.

Kobzev, A. (2018). Methodology for the evaluation of ore sorting potential: approach in CIS, Proceedings of the Eighth Conference on Sensor-Based Sorting & Control, Aachen, pp. 152–160.

Kojovic. T. (2016). HIT – a portable field device for rapid testing at site. 13th AUSIMM Mill Operator's Conference. Perth, WA, 10–12 October, 2016.

Kurth, H. (2017). Suitability of on-belt elemental analysis for real-time ore quality measurement and bulk sorting. Proceedings of the Conference of Metallurgists. Aug 27-30, 2017. Vancouver, Canada.

La Rosa, D., Caron., K., Valery, W., Diaz, R., & Mamani, H. (2015). Blast fragmentation impacts on downstream processing at Goldfields Cerro Corona. 11th International Symposium on Rock Fragmentation by Blasting. August 24-26, 2015. Sydney, NSW. Australia.

Laubscher D. H. (2000). A practical manual on block caving. International Caving Study. Julius Kruttschnitt Mineral Research Centre, Isles Road, Indooroopilly, Queensland 4068, Australia. Laubscher DH. 2011. Cave Mining. SME Mining Engineering Handbook, Third Edition.

Lessard, J., Sweetser, W., Bartram, K., Figueroa, J., & McHugh, L. (2016). Bridging the gap: Understanding the economic impact of ore sorting on a mineral processing circuit. Minerals Engineering 91. P92-99.

Lovitt M. B. & Degay, B. (2004). Single shot drawbell blasting with electronic detonators at Freeport. Proceedings of the thirtieth annual Conference on Explosives and Blasting Technique. International Society of Explosives Engineers. New Orleans, Louisiana USA

Liu Y., Nadolski S., Elmo D., Klein B., & Scoble M. (2015). Use of digital imaging processing techniques to characterise block caving secondary fragmentation and implications for a proposed Cave-to-Mill approach. 49th US Rock Mechanics / Geomechanics Symposium. June 28 – July 1. San Francisco, CA, USA.

Lotter, N. (2011). Modern process mineralogy: an integrated multi-disciplined approach to flowsheeting, Minerals Engineering, Vol. 24, Issue 12, Pg. 1229 – 1237.

Manca, L. (2013). Modern planning practices for cave mining, 3rd International Seminar on Mine Planning, Santiago Chile, 24/26 July 2013, Chile.

Matthews. D., & du Toit, T. (2011). Real-time online analysis of iron ore, validation of material stockpiles and roll out for overall elemental balance as observed in the Khumani iron ore mines, South Africa. Iron ore Conference. July 11-13, 2011. Western Australia.

Mazhary, A., & Klein, B. (2015). Heterogeneity of low-grade ores and amenability to sensor-based sorting. Proceedings of the 47th Annual Canadian Mineral Processors Operators Conference, Ottawa, Ontario, January 20-22, 2015.

Mazhary, A. (2018). Sensor response data and assay results for New Afton ore testing with a Steinert sorter. Test data, Vancouver, British Columbia, January 5, 2018.

Mckee, D. (2013). Understanding Mine to Mill. The Cooperative Research Centre for Optimising Resource Extraction (CRC ORE). Queensland, Australia.

Mindat (2018). Definition of monzonite. https://www.mindat.org/glossary/monzonite. Accessed: November 11th, 2018

Moose Mountain Technical Services. (2017). NI43-101 Technical Report for the Kwanika Project. April, 28, 2017. Cranbrook, BC. Canada.

Morrell, S. (2014). Using the SMC Test® to predict comminution circuit performance. https://www.smctesting.com/documents/Using_the_SMC_Test.pdf Accessed, June 6th. 2018.

Morrell, S., & Valery, W. (2001). Influence of feed size on AG/SAG Mill performance. The Third International Conference on Autogenous and Semiautogenous Grinding Technology, September 30th - October 3rd, 2001. Vancouver, Canada.

Moss, A. (2017) Personal Communication

Moss A. (2004). Caving and fragmentation at Palabora: Prediction to fragmentation. Fourth International Conference and Exhibition on Mass Mining, August 22 – 25. Santiago, Chile. p. 585 – 590.

Motion Metrics Inernational Corp. (2017). Vancouver, Canada. [June, 15th, 2017] http://www.motionmetrics.com/portable/. PortaMetrics™ Portable Fragmentation analysis.

Narendrula, R. (2004). Effect of fragmentation on productivity of loading equipment. Master's dissertation. Laurentian University.

Newcrest Mining Limited. (2012). Panel Session on Technology and Delivery, 2012.

Oancea, D. (2013). Underground Block Caving: A Guide for Investors. Resource Investing News. April 16, 2013.

Orozco, P. (2010). Operating Designs in Early Stage Panel Caving with Sizers, PhD Dissertation, University of Chile.

Paredes, P., Gajardo, D., Leaño, T., Peñaloza, S., & Tramón, C. (2016). Simplifying the ore handling system through the use of current technology at Chuquicamata Underground Mine Project. Seventh International Conference and Exhibition on Mass Mining; May 9 – 11. Sydney, Australia.

Paredes, P. S., & Pineda, M. F. (2014). An analysis of the lateral dilution entry mechanisms in panel caving. Proceedings of the 3rd International Symposium on Block and Sublevel Caving, Santiago Chile.

Pierce, M. (2010). A model for gravity flow of fragmented rock in block caving mines, PhD dissertation, The University of Queensland, Brisbane, Australia.

Rahal, D., Smith, M., van Hout, G., & von Johannides, A. (2003). The use of mixed integer linear programming for long-term scheduling in block caving mines, Application of Computers and Operations Research in the Mineral Industries, South African Institute of Mining and Metallurgy, pp. 123 -131.

Robben, C. (2014). Characteristics of sensor-based sorting technology and implementation in mining. PhD thesis dissertation. RWTH Aachen, Germany.

Rogers. S., Elmo, D., Webb, G., & Catalan, A. (2010). A DFN based approach to defining in situ, primary and secondary fragmentation distributions for the Cadia East panel cave project, Proceedings of the Second International Symposium on Block and Sublevel Caving, April 20/22 2010, Perth, Australia.

Ross, I. (2012). Sampling in block cave mines. Sampling Conference. August 21 to 22, 2012. Perth, WA, Australia.

Rowland, C. A. (1982). Selection of rod mills, ball mills, pebble mills and regrind mills. Ch. 23. Designa and Installation of Comminution Circuits. SME, pp. 393 – 438.

Rule, C., Fouchee, R., & Stewart, W. (2015). Run of Mine Ore Upgrading – Proof of Concept Plant for XRF Ore Sorting, in Proceedings of the 2015 SAG Conference, Vancouver, BC Canada.

Sagawa, Y., and Yamatomi, J. (2009). Technology of block caving mining method in Northparkes E48 Mine, Australia. Journal of MMIJ. The Mining and Minerals Processing Institute of Japan. Vol. 125. Pg. 409 – 419.

Salter, J. D., & Wyatt, N. P. G. (1991). Sorting in the minerals industry: past, present and future. Minerals Engineering Journal. Vol.4, Nos 7 – 11, pp. 779-796. United Kingdom.

Sandvik Automine System – Rio Tinto Northparkes Mine. (2012). Maquinaria Magazine, Dec 21, 2012. Video presentation.

Singer D. A. (2017). Future copper resources. Ore Geology Reviews. Vol. 86, June 2017. Pg. 271-279.

Srikant A., Nicholas D. E., & Rachmad, L. (2004). Visual estimation of fragment size distributions in the DOZ block cave. Fourth International Conference and Exhibition on Mass Mining. August 22 – 25. Santiago, Chile. p. 286 – 290.

Srikant, A. (2006). Fragment size measurement and estimation in the DOZ block cave. Mining Engineering, Volume 58, Issue 10.

Stark, S., Perkins, T., & Napier-Munn, T. J. (2008). JK Drop Weigh Parameters – a statistical analysis of their accuracy and precision, and the effect on SAG mill comminution circuit simulation. Proceedings of the Metallurgical Plant Design and Operating Strategies Conference, Perth, WA, 18-19 August, 2008.

Stewart, C. A., & Butcher, R. J. (2016). Block cave evaluation. Proceedings of the 7th International Conference and Exhibition on Mass Mining - MassMin 2016, Sydney, Australia, May 9 -11, 2016.

Talu, S., Van As, A., Henry, R., Hilton, J., & Whiteman D. (2010). Installation of 'Smart Markers' to monitor Lift 2 North Extension ore flow behavior. Proceedings of the Second International Symposium on Block and Sublevel Caving, Australian Centre for Geomechanics, Perth.

Teck. (2018). 'Building a smarter shovel', https://www.teck.com/news/stories/2018/building-a-smarter-shovel. Published March 29, 2018, Accessed May 5th, 2018.

Tetra Tech. (2016). KSM Prefeasibility study update and preliminary economic assessment. October 6th, 2016. Vancouver, BC. Canada.

Thurley, M. J., Wimmer, M., & Nordqvist, A. (2015). Blast fragmentation measurement based on 3D imaging in sublevel caving draw-points and LHD buckets at LKAB Kiruna. 11th International Symposium on Rock Fragmentation by Blasting. 24 - 26 August, 2015. Sydney, Australia. Paper No. 161.

Tokimatsu, K., Murakami, S., Adachi, T. Ryota I., Rieko Y., & Masahiro N. (2017). Long-term demand and supply of non-ferrous mineral resources by a mineral balance model. Mineral Economics (2017) 30: 193. https://doi.org/10.1007/s13563-017-0109-8.

Tollenaar, R. N. (2008). Characterization of discrete fracture networks and their influence on caveability and fragmentation, Master of Applied Science Dissertation, The University of British Columbia, Vancouver, Canada.

Tong, L., Khoshaba, B., Bamber, A., Klein, B. (2015). Correlation and regression analysis in the X-ray fluorescence sorting of a low grade copper ore. The 6th International Conference on Semi-Autogenous and High Pressure Grinding Technology, September 20-23. Vancouver, Canada.

Whiteman D., Talu, S., Wilson, M., Watt, G., Van As, A. & Kuiper, P. (2016). Cave tracker flow monitoring system installation at Argyle Diamond Mine. Seventh International Conference and Exhibition on Mass Mining; May 9 – 11. Sydney, Australia.

Whiteman D. (2010). Smart Marker System – a new tool for measuring underground orebody flow in block and sublevel mines, Mining Technology, 119:3, 182-192.

Wyman, R. A. (1966). The application of electronic sorting to minerals beneficiation. Mineral Processing Division of the Department of Energy, Mines and Resources. Mines Branch. Ottawa. July 1966.

Viera, E., & Diez, E. (2014). Analysis of hangup frequency in bloque 1-2, Esmeralda Sur Mine. Proceedings of the 3rd International Symposium on Block and Sublevel Caving, Santiago Chile. Conference proceedings.

Villa, D., Farías, F. (2016). Remnant ore model generation and categorisation post-block caving extraction at Salvador Mine. Proceedings of the 7th International Conference and Exhibition on Mass Mining - MassMin 2016, Sydney, Australia, May 9 -11, 2016.

WipWare Incorporated. (2017). WipFragTM, 2.7.28, North Bay, Ontario, www.wipware.com

Woo, K., Eberhardt, E., Elmo, D., & Stead, D. (2013). Empirical investigation and characterization of surface subsidence related to block cave mining. International Journal of Rock Mechanics and Mining Scieences.Vol. 61. Pg. 31-42.

de Wolfe, C. & I, Ross. (2016). Super caves – benefits, considerations and risks. Seventh International Conference and Exhibition on Mass Mining; May 9 – 11. Sydney, Australia.

Appendices

Appendix A Vertimill Operational Data

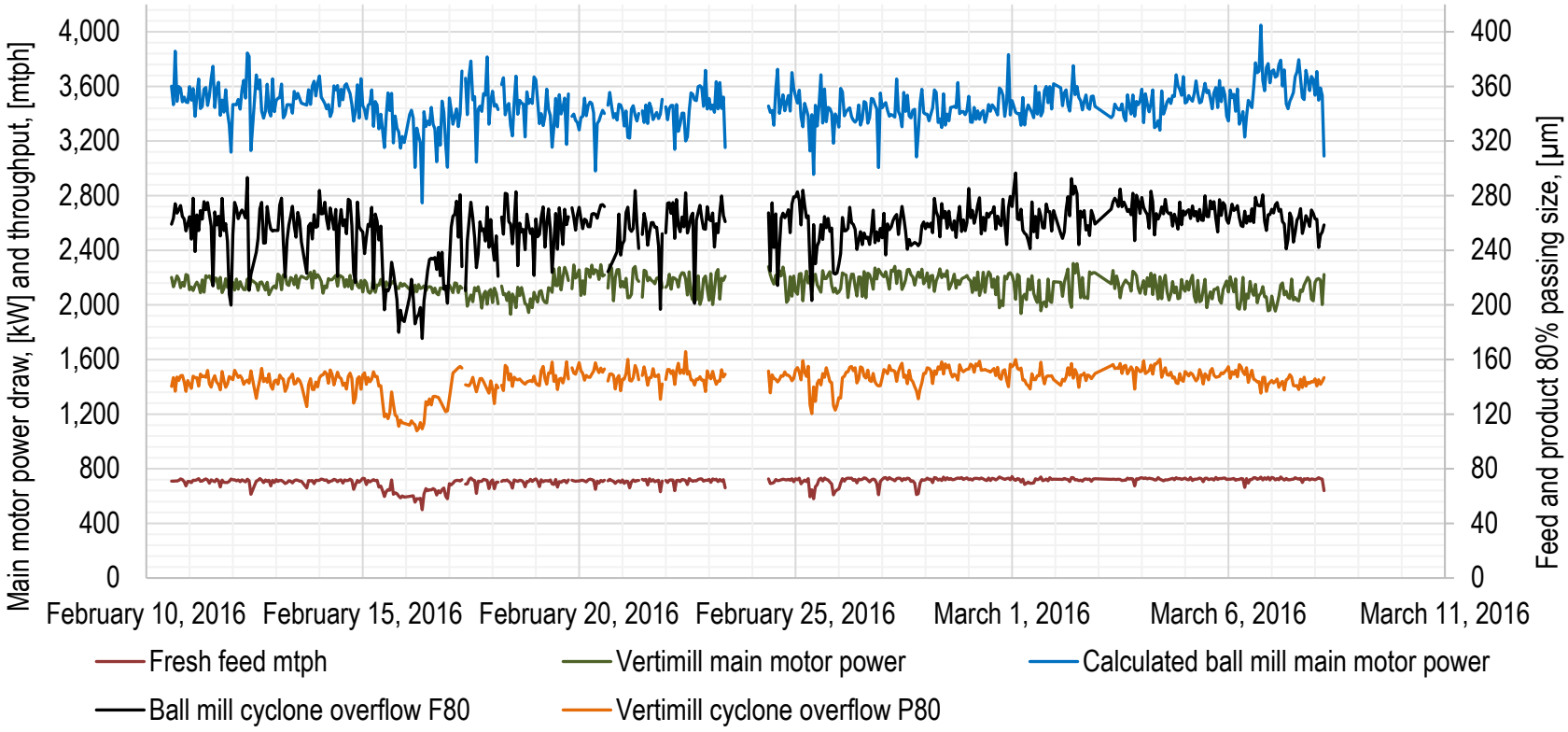

Figure A.1 Vertimill operating performance and calculated ball mill main motor requirements for equivalent duty based on a Bond ball mill work index of 18.4 kWh/t, Rowland's (1982) efficiency factors for mill diameter (> 3.81 m) and low reduction ratio, and overall drivetrain efficiency of 0.93

Appendix B An Abbreviated DropWeight Test Method for Lump Rock

B.1 Introduction

This technical note presents a method for generating impact breakage parameters using lump rock with lower sample and time commitments than the standard JKDropWeight test. The method does not rely on confidential calculation methods or privately-owned databases for calibration factors, which makes it a distinguishing feature from other abbreviated DropWeight test methods that are in use within industry.

The results of DropWeight impact breakage tests are used in crusher and SAG mill models included in the JKSimMet simulation package. Critical test outcomes include A and b parameters, which describe the proportion of product that passes a tenth of the feed size for a specific energy input, and, an appearance function, which describes the shape of the product size distribution. Current versions of JKSimMet use the A and b breakage parameters with the assumption that particles of a different size will break in a similar way. The standard DropWeight test and JKSimMet simulation package has been recognized by industry as being sufficiently accurate to generate useful predictions of crushing and grinding circuit performance.

B.2 Background

The standard JKDropWeight test method involves testing of three energy levels and five size fractions ranging from 13.2 to 63 mm in size and specific energy inputs of 0.25 to 2.5 kWh/mt (Stark et al., 2008). Overall, 345 particles in different size classes are tested. One abbreviated method is the SMC test, where five energy levels are tested using 100 particles from the same size fraction; 20 particles per energy level (Morrell, 2012). The SMC method relies on confidential calculation methods or privately-owned databases for calibration factors.

The standard DropWeight test has been reported to be accurate to ±3.6 per cent (Kojovic, 2016). Stark et al. (2008) analyzed the errors associated with the steps of standard DropWeight testing

and found that Axb can be estimated to an accuracy of ±2.68 at 95% confidence. The analysis showed that the dominant sources of error are attributed to particle selection and the test itself, which includes setting of the drop weight height and sieving of the products. Based on the analysis, a focus of designing the abbreviated test method was to reduce the error associated with particle selection and drop-weight height specification.

B.3 Methodology

The trade-off between accuracy and test time was considered when designing the test method for lump rock. Table B.1 shows the test methodology, where one size fraction is tested at five different energy levels. The size fraction tested is the median size used for the full DropWeight test, therefore no size correction is applied. As shown in the table, particles are grouped according to their mass and designated as light, medium and heavy. Eleven lump rock samples, representing different locations at the New Afton block cave mine, were tested using the presented method.

Table B.1 Abbreviated DropWeight Test Regimen

Target specific energy level, kWh/mt	Size range, mm	Particle weight grouping
2.5	-31.5, + 26.5	Heavy Medium Light
1.8	-31.5, + 26.5	Heavy Medium Light
1	-31.5, + 26.5	Heavy Medium Light
0.5	-31.5, + 26.5	Heavy Medium Light
0.25	-31.5, + 26.5	Heavy Medium Light

B.3.1 Particle selection according to mass

The full DropWeight test involves random sub-sampling to generate 15 lots of particles for testing using a unique size and energy input. For each lot containing 10 to 30 particles, one drop-weight height and weight is assigned based on the target specific energy input. The natural variation in particle masses due to differences in density and shape results in individual particles being impacted at specific energies that are higher or lower than the setpoint. An example of the mass distribution of a set of particles is shown in Figure B.1. One approach to minimizing the error would be to adjust the drop-weight height according to the individual mass of each particle such that the target energy input is achieved. However, this would result in a test that would take too long to complete to be practical. A compromise of the two extremes is put forward, where particles are placed into three groups according to their masses. The range of particle masses accepted into each group is calculated such that the specific energy is a minimum, as shown in equation B.1.

$$Total\ Mass\ Variation = \sum_{i_h=1}^{n_h}\left(\frac{1}{\overline{mass_{heavy}}} - \frac{1}{mass_{i_h}}\right)^2 + \sum_{i_m=1}^{n_m}\left(\frac{1}{\overline{mass_{medium}}} - \frac{1}{mass_{i_m}}\right)^2 + \sum_{i_l=1}^{n_i}\left(\frac{1}{\overline{mass_{light}}} - \frac{1}{mass_{i_l}}\right)^2 \quad \text{(B.1)}$$

Where n_h, n_m and n_i are the number of particles in the heavy, medium and light weight groupings. $mass_{heavy}$, $mass_{medium}$ and $mass_{light}$ are the average mass of individual particles in each respective group. $mass_{ih}$, $Mass_{im}$ and $mass_{il}$ are individual masses of particles within each heavy, medium and light weight grouping. The calculation is constrained by the requirement of having integer values for the resulting number of particles in each group (as fractions of a particle can not be tested). Figure B.1 shows the resulting solution for sample #1.

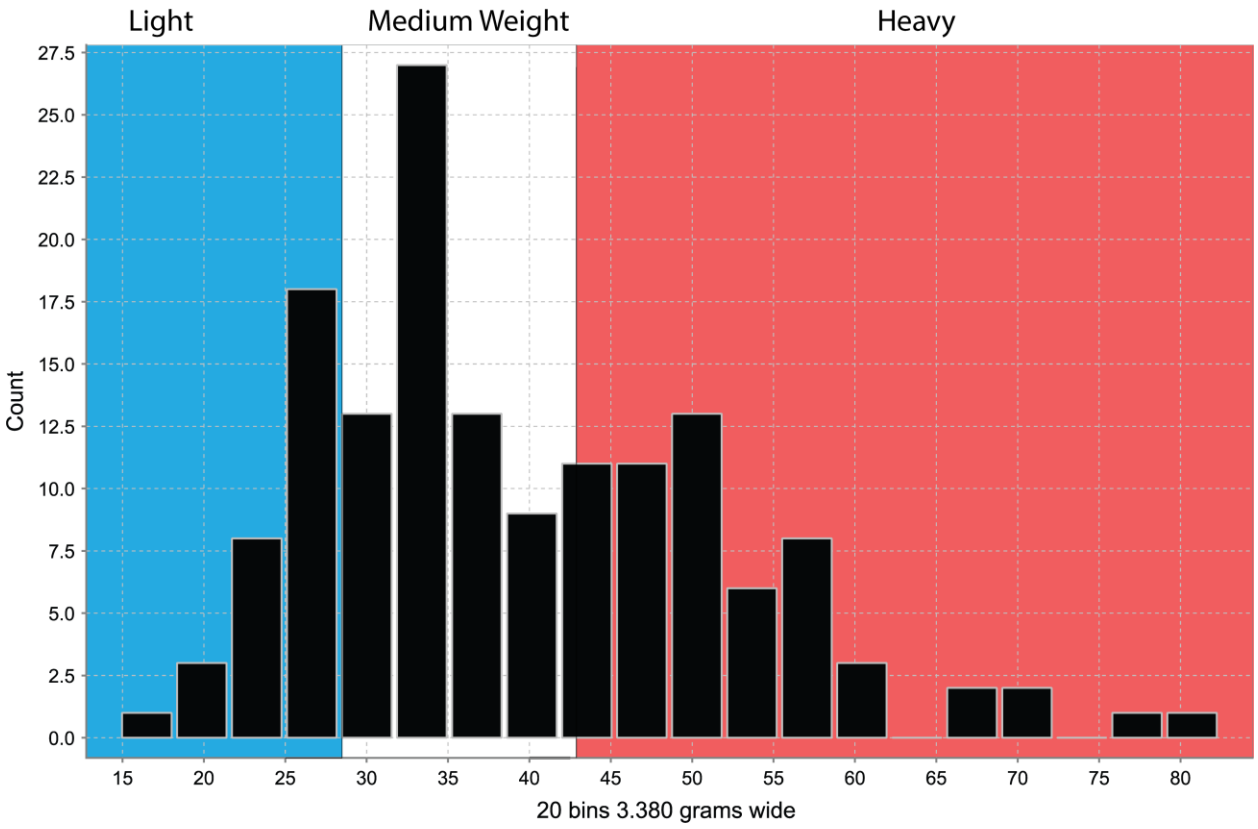

Figure B.1 Distribution of particle masses for sample #1 and example of mass groupings for minimum error in specific energy input

B.4 Comparison of Testing Methods

After particles have been selected for breakage, the full DropWeight test method relies on the average particle mass to select the potential energy required to achieve the setpoint specific energy (Bbosa et al., 2014).

Figures B.2 and B.3 show the distribution of specific energies in the case where thirty particles are randomly sampled and a drop-weight height and weight are set to target a specific energy consumption of 1 kWh/mt. For Figure B.2, the average particle mass was used to specify the drop-weight energy, whereas for Figure B.3, three dropweight setpoint energies were specified for application to heavy, medium and light particles as determined using the proposed method. The calculation was carried out for eleven samples, representing eleven spatial domains in a block cave mine. The box plots show that use of the proposed method reduces the deviation of

specific energy from the target of 1 kWh/mt. For both the standard and proposed method, it can be seen than the average specific energy for each sample is higher than the target of 1 kWh/mt. The calculation methods for both cases results in an average mass-weighted specific energy consumption that is equal to the setpoint.

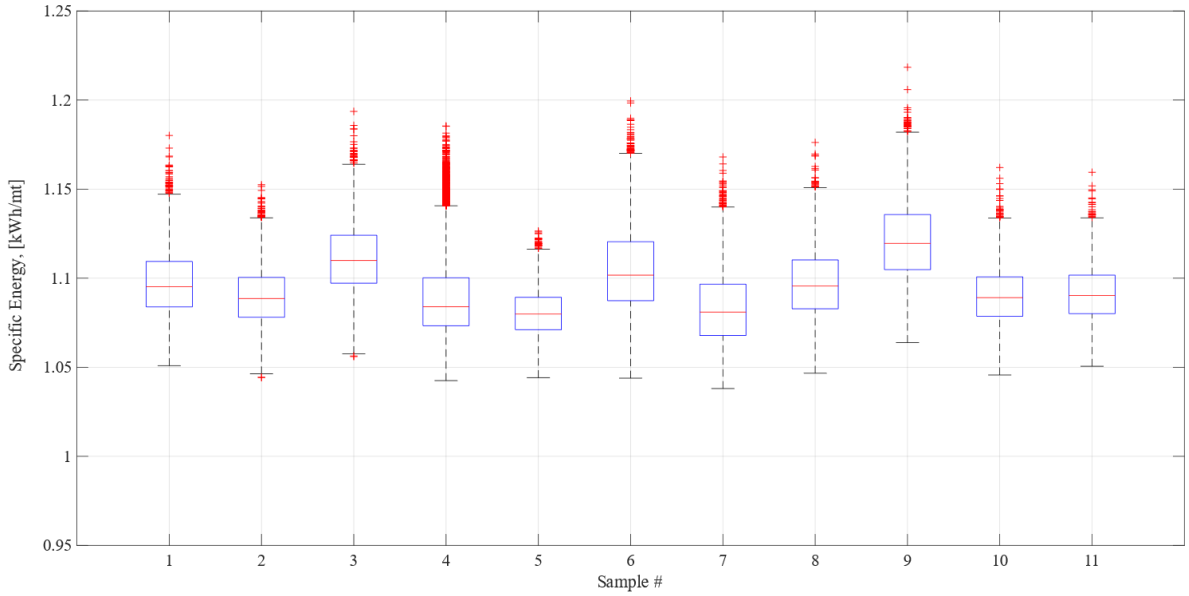

Figure B.2 Distribution of specific energies for 11 samples, where 30 particles are randomly sub-sampled as per the standard DropWeight test method. For each sample, the average particle mass was used to specify a drop-weight height which corresponds to a specific energy input of 1 kWh/mt

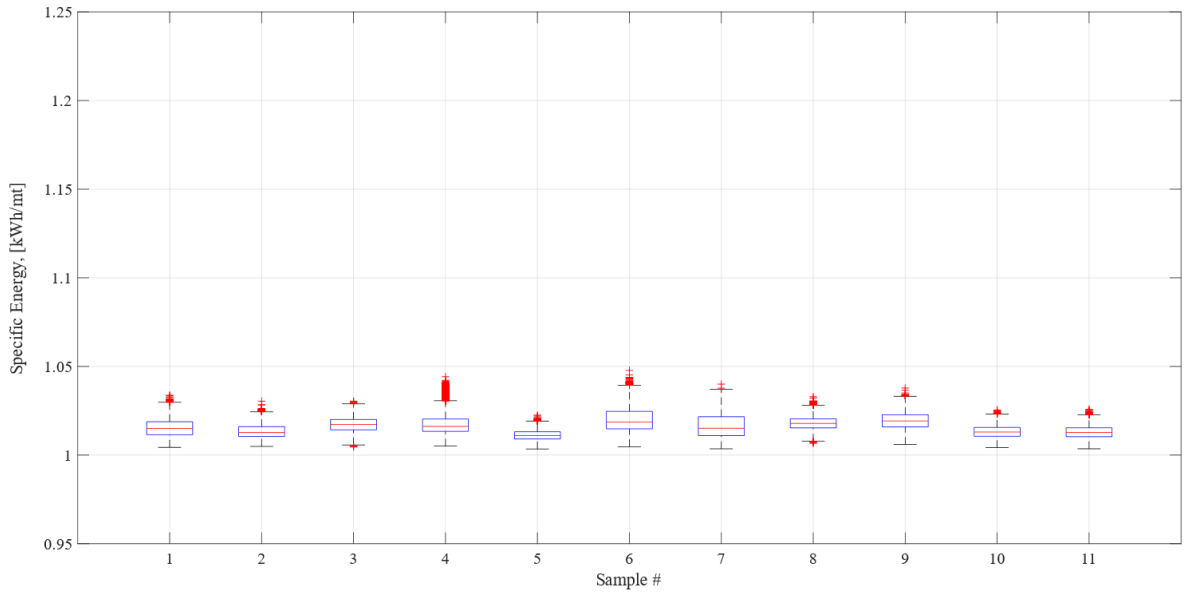

Figure B.3 Distribution of specific energies for 11 samples, where 30 particles are randomly sub-sampled as per standard DropWeight test method. For each sample, particles were grouped into heavy, medium and light weight groupings and treated separately at a target specific energy input of 1 kWh/mt

The reduction in variation of specific energy input was assessed using random sampling algorithms in Matlab 2018a. For each of the 11 geometallurgical samples, 150 particles were weighed and the process of sub-sampling particles into five lots of thirty, representing a sample for an energy-breakage setpoint, was simulated. The mean squared error was calculated assuming a setpoint of 1 kWh/mt. To simulate a typical DropWeight test approach, a case was evaluated where each lot of 30 particles is impacted using the one drop-weight potential energy, which is based on the setpoint of 1 kWh/mt and the average particle mass.

To simulate the proposed abbreviated method, a case was evaluated where each sample set of 150 particles is separated into heavy, medium and light particle groupings according to equation B.1. Particles from heavy, medium and light mass groupings are then randomly sub-sampled to generate five lots of 30 particles (while keeping heavy, medium and light particles separate). For each sample containing 30 particles, three drop-weight potential energies are applied based on their mass grouping, as shown in Table B.1. The drop-weight potential energy to be used is calculated using the setpoint of 1 kWh/mt and the average particle mass in the heavy, medium and light groups.

Although a typical test approach would involve testing of different specific energy levels, to illustrate the error associated with the two test methods, a specific energy input of 1 kWh/mt was assumed for all five sub-samples (containing 30 particles). The simulation was repeated a thousand times to determine the distribution of mean squared error associated with each method.

Figures B.4 and B.5 show the resulting mean squared errors for one thousand simulations of sampling based on the standard approach and the proposed method, respectively. The median of the error in specific energy consumption for the standard method ranged from 0.097 to 0.156 for the eleven samples. For the proposed method, the median of the error ranged from 0.011 to 0.020. Overall, the mean squared error of specific energy consumption decreased by approximately 85%.

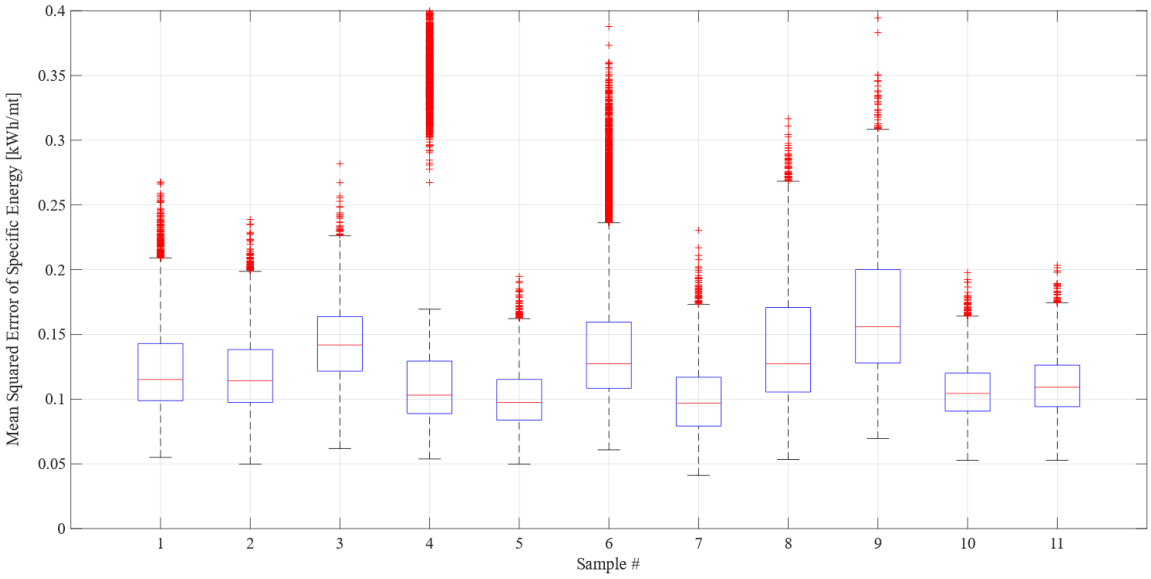

Figure B.4 Mean squared error of specific energy for 11 samples using a typical DropWeight approach where 30 particles are sub-sampled. The mean particle mass was used to specify a drop-weight potential energy which corresponds to a specific energy input of 1 kWh/t

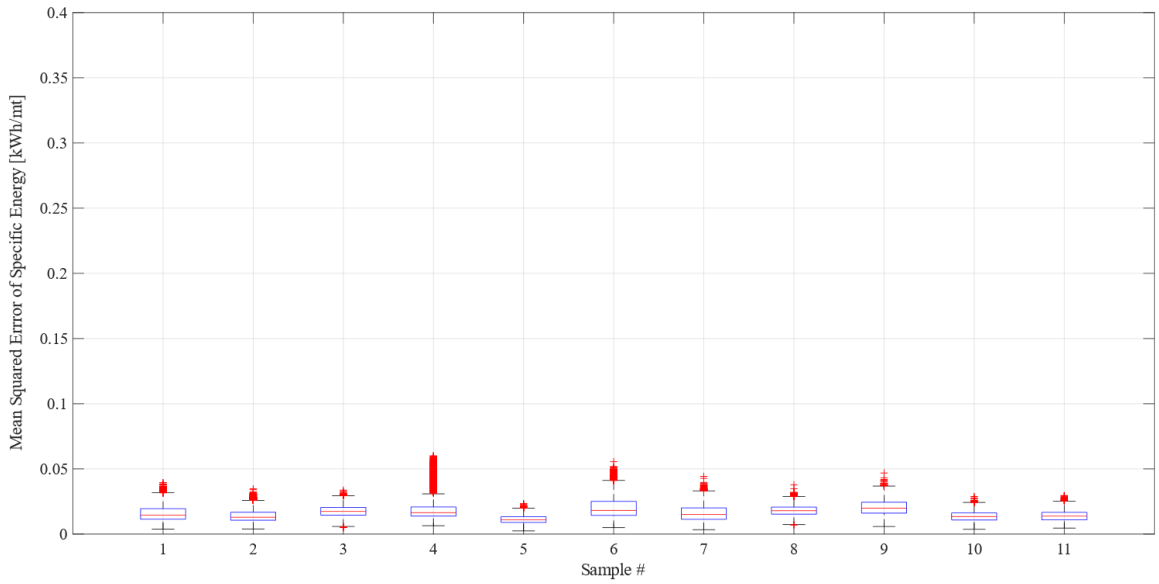

Figure B.5 Mean squared error of specific energy for 11 samples using the proposed DropWeight method, where heavy, medium and light weight particles are randomly sub-sampled to generate a 30 particle sub-sample.

Table B.2 shows a comparison of the Axb values resulting from the standard DropWeight test procedure and the proposed abbreviated method. For the two samples, the difference in DWI was less than 5%.

Table B.2 Comparison of Axb results

Sample	Standard Method				Abbreviated Method			
	A	b	Axb	DWI (kWh/m^3)	A*	b	Axb	DWI (kWh/m^3)
Copper Mountain #1	62.7	0.47	29.5	9.52	80	0.381	30.5	9.20
Copper Mountain #2	62.4	0.48	30.0	9.59	80	0.377	30.1	9.53

** A was limited to 80% during fitting*

B.5 Conclusions and Recommendations

The abbreviated DropWeight method allows energy-breakage parameters A and b to be determined for material characterization using less sample than the full DropWeight method. The variation in specific energy was reduced by systematically separating particles into heavy, medium and light groups, and adjusting the dropweight height according to the mean of their masses. The difference in DWI results, from the standard DropWeight procedure and the abbreviated method, was within 5% for the two samples that were used for the final comparison.

References

Bbosa, L. S., Mainza, A. N. & Powell M. (2014). Analysis of the breakage data of a series of devices. Proceedings of the XXVII International Mineral Processing Congress – IMPC 2014.

Kojovic. T. (2016). HIT – a portable field device for rapid testing at site. 13th AUSIMM Mill Operator's Conference. Perth, WA, 10–12 October, 2016.

Stark, S., Perkins, T., & Napier-Munn, T. J. (2008). JK Drop Weight Parameters – a statistical analysis of their accuracy and precision, and the effect on SAG mill comminution circuit simulation. Proceedings of the Metallurgical Plant Design and Operating Strategies Conference, Perth, WA, 18-19 August, 2008.

Appendix C PGNAA and XRF Test Results

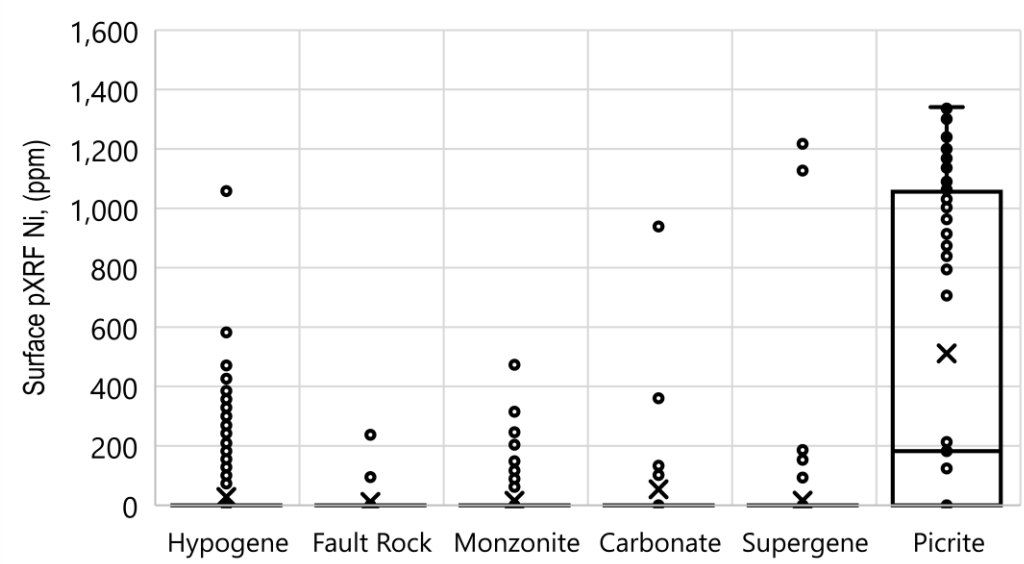

Figure C.1 Rock type and pXRF measurement for Ni. Maximum of four readings. 1,226 rocks in presented dataset.

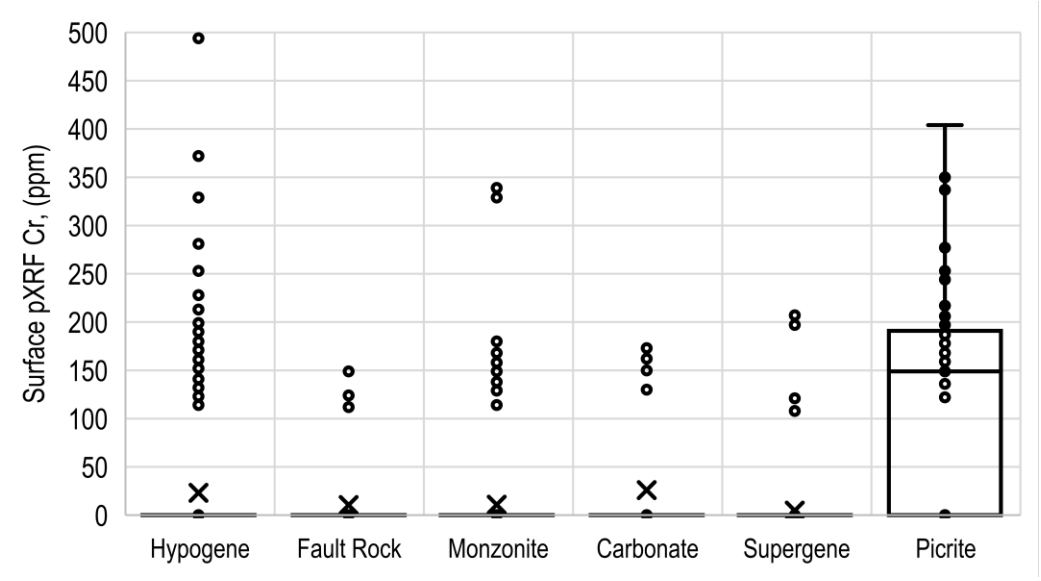

Figure C.2 Rock type pXRF surface measurement for Cr. Maximum of four surface readings. 1,226 rocks in presented dataset.

Table C.1 Bulk samples used for PGNAA testing. Sample weights were approximately 220kg each. Mill feed was hypogene with minor amounts of secondary hypogene alteration

Sample	Abbreviation	Copper grade (ICP), (%)	Calibration/Blind
Mill feed, low Grade	Blend, LG	0.56	Calibration
Mill feed, medium Grade	Blend, MG	0.68	Blind
Mill feed, high Grade	Blend, HG	0.89	Calibration
Monzonite	Monzonite	0.23	Blind
Picrite	Picrite	0.31	Blind
Hypogene	Hypogene	1.55	Calibration
Surface Supergene	Surface Supergene	0.27	Calibration
Underground Supergene	UG Supergene	0.68	Calibration
Hypogene “Waste”	Hypogene Waste	0.19	Calibration

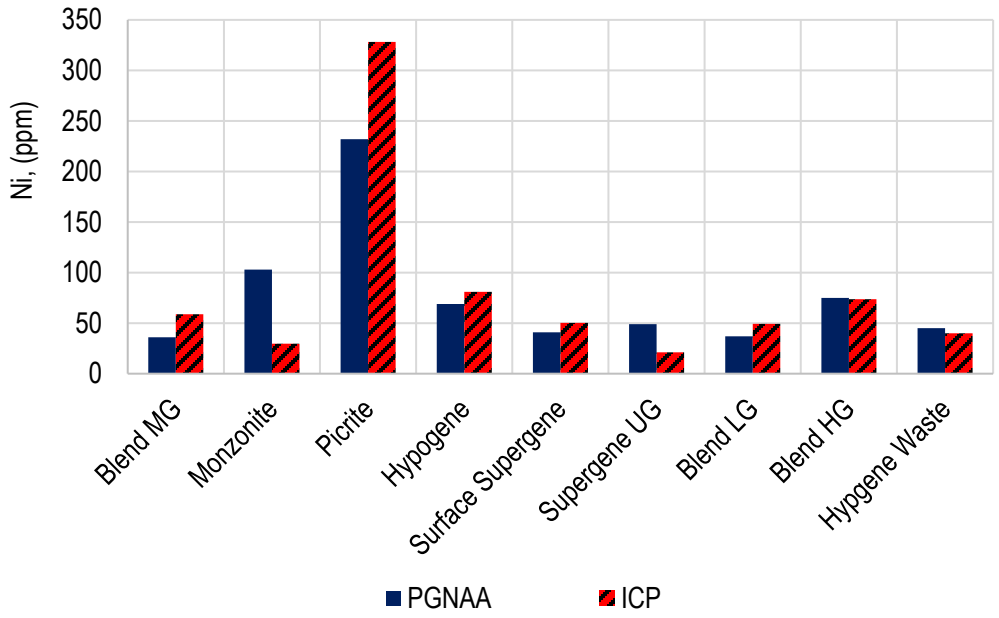

Figure C.3 PGNAA and ICP measurements for Ni. Nine bulk samples of approximately 220kg each

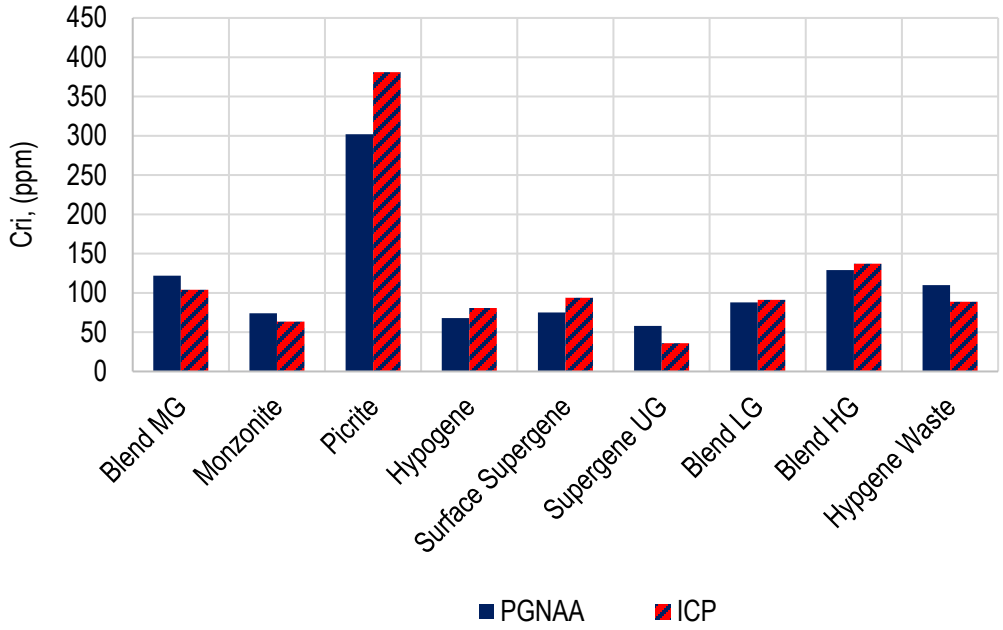

Figure C.4 PGNAA and ICP measurements for Cr. Nine bulk samples of approximately 220kg each

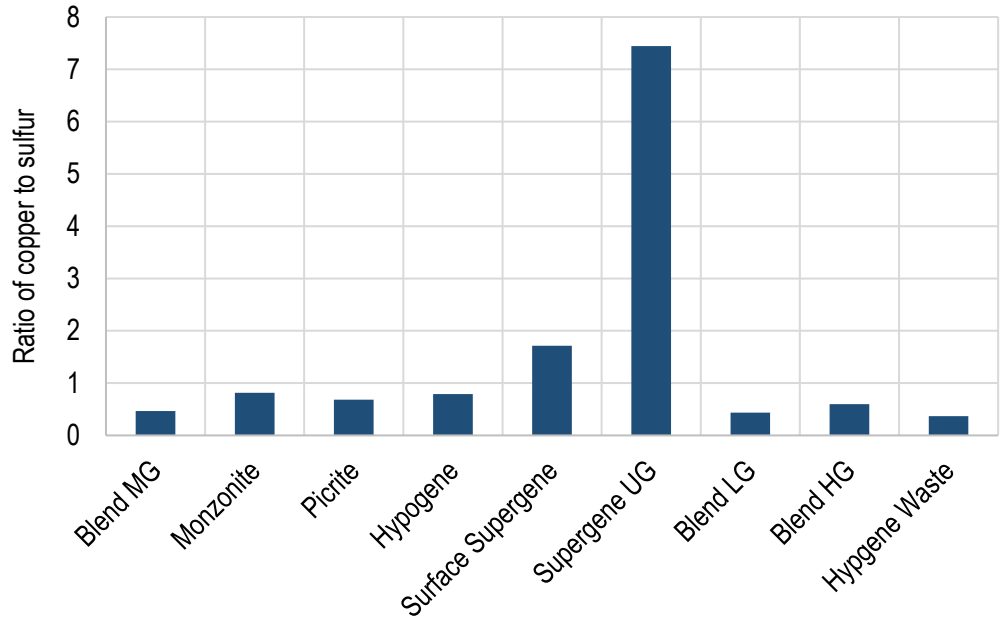

Figure C.5 Ratio of copper to sulfur from PGNAA measurements. Nine bulk samples of approximately 220kg each

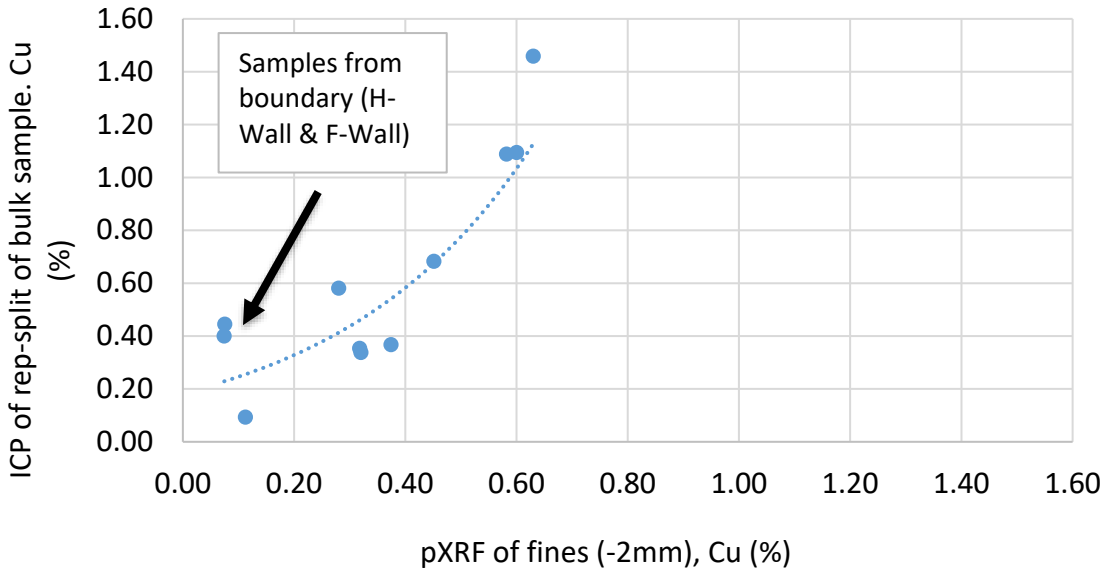

Figure C.6 Copper grade of drawpoint sample, based on ICP analysis of a representative sub-sample, and copper grade of fines (-2 mm), measured using pXRF

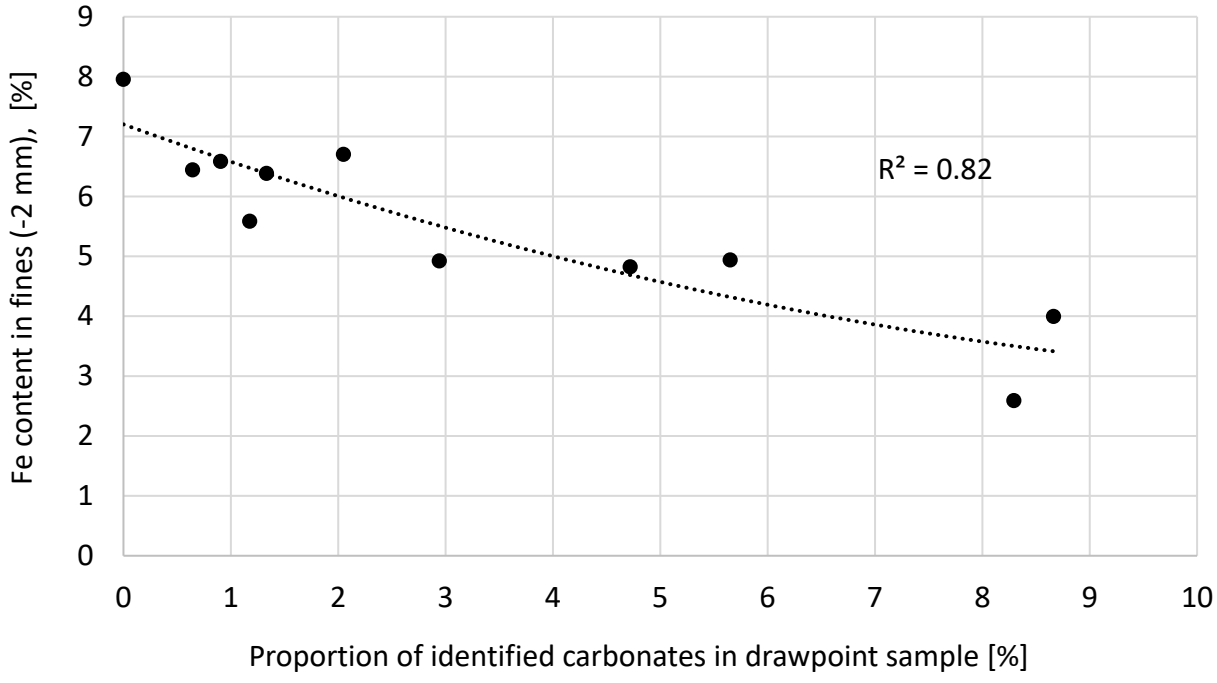

Figure C.7 Fe content in fines (-2 mm), measured by pXRF, and the proportion of carbonate rock in drawpoint samples

Appendix D Point Load Test Results

Point load tests were carried out according ASTM D5731-08 (2013) standards for lump rock. Lithology and alteration data are reported according to guideline shown in Table 3.1. Based on discussion with New Afton representatives, the following conversion factors were applied to $I_{s(50)}$ results to estimate an equivalent UCS value:

Hypogene, Mesogene and DMZ (demineralized):	17
Supergene ore:	15

Note: blank values indicate an unsuccessful test result due to breakage occurring that does not meet ASTM guidelines (eg. chipping etc.)

Table D.1 Point load test results for mill feed sample taken in March 2016

Specimen #	Size [mm]	Lithology/ Alteration Group	Magnetic (Yes = 1, No = 0)	Specific Gravity	Width 1 [mm]	Width 2 [mm]	Diameter [mm]	Load P [kN]	De^2 [mm^2]	De [mm]	Is [MPa]	Correction Factor F	Is(50) [MPa]
Mill #1	-100,+75	1	1	2.81	58	63	37	22.6	2,732	52.3	8.3	1.0	8.4
Mill #2	-100,+75	1	0	2.75	87	88	29	30.5	3,212	56.7	9.5	1.1	10.0
Mill #3	-100,+75	1	0	2.76	101	80	25	18.6	2,546	50.5	7.3	1.0	7.3
Mill #4	-100,+75	1	0	2.67	88	91	36	12.0	4,034	63.5	3.0	1.1	3.3
Mill #5	-100,+75	1	0	2.77	97	75	39	24.1	3,724	61.0	6.5	1.1	7.1
Mill #6	-100,+75	1	0	2.87	66	93	27	9.7	2,269	47.6	4.3	1.0	4.2
Mill #7	-100,+75	1	0	2.73	89	56	29	12.7	2,068	45.5	6.1	1.0	5.9
Mill #8	-100,+75	1	0	2.74	73	61	57	13.7	4,427	66.5	3.1	1.1	3.5
Mill #9	-100,+75	1	0	2.68	54	74	42	15.2	2,888	53.7	5.3	1.0	5.5
Mill #10	-100,+75	1	0	2.69	91	96	55	16.9	6,373	79.8	2.6	1.2	3.3
Mill #11	-100,+75	1	0	2.88	64	57	41	32.5	2,976	54.5	10.9	1.0	11.4
Mill #12	-100,+75	1	0	2.73	90	83	34	28.5	3,593	59.9	7.9	1.1	8.6
Mill #13	-100,+75	3	0	2.72	77	50	50	16.4	3,183	56.4	5.2	1.1	5.5
Mill #14	-100,+75	3	0	2.67	54	92	43	12.0	2,956	54.4	4.1	1.0	4.2
Mill #15	-100,+75	3	0	2.64	89	45	47	16.3	2,693	51.9	6.0	1.0	6.1
Mill #16	-100,+75	3	0	2.66	71	67	55	10.7	4,692	68.5	2.3	1.2	2.6
Mill #17	-100,+75	3	0	2.68	86	84	58	15.2	6,203	78.8	2.4	1.2	3.0
Mill #18	-100,+75	3	1	2.72	54	89	49.5	11.1	3,403	58.3	3.3	1.1	3.5
Mill #19	-100,+75	3	1	2.76	53	68	54.5	34.4	3,678	60.6	9.4	1.1	10.2
Mill #20	-100,+75	3	0	2.78	42	79	50	4.8	2,674	51.7	1.8	1.0	1.8
Mill #21	-100,+75	3	0	2.68	89	71	51	16.0	4,610	67.9	3.5	1.1	4.0
Mill #22	-100,+75	3	1	2.70	82	81	41	15.0	4,228	65.0	3.6	1.1	4.0
Mill #23	-100,+75	3	0	2.69	65	68	49	23.9	4,055	63.7	5.9	1.1	6.6
Mill #24	-100,+75	3	0	2.77	53	69	37	13.0	2,497	50.0	5.2	1.0	5.2
Mill #25	-100,+75	7	0	2.88	78	95	70	14.1	6,952	83.4	2.0	1.3	2.6
Mill #26	-100,+75	6	0	2.85	84	69	73	27.6	6,413	80.1	4.3	1.2	5.3
Mill #27	-100,+75	6	0	2.66	41	55	39	12.9	2,036	45.1	6.4	1.0	6.1

Specimen #	Size [mm]	Lithology/ Alteration Group	Magnetic (Yes = 1, No = 0)	Specific Gravity	Width 1 [mm]	Width 2 [mm]	Diameter [mm]	Load P [kN]	De^2 [mm^2]	De [mm]	Is [MPa]	Correction Factor F [MPa]	Is(50) [MPa]
Mill #28	-100,+75	5	0	2.62	103	50							
Mill #29	-100,+75	5	0	2.78	53	78	70	39.6	4,724	68.7	8.4	1.2	9.7
Mill #30	-100,+75	5	0	2.69	62	83	59	33.4	4,658	68.2	7.2	1.2	8.2
Mill #31	-100,+75	5	0	2.70	87	79							
Mill #32	-100,+75	5	0	2.65	78	80	65	32.5	6,455	80.3	5.0	1.2	6.2
Mill #33	-100,+75	5	1	2.76	79	86							
Mill #34	-100,+75	5	0	2.74	78	83	65	39.1	6,455	80.3	6.1	1.2	7.5
Mill #35	-100,+75	5	0	2.74	77	40							
Mill #36	-100,+75	5	0	2.71	86	65	74	16.0	6,124	78.3	2.6	1.2	3.2
Mill #37	-100,+75	1	0	2.74	103	94	45	21.5	5,386	73.4	4.0	1.2	4.7
Mill #38	-100,+75	1	1	3.03	79	49	48	20.2	2,995	54.7	6.7	1.0	7.0
Mill #39	-100,+75	1	0	2.74	72	84	62	18.3	5,684	75.4	3.2	1.2	3.9
Mill #40	-100,+75	1	1	2.82	61	75	54	23.7	4,194	64.8	5.7	1.1	6.4
Mill #41	-100,+75	1	0	2.77	90	90	46.5	40.3	5,329	73.0	7.6	1.2	9.0
Mill #42	-100,+75	1	1	2.75	100	63	51	11.0	4,091	64.0	2.7	1.1	3.0
Mill #43	-100,+75	1	1	2.70	62	30	45.5	17.0	1,738	41.7	9.8	0.9	9.0
Mill #44	-100,+75	1	0	2.75	78	74	35	28.3	3,298	57.4	8.6	1.1	9.1
Mill #45	-100,+75	1	0	2.82	65	55	59	22.5	4,132	64.3	5.4	1.1	6.1
Mill #46	-100,+75	1	1	2.87	81	86	38	20.6	3,919	62.6	5.3	1.1	5.8
Mill #47	-75, +63	7	-	-	78	74	29	11.6	2,732	52.3	4.3	1.0	4.3
Mill #48	-75, +63	7	-	-	46	53	49.5	15.1	2,899	53.8	5.2	1.0	5.4
Mill #49	-75, +63	7	-	-	66	46	52	19.5	3,046	55.2	6.4	1.0	6.7
Mill #50	-75, +63	7	-	-	84	55	48	8.3	3,361	58.0	2.5	1.1	2.6
Mill #51	-75, +63	7	-	-	65	44	37	13.1	2,073	45.5	6.3	1.0	6.1
Mill #52	-75, +63	7	-	-	49	58	44	39.4	2,745	52.4	14.4	1.0	14.7
Mill #53	-75, +63	7	-	-	51	58	44	22.0	2,857	53.5	7.7	1.0	7.9
Mill #54	-75, +63	6	-	-	64	64	33	11.3	2,689	51.9	4.2	1.0	4.3
Mill #55	-75, +63	6	-	-	56	59	30	5.3	2,139	46.2	2.5	1.0	2.4

Specimen #	Size [mm]	Lithology/ Alteration Group	Magnetic (Yes = 1, No = 0)	Specific Gravity	Width 1 [mm]	Width 2 [mm]	Diameter [mm]	Load P [kN]	De² [mm²]	De [mm]	Is [MPa]	Correction Factor F [MPa]	Is(50) [MPa]
Mill #56	-75, +63	6	-	-	74	57	37	15.9	2,685	51.8	5.9	1.0	6.0
Mill #57	-75, +63	6	-	-	69	43	33	8.6	1,807	42.5	4.8	0.9	4.4
Mill #58	-75, +63	6	-	-	75	44	53	12.1	2,969	54.5	4.1	1.0	4.2
Mill #59	-75, +63	6	-	-	70	50	37	14.3	2,355	48.5	6.1	1.0	6.0
Mill #60	-75, +63	6	-	-	61	64	44	9.2	3,417	58.5	2.7	1.1	2.9
Mill #61	-75, +63	1	-	-	81	59	29	19.6	2,179	46.7	9.0	1.0	8.7
Mill #62	-75, +63	1	-	-	67	57	27	19.1	1,960	44.3	9.8	0.9	9.2
Mill #63	-75, +63	1	-	-	63	42	45	15.9	2,406	49.1	6.6	1.0	6.6
Mill #64	-75, +63	1	-	-	57	63	30	23.7	2,177	46.7	10.9	1.0	10.6
Mill #65	-75, +63	1	-	-	58	57	37	15.1	2,685	51.8	5.6	1.0	5.7
Mill #66	-75, +63	1	-	-	54	67	43	23.9	2,956	54.4	8.1	1.0	8.4
Mill #67	-75, +63	3	-	-	50	74	31	20.9	1,974	44.4	10.6	0.9	10.0
Mill #68	-75, +63	3	-	-	63	63	29	11.9	2,326	48.2	5.1	1.0	5.0
Mill #69	-75, +63	3	-	-	58	81	35	15.3	2,585	50.8	5.9	1.0	5.9
Mill #70	-75, +63	3	-	-	61	56	45	31.8	3,209	56.6	9.9	1.1	10.5
Mill #71	-75, +63	3	-	-	54	75	30	20.9	2,063	45.4	10.1	1.0	9.7
Mill #72	-75, +63	3	-	-	57	50	38	21.1	2,419	49.2	8.7	1.0	8.7
Mill #73	-75, +63	5	-	-	64	58	47	14.8	3,471	58.9	4.2	1.1	4.6
Mill #74	-75, +63	5	-	-	65	65	36	22.5	2,979	54.6	7.6	1.0	7.9
Mill #75	-75, +63	5	-	-	62	60	44	18.3	3,361	58.0	5.4	1.1	5.8
Mill #76	-75, +63	5	-	-	62	56	45	15.7	3,209	56.6	4.9	1.1	5.2
Mill #77	-75, +63	5	-	-	57	52	47	18.2	3,112	55.8	5.8	1.1	6.1
Mill #78	-75, +63	5	-	-	81	80	29	17.4	2,954	54.3	5.9	1.0	6.1

Mean Is(50):	**6.2**	**MPa**
Median Is(50)	**6.0**	**MPa**
Standard deviation	**2.5**	**MPa**
Equivalent UCS (NX 54mm Core)	**106**	**MPa**

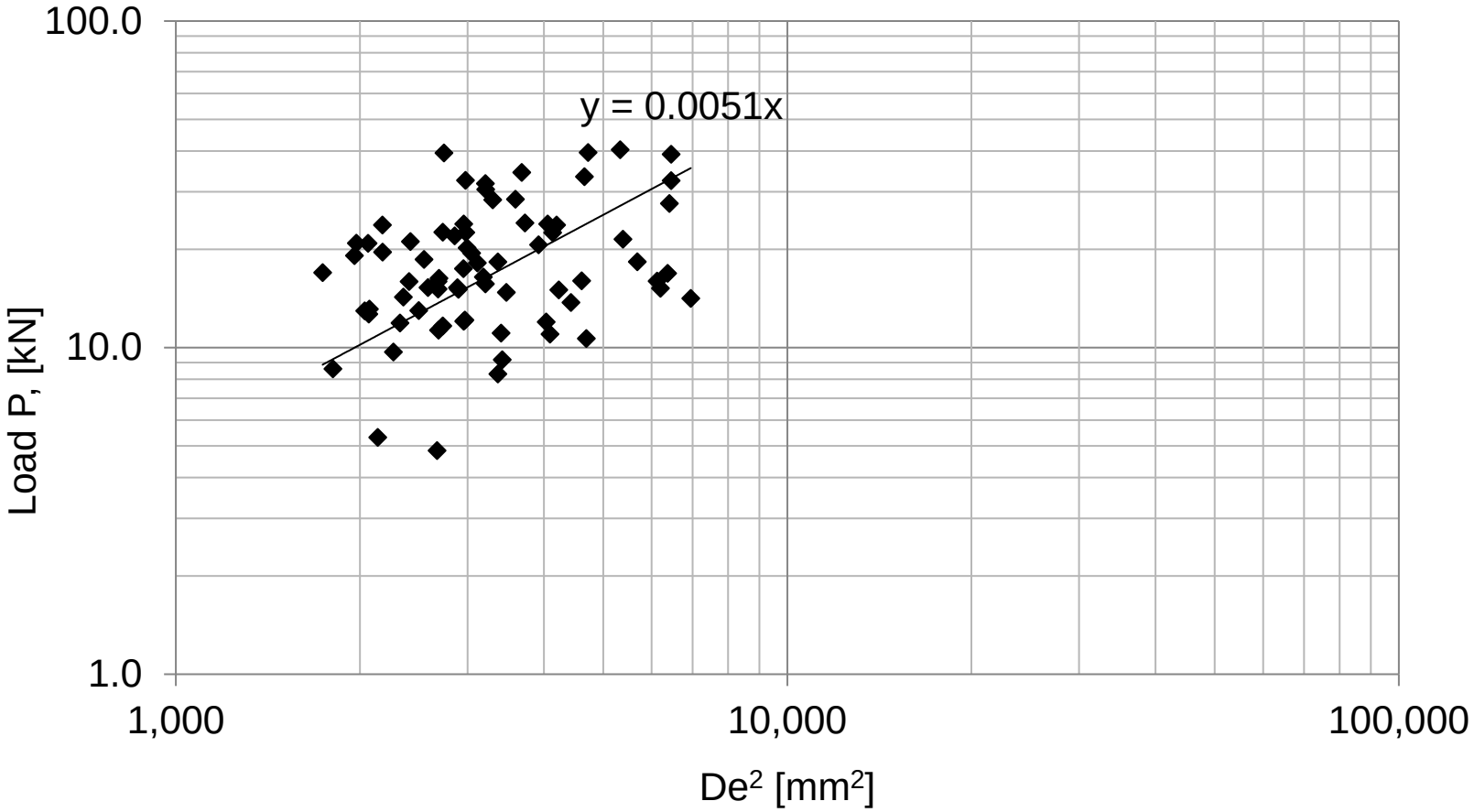

Figure D.1 Point load test results for Mill Feed (sample collected March 2016)

Table D.2 Point load test results for drawpoint sample B13S taken Nov 2015

Specimen #	Specific Gravity	Width 1 [mm]	Width 2 [mm]	Diameter [mm]	Load P [kN]	De^2 [mm^2]	De [mm]	Is [MPa]	Correction Factor F [MPa]	Is(50) [MPa]
2	2.70	57	67	67	15.6	5,289	72.7	3.0	1.2	3.5
4	2.66	62	70	63	14.5	5,294	72.8	2.7	1.2	3.2
8	2.72									
9	2.55	104	99	84	1.0	10,856	104.2	0.1	1.4	0.1
11	2.63	76	77	36	5.4	3,507	59.2	1.5	1.1	1.7
12	2.76	27	81	72	10.4	4,950	70.4	2.1	1.2	2.4
13	2.68	82	88	14	8.5	1,515	38.9	5.6	0.9	5.0
14	2.61	23	67	73	3.5	4,183	64.7	0.8	1.1	0.9
16	2.75	54	54	33	6.4	2,269	47.6	2.8	1.0	2.8
19	2.73	36	53	57	19.4	3,230	56.8	6.0	1.1	6.4
21	2.70	49	70	35	4.2	2,652	51.5	1.6	1.0	1.6
22	2.86	85	101	41	12.8	4,855	69.7	2.6	1.2	3.1
23	2.65	117	83	46	4.6	5,857	76.5	0.8	1.2	0.9
24	2.72	60	42	63	3.6	4,091	64.0	0.9	1.1	1.0
25	2.63	35	56	36	4.0	2,086	45.7	1.9	1.0	1.9
26	2.80	41	50	34	16.2	1,970	44.4	8.2	0.9	7.8
29	2.77									
31	2.71	81	82	58	3.2	6,019	77.6	0.5	1.2	0.6
32	2.68	63	56	53	3.8	4,015	63.4	0.9	1.1	1.0
33	2.58	47	46	44	4.4	2,605	51.0	1.7	1.0	1.7
36	2.72	60	55	40	16.5	2,928	54.1	5.6	1.0	5.9
39	2.71	72	72	28	17.6	2,567	50.7	6.8	1.0	6.9
40	2.84	44	50	33	21.3	1,975	44.4	10.8	0.9	10.3
41	2.72	26	61	62	9.1	3,434	58.6	2.6	1.1	2.8
42	2.74	51	65	31	13.8	2,289	47.8	6.0	1.0	5.9
43	2.76	45	53	48	11.4	2,995	54.7	3.8	1.0	4.0
46	2.71	83	84	52	32.8	5,528	74.4	5.9	1.2	7.1

Specimen #	Specific Gravity	Width 1 [mm]	Width 2 [mm]	Diameter [mm]	Load P [kN]	De^2 [mm^2]	De [mm]	Is [MPa]	Correction Factor F [MPa]	Is(50) [MPa]
49	2.73	23	61	60	26.5	3,209	56.6	8.3	1.1	8.7
50	2.73	46	63	47	19.7	3,261	57.1	6.0	1.1	6.4
51	2.77	55	63	66	8.6	4,958	70.4	1.7	1.2	2.0
52	2.65	48	44	36	8.3	2,108	45.9	3.9	1.0	3.8

B13S Mean Is(50):	3.8	MPa
B13S Median Is(50)	3.1	MPa
Standard deviation	2.7	MPa
Equivalent UCS (NX 54mm Core):	64	MPa

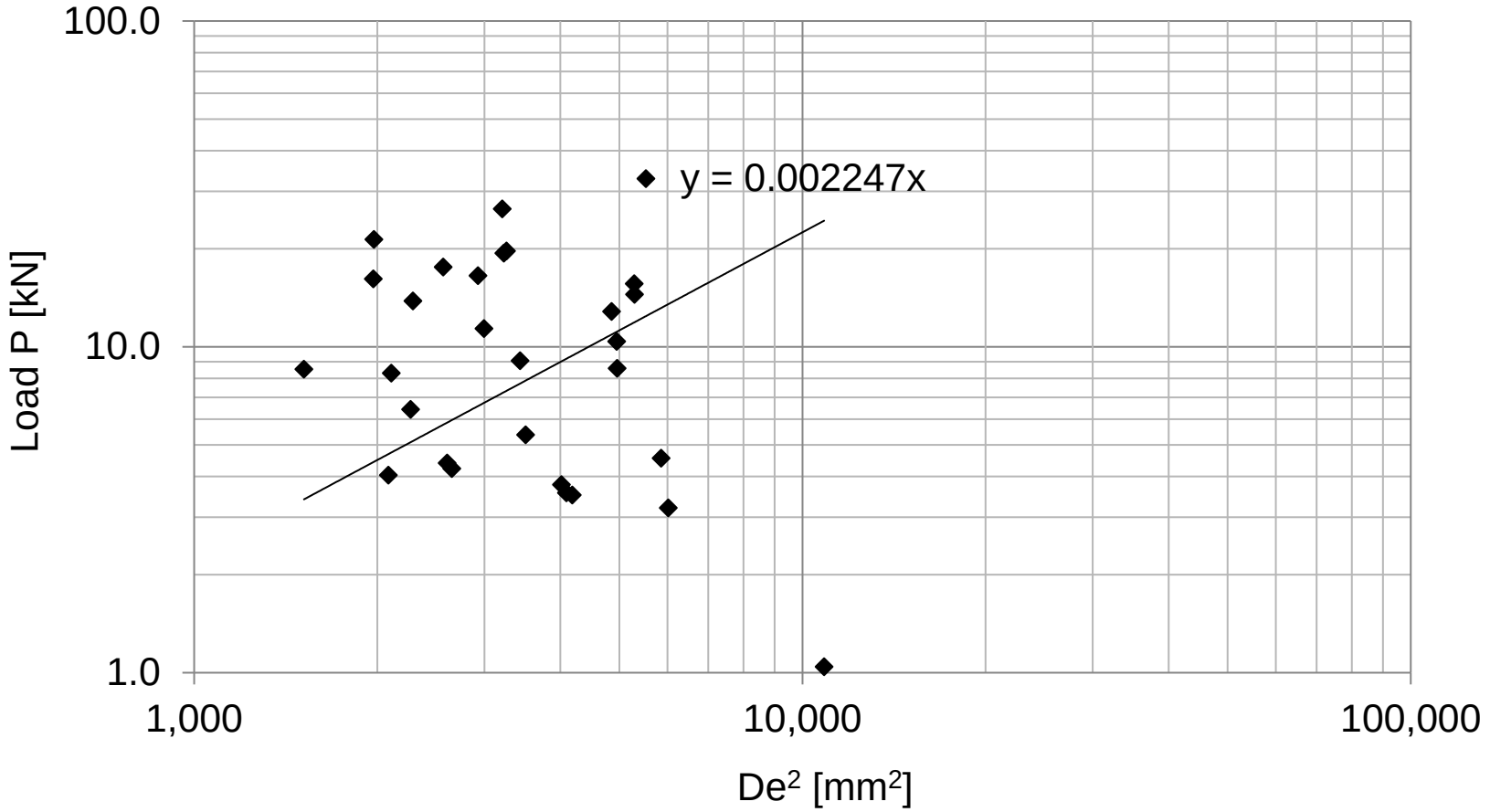

Figure D.2 Point load test results for drawpoint sample B13S taken Nov 2015

Table D.3 Point load test results for drawpoint sample D7S taken Nov 2015

Specimen #	Specific Gravity	Width 1 [mm]	Width 2 [mm]	Diameter [mm]	Load P [kN]	De^2 [mm^2]	De [mm]	Is [MPa]	Correction Factor F [MPa]	Is(50) [MPa]
1	2.81	95	91	76	25.0	8,999	94.9	2.8	1.3	3.7
2	2.71	59	83	84	13.4	7,594	87.1	1.8	1.3	2.3
3	2.82	87	76	67	43.8	6,953	83.4	6.3	1.3	7.9
4	2.73	22	85	56	6.5	3,815	61.8	1.7	1.1	1.9
5	2.82	18	82	55	27.4	3,501	59.2	7.8	1.1	8.5
7	2.82	13	45	42	28.3	1,551	39.4	18.3	0.9	16.4
8	2.69	50	45	48	20.7	2,903	53.9	7.1	1.0	7.4
10	2.79	51	112	63	35.8	6,537	80.9	5.5	1.2	6.8
13	2.67	40	82	43	17.8	3,340	57.8	5.3	1.1	5.7
14	2.73	78	84	22	7.2	2,269	47.6	3.2	1.0	3.1
15	2.83	32	56	44	18.9	2,465	49.6	7.7	1.0	7.6
17	2.74	47	43	30	5.3	1,719	41.5	3.1	0.9	2.8
18	2.76	67	53	42	19.8	3,209	56.6	6.2	1.1	6.5
19	2.72	48	52	42	12.0	2,674	51.7	4.5	1.0	4.6
21	2.67	55	43	35	30.4	2,184	46.7	13.9	1.0	13.5
22	2.80	53	57	24	10.0	1,681	41.0	5.9	0.9	5.4
23	2.68	40	78	74	31.5	5,559	74.6	5.7	1.2	6.8
24	2.73	42	54	49	29.4	2,995	54.7	9.8	1.0	10.2
25	2.74	52	44	25	13.2	1,528	39.1	8.6	0.9	7.7
26	2.64	50	52	36	7.1	2,338	48.3	3.0	1.0	3.0
27	2.76	24	50	29	6.5	1,366	37.0	4.8	0.9	4.2
30	2.71	25	48	40	16.5	1,859	43.1	8.9	0.9	8.3
31	2.73	29	82	36	13.6	2,544	50.4	5.4	1.0	5.4
32	2.81	54	74	48	4.5	3,911	62.5	1.1	1.1	1.3
33	2.66	56	42	45	11.3	2,807	53.0	4.0	1.0	4.1
34	2.82	41	59	47	13.2	2,992	54.7	4.4	1.0	4.6
35	2.82	31	42	41	6.0	1,905	43.7	3.2	0.9	3.0

Specimen #	Specific Gravity	Width 1 [mm]	Width 2 [mm]	Diameter [mm]	Load P [kN]	De^2 [mm^2]	De [mm]	Is [MPa]	Correction Factor F [MPa]	Is(50) [MPa]
36	2.81	57	61	41	5.1	3,080	55.5	1.7	1.0	1.7
37	2.73	32	60	41	22.8	2,401	49.0	9.5	1.0	9.4
38	2.89	61	58	39	5.5	2,955	54.4	1.9	1.0	1.9
39	2.64	54	40	37	4.2	2,214	47.1	1.9	1.0	1.8
43	2.61	30	54	40	3.4	2,139	46.2	1.6	1.0	1.5
44	2.82	41	49	36	3.1	2,063	45.4	1.5	1.0	1.5
45	2.63	47	59	35	12.7	2,362	48.6	5.4	1.0	5.3
46	2.64	26	43	29	8.8	1,274	35.7	6.9	0.9	5.9
47	2.72	57	52	30	11.0	2,082	45.6	5.3	1.0	5.1
48	2.64	57	51	40	7.5	2,750	52.4	2.7	1.0	2.8
51	2.68	35	56	36	22.0	2,086	45.7	10.5	1.0	10.1
54	2.83	44	67	40	22.1	2,827	53.2	7.8	1.0	8.1
55	2.69	40	40	40	6.0	2,037	45.1	3.0	1.0	2.8
56	2.80	34	53	53	4.9	2,935	54.2	1.7	1.0	1.7
58	2.74	46	39	49	8.5	2,652	51.5	3.2	1.0	3.2
59	2.79	54	46	38	10.5	2,419	49.2	4.3	1.0	4.3
64	2.88	43	73	40	25.3	2,954	54.3	8.6	1.0	8.9
66	2.69	50	59	50	15.1	3,470	58.9	4.3	1.1	4.7

D7S Mean Is(50):	5.4	MPa
D7S Median Is(50)	4.7	MPa
Standard deviation	3.3	MPa
Equivalent UCS (NX 54mm Core):	92	MPa

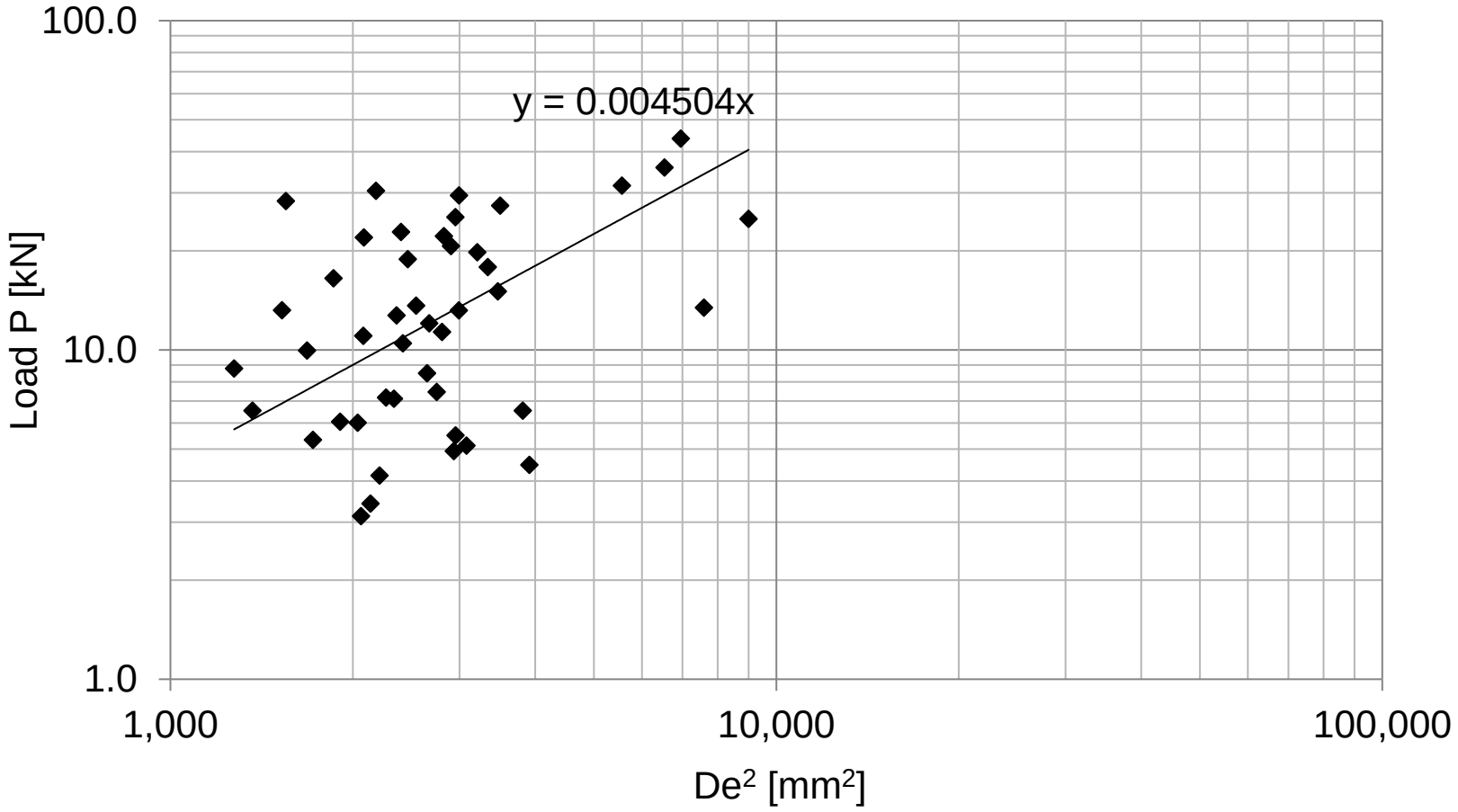

Figure D.3 Point load test results for drawpoint sample D7S taken Nov 2015

Table D.4 Point load test results for drawpoint sample D11N taken Nov 2015

Specimen #	Specific Gravity	Width 1 [mm]	Width 2 [mm]	Diameter [mm]	Load P [kN]	De^2 [mm^2]	De [mm]	Is [MPa]	Correction Factor F	Is(50) [MPa]
2	2.79	54	54	34	3.9	2,338	48.3	1.7	1.0	1.7
3	2.72	68	81	57	41.6	4,935	70.3	8.4	1.2	9.8
5	2.72	44	68	48	40.4	2,689	51.9	15.0	1.0	15.3
7	2.73	76	38	43	22.1	2,080	45.6	10.6	1.0	10.2
8	2.81	58	81	46	24.9	3,397	58.3	7.3	1.1	7.9
9	2.75	45	70	61	22.9	3,495	59.1	6.6	1.1	7.1
10	2.75	54	48	29	3.5	1,772	42.1	2.0	0.9	1.9
11	2.61	104	77	48	14.7	4,706	68.6	3.1	1.2	3.6
12	2.66	43	48	32	20.7	1,752	41.9	11.8	0.9	10.9
13	2.69	56	47	33	10.9	1,975	44.4	5.5	0.9	5.2
14	2.65	85	93	26	16.0	2,814	53.0	5.7	1.0	5.8
15	2.68	80	90	39	5.4	3,973	63.0	1.4	1.1	1.5
16	2.85	93	61	45	20.8	3,495	59.1	6.0	1.1	6.4
17	2.69	60	50	53	10.3	3,374	58.1	3.1	1.1	3.3
18	2.65									
19	2.69	54	35	30	5.8	1,337	36.6	4.4	0.9	3.8
22	2.67	83	63	54	15.4	4,332	65.8	3.5	1.1	4.0
23	2.73	83	84	74	18.0	7,820	88.4	2.3	1.3	3.0
25	2.70	69	70	22	14.9	1,933	44.0	7.7	0.9	7.3
26	2.75	47	45	35	8.3	2,005	44.8	4.2	1.0	4.0
28	2.68	103	70	59	25.0	5,258	72.5	4.8	1.2	5.6
29	2.95	80	77	45	30.1	4,412	66.4	6.8	1.1	7.7
30	2.77	52	45	47	22.1	2,693	51.9	8.2	1.0	8.4
32	2.63	40	45	23	5.3	1,171	34.2	4.5	0.8	3.8
33	2.68	44	63	38	15.7	2,129	46.1	7.4	1.0	7.1
34	2.67									
36	2.75	55	58	38	22.6	2,661	51.6	8.5	1.0	8.6

Specimen #	Specific Gravity	Width 1 [mm]	Width 2 [mm]	Diameter [mm]	Load P [kN]	De^2 [mm^2]	De [mm]	Is [MPa]	Correction Factor F [MPa]	Is(50) [MPa]
37	2.72	52	56	42	17.2	2,781	52.7	6.2	1.0	6.3
41	2.70	53	54	38.4	15.3	2,591	50.9	5.9	1.0	5.9
42	2.57	59	45	28	10.2	1,604	40.1	6.3	0.9	5.7
43	2.68	81	70	43	11.4	3,832	61.9	3.0	1.1	3.3
44	2.68	53	45	29	9.6	1,662	40.8	5.8	0.9	5.3
48	2.68	29	53	34	6.0	1,255	35.4	4.8	0.9	4.1
49	2.58	42	36	44	10.4	2,185	46.7	4.8	1.0	4.6
50	2.67	45	55	39	8.0	2,483	49.8	3.2	1.0	3.2
52	2.79	58	58	49	16.4	3,619	60.2	4.5	1.1	4.9
54	2.64	43	70	38	11.8	2,734	52.3	4.3	1.0	4.4
56	2.79	61	55	49	11.5	3,619	60.2	3.2	1.1	3.4
57	2.57	46	47	26	5.9	1,539	39.2	3.8	0.9	3.4
58	2.72	51	52	47	17.7	3,082	55.5	5.7	1.0	6.0
59	2.69	36	44	31	18.0	1,579	39.7	11.4	0.9	10.3
60	2.68	74	88	45	13.7	4,641	68.1	2.9	1.1	3.4
61	2.68	68	59	37	17.0	2,991	54.7	5.7	1.0	5.9
62	2.73	54	53	51	15.4	3,474	58.9	4.4	1.1	4.8

D11N Mean Is(50):	5.7	MPa
D11N Median Is(50)	5.3	MPa
Standard deviation	2.8	MPa
Equivalent UCS (NX 54mm Core):	97	MPa

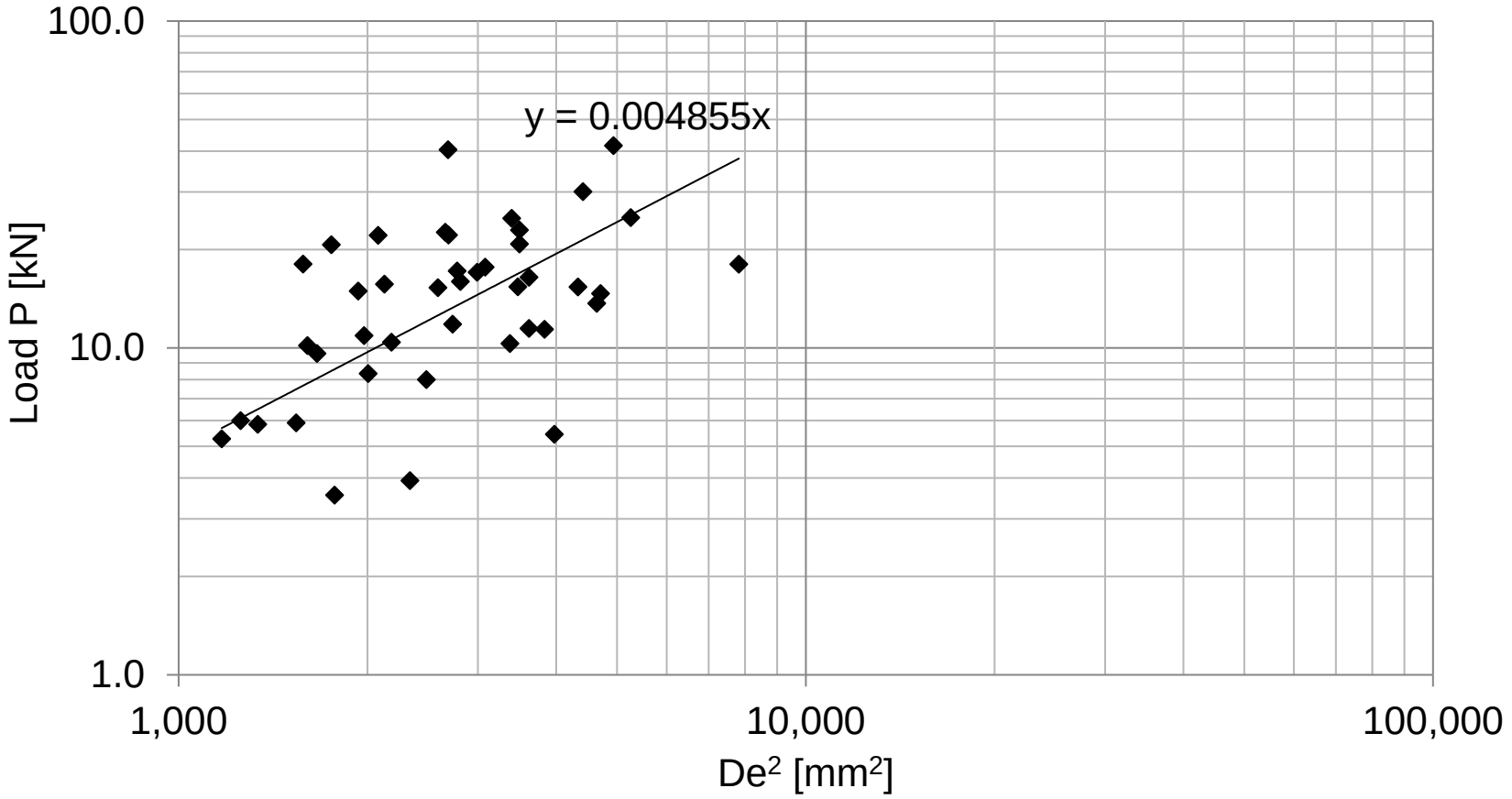

Figure D.4 Point load test results for drawpoint sample D11N taken Nov 2015

Table D.5 Point load test results for drawpoint sample D11S taken Nov 2015

Specimen #	Specific Gravity	Width 1 [mm]	Width 2 [mm]	Diameter [mm]	Load P [kN]	De^2 [mm^2]	De [mm]	Is [MPa]	Correction Factor F [MPa]	Is(50) [MPa]
3	2.70	53	37	37	6.0	1,743	41.8	3.5	0.9	3.2
4	2.71	81	49	35	7.3	2,184	46.7	3.3	1.0	3.2
5	2.77	63	54	49	12.9	3,369	58.0	3.8	1.1	4.1
7	2.78	76	45	58.5	9.1	3,352	57.9	2.7	1.1	2.9
8	2.69	53	40	41	13.0	2,088	45.7	6.2	1.0	6.0
11	2.73	79	75	62	26.5	5,921	76.9	4.5	1.2	5.4
12	2.61	38	73	42	12.9	2,032	45.1	6.4	1.0	6.1
13	2.69	37	34	33.7	4.8	1,459	38.2	3.3	0.9	2.9
14	2.66	57	51	27	6.1	1,753	41.9	3.5	0.9	3.2
15	2.78	35	44	36.1	20.6	1,609	40.1	12.8	0.9	11.6
16	2.64	54	59	39	10.9	2,681	51.8	4.1	1.0	4.1
18	2.71	45	60	65	8.8	3,724	61.0	2.4	1.1	2.6
19	2.70	40	59	40	3.4	2,037	45.1	1.7	1.0	1.6
21	2.71	42	53	30	13.7	1,604	40.1	8.5	0.9	7.7
23	2.69	71	63	32	19.8	2,567	50.7	7.7	1.0	7.8
24	2.74	45	65	66	6.5	3,782	61.5	1.7	1.1	1.9
25	2.73	42	35	30	10.4	1,337	36.6	7.8	0.9	6.8
26	2.71									
27	2.71	66	55	39.6	16.2	2,773	52.7	5.9	1.0	6.0
28	2.74	58	59	50	9.5	3,692	60.8	2.6	1.1	2.8
29	2.74	71	74	42	7.9	3,797	61.6	2.1	1.1	2.3
30	2.70	77	47	57	17.8	3,411	58.4	5.2	1.1	5.6
31	2.76	49	71	31	15.4	1,934	44.0	8.0	0.9	7.5
32	2.75	75	80	51	8.2	4,870	69.8	1.7	1.2	1.9
33	2.74	72	78	49	10.2	4,492	67.0	2.3	1.1	2.6
34	2.70	38	35	35	20.2	1,560	39.5	12.9	0.9	11.6
37	2.76	71	71	66	15.1	5,966	77.2	2.5	1.2	3.1

Specimen #	Specific Gravity	Width 1 [mm]	Width 2 [mm]	Diameter [mm]	Load P [kN]	De^2 [mm^2]	De [mm]	Is [MPa]	Correction Factor F [MPa]	Is(50) [MPa]
40	2.85	55	73	47	23.5	3,291	57.4	7.1	1.1	7.6
42	3.27	59	42	23	7.7	1,230	35.1	6.3	0.9	5.3
43	2.87	24	61	29	14.9	886	29.8	16.8	0.8	13.3
44	2.75	35	41	46						
45	2.74	77	65	59.3	13.8	4,908	70.1	2.8	1.2	3.3
46	2.76	70	76	45.4	7.9	4,046	63.6	2.0	1.1	2.2
48	2.74	59	55	54.3	32.3	3,803	61.7	8.5	1.1	9.3
49	2.73	57	45	35	5.3	2,005	44.8	2.6	1.0	2.5
54	2.76	45	49	25.4	8.4	1,455	38.1	5.8	0.9	5.1
55	2.74	79	50	42						
59	2.72	35	33	33.2	11.6	1,395	37.3	8.3	0.9	7.3
61	2.76	47	63	46	7.1	2,753	52.5	2.6	1.0	2.6
62	2.71	37	47	34.5	6.7	1,625	40.3	4.1	0.9	3.8
63	2.73									
41		51	85	63.2	22.5	4,104	64.1	5.5	1.1	6.1

D11S Mean Is(50):	5.1	MPa
D11S Median Is(50)	4.1	MPa
Standard deviation	2.9	MPa
Equivalent UCS (NX 54mm Core):	86	MPa

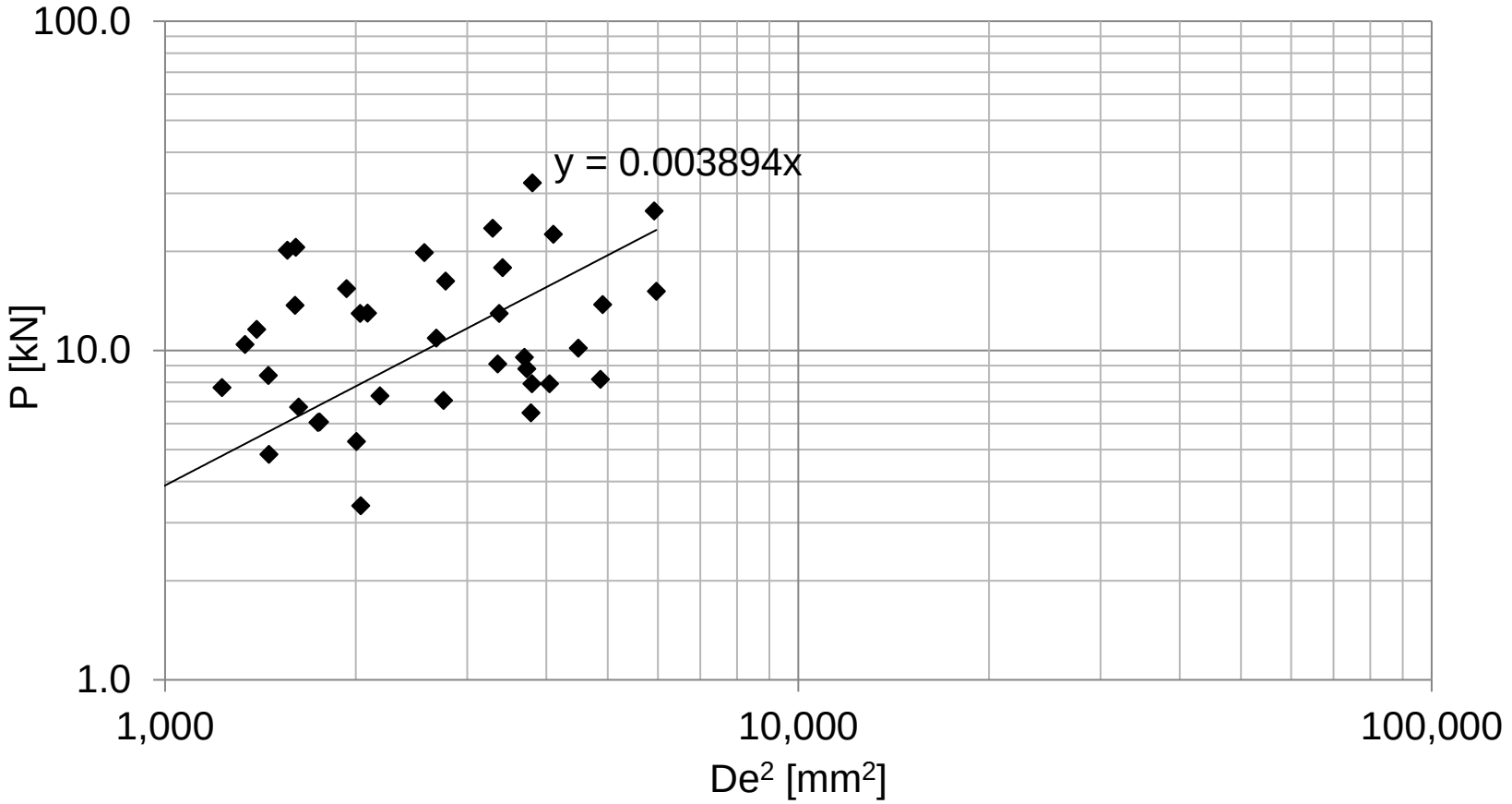

Figure D.5 Point load test results for drawpoint sample D11S taken Nov 2015

Table D.6 Point load test results for drawpoint sample D38N taken Nov 2015

Specimen #	Specific Gravity	Width 1 [mm]	Width 2 [mm]	Diameter [mm]	Load P [kN]	De^2 [mm^2]	De [mm]	Is [MPa]	Correction Factor F [MPa]	Is(50) [MPa]
1	2.71	53	60	31	5.3	2,230	47.2	2.4	1.0	2.3
2	2.69	47	61	35	2.3	2,406	49.1	0.9	1.0	0.9
3	2.66	75	66	36	5.2	3,231	56.8	1.6	1.1	1.7
4	2.72	29	63	33	3.5	1,933	44.0	1.8	0.9	1.7
5	2.60	56	39	38	3.1	2,298	47.9	1.3	1.0	1.3
6	2.63	44	53	55	3.5	3,396	58.3	1.0	1.1	1.1
9	2.74	48	51	29	13.0	1,828	42.8	7.1	0.9	6.6
11	2.79	18	57	37	4.0	1,767	42.0	2.3	0.9	2.1
13	2.75	64	60	53	13.0	4,184	64.7	3.1	1.1	3.5
14	2.70	67	45	27	3.4	1,925	43.9	1.8	0.9	1.7
15	2.66	75	55	29	3.6	2,400	49.0	1.5	1.0	1.5
16	2.79	38	44	34	6.5	1,775	42.1	3.7	0.9	3.4
18	2.77	90	85	44.2	10.4	4,924	70.2	2.1	1.2	2.5
20	2.69	36	65	48	4.6	3,074	55.4	1.5	1.0	1.6
21	2.76	60	40	38	6.2	2,419	49.2	2.6	1.0	2.5
26	2.72	105	77	50	16.5	5,793	76.1	2.8	1.2	3.4
28	2.78	43	45	29	7.2	1,625	40.3	4.4	0.9	4.0
30	2.69	55	45	39	8.4	2,483	49.8	3.4	1.0	3.4
32	2.81	64	20	34	3.4	1,818	42.6	1.9	0.9	1.7
33	2.72	55	29	50	5.6	2,674	51.7	2.1	1.0	2.1
34	2.83	56	53	38	7.2	2,637	51.4	2.7	1.0	2.8
35	2.78	51	20	40	2.1	1,808	42.5	1.1	0.9	1.1
36	2.76	48	50	35	5.2	2,184	46.7	2.4	1.0	2.3
37	2.70	75	29	27	7.9	1,788	42.3	4.4	0.9	4.1
39	2.70	50	29	44	3.1	2,213	47.0	1.4	1.0	1.4
41	2.65	44	49	34	0.9	2,013	44.9	0.4	1.0	0.4
43	2.53	56	45	33	3.0	2,122	46.1	1.4	1.0	1.3

Specimen #	Specific Gravity	Width 1 [mm]	Width 2 [mm]	Diameter [mm]	Load P [kN]	De^2 [mm^2]	De [mm]	Is [MPa]	Correction Factor F [MPa]	Is(50) [MPa]
44	2.70	57	54	34	5.1	2,403	49.0	2.1	1.0	2.1
47	2.73	46	19	31	0.6	1,283	35.8	0.5	0.9	0.4
49	2.71	61	68	28	2.4	2,299	48.0	1.0	1.0	1.0

D38N Mean Is(50):	2.2	MPa
D38N Median Is(50)	1.9	MPa
Standard deviation	1.3	MPa
Equivalent UCS (NX 54mm Core):	37	MPa

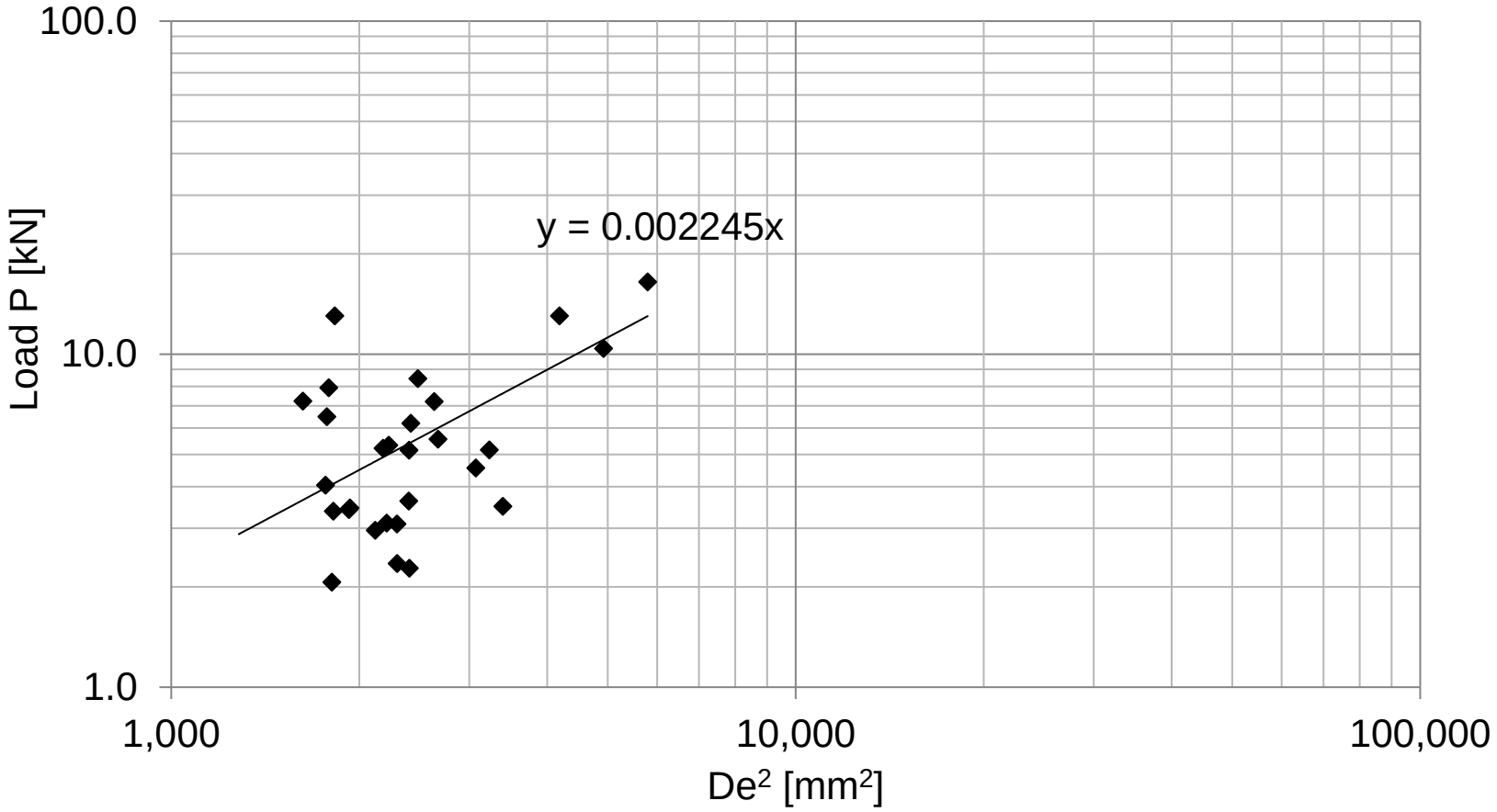

Figure D.6 Point load test results for drawpoint sample D38N taken Nov 2015

Table D.7 Point load test results for drawpoint sample E13S taken Nov 2015

Specimen #	Specific Gravity	Width 1 [mm]	Width 2 [mm]	Diameter [mm]	Load P [kN]	De^2 [mm^2]	De [mm]	Is [MPa]	Correction Factor F [MPa]	Is(50) [MPa]
2	3.15	60	78	61.4	23.4	5,386	73.4	4.3	1.2	5.2
4	2.80	68	72	25.2	11.5	2,240	47.3	5.2	1.0	5.0
6	2.82	62	60	46.5	17.7	3,612	60.1	4.9	1.1	5.3
7	2.76	61	60	36.6	7.9	2,819	53.1	2.8	1.0	2.9
8	2.76	56	22							
9	2.75	57	58	47.4	12.8	3,470	58.9	3.7	1.1	4.0
10	2.76	68	60	63	14.8	5,134	71.6	2.9	1.2	3.4
11	2.74	54	49	40	10.5	2,623	51.2	4.0	1.0	4.0
13	2.68	71	66	49.8	26.9	4,343	65.9	6.2	1.1	7.0
14	2.73	78	54	62.5	17.5	5,252	72.5	3.3	1.2	3.9
15	2.63	64	61	35.9	9.4	2,857	53.4	3.3	1.0	3.4
18	2.78	50	51	32	13.5	2,058	45.4	6.6	1.0	6.3
19	2.69	38	61	35.8	11.1	2,256	47.5	4.9	1.0	4.8
20	2.76	59	63	35.2	24.7	2,734	52.3	9.1	1.0	9.2
22	2.66	58	17	47.9	4.5	2,287	47.8	2.0	1.0	1.9
23	2.69	80	70	50.5	10.0	4,822	69.4	2.1	1.2	2.4
24	2.71	52	76	45	17.9	3,667	60.6	4.9	1.1	5.3
25	2.61	65	63	34.9	14.1	2,844	53.3	5.0	1.0	5.1
26	2.86	21	53	48.5	7.4	2,285	47.8	3.2	1.0	3.2
27	2.63	38	61	50	13.5	3,151	56.1	4.3	1.1	4.5
30	2.68	68	79	65	8.6	6,083	78.0	1.4	1.2	1.7
31	2.71	60	56	36	22.4	2,659	51.6	8.4	1.0	8.5
32	2.68	56	17	34	10.9	1,580	39.8	6.9	0.9	6.2
35	2.92	100	90	85.3	22.4	10,318	101.6	2.2	1.4	3.0
36	2.68	63	82	70	19.7	6,462	80.4	3.1	1.2	3.8
40	2.69	79	64	41.3	15.5	3,760	61.3	4.1	1.1	4.5
41	2.71	43	70	42.4	18.6	3,050	55.2	6.1	1.0	6.4

Specimen #	Specific Gravity	Width 1 [mm]	Width 2 [mm]	Diameter [mm]	Load P [kN]	De^2 [mm^2]	De [mm]	Is [MPa]	Correction Factor F [MPa]	Is(50) [MPa]
42	2.67	58	61	47.3	15.3	3,583	59.9	4.3	1.1	4.6
43	2.68	33	71	37.7	13.4	2,496	50.0	5.4	1.0	5.4
44	2.73	67	60	52.4	20.1	4,230	65.0	4.7	1.1	5.3
45	2.73	66	22							
47	2.78	49	50	35.7	10.4	2,250	47.4	4.6	1.0	4.5
48	2.67	68	91	41.4	22.2	4,191	64.7	5.3	1.1	5.9
49	2.64	71	84	35.9	9.5	3,542	59.5	2.7	1.1	2.9
50	2.69	46	69	33	23.3	2,416	49.2	9.7	1.0	9.6
51	2.65	52	60	42.7	10.4	3,045	55.2	3.4	1.0	3.6
52	2.73	44	48	42	4.5	2,460	49.6	1.8	1.0	1.8
53	2.68	51	20	35	22.3	1,582	39.8	14.1	0.9	12.7
54	2.75	31	54	38	20.4	2,056	45.3	9.9	1.0	9.5
56	2.61	53	18	39.1	11.1	1,767	42.0	6.3	0.9	5.8
57	2.83	46	52	32.4	20.0	2,021	45.0	9.9	1.0	9.4
58	2.80	22	45							
59	2.66	32	50	41.5	10.8	2,174	46.6	5.0	1.0	4.8
60	2.72	58	61	57	10.4	4,318	65.7	2.4	1.1	2.7
62	2.61	52	41	54	17.7	3,197	56.5	5.5	1.1	5.8
63	2.66	53	32	37.2	8.1	2,013	44.9	4.0	1.0	3.8
64	2.82	34	38	23	5.9	1,054	32.5	5.6	0.8	4.6
66	2.74	54	43	31.3	21.6	1,933	44.0	11.2	0.9	10.5
68	2.69	43	54	39.1	9.4	2,415	49.1	3.9	1.0	3.8
69	2.76	47	37	43	6.8	2,299	48.0	3.0	1.0	2.9
70	3.01	65	21	29.4	11.5	1,610	40.1	7.2	0.9	6.5
71	2.78	19	57	31	13.0	1,500	38.7	8.7	0.9	7.7
73	2.61	32	30	44.2	18.9	1,742	41.7	10.9	0.9	10.0
74	2.81	32	56	50.6	9.6	2,835	53.2	3.4	1.0	3.5
76	2.73	42	33	37	12.7	1,767	42.0	7.2	0.9	6.7

E13S Mean Is(50):	5.3	MPa
E13S Median Is(50)	4.8	MPa
Standard deviation	2.5	MPa
Equivalent UCS (NX 54mm Core):	90	MPa

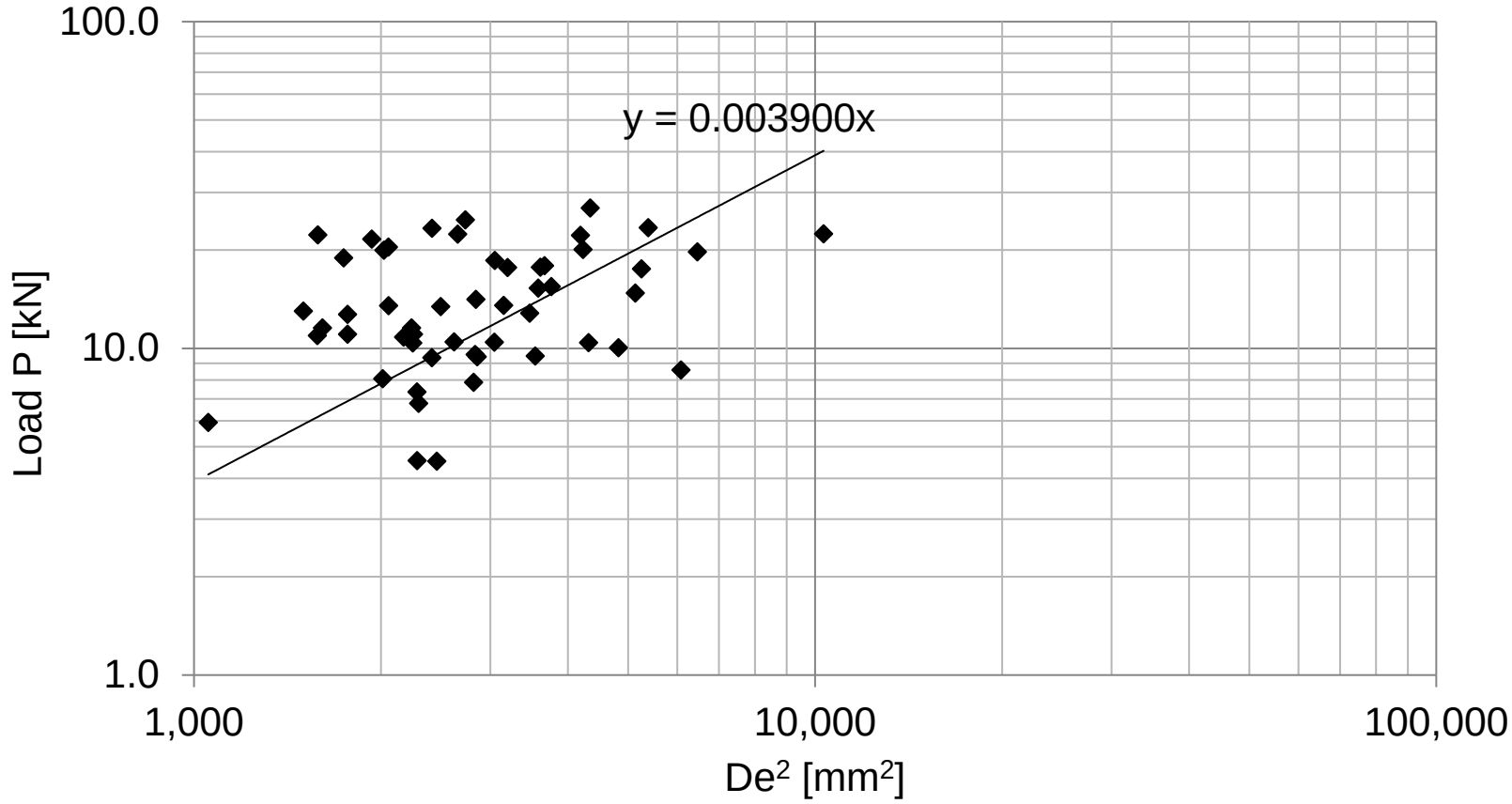

Figure D.7 Point load test results for drawpoint sample E13S taken Nov 2015

Table D.8 Point load test results for drawpoint sample E15N taken Nov 2015

Specimen #	Specific Gravity	Width 1 [mm]	Width 2 [mm]	Diameter [mm]	Load P [kN]	De^2 [mm^2]	De [mm]	Is [MPa]	Correction Factor F [MPa]	Is(50) [MPa]
1	2.71	75	79	68	36.6	6,667	81.6	5.5	1.2	6.8
2	2.67	73	58	59						
5	2.68	58	50	27	9.1	1,856	43.1	4.9	0.9	4.6
6	2.69	27	46	44	20.0	2,045	45.2	9.8	1.0	9.3
7	2.70	52	64	24	18.6	1,772	42.1	10.5	0.9	9.7
8	2.80	45	39	30	18.2	1,604	40.1	11.3	0.9	10.2
9	2.81	34	53	38	20.4	2,105	45.9	9.7	1.0	9.3
10	2.82	42	30	30	12.5	1,375	37.1	9.1	0.9	8.0
11	2.63	55	47	31	6.1	2,013	44.9	3.1	1.0	2.9
13	2.74	51	59	34	17.6	2,381	48.8	7.4	1.0	7.3
14	2.75	42	43	65	13.4	3,517	59.3	3.8	1.1	4.1
15	2.67	65	69	46	30.4	3,924	62.6	7.7	1.1	8.6
16	2.70	34	64	50	12.2	3,119	55.9	3.9	1.1	4.1
17	2.70	86	78	50	19.5	5,220	72.3	3.7	1.2	4.4
18	2.66	30	53	50	7.2	2,642	51.4	2.7	1.0	2.8
20	2.68	50	64	26	3.7	1,887	43.4	2.0	0.9	1.8
22	2.66	53	59	40	17.5	2,852	53.4	6.1	1.0	6.3
23	2.70	50	71	35	6.8	2,696	51.9	2.5	1.0	2.6
24	2.85	55	66	51	19.9	3,929	62.7	5.1	1.1	5.6
25	2.80	48	56	30	10.3	1,986	44.6	5.2	0.9	4.9
27	2.68	88	77	73	11.7	7,668	87.6	1.5	1.3	2.0
31	2.67	50	57	24	10.4	1,635	40.4	6.4	0.9	5.8
32	2.75	37	56	43	13.9	2,546	50.5	5.5	1.0	5.5
33	2.83	50	51	45	14.7	2,893	53.8	5.1	1.0	5.3
34	2.74	46	52	33	12.2	2,059	45.4	5.9	1.0	5.7
35	2.77	81	90	56	27.8	6,096	78.1	4.6	1.2	5.6
36	2.64	33	49	38	9.8	1,984	44.5	5.0	0.9	4.7

Specimen #	Specific Gravity	Width 1 [mm]	Width 2 [mm]	Diameter [mm]	Load P [kN]	De^2 [mm^2]	De [mm]	Is [MPa]	Correction Factor F [MPa]	Is(50) [MPa]
37	2.73	57	63	41	17.2	3,132	56.0	5.5	1.1	5.8
38	2.70	37	50	31	5.4	1,717	41.4	3.2	0.9	2.9
41	2.74	37	48	52	9.9	2,814	53.0	3.5	1.0	3.6
43	2.75	16	64	36	4.8	1,833	42.8	2.6	0.9	2.4
44	2.60	50	52	27	11.4	1,753	41.9	6.5	0.9	6.0
45	2.69	51	55	29	13.2	1,957	44.2	6.7	0.9	6.4
46	2.83	59	63	36	18.3	2,796	52.9	6.6	1.0	6.7
48	2.74	39	75	49	14.5	3,556	59.6	4.1	1.1	4.4
49	2.69	44	52	32	14.0	1,956	44.2	7.2	0.9	6.8
50	2.70	36	55	35	26.1	2,028	45.0	12.9	1.0	12.3
51	2.66	50	32	37	16.4	1,932	43.9	8.5	0.9	8.0
52	2.69	43	56	47	12.1	2,962	54.4	4.1	1.0	4.2
53	2.68	57	65	30	13.0	2,330	48.3	5.6	1.0	5.5
54	2.70	53	58	24	13.7	1,696	41.2	8.1	0.9	7.4
55	2.69	44	54	29	9.1	1,809	42.5	5.0	0.9	4.7
57	2.66	72	74	57	17.5	5,298	72.8	3.3	1.2	3.9
58	2.76	63	60	27	11.8	2,114	46.0	5.6	1.0	5.4
59	2.73	38	37	32	17.7	1,528	39.1	11.6	0.9	10.4
62	2.65	34	55	38	14.3	2,153	46.4	6.6	1.0	6.4
63	2.71	45	46	43	8.2	2,491	49.9	3.3	1.0	3.3
64	2.75	22	48	50	14.8	2,228	47.2	6.7	1.0	6.5
68	2.79	67	63	28	14.0	2,317	48.1	6.1	1.0	6.0

E15N Mean Is(50):	5.8	MPa
E15N Median Is(50)	5.6	MPa
Standard deviation	2.3	MPa
Equivalent UCS (NX 54mm Core):	98	MPa

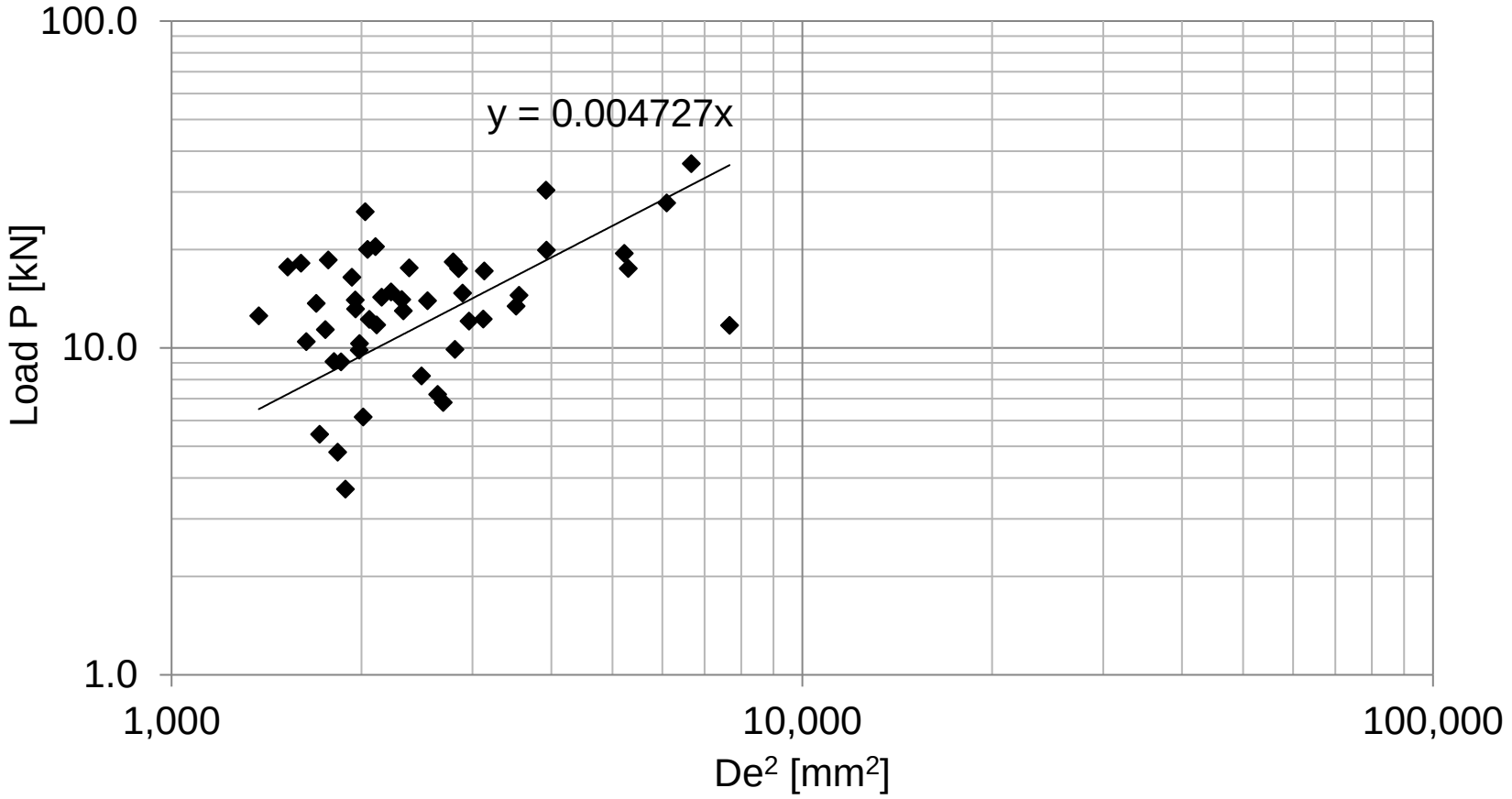

Figure D.8 Point load test results for drawpoint sample E15N taken Nov 2015

Table D.9 Point load test results for drawpoint sample E23N taken Nov 2015

Specimen #	Specific Gravity	Width 1 [mm]	Width 2 [mm]	Diameter [mm]	Load P [kN]	De^2 [mm^2]	De [mm]	Is [MPa]	Correction Factor F [MPa]	Is(50) [MPa]
2	2.74	102	100	62	20.9	7,973	89.3	2.6	1.3	3.4
4	2.74	39	108	44	28.8	4,118	64.2	7.0	1.1	7.8
5	2.71	51	53	31	19.5	2,052	45.3	9.5	1.0	9.1
7	2.72	39	39	33	12.4	1,639	40.5	7.5	0.9	6.9
9	2.73	37	68	42	11.6	2,807	53.0	4.1	1.0	4.2
10	2.71	31	69	29	13.8	1,846	43.0	7.5	0.9	7.0
11	2.75	61	61	51	29.7	3,961	62.9	7.5	1.1	8.3
12	2.67	68	66	45	11.1	3,839	62.0	2.9	1.1	3.2
13	2.64	74	41	34	15.0	2,489	49.9	6.0	1.0	6.0
14	2.70	60	16	40	15.0	1,935	44.0	7.7	0.9	7.3
15	2.71	62	26	24	15.5	1,345	36.7	11.5	0.9	10.0
16	2.77	57	51	43	25.6	2,956	54.4	8.7	1.0	9.0
17	2.74	38	61	39						
18	2.76	52	42	58	18.4	3,471	58.9	5.3	1.1	5.7
20	2.69	43	58	47	13.3	3,022	55.0	4.4	1.0	4.6
21	2.70	28	65	58	15.6	3,434	58.6	4.6	1.1	4.9
22	2.77	51	58	24	13.2	1,665	40.8	7.9	0.9	7.2
23	2.74	16	55	40	11.4	1,808	42.5	6.3	0.9	5.8
24	2.74	20	33	33	5.4	1,113	33.4	4.9	0.8	4.0
27	2.64	29	51	43	6.2	2,190	46.8	2.8	1.0	2.7
28	2.68	36	54	56	5.4	3,209	56.6	1.7	1.1	1.8
29	2.76	63	59	42	10.7	3,262	57.1	3.3	1.1	3.5
30	2.71	71	72	31	9.7	2,822	53.1	3.4	1.0	3.5
32	2.71	71	72	36	13.6	3,277	57.2	4.1	1.1	4.4
33	2.76	33	62	45	14.1	2,722	52.2	5.2	1.0	5.3
37	2.78	45	78	37	5.2	2,897	53.8	1.8	1.0	1.9
38	2.74	80	61	35	25.4	3,142	56.1	8.1	1.1	8.5

Specimen #	Specific Gravity	Width 1 [mm]	Width 2 [mm]	Diameter [mm]	Load P [kN]	De^2 [mm^2]	De [mm]	Is [MPa]	Correction Factor F [MPa]	Is(50) [MPa]
40	2.75	46	77	42	33.5	3,289	57.3	10.2	1.1	10.8
41	2.66	113	84	64	16.6	8,027	89.6	2.1	1.3	2.7
42	2.75	74	79	59	30.1	5,747	75.8	5.2	1.2	6.3
43	2.71	33	63	42						
44	2.68	67	51	46	17.7	3,456	58.8	5.1	1.1	5.5
45	2.69	76	103	72	17.3	8,205	90.6	2.1	1.3	2.7
47	2.75	70	45	40	20.3	2,928	54.1	6.9	1.0	7.2
49	2.72	75	79	47	22.2	4,608	67.9	4.8	1.1	5.5
50	2.67	54	72	40	17.8	3,209	56.6	5.6	1.1	5.9
51	2.75	58	76	45	23.9	3,839	62.0	6.2	1.1	6.9
52	2.76	47	66	28	15.6	2,014	44.9	7.8	1.0	7.4
53	2.72	50	45	40	15.3	2,419	49.2	6.3	1.0	6.3
56	2.70	50	56	37	8.6	2,497	50.0	3.4	1.0	3.4
57	2.67	18	41	45						
58	2.72	95	101	45	18.1	5,615	74.9	3.2	1.2	3.9
60	2.74	33	61	57	14.2	3,411	58.4	4.2	1.1	4.5
61	2.83	59	28	32	8.2	1,772	42.1	4.6	0.9	4.3
62	2.66	29	55	26	6.2	1,390	37.3	4.5	0.9	3.9
63	2.70	26	42	39						
66	2.66	40	52	33	7.2	1,933	44.0	3.7	0.9	3.5
68	2.90	42	59	41	26.0	2,636	51.3	9.9	1.0	10.0
69	2.67	66	55	30	8.5	2,311	48.1	3.7	1.0	3.6
70	2.70	56	47	44	19.9	2,885	53.7	6.9	1.0	7.1
71	2.63	28	54	37	15.9	1,932	43.9	8.2	0.9	7.8

E23N, Mean Is(50):	5.6	MPa
E23N, Median Is(50)	5.5	MPa
Standard deviation	2.3	MPa
Equivalent UCS (NX 54mm Core):	96	MPa

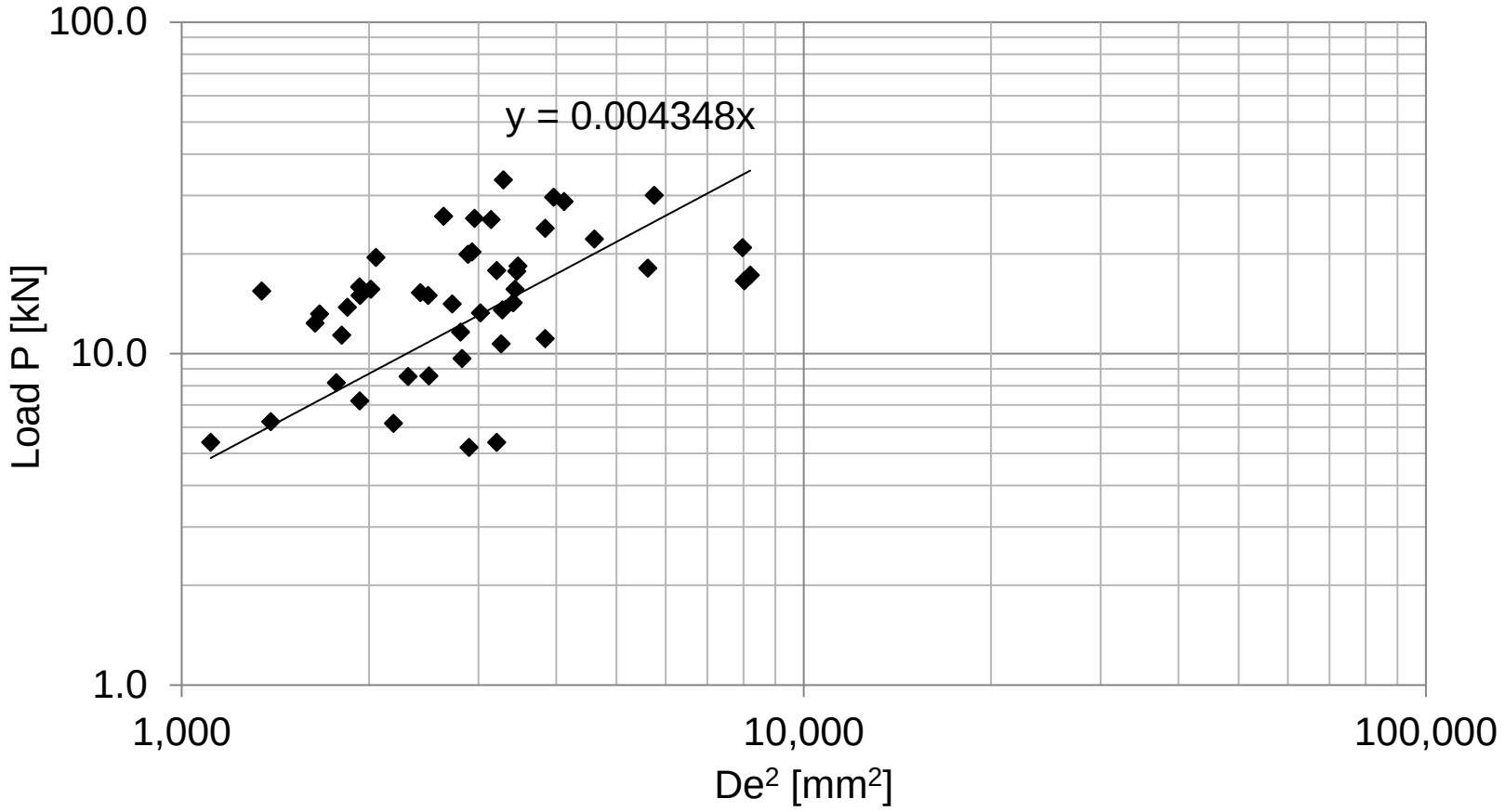

Figure D.9 Point load test results for drawpoint sample E23N taken Nov 2015

Table D.10 Point load test results for drawpoint sample E30N taken Nov 2015

Specimen #	Specific Gravity	Width 1 [mm]	Width 2 [mm]	Diameter [mm]	Load P [kN]	De^2 [mm^2]	De [mm]	Is [MPa]	Correction Factor F [MPa]	Is(50) [MPa]
2	2.70	103	102	51	10.2	6,656	81.6	1.5	1.2	1.9
4	2.71	61	55	54	13.9	3,988	63.1	3.5	1.1	3.9
5	2.72	70	56	36	4.8	2,888	53.7	1.7	1.0	1.7
7	2.75	48	40	38	13.0	2,129	46.1	6.1	1.0	5.9
8	2.79	63	70	58	22.5	4,911	70.1	4.6	1.2	5.3
10	2.65	54	39	46	29.7	2,723	52.2	10.9	1.0	11.1
11	2.71									
12	2.70	43	57	34	22.6	2,165	46.5	10.4	1.0	10.1
14	2.68	80	36	38	20.1	2,806	53.0	7.2	1.0	7.3
15	2.63	49	49	48	6.8	2,995	54.7	2.3	1.0	2.4
16	2.70	46	46	36	10.1	2,108	45.9	4.8	1.0	4.6
18	2.67	37	58	51	11.1	3,084	55.5	3.6	1.0	3.8
21	2.82	58	48	49	14.4	3,307	57.5	4.4	1.1	4.7
22	2.76	94	84	45	21.3	5,099	71.4	4.2	1.2	4.9
23	2.63	61	42	50	27.0	3,279	57.3	8.2	1.1	8.8
24	2.73	52	51	46	13.2	3,002	54.8	4.4	1.0	4.6
25	2.87	46	60	57	23.1	3,846	62.0	6.0	1.1	6.6
28	2.75									
29	2.64	59	1	28	25.7	1,070	32.7	24.1	0.8	19.9
31	2.69	50	57	51	30.0	3,474	58.9	8.6	1.1	9.3
32	2.71	30	41	53	12.9	2,396	48.9	5.4	1.0	5.3
33	2.75	45	55	39	18.0	2,483	49.8	7.3	1.0	7.2
34	2.67	45	33	32	7.9	1,589	39.9	5.0	0.9	4.5
36	2.67	39	47	36	10.4	1,971	44.4	5.3	0.9	5.0
38	2.73	70	76	39	25.8	3,625	60.2	7.1	1.1	7.8
39	2.64	52	43	28	6.3	1,693	41.2	3.7	0.9	3.4
42	2.74	73	47	39	30.1	2,979	54.6	10.1	1.0	10.5

Specimen #	Specific Gravity	Width 1 [mm]	Width 2 [mm]	Diameter [mm]	Load P [kN]	De^2 [mm^2]	De [mm]	Is [MPa]	Correction Factor F [MPa]	Is(50) [MPa]
43	2.90	92	93	65	21.9	7,655	87.5	2.9	1.3	3.7
44	2.00	79	84	63	26.8	6,537	80.9	4.1	1.2	5.1
45	2.79									
48	2.71	91	85	50	21.6	5,602	74.8	3.9	1.2	4.6
49	2.81	73	66	30	26.5	2,655	51.5	10.0	1.0	10.1
54	2.65	26	55	38	14.8	1,960	44.3	7.6	0.9	7.2
55	2.71									
56	2.69	40	63	37	11.4	2,426	49.3	4.7	1.0	4.7
57	2.64	35	50	42	20.0	2,273	47.7	8.8	1.0	8.6
58	2.76	15	42	50	12.3	1,814	42.6	6.8	0.9	6.3
59	2.79	50	55	44	11.4	2,941	54.2	3.9	1.0	4.0
60	2.70	36	46	48	20.8	2,506	50.1	8.3	1.0	8.3
61	2.67	53	10	34	10.0	1,364	36.9	7.4	0.9	6.4
62	2.68	60	58	40	4.7	3,005	54.8	1.6	1.0	1.6
63	2.88	81	32	28	20.9	2,014	44.9	10.4	1.0	9.9
64	2.75	44	50	32	12.1	1,915	43.8	6.3	0.9	5.9

E30N Mean Is(50):	6.3	MPa
E30N Median Is(50)	5.3	MPa
Standard deviation	3.4	MPa
Equivalent UCS (NX 54mm Core):	108	MPa

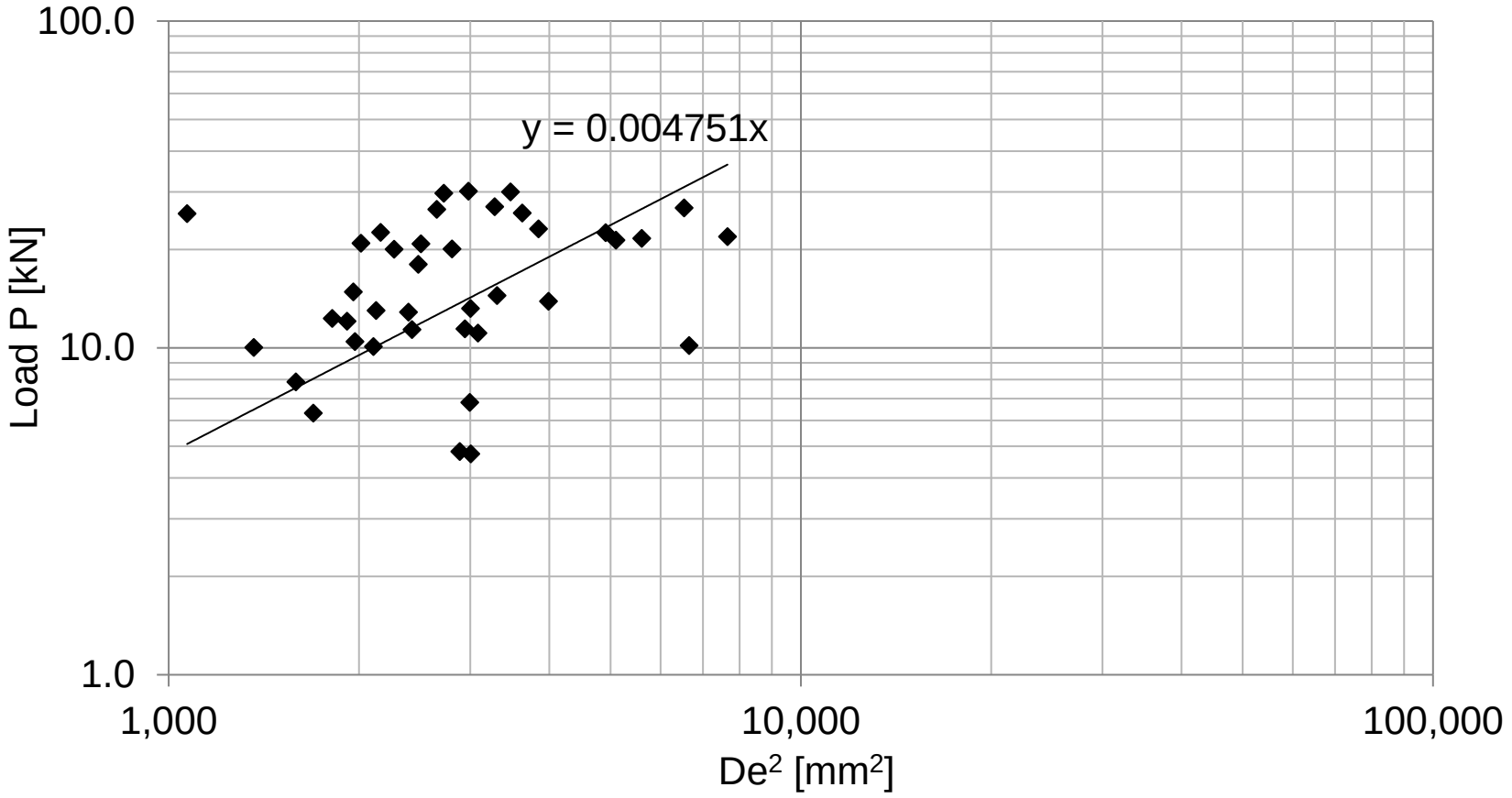

Figure D.10 Point load test results for drawpoint sample E30N taken Nov 2015

Table D.11 Point load test results for drawpoint sample F33S taken Nov 2015

Specimen #	Specific Gravity	Width 1 [mm]	Width 2 [mm]	Diameter [mm]	Load P [kN]	De^2 [mm^2]	De [mm]	Is [MPa]	Correction Factor F [MPa]	Is(50) [MPa]
3	2.52	87	70	52	7.0	5,197	72.1	1.3	1.2	1.6
4	2.65	81	74	53	7.0	5,230	72.3	1.3	1.2	1.6
7	2.90	88	77	53	9.2	5,567	74.6	1.7	1.2	2.0
9	2.70	99	85	77	11.1	9,020	95.0	1.2	1.3	1.6
13	2.89	72	68	62	15.1	5,526	74.3	2.7	1.2	3.3
17	2.58	124	131	44	7.6	7,143	84.5	1.1	1.3	1.4
21	2.65	36	33	35	0.8	1,537	39.2	0.5	0.9	0.5
23	2.81	47	46	34	13.0	2,013	44.9	6.5	1.0	6.2
24	2.48	65	42	47	1.6	3,202	56.6	0.5	1.1	0.5
25	2.69	51	58	35	16.5	2,429	49.3	6.8	1.0	6.7
26	2.63	48	50	33	4.0	2,059	45.4	2.0	1.0	1.9
30	2.48	43	51	34	1.2	2,035	45.1	0.6	1.0	0.5
31	2.70	66	79	56	9.9	5,169	71.9	1.9	1.2	2.3
32	2.73	61	73	56	21.2	4,777	69.1	4.4	1.2	5.1
34	2.49	63	63	52	0.8	4,171	64.6	0.2	1.1	0.2
39	2.46	82	88	70	0.8	7,576	87.0	0.1	1.3	0.1
1	2.73	43	41	32	8.6	1,711	41.4	5.0	0.9	4.6
6	2.71	36	32	29	8.7	1,255	35.4	7.0	0.9	6.0
7	2.76	41	41	30	13.4	1,566	39.6	8.6	0.9	7.7
12	2.67	42	44	35	2.9	1,916	43.8	1.5	0.9	1.4
16	2.45									
31	2.72	46	43	31	10.5	1,756	41.9	6.0	0.9	5.5
44	2.66	32	27	32	8.5	1,202	34.7	7.1	0.8	6.0
46	2.66	50	40	30	12.6	1,719	41.5	7.3	0.9	6.8
64	2.67	38	34	34	8.8	1,558	39.5	5.6	0.9	5.1
72	2.73	42	43	36	2.1	1,948	44.1	1.1	0.9	1.0
76	2.85	31	31	31	4.0	1,224	35.0	3.3	0.9	2.8

Specimen #	Specific Gravity	Width 1 [mm]	Width 2 [mm]	Diameter [mm]	Load P [kN]	De^2 [mm^2]	De [mm]	Is [MPa]	Correction Factor F [MPa]	Is(50) [MPa]
89	2.62	34	40	31	8.0	1,460	38.2	5.5	0.9	4.9

F33S Mean Is(50):	3.2	MPa
F33S Median Is(50)	2.3	MPa
Standard deviation	2.4	MPa
Equivalent UCS (NX 54mm Core):	55	MPa

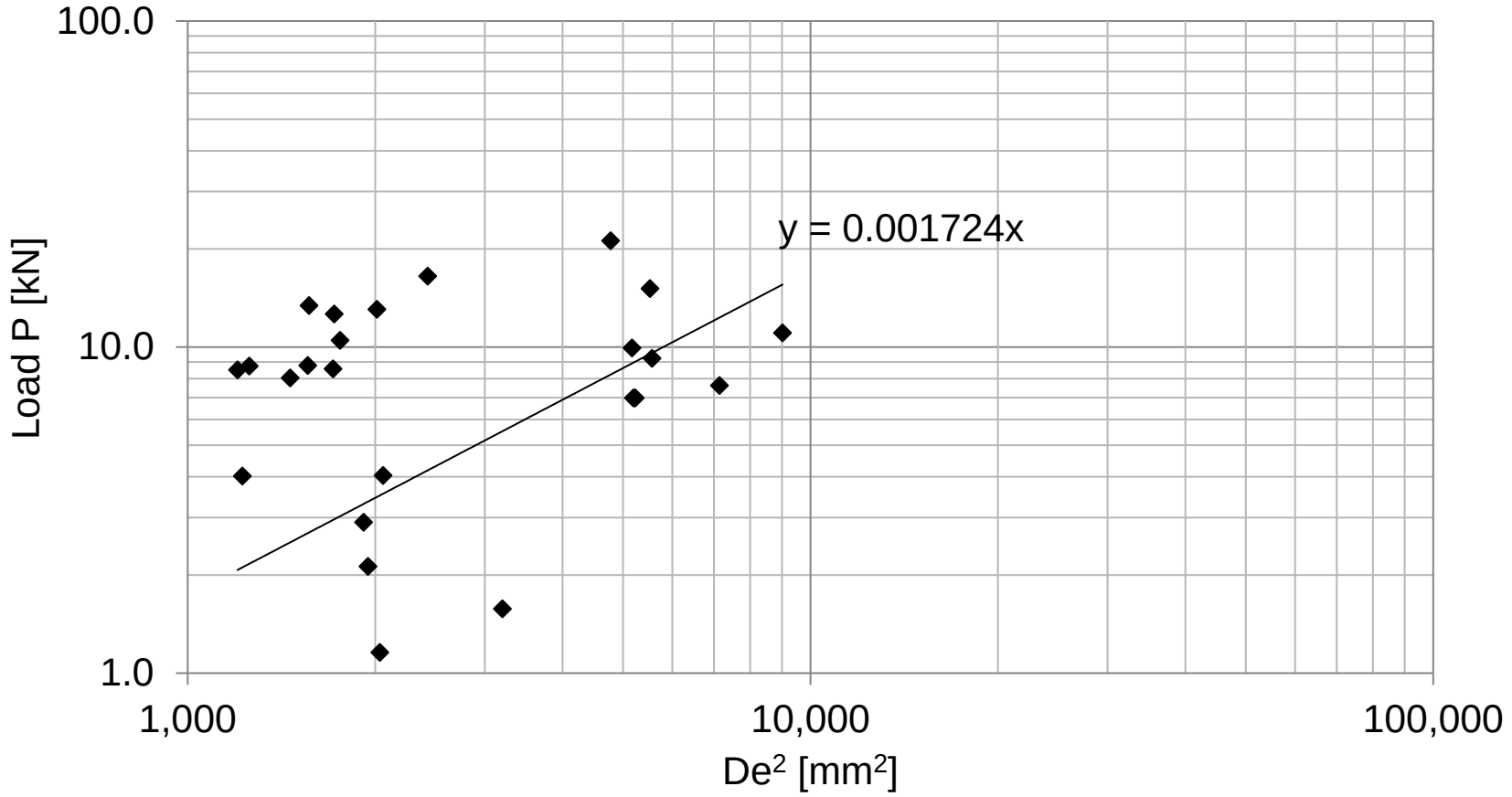

Figure D.11 Point load test results for drawpoint sample F33S taken Nov 2015

Table D.12 Point load test results for drawpoint sample G40N taken Nov 2015

Specimen #	Specific Gravity	Width 1 [mm]	Width 2 [mm]	Diameter [mm]	Load P [kN]	De^2 [mm^2]	De [mm]	Is [MPa]	Correction Factor F [MPa]	Is(50) [MPa]
4	2.54	84	79	51	15.5	5,292	72.7	2.9	1.2	3.5
6	2.65				16.4	3,441	58.7	4.8	1.1	5.1
7	2.61	59	56	47	7.5	3,748	61.2	2.0	1.1	2.2
8	2.60	63	65	46	21.3	5,407	73.5	3.9	1.2	4.7
10	2.74	76	73	57	21.3	5,407	73.5	3.9	1.2	4.7
14	2.68	62	27	53	6.5	3,003	54.8	2.2	1.0	2.3
15	2.59	68	60	42	6.0	3,422	58.5	1.8	1.1	1.9
16	2.68	65	62	56	4.3	4,528	67.3	0.9	1.1	1.1
17	2.61	78	80	56	9.8	5,633	75.1	1.7	1.2	2.1
19	2.68	63	58	40	11.1	3,081	55.5	3.6	1.0	3.8
20	2.64	77	76	39	8.2	3,799	61.6	2.2	1.1	2.4
21	2.66	75	70	37	3.7	3,415	58.4	1.1	1.1	1.2
22	2.62	113	94	52	15.7	6,853	82.8	2.3	1.3	2.9
23	2.72	136	120	62						
25	2.65	76	65	48	19.4	4,309	65.6	4.5	1.1	5.1
26	2.70									
27	2.58	68	30	43	6.8	2,683	51.8	2.5	1.0	2.6
29	2.68	77	71	41	5.6	3,863	62.2	1.5	1.1	1.6
31	2.75	38	84	41	17.8	3,184	56.4	5.6	1.1	5.9
33	2.64	73	89	48	11.1	4,950	70.4	2.2	1.2	2.6
34	2.66	103	95	46	18.7	5,798	76.1	3.2	1.2	3.9
35	2.72	55	70	44	3.6	3,501	59.2	1.0	1.1	1.1
36	2.67	39	59	44	21.4	2,745	52.4	7.8	1.0	8.0
37	2.64	95	39	56	7.4	4,777	69.1	1.5	1.2	1.8
41	2.67	23	46	39	12.9	1,713	41.4	7.5	0.9	6.9
43	2.64	22	38	39	12.9	1,490	38.6	8.7	0.9	7.7
46	2.68	23	50	31.8	9.9	1,478	38.4	6.7	0.9	6.0

Specimen #	Specific Gravity	Width 1 [mm]	Width 2 [mm]	Diameter [mm]	Load P [kN]	De^2 [mm^2]	De [mm]	Is [MPa]	Correction Factor F [MPa]	Is(50) [MPa]
47	2.72	55	13	24	6.5	1,039	32.2	6.3	0.8	5.2
48	2.57	45	51	38	1.6	2,322	48.2	0.7	1.0	0.7
50	2.67	51	55	24	3.3	1,620	40.2	2.0	0.9	1.8
51	2.71	39	50	31	7.4	1,756	41.9	4.2	0.9	3.9
52	2.63	40	63	20	9.5	1,313	36.2	7.3	0.9	6.3

G40N Mean Is(50):	3.6	MPa
G40N Median Is(50)	3.2	MPa
Standard deviation	2.1	MPa
Equivalent UCS (NX 54mm Core):	62	MPa

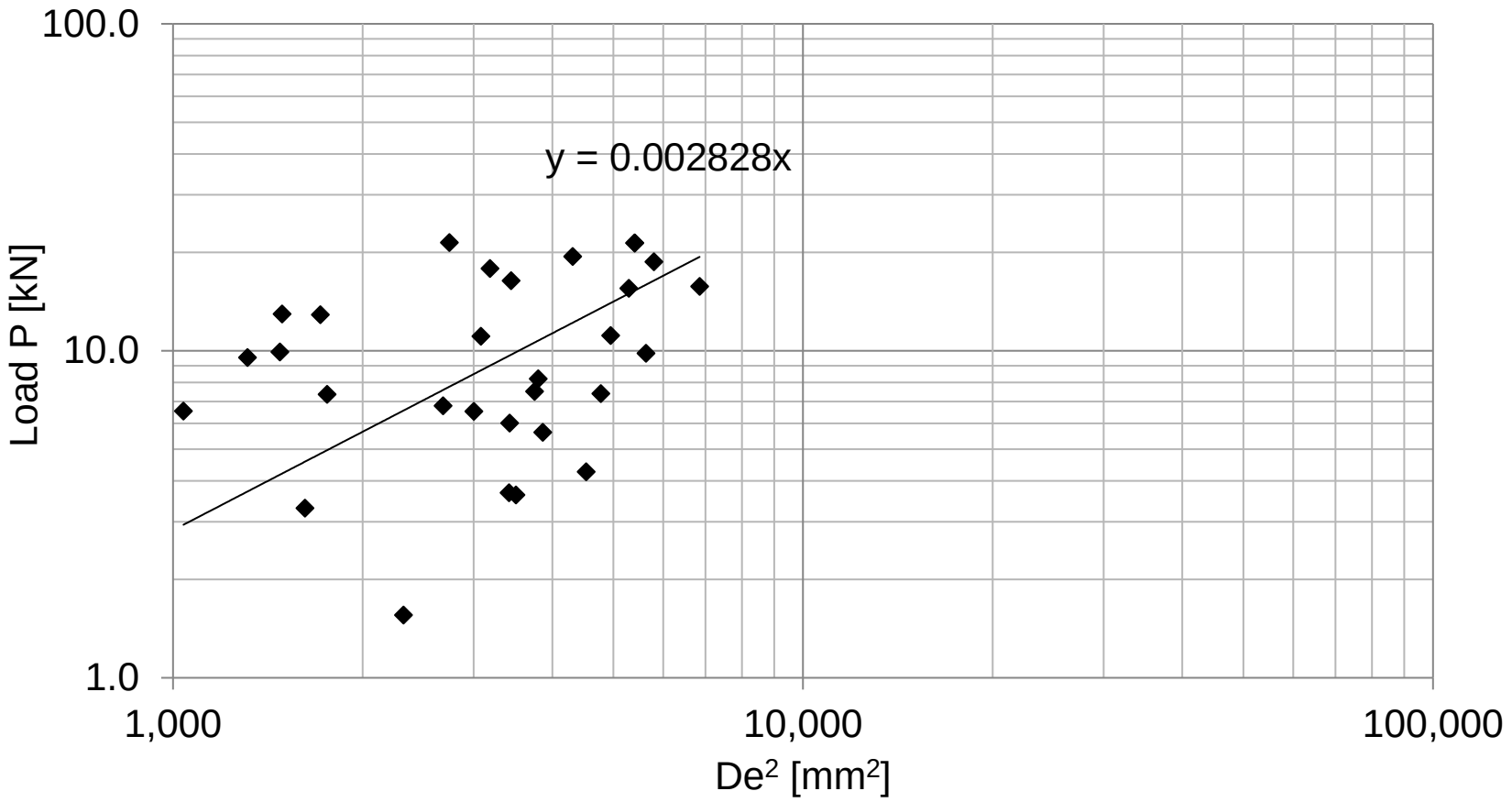

Figure D.12 Point load test results for drawpoint sample G40N taken Nov 2015

Appendix E DropWeight Test Results

In addition to standard DropWeight parameters A and b, material parameters of an alternative energy-breakage equation from the work of Shi and Kojovic (2007) were also reported:

$$t_{10} = M(1 - e^{-fmat.x^n(E_{cs}-E_{min})}) \quad \textbf{(E.1)}$$

Where t_{10} is the percentage passing $1/10^{th}$ of the feed size, M and fmat are material parameters, x is feed size, E_{cs} represents input energy, E_{min} is the energy threshold of the material and n describes the effect of feed size on breakage.

A New Afton mill feed sample was tested using twenty-one energy-size setpoints to determine material parameters M, fmat and n, shown in Table F.1. The fitted parameter n, having a value of 0.37, was used to determine unique fmat and M parameters for each New Afton geometallurgical unit, which were tested using the abbreviated DropWeight method described in Appendix B. Equation (F.1) was rearranged to estimate Ecs for different t10 and feed size values x, so that a table of energy-breakage data could be generated for use in the JKSimMet crusher model.

$$E_{cs} = \frac{\ln(1-\frac{t_{10}}{M})}{-fmat.x^n} + E_{min} \quad \textbf{(E.2)}$$

Reported DWI values were calculated using the following equation from Doll (2016)

$$DWI\ \left(\frac{kWh}{m^3}\right) = \text{p}.\frac{96.703}{(A.b)^{0.992}} \quad \textbf{(E.3)}$$

Where p is the average specific gravity of sample determined from the dry weight and apparent weight of samples after immersion in water.

Table E.1 DropWeight test results for mill feed sample collected March, 2016

Drop Weight Test Parameters for Crushers and SAG Mills

Stefan Nadolski — *New Gold / UBC Cave-to-Mill Program*

Project:	**New Gold**						**Test Date:**		**26-Jul-16**	
Deposit:	**New Afton**						**Tester:**		**Stefan Nadolski**	
Sample ID:	**Mill Feed, Collected 11 AM March 16th, 2016, Extended DropWeight Test (21 energy-size combinations)**									
Base Data										
t_1	t_{10}	E_{cs}	t_{10}	E_{cs}	t_{10}	E_{cs}	t_{10}	E_{cs}	t_{10}	E_{cs}
57.8	17.0	0.40	9.2	0.25	4.2	0.10				
41.1	35.5	0.96	9.9	0.25	4.6	0.10				
28.9	54.8	3.33	50.7	2.49	31.8	1.00	15.9	0.50	9.4	0.25
20.6	55.5	3.49	50.8	2.49	27.9	1.00	14.1	0.50	9.2	0.25
14.5	53.3	3.49	44.4	2.50	23.7	1.00	13.4	0.50	6.6	0.25
SAG/AG MILL PARAMETERS										
A:	61.3		**b:**	0.64		**A*b:**	39.2		**Ta:**	0.29
DWi (kWh/m^3):	6.98									
M:	65.2		**fmat:**	0.18		**n:**	0.37		**Emin (kWh/t):**	0.01
CRUSHER PARAMETERS										
CRUSHER APPEARANCE FUNCTION DATA										
t_{10}	t_{75}		t_{50}		t_{25}		t_4		t_2	
10	2.7		3.6		5.5		25.7		58.5	
20	5.5		7.1		11.1		46.6		83.4	
30	8.2		10.7		16.6		63.6		93.9	
POWER DATA										
	Mean Size (mm)									
	14.5		20.6		28.9		41.1		57.8	
t_{10}	**Ecs (kWh/t)**									
10	0.36		0.32		0.28		0.25		0.22	
20	0.77		0.68		0.60		0.53		0.47	
30	1.29		1.14		1.01		0.89		0.78	
DENSITY DATA										
Mean	2.75		**Std Dev**	0.07		**Max**	2.89		**Min**	2.63

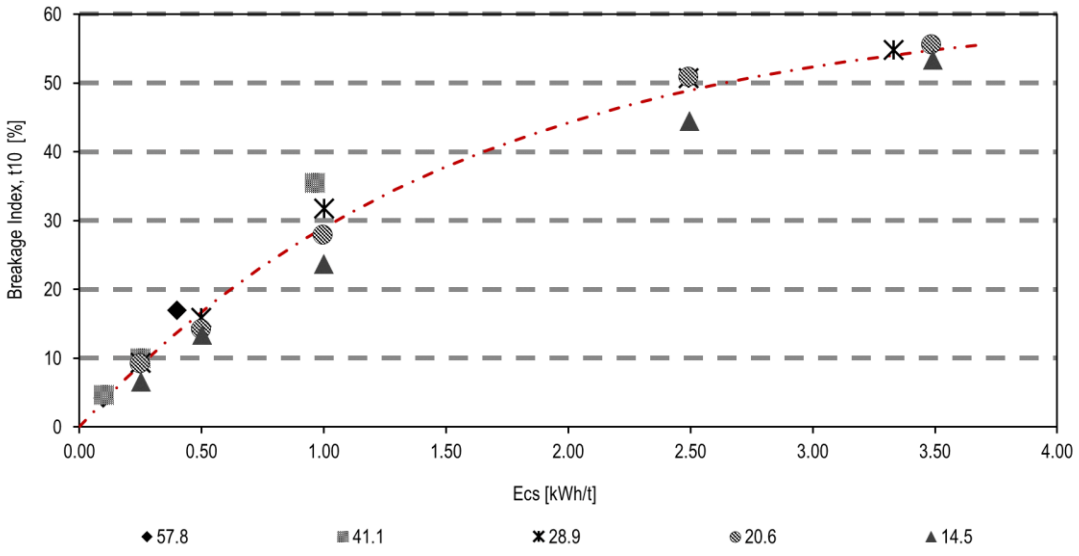

Figure E.1 Breakage index t10 and input energy with the standard A & b model

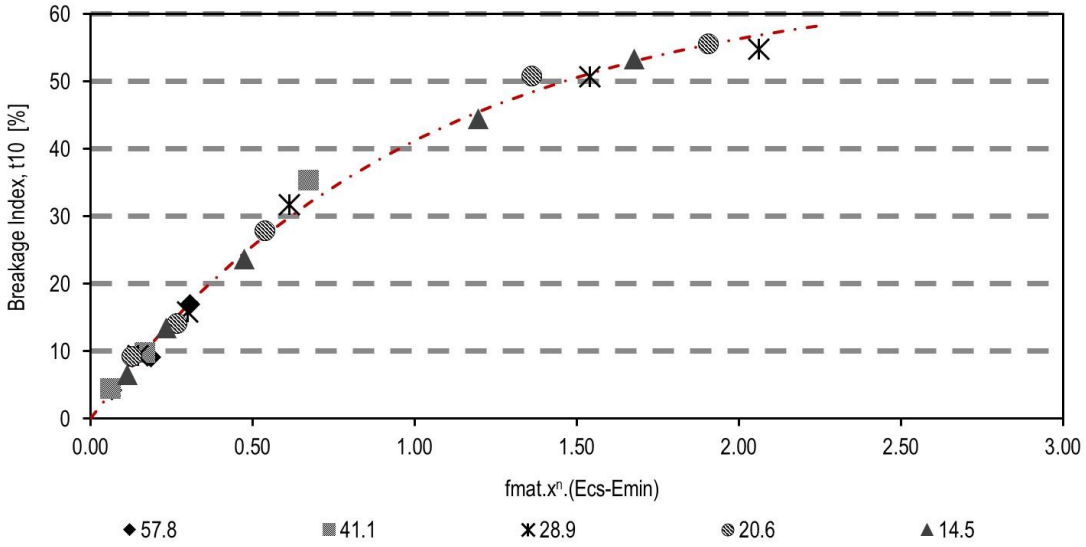

Figure E.2 Breakage index t10 and input energy and fitted M and fmat model

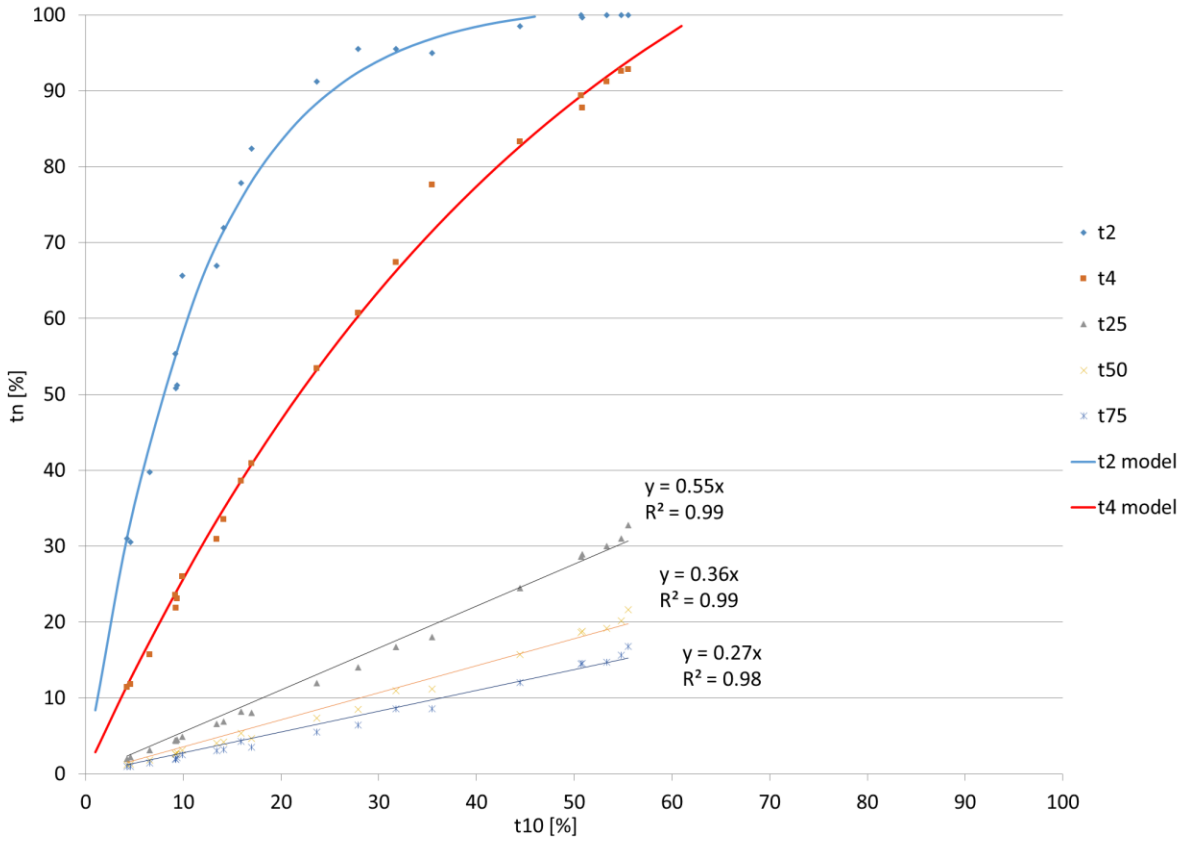

Figure E.3 Breakage index t10 and tn for mill feed (21 energy-size combinations)

Table E.2 DropWeight test results for 2015 mill feed sample, SMC method (-31.5, 26.5 mm)

Ecs, [kWh/t]	0.247	0.499	0.998	2.058	3.119
t10, [%]	9.05	14.50	27.54	47.17	55.05

Sample Designation	***Dwi*** **(kWh/m^3)**	***Dwi*** **(%)**	***Mi*** **Parameters (kWh/t)**			***A***	***b***	***SG***	***t_a***
			Mia	***Mih***	***Mic***				
New Afton 1	7.58	74	21.3	16.2	8.4	70.3	0.51	2.72	0.34

Sample Designation	**Particle Size (mm)**								
	14.5			**28.9**			**57.8**		
	t_{10} Values (%) for Given Specific Energies in kWh/t								
	10	**20**	**30**	**10**	**20**	**30**	**10**	**20**	**30**
New Afton 1	0.38	0.81	1.29	0.29	0.61	0.98	0.22	0.47	0.74

Results taken from SMC test report provided by ALS Metallurgy KM4697

Note: Abrasion results, ta, were derived by undisclosed SMC methods, which are assumed to reference drop-weight test results and specific gravity

Table E.3 DropWeight test results for drawpoint sample B13S (collected Nov, 2015)

Drop Weight Test Parameters for Crushers and SAG Mills										
							New Gold / UBC Cave-to-Mill Program			
Deposit:	**New Afton**						**Tester:**		**Stefan**	
Sample ID:	**Drawpoint Sample B13S (Collected Nov, 2015)**									
Base Data										
t_1	t_{10}	E_{cs}	t_{10}	E_{cs}	t_{10}	E_{cs}	t_{10}	E_{cs}	t_{10}	E_{cs}
28.9	57.2	2.50	48.0	1.80	36.4	1.00	19.7	0.50	9.8	0.25
SAG/FAG MILL PARAMETERS										
A:	71.5		**b:**	0.64		**A*b:**	46.1		**Ta:**	0.44
DWi (kWh/m^3):	5.82									
M:	65.0		**fmat:**	0.24		**n*:**	0.37		**Emin (kWh/t):**	0.05
						* Value from calibration sample				
CRUSHER PARAMETERS										
CRUSHER APPEARANCE FUNCTION DATA										
t_{10}	t_{75}		t_{50}		t_{25}		t_4		t_2	
10	2.7		3.6		5.5		25.7		58.5	
20	5.5		7.1		11.1		46.6		83.4	
30	8.2		10.7		16.6		63.6		93.9	
POWER DATA										
	Mean Size (mm)									
	14.5		20.6		28.9		41.1		57.8	
t_{10}	Ecs (kWh/t)									
10	0.32		0.28		0.26		0.23		0.21	
20	0.63		0.56		0.50		0.45		0.40	
30	1.02		0.90		0.80		0.71		0.64	
DENSITY DATA										
Mean	2.69		**Std Dev**	0.12		**Max**	3.22		**Min**	2.48

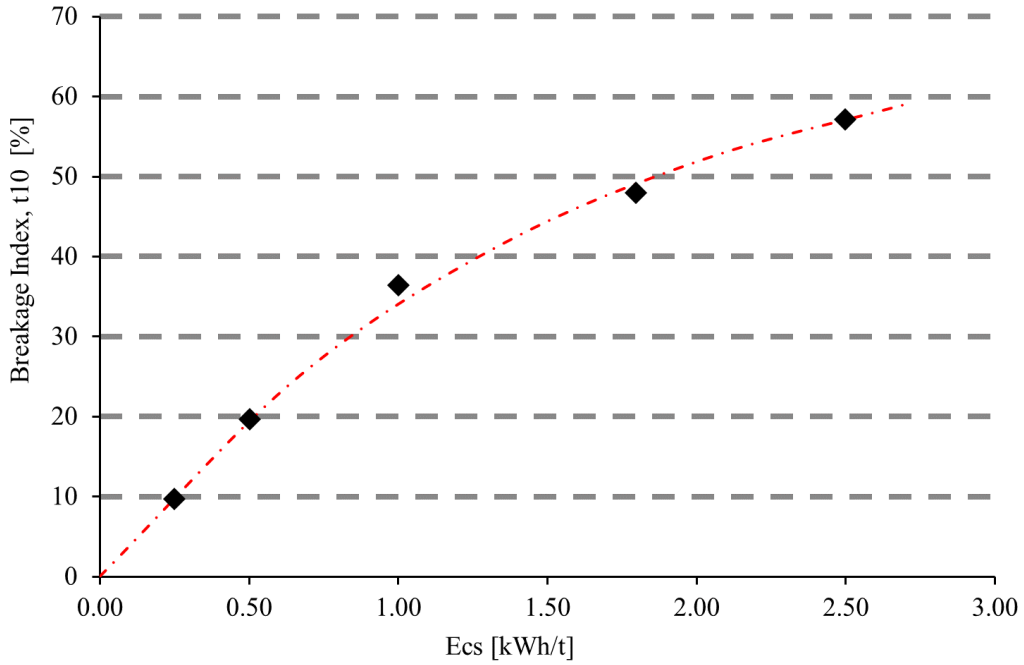

Figure E.4 Breakage index t10 and energy with fitted A & b curve for drawpoint sample B13S

Table E.4 DropWeight test results for drawpoint sample D7S (collected Nov, 2015)

Drop Weight Test Parameters for Crushers and SAG Mills										
							New Gold / UBC Cave-to-Mill Program			
Deposit:	**New Afton**						**Tester:**		**Stefan**	
Sample ID:	**Drawpoint Sample D7S (Collected Nov, 2015)**									
Base Data										
t_1	t_{10}	E_{cs}	t_{10}	E_{cs}	t_{10}	E_{cs}	t_{10}	E_{cs}	t_{10}	E_{cs}
28.9	51.9	2.43	47.7	1.80	30.4	1.00	17.9	0.50	8.4	0.25
SAG/FAG MILL PARAMETERS										
A:	73.3		**b:**	0.54		**A*b:**	39.5		**Ta:**	0.40
DWi (kWh/m^3):	6.86									
M:	65.4		**fmat:**	0.20		**n*:**	0.37		**Emin (kWh/t):**	0.05
						* Value from calibration sample				
CRUSHER PARAMETERS										
CRUSHER APPEARANCE FUNCTION DATA										
t_{10}	t_{75}		t_{50}		t_{25}		t_4		t_2	
10	2.75		3.56		5.53		25.71		58.51	
20	5.49		7.12		11.06		46.62		83.37	
30	8.24		10.68		16.59		63.61		93.93	
POWER DATA										
	Mean Size (mm)									
	14.5		20.6		28.9		41.1		57.8	
t_{10}	**Ecs (kWh/t)**									
10	0.36		0.32		0.29		0.26		0.24	
20	0.73		0.65		0.58		0.51		0.46	
30	1.19		1.06		0.94		0.83		0.74	
DENSITY DATA										
Mean	2.72		**Std Dev**	0.07		**Max**	2.86		**Min**	2.62

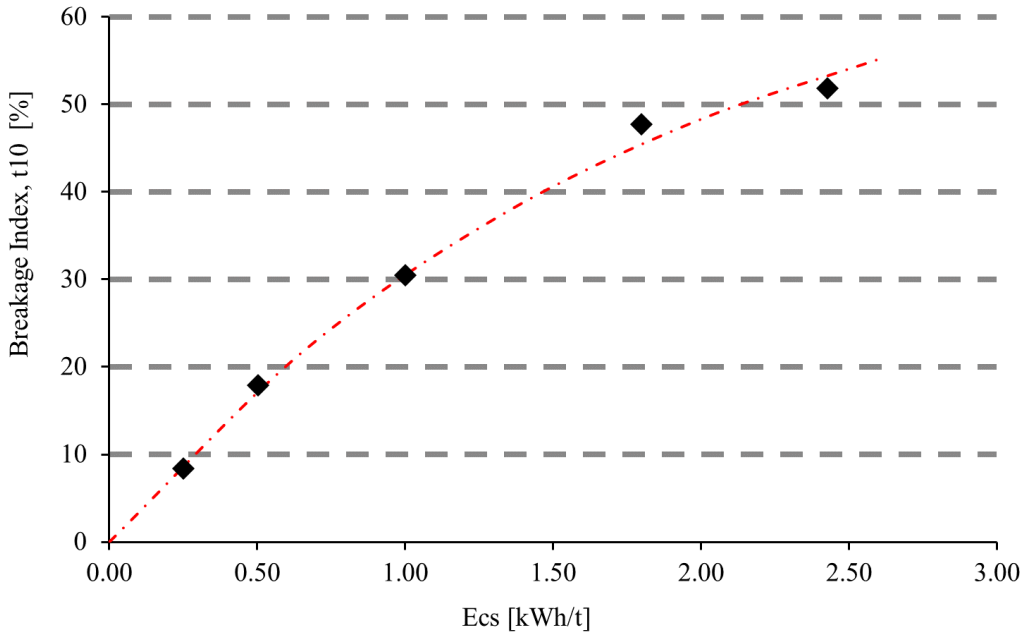

Figure E.5 Breakage index t10 and energy with fitted A & b curve for drawpoint sample D7S

Table E.5 DropWeight test results for drawpoint sample D11N (collected Nov, 2015)

Drop Weight Test Parameters for Crushers and SAG Mills										
							New Gold / UBC Cave-to-Mill Program			
Deposit:	**New Afton**						**Tester:**		**Stefan**	
Sample ID:	**Drawpoint Sample D11N (Collected Nov, 2015)**									
Base Data										
t_1	t_{10}	E_{cs}	t_{10}	E_{cs}	t_{10}	E_{cs}	t_{10}	E_{cs}	t_{10}	E_{cs}
28.9	52.9	2.40	46.7	1.80	31.4	1.00	17.9	0.50	7.7	0.25
SAG/FAG MILL PARAMETERS										
A:	77.9		**b:**	0.49		**A*b:**	38.4		**Ta:**	0.39
DWi (kWh/m^3):	6.91									
M:	64.4		**fmat:**	0.21		**n*:**	0.37		**Emin (kWh/t):**	0.08
						* Value from calibration sample				
CRUSHER PARAMETERS										
CRUSHER APPEARANCE FUNCTION DATA										
t_{10}	t_{75}		t_{50}		t_{25}		t_4		t_2	
10	2.75		3.56		5.53		25.71		58.51	
20	5.49		7.12		11.06		46.62		83.37	
30	8.24		10.68		16.59		63.61		93.93	
POWER DATA										
	Mean Size (mm)									
	14.5		20.6		28.9		41.1		57.8	
t_{10}	**Ecs (kWh/t)**									
10	0.37		0.33		0.30		0.27		0.25	
20	0.72		0.64		0.58		0.52		0.46	
30	1.16		1.03		0.92		0.82		0.73	
DENSITY DATA										
Mean	2.67		**Std Dev**	0.17		**Max**	3.02		**Min**	2.01

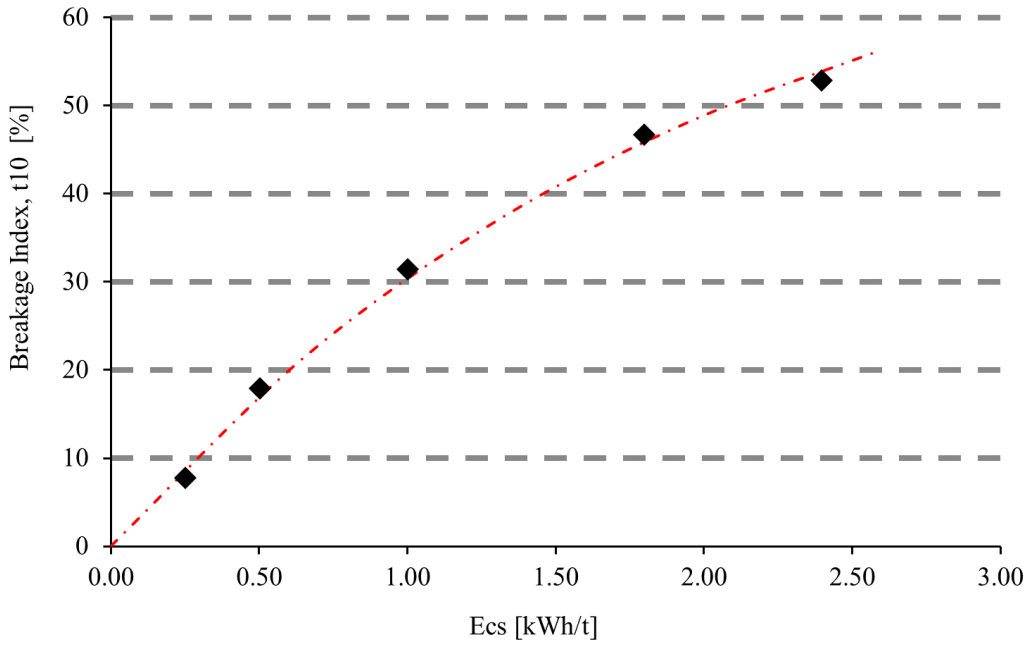

Figure E.6 Breakage index t10 and energy with fitted A & b curve for drawpoint sample D11N

Table E.6 DropWeight test results for drawpoint sample D11S (collected Nov, 2015)

Drop Weight Test Parameters for Crushers and SAG Mills										
							New Gold / UBC Cave-to-Mill Program			
Deposit:	**New Afton**						**Tester:**		**Stefan**	
Sample ID:	**Drawpoint Sample D11S (Collected Nov, 2015)**									
Base Data										
t_1	t_{10}	E_{cs}	t_{10}	E_{cs}	t_{10}	E_{cs}	t_{10}	E_{cs}	t_{10}	E_{cs}
28.9	59.3	3.14	55.0	2.50	29.1	1.00	14.1	0.50	6.8	0.25
SAG/FAG MILL PARAMETERS										
A:	90.7		**b:**	0.36		**A*b:**	32.3		**Ta:**	0.41
DWi (kWh/m^3):	8.31									
M:	87.0		**fmat:**	0.11		**n*:**	0.37		**Emin (kWh/t):**	0.01
						* Value from calibration sample				
CRUSHER PARAMETERS										
CRUSHER APPEARANCE FUNCTION DATA										
t_{10}	t_{75}		t_{50}		t_{25}		t_4		t_2	
10	2.7		3.6		5.5		25.7		58.5	
20	5.5		7.1		11.1		46.6		83.4	
30	8.2		10.7		16.6		63.6		93.9	
POWER DATA										
	Mean Size (mm)									
	14.5		20.6		28.9		41.1		57.8	
t_{10}	**Ecs (kWh/t)**									
10	0.42		0.37		0.33		0.29		0.26	
20	0.89		0.78		0.69		0.61		0.54	
30	1.43		1.26		1.11		0.98		0.87	
DENSITY DATA										
Mean	2.70		**Std Dev**	0.05		**Max**	2.81		**Min**	2.61

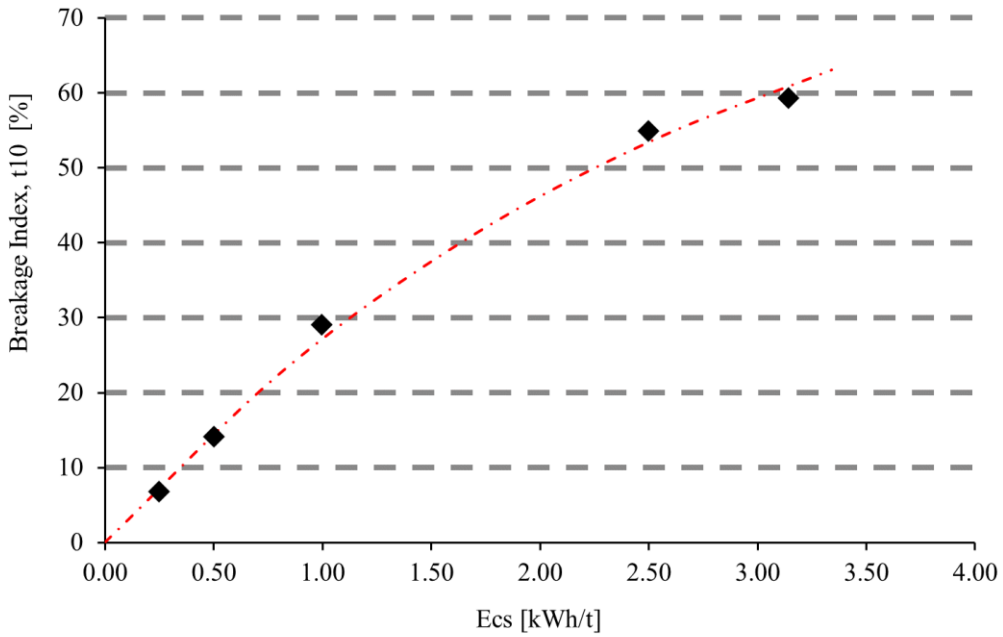

Figure E.7 Breakage index t10 and energy with fitted A & b curve for drawpoint sample D11S

Table E.7 DropWeight test results for drawpoint sample D38N (collected Nov, 2015)

Drop Weight Test Parameters for Crushers and SAG Mills										
							New Gold / UBC Cave-to-Mill Program			
Deposit:	**New Afton**									
Sample ID:	**Drawpoint Sample D38N (Collected Nov, 2015)**						**Tester:**		**Stefan**	
Base Data										
t_1	t_{10}	E_{cs}	t_{10}	E_{cs}	t_{10}	E_{cs}	t_{10}	E_{cs}	t_{10}	E_{cs}
28.9	56.5	2.40	49.3	1.80	36.9	1.00	24.6	0.50	14.3	0.25
SAG/FAG MILL PARAMETERS										
A:	60.1		**b:**	1.02		**A*b:**	61.2		**Ta:**	0.92
DWi (kWh/m^3):	4.45									
M:	60.1		**fmat:**	0.29		**n*:**	0.37		**Emin (kWh/t):**	0.00
						*** Value from calibration sample**				
CRUSHER PARAMETERS										
CRUSHER APPEARANCE FUNCTION DATA										
t_{10}	t_{75}		t_{50}		t_{25}		t_4		t_2	
10	2.7		3.6		5.5		25.7		58.5	
20	5.5		7.1		11.1		46.6		83.4	
30	8.2		10.7		16.6		63.6		93.9	
POWER DATA										
	Mean Size (mm)									
	14.5		20.6		28.9		41.1		57.8	
t_{10}	**Ecs (kWh/t)**									
10	0.23		0.20		0.18		0.16		0.14	
20	0.51		0.45		0.40		0.35		0.31	
30	0.88		0.77		0.68		0.60		0.53	
DENSITY DATA										
Mean	2.72		**Std Dev**	0.06		**Max**	2.85		**Min**	2.59

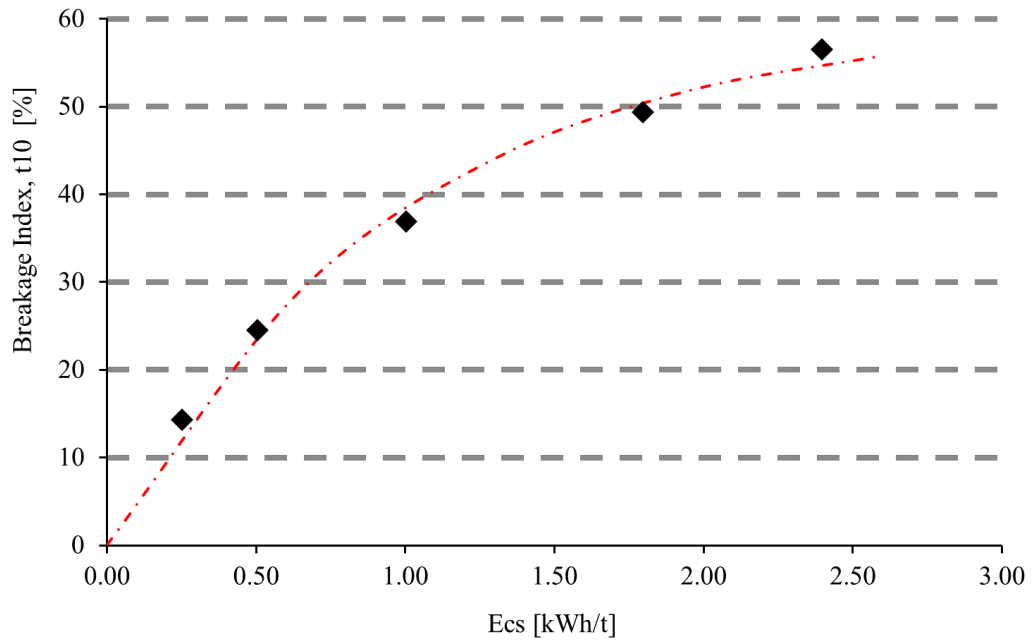

Figure E.8 Breakage index t10 and energy with fitted A & b curve for drawpoint sample D38N

Table E.8 DropWeight test results for drawpoint sample E13S (collected Nov, 2015)

Drop Weight Test Parameters for Crushers and SAG Mills										
							New Gold / UBC Cave-to-Mill Program			
Deposit:	**New Afton**						**Tester:**		**Stefan**	
Sample:	**Drawpoint Sample E13S (Collected Nov, 2015)**									
Base Data										
t_1	t_{10}	E_{cs}	t_{10}	E_{cs}	t_{10}	E_{cs}	t_{10}	E_{cs}	t_{10}	E_{cs}
28.9	51.4	2.50	44.9	1.80	28.3	1.00	16.5	0.50	6.4	0.25
SAG/FAG MILL PARAMETERS										
A:	84.3		**b:**	0.40		**A*b:**	33.5		**Ta:**	0.27
DWi (kWh/m^3):	8.08									
M:	63.9		**fmat:**	0.20		**n*:**	0.37		**Emin (kWh/t):**	0.09
						* Value from calibration sample				
CRUSHER PARAMETERS										
CRUSHER APPEARANCE FUNCTION DATA										
t_{10}	t_{75}		t_{50}		t_{25}		t_4		t_2	
10	2.7		3.6		5.5		25.7		58.5	
20	5.5		7.1		11.1		46.6		83.4	
30	8.2		10.7		16.6		63.6		93.9	
POWER DATA										
Mean Size (mm)										
	14.5		20.6		28.9		41.1		57.8	
t_{10}	**Ecs (kWh/t)**									
10	0.41		0.37		0.34		0.31		0.28	
20	0.80		0.71		0.64		0.57		0.52	
30	1.28		1.14		1.02		0.90		0.81	
DENSITY DATA										
Mean	2.72		**Std Dev**	0.07		**Max**	2.89		**Min**	2.62

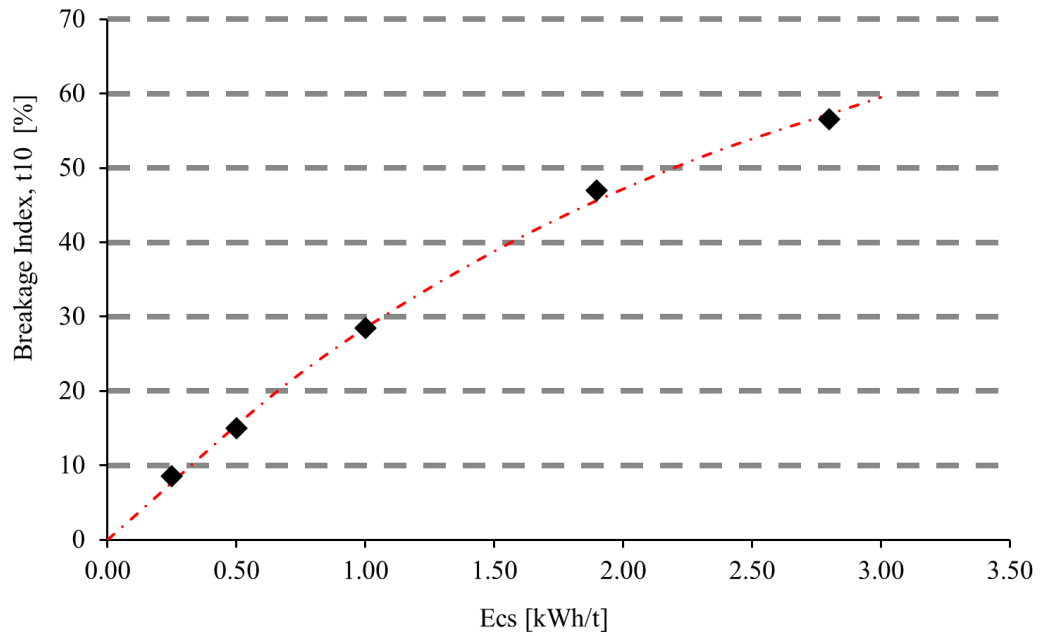

Figure E.9 Breakage index t10 and energy with fitted A & b curve for drawpoint sample E13S

Table E.9 DropWeight test results for drawpoint sample E15N (collected Nov, 2015)

Drop Weight Test Parameters for Crushers and SAG Mills										
							New Gold / UBC Cave-to-Mill Program			
Deposit:	**New Afton**						**Tester:**		**Stefan**	
Sample:	**Drawpoint Sample E15N (Collected Nov, 2015)**									
Base Data										
t_1	t_{10}	E_{cs}	t_{10}	E_{cs}	t_{10}	E_{cs}	t_{10}	E_{cs}	t_{10}	E_{cs}
28.9	51.4	2.50	44.9	1.80	28.3	1.00	16.5	0.50	6.4	0.25
SAG/FAG MILL PARAMETERS										
A:	84.3		**b:**	0.40		**A*b:**	33.5		**Ta:**	0.27
DWi (kWh/m^3):	8.08									
M:	63.9		**fmat:**	0.20		**n*:**	0.37		**Emin (kWh/t):**	0.09
						*** Value from calibration sample**				
CRUSHER PARAMETERS										
CRUSHER APPEARANCE FUNCTION DATA										
t_{10}	t_{75}		t_{50}		t_{25}		t_4		t_2	
10	2.7		3.6		5.5		25.7		58.5	
20	5.5		7.1		11.1		46.6		83.4	
30	8.2		10.7		16.6		63.6		93.9	
POWER DATA										
Mean Size (mm)										
	14.5		20.6		28.9		41.1		57.8	
t_{10}	**Ecs (kWh/t)**									
10	0.41		0.37		0.34		0.31		0.28	
20	0.80		0.71		0.64		0.57		0.52	
30	1.28		1.14		1.02		0.90		0.81	
DENSITY DATA										
Mean	2.72		**Std Dev**	0.07		**Max**	2.89		**Min**	2.62

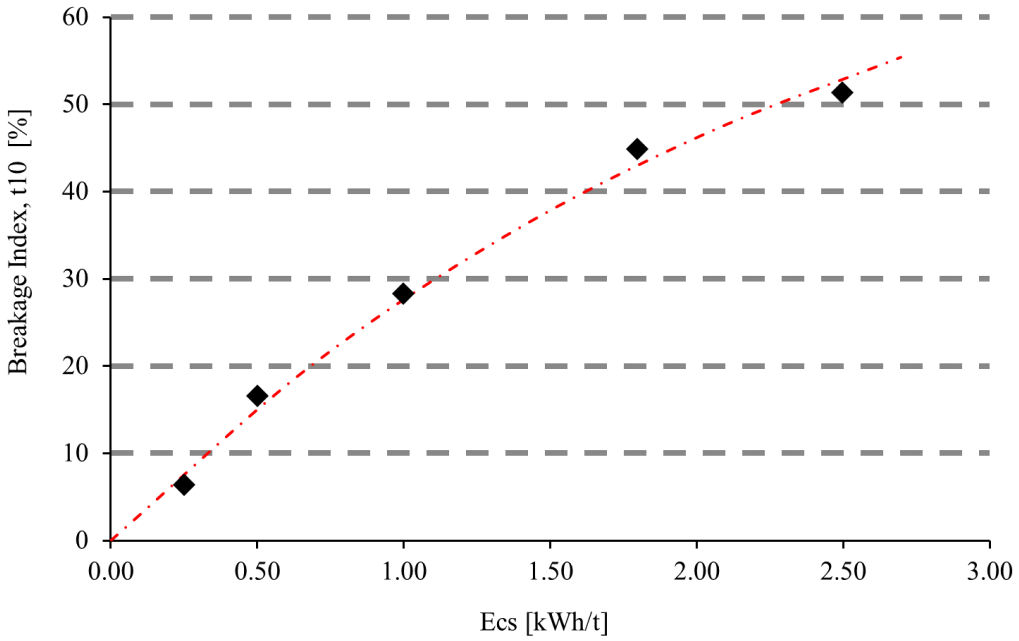

Figure E.10 Breakage index t10 and energy with fitted A & b curve for drawpoint sample E15N

Table E.10 DropWeight test results for drawpoint sample E23N (collected Nov, 2015)

Drop Weight Test Parameters for Crushers and SAG Mills										
									New Gold / UBC Cave-to-Mill Program	
Deposit:	**New Afton**						**Tester:**		**Stefan**	
Sample:	**Drawpoint Sample E23N (Collected Nov, 2015)**									
Base Data										
t_1	t_{10}	E_{cs}	t_{10}	E_{cs}	t_{10}	E_{cs}	t_{10}	E_{cs}	t_{10}	E_{cs}
28.9	56.0	2.80	48.0	2.00	32.5	1.00	15.4	0.50	7.1	0.25
SAG/FAG MILL PARAMETERS										
A:	72.3		**b:**	0.54		**A*b:**	39.2		**Ta:**	0.28
DWi (kWh/m^3):	6.91									
M:	65.6		**fmat:**	0.20		**n*:**	0.37		**Emin (kWh/t):**	0.09
						*** Value from calibration sample**				
CRUSHER PARAMETERS										
CRUSHER APPEARANCE FUNCTION DATA										
t_{10}	t_{75}		t_{50}		t_{25}		t_4		t_2	
10	2.7		3.6		5.5		25.7		58.5	
20	5.5		7.1		11.1		46.6		83.4	
30	8.2		10.7		16.6		63.6		93.9	
POWER DATA										
	Mean Size (mm)									
	14.5		20.6		28.9		41.1		57.8	
t_{10}	**Ecs (kWh/t)**									
10	0.39		0.36		0.33		0.30		0.27	
20	0.76		0.68		0.61		0.54		0.49	
30	1.21		1.07		0.96		0.85		0.76	
DENSITY DATA										
Mean	2.72		**Std Dev**	0.20		**Max**	3.71		**Min**	2.55

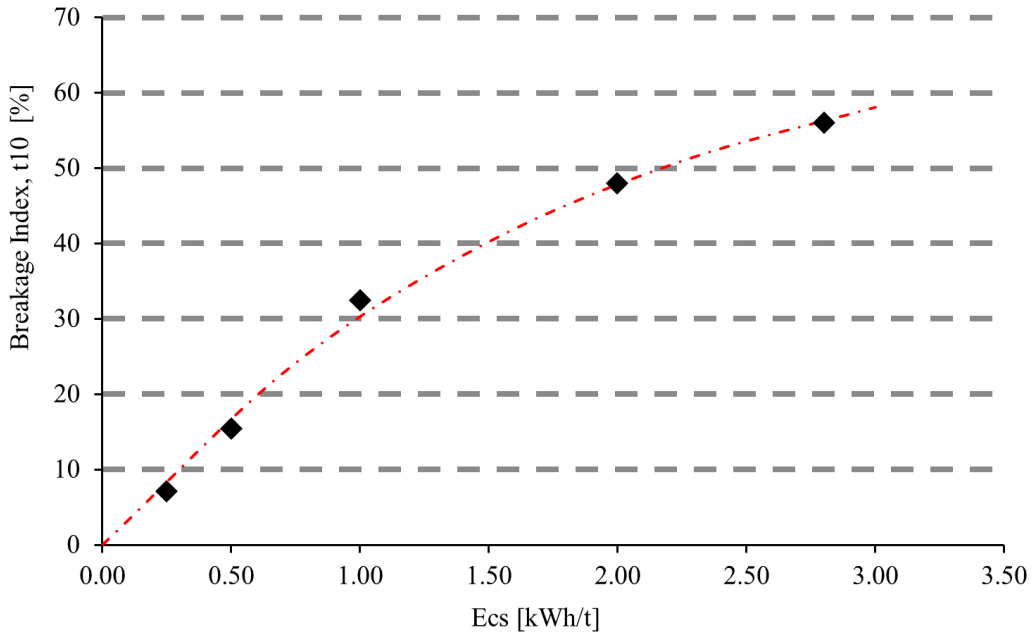

Figure E.11 Breakage index t10 and energy with fitted A & b curve for drawpoint sample E23N

Table E.11 DropWeight test results for drawpoint sample E30N (collected Nov, 2015)

Drop Weight Test Parameters for Crushers and SAG Mills										
							New Gold / UBC Cave-to-Mill Program			
Deposit:	**New Afton**						**Tester:**		**Stefan**	
Sample:	**Drawpoint Sample E30N (Collected Nov, 2015)**									
Base Data										
t_1	t_{10}	E_{cs}	t_{10}	E_{cs}	t_{10}	E_{cs}	t_{10}	E_{cs}	t_{10}	E_{cs}
28.9	50.6	2.40	47.4	1.80	30.9	1.00	17.3	0.50	8.1	0.25
SAG/FAG MILL PARAMETERS										
A:	73.1		**b:**	0.53		**A*b:**	38.8		**Ta:**	0.38
DWi (kWh/m^3):	7.08									
M:	62.5		**fmat:**	0.22		**n*:**	0.37		**Emin (kWh/t):**	0.07
						* Value from calibration sample				
CRUSHER PARAMETERS										
CRUSHER APPEARANCE FUNCTION DATA										
t_{10}	t_{75}		t_{50}		t_{25}		t_4		t_2	
10	2.7		3.6		5.5		25.7		58.5	
20	5.5		7.1		11.1		46.6		83.4	
30	8.2		10.7		16.6		63.6		93.9	
POWER DATA										
	Mean Size (mm)									
	14.5		20.6		28.9		41.1		57.8	
t_{10}	**Ecs (kWh/t)**									
10	0.37		0.33		0.30		0.27		0.25	
20	0.73		0.65		0.58		0.52		0.47	
30	1.19		1.05		0.94		0.83		0.74	
DENSITY DATA										
Mean	2.76		**Std Dev**	0.11		**Max**	2.95		**Min**	2.50

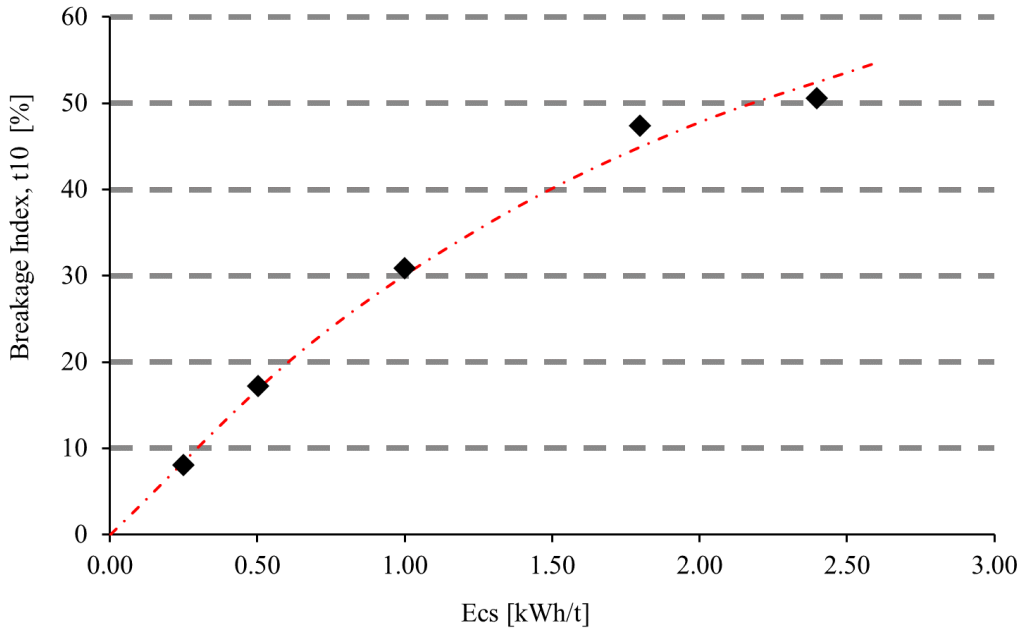

Figure E.12 Breakage index t10 and energy with fitted A & b curve for drawpoint sample E30N

Table E.12 DropWeight test results for drawpoint sample F33S (collected Nov, 2015)

Drop Weight Test Parameters for Crushers and SAG Mills										
							New Gold / UBC Cave-to-Mill Program			
Deposit:	**New Afton**						**Tester:**		**Stefan**	
Sample:	**Drawpoint Sample F33S (Collected Nov, 2015)**									
Base Data										
t_1	t_{10}	E_{cs}	t_{10}	E_{cs}	t_{10}	E_{cs}	t_{10}	E_{cs}	t_{10}	E_{cs}
28.9	56.2	2.35	52.1	1.80	39.9	1.00	26.2	0.50	15.0	0.25
SAG/FAG MILL PARAMETERS										
A:	60.1		**b:**	1.12		**A*b:**	67.5		**Ta:**	0.66
DWi (kWh/m^3):	3.91									
M:	60.1		**fmat:**	0.32		**n*:**	0.37		**Emin (kWh/t):**	0.00
						* Value from calibration sample				
CRUSHER PARAMETERS										
CRUSHER APPEARANCE FUNCTION DATA										
t_{10}	t_{75}		t_{50}		t_{25}		t_4		t_2	
10	2.7		3.6		5.5		25.72		58.51	
20	5.5		7.1		11.1		46.62		83.37	
30	8.2		10.7		16.6		63.61		93.93	
POWER DATA										
	Mean Size (mm)									
	14.5		20.6		28.9		41.1		57.8	
t_{10}	**Ecs (kWh/t)**									
10	0.21		0.18		0.16		0.14		0.13	
20	0.46		0.41		0.36		0.32		0.28	
30	0.79		0.70		0.62		0.54		0.48	
DENSITY DATA										
Mean	2.64		**Std Dev**	0.12		**Max**	2.91		**Min**	2.42

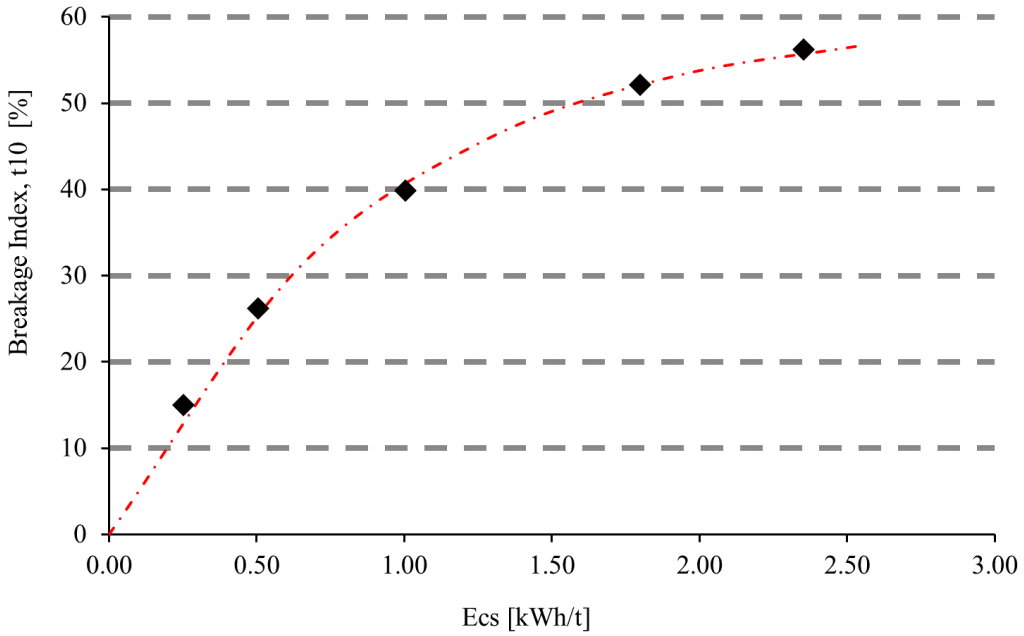

Figure E.13 Breakage index t10 and energy with fitted A & b curve for drawpoint sample F33S

Table E.13 DropWeight test results for drawpoint sample G40N (collected Nov, 2015)

Drop Weight Test Parameters for Crushers and SAG Mills										
							New Gold / UBC Cave-to-Mill Program			
Deposit:	**New Afton**						**Tester:**		**Stefan**	
Sample ID:	**Drawpoint Sample G40N (Collected Nov, 2015)**									
Base Data										
t_1	t_{10}	E_{cs}	t_{10}	E_{cs}	t_{10}	E_{cs}	t_{10}	E_{cs}	t_{10}	E_{cs}
28.9	53.2	2.20	42.8	1.60	30.9	1.00	19.3	0.50	9.9	0.25
SAG/FAG MILL PARAMETERS										
A:	75.4		**b:**	0.54		**A*b:**	40.9		**Ta:**	0.50
DWi (kWh/m^3):	6.47									
M:	72.1		**fmat:**	0.17		**n*:**	0.37		**Emin (kWh/t):**	0.00
						*** Value from calibration sample**				
CRUSHER PARAMETERS										
CRUSHER APPEARANCE FUNCTION DATA										
t_{10}	t_{75}		t_{50}		t_{25}		t_4		t_2	
10	2.7		3.6		5.5		25.7		58.5	
20	5.5		7.1		11.1		46.6		83.4	
30	8.2		10.7		16.6		63.6		93.9	
POWER DATA										
	Mean Size (mm)									
	14.5		20.6		28.9		41.1		57.8	
t_{10}	**Ecs (kWh/t)**									
10	0.33		0.29		0.26		0.22		0.20	
20	0.72		0.63		0.56		0.49		0.43	
30	1.19		1.04		0.92		0.81		0.71	
DENSITY DATA										
Mean	2.66		**Std Dev**	0.07		**Max**	2.88		**Min**	2.56

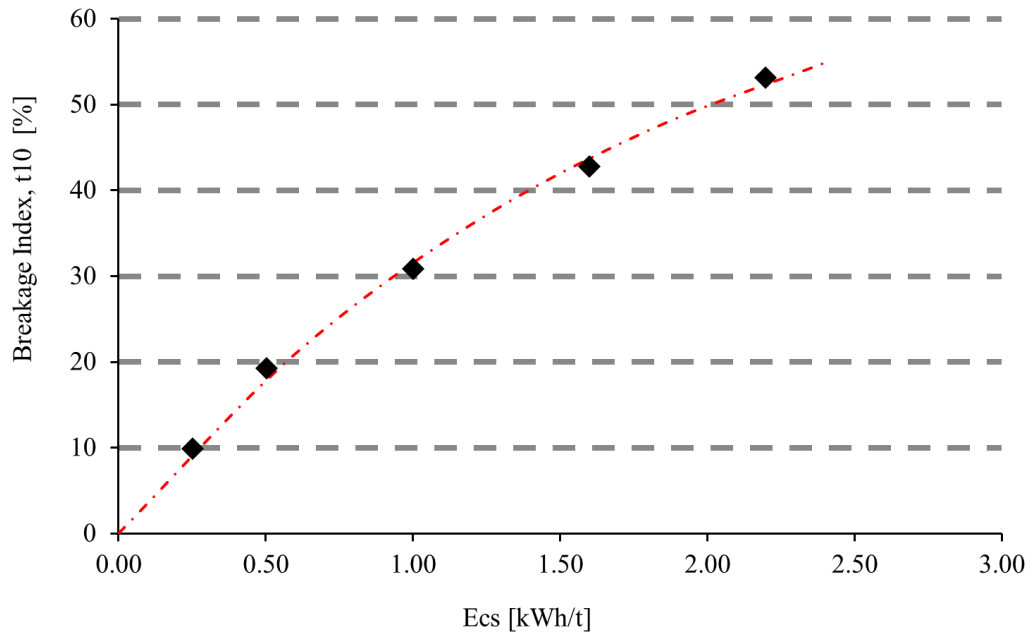

Figure E.14 Breakage index t10 and energy with fitted A & b curve for drawpoint sample G40N

Appendix F Bond Ball Mill Index Results

Table F.1 Bond ball mill work index test results for mill feed sample collected March, 2016

BOND BALL GRINDABILITY TEST New Afton Mill Feed (March 2016)

Weight of 700 ml Sample : 1379.5 g Aperture Test Sieve : 106µm

1/3.5 of Sample Weight : 394.1 g Percent Undersize : 17.6%

Cycle	Weight of New Feed	Number of Revolutions	Weight of Undersize			
			Product	Feed	Net Product	Net/Rev
1	1379.5	200	362.4	242.4	120.0	0.60
2	362.4	551	538.5	63.7	474.8	0.86
3	538.5	347	421.2	94.6	326.6	0.94
4	421.2	341	409.9	74.0	335.9	0.99
5	409.9	327	389.8	72.0	317.8	0.97
6	389.8	335	396.0	68.5	327.5	0.98

BOND WORK INDEX FORMULA

$$Wi = (44.5 \times 1.102) / (Pi^{.23} \times Gpb^{.82} \times (10/\sqrt{P} - 10/\sqrt{F}))$$

Pi = Sieve Size Tested.	106 µm
Gbp = Net undersize produced per revolution of mill.	0.98 g
P = 80% Passing size of test product.	78 µm
F = 80% Passing size of test feed.	2436 µm

BOND BALL WORK INDEX (Wi) 18.4 kw-hr/tonne

BOND BALL SCREEN ANALYSIS

Particle Size		Feed to Cycle 1			Equilibrium Cycle Undersize		
mesh	µm	Weight (g) Retained	Weight % Retained	Cumulative % Passing	Weight (g) Retained	Weight % Retained	Cumulative % Passing
6 Mesh	3360	9.50	1.94	98.1	-	-	-
7 Mesh	2800	42.80	8.75	89.3	-	-	-
8 Mesh	2360	55.20	11.29	78.0	-	-	-
9 Mesh	2000	38.20	7.81	70.2	-	-	-
10 Mesh	1700	40.00	8.18	62.0	-	-	-
12 Mesh	1400	35.40	7.24	54.8	-	-	-
14 Mesh	1180	24.70	5.05	49.7	-	-	-
20 Mesh	850	38.80	7.94	41.8	-	-	-
28 Mesh	600	31.10	6.36	35.4	-	-	-
35 Mesh	425	24.30	4.97	30.5	-	-	-
48 Mesh	300	19.20	3.93	26.5	-	-	-
65 Mesh	212	16.20	3.31	23.2	-	-	-
100 Mesh	150	15.40	3.15	20.1	-	-	-
150 Mesh	106	12.20	2.50	17.6	2.00	1.99	98.0
170 Mesh	90	-	-	-	9.00	8.94	89.1
200 Mesh	75	-	-	-	11.80	11.72	77.4
270 Mesh	53	-	-	-	13.30	13.21	64.2
325 Mesh	45	-	-	-	6.50	6.45	57.7
400 Mesh	38	-	-	-	5.10	5.06	52.6
TOTAL		488.9	100.00	**	100.7	100.00	**
		K80 = 2436µm			**K80 = 78µm**		

Table F.2 Bond ball mill work index test results for mill feed sample collected March, 2015

BOND BALL GRINDABILITY TEST New Afton Mill Feed (March 3rd, 2015)

Weight of 700 ml Sample : 1337 g Aperture Test Sieve : 180µm

1/3.5 of Sample Weight : 382.0 g Percent Undersize : 14.6%

Cycle	Weight of New Feed	Number of Revolutions	Weight of Undersize			
			Product	Feed	Net Product	Net/Rev
1	1336.5	100	329.8	195.7	134.1	1.34
2	329.8	249	337.1	48.3	288.8	1.16
3	337.1	286	389.5	49.4	340.1	1.19
4	389.5	273	387.2	57.0	330.2	1.21
5	387.2	269	390.0	56.7	333.3	1.24
6	390.0	262	389.0	57.1	331.9	1.265
7	389.0	257	381.3	57.0	324.3	1.263
8	381.3	258	382.0	55.8	326.2	1.263

BOND WORK INDEX FORMULA

$$Wi = (44.5 \times 1.102) / (Pi^{.23} \times Gpb^{.82} \times (10/\sqrt{P} - 10/\sqrt{F}))$$

Pi = Sieve Size Tested.	180 µm
Gbp = Net undersize produced per revolution of mill.	1.26 g
P = 80% Passing size of test product.	134 µm
F = 80% Passing size of test feed.	2147 µm

BOND BALL WORK INDEX (Wi) 18.9 kw-hr/tonne

BOND BALL SCREEN ANALYSIS

Particle Size		Feed to Cycle 1			Equilibrium Cycle Undersize		
mesh	µm	Weight (g) Retained	Weight % Retained	Cumulative % Passing	Weight (g) Retained	Weight % Retained	Cumulative % Passing
6 Mesh	3360	0.00	0.00	100.0	-	-	-
7 Mesh	2800	40.70	3.50	96.5	-	-	-
9 Mesh	2000	237.60	20.42	76.1	-	-	-
12 Mesh	1400	219.30	18.85	57.2	-	-	-
16 Mesh	1000	145.80	12.53	44.7	-	-	-
24 Mesh	710	103.30	8.88	35.8	-	-	-
32 Mesh	500	85.40	7.34	28.5	-	-	-
42 Mesh	355	65.50	5.63	22.9	-	-	-
60 Mesh	250	52.70	4.53	18.3	-	-	-
80 Mesh	180	43.00	3.70	14.6	0.00	0.00	100.0
100 Mesh	150	-	-	-	39.80	13.46	86.5
115 Mesh	125	-	-	-	32.20	10.89	75.7
170 Mesh	90	-	-	-	42.00	14.20	61.4
250 Mesh	63	-	-	-	32.50	10.99	50.5
325 Mesh	45	-	-	-	23.20	7.85	42.6
	Pan	170.40	14.64	-			
		-	-	-			
		-	-	-			
		-	-	-			
		-			126	42.61	
TOTAL		1163.7	100.00	**	295.7	100.00	**
		K80 = 2147µm			**K80 = 134µm**		

Table F.3 Bond ball mill work index test results for drawpoint sample B13S collected Nov, 2015

BOND BALL GRINDABILITY TEST B13S Drawpoint sample (Nov 2015)

Weight of 700 ml Sample : 1277 g Aperture Test Sieve : 106µm
1/3.5 of Sample Weight : 364.9 g Percent Undersize : 11.4%

Cycle	Weight of New Feed	Number of Revolutions	Weight of Undersize			
			Product	Feed	Net Product	Net/Rev
1	1277.0	200	252.9	145.4	107.5	0.54
2	252.9	625	542.2	28.8	513.4	0.82
3	542.2	369	414.9	61.8	353.1	0.96
4	414.9	332	363.7	47.3	316.4	0.95
5	363.7	339	366.8	41.4	325.4	0.96
6	366.8	337	363.2	41.8	321.4	0.95

BOND WORK INDEX FORMULA

$Wi = (44.5 \times 1.102) / (Pi^{.23} \times Gpb^{.82} \times (10/\sqrt{P} - 10/\sqrt{F}))$

Pi = Sieve Size Tested. 106 µm
Gbp = Net undersize produced per revolution of mill. 0.96 g
P = 80% Passing size of test product. 79 µm
F = 80% Passing size of test feed. 2604 µm

BOND BALL WORK INDEX (Wi) 18.8 kw-hr/tonne

BOND BALL SCREEN ANALYSIS

Particle Size		Feed to Cycle 1			Equilibrium Cycle Undersize		
mesh	µm	Weight (g) Retained	Weight % Retained	Cumulative % Passing	Weight (g) Retained	Weight % Retained	Cumulative % Passing
6 Mesh	3360	34.60	6.82	93.2	-	-	-
7 Mesh	2800	40.60	8.00	85.2	-	-	-
8 Mesh	2360	59.50	11.72	73.5	-	-	-
9 Mesh	2000	42.30	8.33	65.1	-	-	-
10 Mesh	1700	42.80	8.43	56.7	-	-	-
12 Mesh	1400	38.40	7.57	49.1	-	-	-
14 Mesh	1180	26.50	5.22	43.9	-	-	-
20 Mesh	850	42.20	8.32	35.6	-	-	-
28 Mesh	600	33.70	6.64	28.9	-	-	-
35 Mesh	425	25.90	5.10	23.8	-	-	-
48 Mesh	300	19.60	3.86	20.0	-	-	-
65 Mesh	212	16.50	3.25	16.7	-	-	-
100 Mesh	150	15.00	2.96	13.8	-	-	-
150 Mesh	106	12.10	2.38	11.4	3.40	3.51	96.5
170 Mesh	90	-	-	-	7.90	8.16	88.3
200 Mesh	75	-	-	-	11.20	11.57	76.8
270 Mesh	53	-	-	-	14.60	15.08	61.7
325 Mesh	45	-	-	-	7.40	7.64	54.0
400 Mesh	38	-	-	-	6.30	6.51	47.5
TOTAL		507.5	100.00	**	96.8	100.00	**
		K80 = 2604µm			**K80 = 79µm**		

Table F.4 Bond ball mill work index test results for drawpoint sample D7S collected Nov, 2015

BOND BALL GRINDABILITY TEST D7S Drawpoint sample (Nov 2015)

Weight of 700 ml Sample : 1252.9 g Aperture Test Sieve : 106µm
1/3.5 of Sample Weight : 358.0 g Percent Undersize : 9.7%

Cycle	Weight of New Feed	Number of Revolutions	Weight of Undersize			
			Product	Feed	Net Product	Net/Rev
1	1252.9	200	247.7	121.4	126.3	0.63
2	247.7	529	478.9	24.0	454.9	0.86
3	478.9	362	395.7	46.4	349.3	0.96
4	395.7	331	364.7	38.3	326.4	0.98
5	364.7	328	362.4	35.3	327.1	1.00
6	362.4	323	360.6	35.1	325.5	1.01
7	360.6	321	358.6	34.9	323.7	1.01

BOND WORK INDEX FORMULA

$Wi = (44.5 \times 1.102) / (Pi^{.23} \times Gpb^{.82} \times (10/\sqrt{P} - 10/\sqrt{F}))$

Pi = Sieve Size Tested. 106 µm
Gbp = Net undersize produced per revolution of mill. 1.00 g
P = 80% Passing size of test product. 80 µm
F = 80% Passing size of test feed. 2764 µm

BOND BALL WORK INDEX (Wi) 18.0 kw-hr/tonne

BOND BALL SCREEN ANALYSIS

Particle Size		Feed to Cycle 1			Equilibrium Cycle Undersize		
mesh	µm	Weight (g) Retained	Weight % Retained	Cumulative % Passing	Weight (g) Retained	Weight % Retained	Cumulative % Passing
6 Mesh	3360	43.60	9.08	90.9	-	-	-
7 Mesh	2800	47.60	9.92	81.0	-	-	-
8 Mesh	2360	59.20	12.33	68.7	-	-	-
9 Mesh	2000	41.00	8.54	60.1	-	-	-
10 Mesh	1700	43.90	9.15	51.0	-	-	-
12 Mesh	1400	35.30	7.35	43.6	-	-	-
14 Mesh	1180	24.30	5.06	38.6	-	-	-
20 Mesh	850	36.90	7.69	30.9	-	-	-
28 Mesh	600	28.80	6.00	24.9	-	-	-
35 Mesh	425	21.70	4.52	20.4	-	-	-
48 Mesh	300	16.50	3.44	16.9	-	-	-
65 Mesh	212	13.70	2.85	14.1	-	-	-
100 Mesh	150	11.90	2.48	11.6	-	-	-
150 Mesh	106	9.10	1.90	9.7	2.40	2.22	97.8
170 Mesh	90	-	-	-	10.70	9.89	87.9
200 Mesh	75	-	-	-	12.60	11.65	76.2
270 Mesh	53	-	-	-	14.40	13.31	62.9
325 Mesh	45	-	-	-	7.00	6.47	56.5
400 Mesh	38	-	-	-	5.50	5.08	51.4
TOTAL		480.0	100.00	**	108.2	100.00	**
		K80 = 2764µm			**K80 = 80µm**		

Table F.5 Bond ball mill work index test results for drawpoint sample D11N collected Nov, 2015

BOND BALL GRINDABILITY TEST D11N Drawpoint sample (Nov 2015)

Weight of 700 ml Sample : 1216 g Aperture Test Sieve : 106µm

1/3.5 of Sample Weight : 347.4 g Percent Undersize : 9.0%

Cycle	Weight of New Feed	Number of Revolutions	Weight of Undersize			
			Product	Feed	Net Product	Net/Rev
1	1216.0	200	210.5	109.4	101.1	0.51
2	210.5	650	545.2	18.9	526.3	0.81
3	545.2	368	404.9	49.0	355.9	0.97
4	404.9	322	354.9	36.4	318.5	0.99
5	354.9	319	348.5	31.9	316.6	0.99
6	348.5	318	343.0	31.3	311.7	0.98

BOND WORK INDEX FORMULA

$$Wi = (44.5 \times 1.102) / (Pi^{.23} \times Gpb^{.82} \times (10/\sqrt{P} - 10/\sqrt{F}))$$

Pi = Sieve Size Tested. 106 µm

Gbp = Net undersize produced per revolution of mill. 0.99 g

P = 80% Passing size of test product. 80 µm

F = 80% Passing size of test feed. 2645 µm

BOND BALL WORK INDEX (Wi) 18.4 kw-hr/tonne

BOND BALL SCREEN ANALYSIS

Particle Size		Feed to Cycle 1			Equilibrium Cycle Undersize		
mesh	µm	Weight (g) Retained	Weight % Retained	Cumulative % Passing	Weight (g) Retained	Weight % Retained	Cumulative % Passing
6 Mesh	3360	33.50	6.54	93.5	-	-	-
7 Mesh	2800	47.00	9.17	84.3	-	-	-
8 Mesh	2360	62.80	12.25	72.0	-	-	-
9 Mesh	2000	49.10	9.58	62.5	-	-	-
10 Mesh	1700	48.60	9.48	53.0	-	-	-
12 Mesh	1400	42.20	8.23	44.7	-	-	-
14 Mesh	1180	30.00	5.85	38.9	-	-	-
20 Mesh	850	45.60	8.90	30.0	-	-	-
28 Mesh	600	34.20	6.67	23.3	-	-	-
35 Mesh	425	24.00	4.68	18.6	-	-	-
48 Mesh	300	16.80	3.28	15.4	-	-	-
65 Mesh	212	13.20	2.58	12.8	-	-	-
100 Mesh	150	11.00	2.15	10.6	-	-	-
150 Mesh	106	8.40	1.64	9.0	3.50	3.48	96.5
170 Mesh	90	-	-	-	9.00	8.94	87.6
200 Mesh	75	-	-	-	11.70	11.62	76.0
270 Mesh	53	-	-	-	13.90	13.80	62.2
325 Mesh	45	-	-	-	6.30	6.26	55.9
400 Mesh	38	-	-	-	5.10	5.06	50.8
TOTAL		512.5	100.00	**	100.7	100.00	**
		K80 = 2645µm			**K80 = 80µm**		

Table F.6 Bond ball mill work index test results for drawpoint sample D11S collected Nov, 2015

BOND BALL GRINDABILITY TEST D11S Drawpoint sample (Nov 2015)

Weight of 700 ml Sample : 1274.7 g Aperture Test Sieve : 106µm

1/3.5 of Sample Weight : 364.2 g Percent Undersize : 10.2%

Cycle	Weight of New Feed	Number of Revolutions	Weight of Undersize			
			Product	Feed	Net Product	Net/Rev
1	1274.7	200	242.9	129.6	113.3	0.57
2	242.9	599	487.4	24.7	462.7	0.77
3	487.4	407	408.8	49.5	359.3	0.88
4	408.8	366	375.0	41.6	333.4	0.91
5	375.0	358	366.5	38.1	328.4	0.92
6	366.5	356	368.4	37.3	331.1	0.93
7	368.4	352	367.2	37.4	329.8	0.94
8	367.2	348	362.1	37.3	324.8	0.93

BOND WORK INDEX FORMULA

$Wi = (44.5 \times 1.102) / (Pi^{.23} \times Gpb^{.82} \times (10/\sqrt{P} - 10/\sqrt{F}))$

Pi = Sieve Size Tested. 106 µm
Gbp = Net undersize produced per revolution of mill. 0.93 g
P = 80% Passing size of test product. 81 µm
F = 80% Passing size of test feed. 2701 µm

BOND BALL WORK INDEX (Wi) 19.3 kw-hr/tonne

BOND BALL SCREEN ANALYSIS

Particle Size		Feed to Cycle 1			Equilibrium Cycle Undersize		
mesh	µm	Weight (g) Retained	Weight % Retained	Cumulative % Passing	Weight (g) Retained	Weight % Retained	Cumulative % Passing
6 Mesh	3360	38.60	7.96	92.0	-	-	-
7 Mesh	2800	45.10	9.30	82.7	-	-	-
8 Mesh	2360	59.50	12.27	70.5	-	-	-
9 Mesh	2000	41.50	8.56	61.9	-	-	-
10 Mesh	1700	40.60	8.37	53.5	-	-	-
12 Mesh	1400	35.40	7.30	46.2	-	-	-
14 Mesh	1180	24.70	5.09	41.2	-	-	-
20 Mesh	850	38.50	7.94	33.2	-	-	-
28 Mesh	600	31.30	6.45	26.8	-	-	-
35 Mesh	425	23.90	4.93	21.8	-	-	-
48 Mesh	300	17.90	3.69	18.1	-	-	-
65 Mesh	212	15.10	3.11	15.0	-	-	-
100 Mesh	150	13.20	2.72	12.3	-	-	-
150 Mesh	106	10.40	2.14	10.2	3.50	3.28	96.7
170 Mesh	90	-	-	-	10.00	9.37	87.3
200 Mesh	75	-	-	-	12.80	12.00	75.4
270 Mesh	53	-	-	-	14.30	13.40	61.9
325 Mesh	45	-	-	-	7.10	6.65	55.3
400 Mesh	38	-	-	-	5.70	5.34	50.0
TOTAL		485.0	100.00	**	106.7	100.00	**
		K80 = 2701µm			**K80 = 81µm**		

Table F.7 Bond ball mill work index test results for drawpoint sample D38N collected Nov, 2015

BOND BALL GRINDABILITY TEST D38N Drawpoint sample (Nov 2015)

Weight of 700 ml Sample : 1282 g Aperture Test Sieve : 106µm
1/3.5 of Sample Weight : 366.3 g Percent Undersize : 11.2%

Cycle	Weight of New Feed	Number of Revolutions	Weight of Undersize			
			Product	Feed	Net Product	Net/Rev
1	1282.0	200	254.5	144.0	110.5	0.55
2	254.5	611	536.1	28.6	507.5	0.83
3	536.1	369	416.1	60.2	355.9	0.97
4	416.1	331	371.2	46.7	324.5	0.98
5	371.2	331	365.9	41.7	324.2	0.98
6	365.9	332	368.5	41.1	327.4	0.99

BOND WORK INDEX FORMULA

$$Wi = (44.5 \times 1.102) / (Pi^{.23} \times Gpb^{.82} \times (10/\sqrt{P} - 10/\sqrt{F}))$$

Pi = Sieve Size Tested. 106 µm
Gbp = Net undersize produced per revolution of mill. 0.98 g
P = 80% Passing size of test product. 81 µm
F = 80% Passing size of test feed. 2606 µm

BOND BALL WORK INDEX (Wi) 18.6 kw-hr/tonne

BOND BALL SCREEN ANALYSIS

Particle Size		Feed to Cycle 1			Equilibrium Cycle Undersize		
mesh	µm	Weight (g) Retained	Weight % Retained	Cumulative % Passing	Weight (g) Retained	Weight % Retained	Cumulative % Passing
6 Mesh	3360	30.10	6.23	93.8	-	-	-
7 Mesh	2800	40.60	8.40	85.4	-	-	-
8 Mesh	2360	59.10	12.22	73.2	-	-	-
9 Mesh	2000	38.60	7.98	65.2	-	-	-
10 Mesh	1700	44.20	9.14	56.0	-	-	-
12 Mesh	1400	36.80	7.61	48.4	-	-	-
14 Mesh	1180	25.90	5.36	43.1	-	-	-
20 Mesh	850	40.00	8.27	34.8	-	-	-
28 Mesh	600	31.80	6.58	28.2	-	-	-
35 Mesh	425	23.90	4.94	23.3	-	-	-
48 Mesh	300	18.20	3.76	19.5	-	-	-
65 Mesh	212	15.40	3.19	16.3	-	-	-
100 Mesh	150	13.80	2.85	13.5	-	-	-
150 Mesh	106	10.80	2.23	11.2	2.60	2.39	97.6
170 Mesh	90	-	-	-	11.00	10.09	87.5
200 Mesh	75	-	-	-	13.20	12.11	75.4
270 Mesh	53	-	-	-	14.90	13.67	61.7
325 Mesh	45	-	-	-	6.60	6.06	55.7
400 Mesh	38	-	-	-	5.30	4.86	50.8
TOTAL		483.5	100.00	**	109.0	100.00	**
		K80 = 2606µm			**K80 = 81µm**		

Table F.8 Bond ball mill work index test results for drawpoint sample E13S collected Nov, 2015

Weight of 700 ml Sample : 1311 g Aperture Test Sieve : 106µm
1/3.5 of Sample Weight : 374.6 g Percent Undersize : 11.5%

Cycle	Weight of New Feed	Number of Revolutions	Weight of Undersize			
			Product	Feed	Net Product	Net/Rev
1	1311.0	200	255.3	150.3	105.0	0.52
2	255.3	658	551.5	29.3	522.2	0.79
3	551.5	392	407.6	63.2	344.4	0.88
4	407.6	373	390.6	46.7	343.9	0.92
5	390.6	358	371.7	44.8	326.9	0.91
6	371.7	364	379.9	42.6	337.3	0.93

BOND WORK INDEX FORMULA

$$Wi = (44.5 \times 1.102) / (Pi^{.23} \times Gpb^{.82} \times (10/\sqrt{P} - 10/\sqrt{F}))$$

Pi = Sieve Size Tested. 106 µm
Gbp = Net undersize produced per revolution of mill. 0.92 g
P = 80% Passing size of test product. 78 µm
F = 80% Passing size of test feed. 2544 µm

BOND BALL WORK INDEX (Wi) 19.3 kw-hr/tonne

BOND BALL SCREEN ANALYSIS

Particle Size		Feed to Cycle 1			Equilibrium Cycle Undersize		
mesh	µm	Weight (g) Retained	Weight % Retained	Cumulative % Passing	Weight (g) Retained	Weight % Retained	Cumulative % Passing
6 Mesh	3360	24.50	5.11	94.9	-	-	-
7 Mesh	2800	38.90	8.11	86.8	-	-	-
8 Mesh	2360	56.20	11.72	75.1	-	-	-
9 Mesh	2000	43.90	9.15	65.9	-	-	-
10 Mesh	1700	38.80	8.09	57.8	-	-	-
12 Mesh	1400	35.30	7.36	50.5	-	-	-
14 Mesh	1180	25.30	5.27	45.2	-	-	-
20 Mesh	850	38.30	7.98	37.2	-	-	-
28 Mesh	600	33.60	7.00	30.2	-	-	-
35 Mesh	425	26.30	5.48	24.7	-	-	-
48 Mesh	300	19.60	4.09	20.6	-	-	-
65 Mesh	212	17.00	3.54	17.1	-	-	-
100 Mesh	150	15.20	3.17	13.9	-	-	-
150 Mesh	106	11.80	2.46	11.5	1.90	1.97	98.0
170 Mesh	90	-	-	-	8.60	8.92	89.1
200 Mesh	75	-	-	-	11.40	11.83	77.3
270 Mesh	53	-	-	-	13.70	14.21	63.1
325 Mesh	45	-	-	-	6.30	6.54	56.5
400 Mesh	38	-	-	-	5.30	5.50	51.0
TOTAL		479.7	100.00	**	96.4	100.00	**
			K80 = 2544µm			**K80 = 78µm**	

Table F.9 Bond ball mill work index test results for drawpoint sample E15N collected Nov, 2015

BOND BALL GRINDABILITY TEST E15N Drawpoint sample (Nov 2015)

Weight of 700 ml Sample : 1268.7 g Aperture Test Sieve : 106µm

1/3.5 of Sample Weight : 362.5 g Percent Undersize : 10.7%

Cycle	Weight of New Feed	Number of Revolutions	Weight of Undersize			
			Product	Feed	Net Product	Net/Rev
1	1268.7	200	258.2	135.8	122.4	0.61
2	258.2	547	470.0	27.6	442.4	0.81
3	470.0	386	405.1	50.3	354.8	0.92
4	405.1	347	360.7	43.4	317.3	0.91
5	360.7	355	372.0	38.6	333.4	0.94
6	372.0	343	355.4	39.8	315.6	0.92

BOND WORK INDEX FORMULA

$$Wi = (44.5 \times 1.102) / (Pi^{.23} \times Gpb^{.82} \times (10/\sqrt{P} - 10/\sqrt{F}))$$

Pi = Sieve Size Tested.	106	µm
Gbp = Net undersize produced per revolution of mill.	0.92	g
P = 80% Passing size of test product.	80	µm
F = 80% Passing size of test feed.	2690	µm

BOND BALL WORK INDEX (Wi) 19.4 kw-hr/tonne

BOND BALL SCREEN ANALYSIS

Particle Size		Feed to Cycle 1			Equilibrium Cycle Undersize		
mesh	µm	Weight (g) Retained	Weight % Retained	Cumulative % Passing	Weight (g) Retained	Weight % Retained	Cumulative % Passing
6 Mesh	3360	38.40	8.06	91.9	-	-	-
7 Mesh	2800	42.90	9.01	82.9	-	-	-
8 Mesh	2360	56.30	11.82	71.1	-	-	-
9 Mesh	2000	39.30	8.25	62.9	-	-	-
10 Mesh	1700	39.50	8.29	54.6	-	-	-
12 Mesh	1400	34.10	7.16	47.4	-	-	-
14 Mesh	1180	23.90	5.02	42.4	-	-	-
20 Mesh	850	38.40	8.06	34.3	-	-	-
28 Mesh	600	30.90	6.49	27.9	-	-	-
35 Mesh	425	23.80	5.00	22.9	-	-	-
48 Mesh	300	18.20	3.82	19.0	-	-	-
65 Mesh	212	15.30	3.21	15.8	-	-	-
100 Mesh	150	13.60	2.85	13.0	-	-	-
150 Mesh	106	10.80	2.27	10.7	3.70	3.36	96.6
170 Mesh	90	-	-	-	10.00	9.08	87.6
200 Mesh	75	-	-	-	13.10	11.90	75.7
270 Mesh	53	-	-	-	15.10	13.71	61.9
325 Mesh	45	-	-	-	7.00	6.36	55.6
400 Mesh	38	-	-	-	6.00	5.45	50.1
TOTAL		476.4	100.00	**	110.1	100.00	**
		K80 = 2690µm			**K80 = 80µm**		

Table F.10 Bond ball mill work index test results for drawpoint sample E23N collected Nov, 2015

BOND BALL GRINDABILITY TEST E23N Drawpoint sample (Nov 2015)

Weight of 700 ml Sample : 1277 g Aperture Test Sieve : 106µm
1/3.5 of Sample Weight : 364.9 g Percent Undersize : 9.3%

Cycle	Weight of New Feed	Number of Revolutions	Weight of Undersize			
			Product	Feed	Net Product	Net/Rev
1	1277.0	200	267.5	118.3	149.2	0.75
2	267.5	456	423.2	24.8	398.4	0.87
3	423.2	373	401.5	39.2	362.3	0.97
4	401.5	337	379.0	37.2	341.8	1.01
5	379.0	325	366.7	35.1	331.6	1.02
6	366.7	324	365.2	34.0	331.2	1.02
7	365.2	324	366.5	33.8	332.7	1.03

BOND WORK INDEX FORMULA

$Wi = (44.5 \times 1.102) / (Pi^{.23} \times Gpb^{.82} \times (10/\sqrt{P} - 10/\sqrt{F}))$

Pi = Sieve Size Tested.	106	µm
Gbp = Net undersize produced per revolution of mill.	1.02	g
P = 80% Passing size of test product.	81	µm
F = 80% Passing size of test feed.	2779	µm

BOND BALL WORK INDEX (Wi) 17.9 kw-hr/tonne

BOND BALL SCREEN ANALYSIS

Particle Size		Feed to Cycle 1			Equilibrium Cycle Undersize		
mesh	µm	Weight (g) Retained	Weight % Retained	Cumulative % Passing	Weight (g) Retained	Weight % Retained	Cumulative % Passing
6 Mesh	3360	53.40	10.00	90.0	-	-	-
7 Mesh	2800	50.30	9.42	80.6	-	-	-
8 Mesh	2360	64.80	12.13	68.5	-	-	-
9 Mesh	2000	44.70	8.37	60.1	-	-	-
10 Mesh	1700	44.60	8.35	51.7	-	-	-
12 Mesh	1400	38.40	7.19	44.6	-	-	-
14 Mesh	1180	26.70	5.00	39.6	-	-	-
20 Mesh	850	40.90	7.66	31.9	-	-	-
28 Mesh	600	32.30	6.05	25.9	-	-	-
35 Mesh	425	24.70	4.62	21.2	-	-	-
48 Mesh	300	19.30	3.61	17.6	-	-	-
65 Mesh	212	16.80	3.14	14.5	-	-	-
100 Mesh	150	15.30	2.86	11.6	-	-	-
150 Mesh	106	12.50	2.34	9.3	4.70	3.85	96.2
170 Mesh	90	-	-	-	10.80	8.84	87.3
200 Mesh	75	-	-	-	15.60	12.77	74.5
270 Mesh	53	-	-	-	18.50	15.14	59.4
325 Mesh	45	-	-	-	8.30	6.79	52.6
400 Mesh	38	-	-	-	6.70	5.48	47.1
TOTAL		534.2	100.00	**	122.2	100.00	**
		K80 = 2779µm			**K80 = 81µm**		

Table F.11 Bond ball mill work index test results for drawpoint sample E30N collected Nov, 2015

BOND BALL GRINDABILITY TEST E30N Drawpoint sample (Nov 2015)

Weight of 700 ml Sample : 1267.5 g Aperture Test Sieve : 106µm
1/3.5 of Sample Weight : 362.1 g Percent Undersize : 8.2%

Cycle	Weight of New Feed	Number of Revolutions	Weight of Undersize			
			Product	Feed	Net Product	Net/Rev
1	1267.5	200	209.4	103.4	106.0	0.53
2	209.4	651	485.5	17.1	468.4	0.72
3	485.5	448	421.1	39.6	381.5	0.85
4	421.1	385	344.4	34.3	310.1	0.81
5	344.4	415	371.7	28.1	343.6	0.83
6	371.7	401	366.0	30.3	335.7	0.84
7	366.0	397	355.7	29.9	325.9	0.82

BOND WORK INDEX FORMULA

$$Wi = (44.5 \times 1.102) / (Pi^{.23} \times Gpb^{.82} \times (10/\sqrt{P} - 10/\sqrt{F}))$$

Pi = Sieve Size Tested.	106 µm
Gbp = Net undersize produced per revolution of mill.	0.83 g
P = 80% Passing size of test product.	78 µm
F = 80% Passing size of test feed.	2831 µm

BOND BALL WORK INDEX (Wi) 20.8 kw-hr/tonne

BOND BALL SCREEN ANALYSIS

Particle Size		Feed to Cycle 1			Equilibrium Cycle Undersize		
mesh	µm	Weight (g) Retained	Weight % Retained	Cumulative % Passing	Weight (g) Retained	Weight % Retained	Cumulative % Passing
6 Mesh	3360	47.80	9.80	90.2	-	-	-
7 Mesh	2800	52.80	10.82	79.4	-	-	-
8 Mesh	2360	64.70	13.26	66.1	-	-	-
9 Mesh	2000	46.00	9.43	56.7	-	-	-
10 Mesh	1700	42.80	8.77	47.9	-	-	-
12 Mesh	1400	36.60	7.50	40.4	-	-	-
14 Mesh	1180	24.60	5.04	35.4	-	-	-
20 Mesh	850	37.30	7.64	27.7	-	-	-
28 Mesh	600	28.50	5.84	21.9	-	-	-
35 Mesh	425	20.80	4.26	17.6	-	-	-
48 Mesh	300	15.10	3.09	14.5	-	-	-
65 Mesh	212	12.30	2.52	12.0	-	-	-
100 Mesh	150	10.60	2.17	9.9	-	-	-
150 Mesh	106	8.30	1.70	8.2	3.40	3.41	96.6
170 Mesh	90	-	-	-	7.90	7.92	88.7
200 Mesh	75	-	-	-	11.20	11.22	77.5
270 Mesh	53	-	-	-	13.50	13.53	63.9
325 Mesh	45	-	-	-	6.40	6.41	57.5
400 Mesh	38	-	-	-	5.20	5.21	52.3
TOTAL		488.0	100.00	**	99.8	100.00	**
		K80 = 2831µm			**K80 = 78µm**		

Table F.12 Bond ball mill work index test results for drawpoint sample F33S collected Nov, 2015

BOND BALL GRINDABILITY TEST F33S Drawpoint sample (Nov 2015)

Weight of 700 ml Sample : 1241.6 g Aperture Test Sieve : 106µm
1/3.5 of Sample Weight : 354.7 g Percent Undersize : 14.5%

Cycle	Weight of New Feed	Number of Revolutions	Weight of Undersize			
			Product	Feed	Net Product	Net/Rev
1	1241.6	200	266.6	180.2	86.4	0.43
2	266.6	732	628.0	38.7	589.3	0.81
3	628.0	327	404.2	91.1	313.1	0.96
4	404.2	309	359.1	58.7	300.4	0.97
5	359.1	312	350.9	52.1	298.8	0.96
6	350.9	317	353.7	50.9	302.8	0.96

BOND WORK INDEX FORMULA

$$Wi = (44.5 \times 1.102) / (Pi^{.23} \times Gpb^{.82} \times (10/\sqrt{P} - 10/\sqrt{F}))$$

Pi = Sieve Size Tested. 106 µm
Gbp = Net undersize produced per revolution of mill. 0.96 g
P = 80% Passing size of test product. 74 µm
F = 80% Passing size of test feed. 2667 µm

BOND BALL WORK INDEX (Wi) 17.9 kw-hr/tonne

BOND BALL SCREEN ANALYSIS

Particle Size		Feed to Cycle 1			Equilibrium Cycle Undersize		
mesh	µm	Weight (g) Retained	Weight % Retained	Cumulative % Passing	Weight (g) Retained	Weight % Retained	Cumulative % Passing
6 Mesh	3360	36.30	7.31	92.7	-	-	-
7 Mesh	2800	44.50	8.96	83.7	-	-	-
8 Mesh	2360	61.80	12.44	71.3	-	-	-
9 Mesh	2000	42.50	8.55	62.7	-	-	-
10 Mesh	1700	40.50	8.15	54.6	-	-	-
12 Mesh	1400	34.60	6.96	47.6	-	-	-
14 Mesh	1180	22.90	4.61	43.0	-	-	-
20 Mesh	850	36.20	7.29	35.7	-	-	-
28 Mesh	600	28.90	5.82	29.9	-	-	-
35 Mesh	425	22.30	4.49	25.4	-	-	-
48 Mesh	300	17.20	3.46	22.0	-	-	-
65 Mesh	212	14.60	2.94	19.0	-	-	-
100 Mesh	150	12.70	2.56	16.5	-	-	-
150 Mesh	106	9.70	1.95	14.5	2.50	2.58	97.4
170 Mesh	90	-	-	-	7.10	7.33	90.1
200 Mesh	75	-	-	-	9.50	9.81	80.3
270 Mesh	53	-	-	-	10.70	11.05	69.2
325 Mesh	45	-	-	-	4.90	5.06	64.2
400 Mesh	38	-	-	-	3.90	4.03	60.1
TOTAL		496.8	100.00	**	96.8	100.00	**
		K80 = 2667µm			**K80 = 74µm**		

Table F.13 Bond ball mill work index test results for drawpoint sample G40N collected Nov, 2015

BOND BALL GRINDABILITY TEST G40N Drawpoint sample (Nov 2015)

Weight of 700 ml Sample : 1244.4 g Aperture Test Sieve : 106µm

1/3.5 of Sample Weight : 355.5 g Percent Undersize : 10.5%

Cycle	Weight of New Feed	Number of Revolutions	Weight of Undersize			
			Product	Feed	Net Product	Net/Rev
1	1244.4	200	221.4	130.5	90.9	0.45
2	221.4	731	564.5	23.2	541.3	0.74
3	564.5	400	394.9	59.2	335.7	0.84
4	394.9	375	367.3	41.4	325.9	0.87
5	367.3	364	353.9	38.5	315.4	0.87
6	353.9	368	352.1	37.1	315.0	0.86

BOND WORK INDEX FORMULA

$$Wi = (44.5 \times 1.102) / (Pi^{.23} \times Gpb^{.82} \times (10/\sqrt{P} - 10/\sqrt{F}))$$

Pi = Sieve Size Tested. 106 µm
Gbp = Net undersize produced per revolution of mill. 0.86 g
P = 80% Passing size of test product. 78 µm
F = 80% Passing size of test feed. 2690 µm

BOND BALL WORK INDEX (Wi) 20.1 kw-hr/tonne

BOND BALL SCREEN ANALYSIS

Particle Size		Feed to Cycle 1			Equilibrium Cycle Undersize		
mesh	µm	Weight (g) Retained	Weight % Retained	Cumulative % Passing	Weight (g) Retained	Weight % Retained	Cumulative % Passing
6 Mesh	3360	37.80	7.85	92.1	-	-	-
7 Mesh	2800	44.00	9.14	83.0	-	-	-
8 Mesh	2360	58.10	12.07	70.9	-	-	-
9 Mesh	2000	42.40	8.81	62.1	-	-	-
10 Mesh	1700	40.70	8.45	53.7	-	-	-
12 Mesh	1400	35.70	7.41	46.3	-	-	-
14 Mesh	1180	25.10	5.21	41.1	-	-	-
20 Mesh	850	39.10	8.12	32.9	-	-	-
28 Mesh	600	30.40	6.31	26.6	-	-	-
35 Mesh	425	22.90	4.76	21.9	-	-	-
48 Mesh	300	17.40	3.61	18.3	-	-	-
65 Mesh	212	14.50	3.01	15.2	-	-	-
100 Mesh	150	12.90	2.68	12.6	-	-	-
150 Mesh	106	10.00	2.08	10.5	2.60	2.42	97.6
170 Mesh	90	-	-	-	9.00	8.38	89.2
200 Mesh	75	-	-	-	12.20	11.36	77.8
270 Mesh	53	-	-	-	14.60	13.59	64.2
325 Mesh	45	-	-	-	7.00	6.52	57.7
400 Mesh	38	-	-	-	5.40	5.03	52.7
TOTAL		481.5	100.00	**	107.4	100.00	**

K80 = 2690µm **K80 = 78µm**

Appendix G Drawpoint Logs

Table G.1 Logs of rock types reporting to drawpoints

Date Collected	Units	2015, Nov 12	2015, Nov 12	2015, Nov 12	2015, Nov 12	2015, Nov 12	2015, Nov 12
Drawpoint		E23N	B13S	D7S	D11N	D11S	D38N
Estimated HOD	[m]	99	182	203	251	238	58
Dominant rock type at drawpoint		Monzonite	Phyllic	Hypogene	Hypogene	Hypogene	Supergene
F100	[mm]	1,015	318	532	858	722	568
F80	[mm]	390	98	213	256	381	121
F50	[mm]	123	70	93	93	196	71
I_{S50} Mean	[MPa]	5.6	3.8	5.4	5.7	5.1	2.2
Dropweight Axb		39.19	46.10	39.47	38.43	32.25	61.16
ta		0.28	0.44	0.40	0.39	0.41	0.92
DWi	[kWh/m3]	6.91	5.82	6.86	6.91	8.31	4.45
SG 31.5 x 26.5		2.72	2.69	2.72	2.67	2.70	2.72
Average SG (+50 mm)		2.72	2.71	2.74	2.70	2.74	2.72
Emin	[kWh/t]	0.09	0.05	0.05	0.08	0.07	-0.07
Bond Ball Mill Work Index	[kWh/t]	17.93	18.77	17.99	18.38	19.29	18.55
Lithology/ Alteration, average proportions							
% Group 1, Biotite >50 &/or Group 2* (picrite)	[%]	22	32	46	36	46	46
% Group 3, 50>K-spar>20	[%]	37	33	20	25	50	23
% Group 5, K-spar >50	[%]	41	19	27	36	4	7
% Group 6, Fault rock	[%]	0	15	2	0	1	9
% Group 7, Carbonates	[%]	0	1	5	3	1	1
% Group 8, Oxide	[%]	0	0	0	0	0	14
% Total Carbonates & Fault (Group 6 & Group 7)	[%]	0	16	7	3	1	10
'+50 mm % Group 1, Biotite >50 &/or Group 2* (picrite)	[%]	23	37	31	36	52	42
'+50 mm % Group 3, 50>K-spar>20	[%]	32	27	26	19	41	23
'+50 mm % Group 5, K-spar >50	[%]	45	8	35	42	5	6
'+50 mm % Group 6, Fault rock	[%]	0	25	3	0	2	13
'+50 mm % Group 7, Carbonates	[%]	0	2	5	3	0	0
'+50 mm % Group 8, Oxide	[%]						17
'-50,+25 mm, % Group 1, Biotite >50 &/or Group 2* (picrite)	[%]	19	29	51	36	46	44
'-50,+25 mm, % Group 3, 50>K-spar>20	[%]	42	35	16	20	49	29
'-50,+25 mm, % Group 5, K-spar >50	[%]	38	17	27	42	4	8
'-50,+25 mm, % Group 6, Fault rock	[%]	0	19	4	0	0	5
'-50,+25 mm, % Group 7, Carbonates	[%]	0	0	1	2	0	0
'-50,+25 mm, % Group 8, Oxide	[%]	0	0	0	0	0	14
-25,+ 12.5 mm, % % Group 1, Biotite >50 &/or Group 2* (picrit	[%]	24	29	57	36	38	54
-25,+ 12.5 mm, % % Group 3, 50>K-spar>20	[%]	37	37	17	35	59	18
-25,+ 12.5 mm, % % Group 5, K-spar >50	[%]	40	33	18	25	4	7
-25,+ 12.5 mm, % % Group 6, Fault rock	[%]	0	0	0	0	0	8
-25,+ 12.5 mm, % % Group 7, Carbonates	[%]	0	2	8	4	2	3
-25,+ 12.5 mm, % % Group 8, Oxide	[%]	0	0	0	0	0	10
Average shape for both size fractions)		2.72	2.07	2.28	2.00	2.33	1.99
Shape +50 mm (1 =Round, 3 = Angular)		2.76	2.08	2.11	1.89	2.07	1.88
Shape -50,+25 mm (1 =Round, 3 = Angular)		2.68	2.06	2.45	2.12	2.60	2.11

Table G.2 Logs of rock types reporting to drawpoints

Date Collected	Units	2015, Nov 12	2015, Nov 12	2015, Nov 12	2015, Nov 12	2015, Nov 12
Drawpoint		E13S	E15N	E30N	F33S	G40N
Estimated HOD	[m]	237	229	112	98	64
Dominant rock type at drawpoint		Hypogene	Hypogene	Hypogene	Picrite	2nd. Hypogene
F100	[mm]	990	707	709	495	494
F80	[mm]	397	303	285	138	163
F50	[mm]	190	135	122	73	86
I_{s50} Mean	[MPa]	5.3	5.8	6.3	3.2	3.6
Dropweight Axb		34.83	33.50	38.80	67.46	40.89
ta		0.36	0.27	0.38	0.66	0.50
DWi	[kWh/m3]	7.79	8.08	7.08	3.91	6.47
SG 31.5 x 26.5		2.73	2.72	2.76	2.64	2.66
Average SG (+50 mm)		2.73	2.72	2.73	2.66	2.66
Emin	[kWh/t]	0.00		0.07	-0.02	-0.03
Bond Ball Mill Work Index	[kWh/t]	19.28	19.40	20.77	17.88	20.11
Lithology/ Alteration, average proportions						
% Group 1, Biotite >50 &/or Group 2* (picrite)	[%]	60	57	51	56	27
% Group 3, 50>K-spar>20	[%]	27	34	16	17	30
% Group 5, K-spar >50	[%]	11	8	22	18	34
% Group 6, Fault rock	[%]	0	0	1	3	0
% Group 7, Carbonates	[%]	2	1	9	6	8
% Group 8, Oxide	[%]	0	0	0	0	0
% Total Carbonates & Fault (Group 6 & Group 7)	[%]	2	1	10	9	8
'+50 mm % Group 1, Biotite >50 &/or Group 2* (picrite)	[%]	50	54	58	64	23
'+50 mm % Group 3, 50>K-spar>20	[%]	38	40	17	21	32
'+50 mm % Group 5, K-spar >50	[%]	12	6	18	10	42
'+50 mm % Group 6, Fault rock	[%]	0	0	3	3	0
'+50 mm % Group 7, Carbonates	[%]	0	0	3	3	4
'+50 mm % Group 8, Oxide	[%]	0	0	0	0	
'-50,+25 mm, % Group 1, Biotite >50 &/or Group 2* (picrite)	[%]	70	54	42	45	29
'-50,+25 mm, % Group 3, 50>K-spar>20	[%]	26	32	32	15	29
'-50,+25 mm, % Group 5, K-spar >50	[%]	4	12	19	25	32
'-50,+25 mm, % Group 6, Fault rock	[%]	0	0	1	0	0
'-50,+25 mm, % Group 7, Carbonates	[%]	0	2	6	14	11
'-50,+25 mm, % Group 8, Oxide	[%]	0	0	0	0	
-25,+ 12.5 mm, % % Group 1, Biotite >50 &/or Group 2* (picri	[%]	60	62	53	59	30
-25,+ 12.5 mm, % % Group 3, 50>K-spar>20	[%]	17	30	0	15	30
-25,+ 12.5 mm, % % Group 5, K-spar >50	[%]	16	7	30	19	30
-25,+ 12.5 mm, % % Group 6, Fault rock	[%]			0	7	0
-25,+ 12.5 mm, % % Group 7, Carbonates	[%]	6	2	17	0	10
-25,+ 12.5 mm, % % Group 8, Oxide	[%]	0	0	0	0	
Average shape for both size fractions)		2.16	2.33	2.27	1.86	2.01
Shape +50 mm (1 =Round, 3 = Angular)		2.08	2.19	2.53	1.62	1.87
Shape -50,+25 mm (1 =Round, 3 = Angular)		2.24	2.46	2.01	2.11	2.14

* Note: Sample from drawpoint F33S was the only sample that contained noticeable picrite

Figure G.1 Mill feed sample (~2 tonnes) collected March, 2016 and example of rock type groupings (+50 mm)

Table G.3 Rock types identified in mill feed sample (collected March, 2016)

Size	Mass % of Mill Feed SampleWeight	Lithology / Alteration (% by mass)				
[mm]	[%]	Group #1	Group #3	Group #5	Group #6	Group #7
-150, +125*	0.36					
-125, +100	4.92	50	50			
-100, +75	8.18	63	9	13	10	4
-75, +63	5.10	47	30	17	1	5
-63, +50	5.90	29	37	28	3	4
Mass Weighted Average (-125, +50 mm)		**48**	**29**	**15**	**4**	**3**

Appendix H Image-based Size Distributions

Table H.1 Drawpoint size distributions from image-based measurements and sieving

Date inspected	Units	2015, Nov 12	2015, Nov 12	2015, Nov 12	2015, Nov 12	2015, Nov 12	2015, Nov 12	2015, Nov 12	2015, Nov 12	2015, Nov 12	2015, Nov 12	2015, Nov 12
Drawpoint		E23N	B13S	D7S	D11N	D11S	D38N	E13S	E15N	E30N	F33S	G40N
Estimated HOD	**[m]**	99	182	203	251	238	58	237	229	112	98	64
F100 (bold = measured with tape)	**[mm]**	1015	**318**	**532**	**858**	**722**	568	**990**	**707**	**709**	**495**	494
F80	**[mm]**	389.6	98.4	213.0	256.4	381.3	120.7	397.1	302.8	284.7	138.0	163.4
F50	**[mm]**	122.5	69.7	93.2	93.2	196.2	70.8	189.8	134.6	122.1	73.5	86.4
Image-based measurement												
Size (mm)												
2000	**% Passing from Wipfrag**	100	100	100	100	100	100	100	100	100	100	100
1500		100	100	100	100	100	100	100	100	100	100	100
1200		100	100	100	100	100	100	100	100	100	100	100
1000		92	100	100	100	100	100	100	100	100	100	100
820		92	100	100	97	96	100	98	100	100	100	100
800		92	100	100	97	96	100	97	100	100	100	100
700		92	100	100	95	94	100	96	100	100	100	100
600		86	100	100	92	91	99	90	95	99	99	98
500		84	100	100	89	88	97	85	90	98	99	97
400		81	100	97	89	82	97	80	90	91	99	97
300		76	98	90	83	73	96	68	80	83	95	93
250		70	96	84	79	63	95	61	74	74	91	89
200		66	95	78	74	51	92	52	65	73	91	87
150		57	90	68	67	34	88	41	56	61	83	77
100		44	81	52	53	17	75	24	37	42	70	57
Sieved -25 mm drawpoint samples												
Size (mm)												
25	**% Passing**	100.0	100.0	100.0	100.0	-	100.0	100.0	100.0	100.0	100.0	100.0
19		83.6	86.2	88.3	78.4		65.8	56.4	70.0	55.9	86.4	87.8
12.5		65.3	68.9	68.2	55.8		37.6	20.0	36.3	30.5	63.3	68.0
5.6		38.3	46.5	38.5	29.5		8.5	6.6	10.7	13.9	34.5	37.3
2		19.8	29.1	20.7	16.7		4.4	3.5	5.4	7.5	18.8	19.2
0.5		9.2	15.1	10.8	7.1		2.8	1.7	3.6	4.0	8.2	9.0

Table H.2 Drawpoint size distributions from image-based measurements

Date inspected	Units	2016, Nov 21	2016, Nov 21	2016, Nov 21	2016, Nov 21	2016, Nov 21	2016, Nov 21	2016, Nov 21	2016, Nov 21	2016, Nov 21	2016, Nov 21
Drawpoint		E23S	C36N	C37N	C39N	D37N	E11S	E19N	E30N	E32N	E38N
Estimated HOD	**[m]**	190	107	115	64	167	289	272	168	179	143
F100 (bold = measured with tape)	**[mm]**	**160**	**280**	**280**	**520**	**490**	**300**	**580**	**310**	**270**	**210**
F80	**[mm]**	142.5	143.5	139.1	228.3	149.9	146.6	212.0	215.7	171.0	140.6
F50	**[mm]**	124.7	123.5	107.2	126.8	123.9	122.1	129.5	122.6	128.7	110.8
Image-based measurement											
Size (mm)											
2000		100	100	100	100	100	100	100	100	100	100
1500		100	100	100	100	100	100	100	100	100	100
1200		100	100	100	100	100	100	100	100	100	100
1000		100	100	100	100	100	100	100	100	100	100
820		100	100	100	100	100	100	100	100	100	100
800		100	100	100	100	100	100	100	100	100	100
700		100	100	100	96	100	100	96	100	100	100
600	**% Passing**	100	100	100	96	96	100	96	96	100	100
500		100	100	100	91	93	100	89	96	100	100
400		100	100	100	88	90	100	87	93	100	100
300		100	98	100	83	88	98	83	86	93	100
250		100	96	100	82	87	94	81	83	90	99
200		97	94	95	77	84	90	80	79	85	95
150		93	90	90	73	80	84	71	74	76	90
100		8	15	43	23	22	23	19	30	15	39

Table H.3 Drawpoint size distributions from image-based measurements

Date inspected	Units	2016, Nov 21	2016, Nov 21	2016, Nov 21	2016, Nov 21	2016, Nov 21	2016, Nov 21	2016, Nov 21	2016, Nov 21	2014, Mar 27	2014, Mar 27
Drawpoint		E39S	E40S	E43N	E43S	G33S	G34S	G40N	G40S	B9S	C7S
Estimated HOD	**[m]**	127	23	38	33	60	59	64	52	75	145
F100 (bold = measured with tape)	**[mm]**	**390**	**570**	**430**	**480**	**390**	**180**	**520**	**270**	405	594
F80	**[mm]**	174.6	149.9	205.9	188.1	147.4	139.8	140.3	142.2	133.8	236.1
F50	**[mm]**	126.7	126.7	128.1	122.6	119.3	117.8	110.3	116.3	71.5	94.7
Image-based measurement											
Size (mm)											
2000		100	100	100	100	100	100	100	100	100	100
1500		100	100	100	100	100	100	100	100	100	100
1200		100	100	100	100	100	100	100	100	100	100
1000		100	100	100	100	100	100	100	100	100	100
820		100	100	100	100	100	100	100	100	100	100
800		100	100	100	100	100	100	100	100	100	100
700		100	100	100	100	100	100	100	100	100	100
600	**% Passing**	100	93	100	100	100	100	100	100	100	100
500		100	93	97	100	96	100	100	97	100	94
400		96	93	94	99	96	98	95	97	99	90
300		91	91	89	93	94	97	95	97	98	88
250		87	86	85	91	91	97	95	96	95	82
200		84	85	79	82	89	96	95	94	91	74
150		76	80	69	73	83	94	90	89	84	64
100		20	15	26	31	29	26	40	31	72	52

Table H.4 Drawpoint size distributions from image-based measurements

Date inspected	Units	2014, Mar 27	2014, Mar 27	2014, Mar 27	2014, Mar 27	2014, Mar 27	2014, Mar 27	2014, Mar 27	2014, Mar 27	2014, Mar 27	2014, Mar 27
Drawpoint		C8N	E9S	E10S	G35N	E10N - Berm	E12S - Berm	E31N - Berm (OK)	E31S - Blast (OK)	E33N - (OK)	E34S - Berm
Estimated HOD	**[m]**	95	155	158	34	157	145	35	40	26	25
F100 (bold = measured with tape)	**[mm]**	367	896	820	706	251	261	552	645	235	527
F80	**[mm]**	224	347	257	172	80	91	79	507	80	261
F50	**[mm]**	148.9	128.8	74.8	73.5	67.5	68.8	68.1	334.4	68.4	75.6
Image-based measurement											
Size (mm)											
2000		100	100	100	100	100	100	100	100	100	100
1500		100	100	100	100	100	100	100	100	100	100
1200		100	100	100	100	100	100	100	100	100	100
1000		100	100	100	100	100	100	100	100	100	100
820		100	96	100	100	100	100	100	100	100	100
800		100	95	95	100	100	100	100	100	100	100
700		100	95	90	96	100	100	100	100	100	100
600	**% Passing**	100	92	90	96	100	100	100	96	100	100
500		100	89	90	96	100	100	95	79	100	93
400		100	84	86	96	100	100	95	66	100	87
300		95	77	83	92	100	100	95	42	100	83
250		88	71	80	89	98	99	95	29	100	79
200		73	61	76	85	95	95	95	17	98	74
150		51	53	69	76	92	90	93	8	92	69
100		17	46	63	66	85	81	86	2	84	62

Table H.5 Drawpoint size distributions from image-based measurements

Date inspected	Units	2014, Mar 27	2014, Mar 27	2012, Jan 13	2013, Nov 4	2013, Nov 4	2012, Oct 31	2012, Apr 19	2013, Nov 4	2013, Nov 4	2013, Nov 4
Drawpoint		F19S - Berm (OK)	F21S - Berm	C7S	F8N	F10N	F10N	F10N	C5S	C8S	C10S
Estimated HOD	**[m]**	114	98	65	116	130	70	33	129	123	120
F100 (bold = measured with tape)	**[mm]**	432	315	476	921	728	649	511	997	775	652
F80	**[mm]**	126	184	181	430	350	278	293	589	354	131
F50	**[mm]**	71.0	129.3	91.9	209.9	201.2	85.7	128.8	196.5	158.7	69.9
Image-based measurement											
Size (mm)											
2000		100	100	100	100	100	100	100	100	100	100
1500		100	100	100	100	100	100	100	100	100	100
1200		100	100	100	100	100	100	100	100	100	100
1000		100	100	100	100	100	100	100	100	100	100
820		100	100	100	96	100	100	100	81	100	100
800		100	100	100	96	100	100	100	81	100	100
700		100	100	100	93	97	100	100	81	92	100
600	**% Passing**	100	100	100	90	97	97	100	81	92	98
500		100	100	100	84	94	90	98	72	88	95
400		96	100	96	78	88	87	91	70	85	94
300		93	92	94	64	72	81	81	62	74	89
250		91	92	90	57	62	79	74	57	69	88
200		88	89	84	48	50	74	68	51	60	86
150		84	62	73	40	40	68	57	43	48	83
100		76	33	54	28	29	55	40	34	29	76

Table H.6 Drawpoint size distributions from image-based measurements

Date inspected	Units	2013, Nov 4	2013, Nov 4	2012, Feb 24	2012, Dec 11	2012, Oct 17	2012, Mar 22	2012, Jun 27	2012, Apr 19	2012, June 27	2012, May 3
Drawpoint		B11S	B12S	C5S	C6S	C7S	D7S	D11S	E10N	F10S	G11N
Estimated HOD	**[m]**	52	50	43	72	54	32	24	20	42	10
F100 (bold = measured with tape)	**[mm]**	384	626	765	741	715	1029	568	581	662	537
F80	**[mm]**	104	256	391	346	397	527	155	140	269	197
F50	**[mm]**	69.4	74.7	170.6	86.7	196.0	252.3	75.0	74.6	96.2	90.1
Image-based measurement											
Size (mm)											
2000		100	100	100	100	100	100	100	100	100	100
1500		100	100	100	100	100	100	100	100	100	100
1200		100	100	100	100	100	100	100	100	100	100
1000		100	100	100	100	100	90	100	100	100	100
820		100	100	100	100	100	90	100	100	100	100
800		100	100	100	100	100	90	100	100	100	100
700		100	100	93	96	94	90	100	100	100	100
600	**% Passing**	100	97	91	96	94	82	100	100	96	100
500		100	93	88	93	94	79	98	97	93	97
400		100	89	81	83	80	69	98	95	90	94
300		97	85	69	77	69	60	95	94	82	89
250		97	79	62	74	60	50	91	92	79	86
200		93	76	55	67	51	42	86	91	71	81
150		87	70	46	61	40	30	79	83	64	70
100		79	64	35	53	29	18	66	67	51	54

Table H.7 Drawpoint size distributions from image-based measurements

Date inspected	Units	2012, Dec 11	2012, Nov 16	2012, Oct 31	2012, Dec 11	2013, Jan 24	2012, Nov 16	2012, Oct 31	2012, Dec 11	2012, Dec 11	2012, Oct 17
Drawpoint		B9S	B9S	B9S	B11S	F19S	B11S	B11S	B12S	C5S	C5S
Estimated HOD	**[m]**	17	15	13	14	21	11	9	13	79	73
F100 (bold = measured with tape)	**[mm]**	419	2046	566	1028.0	971	574	310	307	492	651
F80	**[mm]**	270	950	238	275	796	481	275	142	267	421
F50	**[mm]**	139.2	139.8	136.5	134.7	415.2	309.4	131.0	125.8	140.7	251.3
Image-based measurement											
Size (mm)											
2000		100	98	100	100	100	100	100	100	100	100
1500		100	81	100	100	100	100	100	100	100	100
1200		100	81	100	100	100	100	100	100	100	100
1000		100	81	100	95	100	100	100	100	100	100
820		100	78	100	93	83	100	100	100	100	100
800		100	77	100	92	80	100	100	100	100	100
700		100	77	100	92	76	100	100	100	100	100
600	**% Passing**	100	77	100	90	70	100	100	100	100	96
500		100	77	98	87	63	84	100	100	100	85
400		98	77	96	87	48	65	100	100	93	79
300		85	72	88	81	26	48	86	99	83	57
250		77	69	81	79	14	36	74	98	79	50
200		70	65	76	76	7	20	71	96	71	41
150		62	63	67	71	3	7	62	95	60	32
100		6	0	3	2	0	2	30	2	6	4

Table H.8 Drawpoint size distributions from image-based measurements

Date inspected	Units	2012, July 11	2012, June 27	2012, May 31	2012, May 3	2012, Oct 17	2012, Feb 02	2012, Dec 11	2012, Oct 17
Drawpoint		C5S	C5S	C5S	C5S	E9S	F8N	C8N	B9S
Estimated HOD	**[m]**	63	61	54	50	61	13	32	12
F100 (bold = measured with tape)	**[mm]**	637	846	929	799	431	330	384	1210
F80	**[mm]**	599	486	703	344	272	78	195	494
F50	**[mm]**	384.8	138.6	144.8	139.7	180.1	67.7	135.1	278.6
Image-based measurement									
Size (mm)									
2000		100	100	100	100	100	100	100	100
1500		100	100	100	100	100	100	100	100
1200		100	100	100	100	100	100	100	90
1000		100	100	100	100	100	100	100	90
820		100	97	88	100	100	100	100	90
800		100	94	88	100	100	100	100	90
700		100	90	80	97	100	100	100	90
600	**% Passing**	80	87	80	95	100	100	100	87
500		58	80	80	91	100	100	100	81
400		52	77	69	85	94	100	100	72
300		39	72	67	76	85	98	90	54
250		35	70	64	72	76	96	86	44
200		29	67	61	67	59	96	81	31
150		21	64	56	63	37	93	71	15
100		8	2	2	0	7	87	2	3

Appendix I Mill Survey Results for Survey Carried Out March 3rd, 2015 (survey used for model validation)

Table I.1 Summary of samples taken March 3rd, 2015

Samples collected on:	March 3rd, 2015	12:45 to 1:15 AM	(30 minute span)			
	SAG Mill Feed taken at ~2AM just prior to mill shut-down					
	Gross Weight	**Packaging weight**	**Net Sample Weight - Wet**	**Net Sample Weight - Dry**	**% Solids**	**% Moisture**
	[kg]	**[kg]**	**[kg]**	**[kg]**		
SAG Mill Feed	667.8	30.8	637.0	620.2	97.4	2.6
Cyclone Underflow #1/2	35.3	1.3	34.0	27.7	81.3	18.7
Cyclone Underflow #2/2	36.2	1.3	34.9	28.7	82.3	17.7
Cyclone Underflow (Total)	**71.5**	**2.6**	**68.9**	**56.4**	**81.8**	**18.2**
SAG Mill Screen Over-Size	53.4	2.3	51.1	50.5	98.8	1.2
Cyclone Overflow #1/2	20.4	1.3	19.1	7.1	37.1	62.9
Cyclone Overflow #2/2	21.4	1.3	20.1	7.7	38.2	61.8
Cyclone Overflow (Total)	**41.8**	**2.6**	**39.2**	**14.7**	**37.6**	**62.4**

Table I.2 Summary of samples taken March 3rd, 2015

Survey Date:	March 3rd, 2015. 1 to 3 AM				
Item	**Specific Energy**	**Power**			
	[kWh/mt]	**[kW]**			
SAG mill main motor	6.64	4,324			
Pebble circuit conveyors S1-S4	0.16	101			
Pebble crusher	0.35	228			
SAG mill screen	0.03	20			
Ball mill main motor	8.37	5,446			
Slurry pump motor	0.78	508			
Total:	**16.32**	**10,628**			
Stream:	**Solids throughput rate**	**% Moisture (measured, wt/wt)**	**% Solids (measured, wt/wt)**	**F80**	**F50**
	[mtph]	**[%]**	**[%]**	**[µm]**	**[µm]**
SAG Mill Feed (S1)	651	2.6	97.4	34,583	
SAG Mill Screen Over-Size	151	1.2	98.8	42,748	25,837
Ball Mill Cyclone Underflow		18.2	81.8	4,004	1,004
Ball Mill Cyclone Overflow	651	62.4	37.6	226	78

* Note: mill F80 feed size was finer than expected. Potentially due to size segregation in mill feed stockpile

Table I.3 Size distributions for samples taken March 3rd, 2015

Stream:		SAG Mill Feed	Pebble Crusher Feed	Cyclone Underflow	Cyclone Overflow
Size		Cumulative % Passing	Cumulative % Passing	Cumulative % Passing	Cumulative % Passing
[mm]	[µm]	[%]	[%]	[%]	[%]
150	150,000	100.0	100.0	100.0	100.0
125	125,000	99.4	100.0	100.0	100.0
100	100,000	98.1	100.0	100.0	100.0
75	75,000	95.8	98.5	100.0	100.0
50	50,000	88.2	87.9	100.0	100.0
37.5	37,500	82.2	74.0	100.0	100.0
25	25,000	71.7	47.8	100.0	100.0
19	19,000	64.5	33.1	100.0	100.0
13.2	13,200	52.1	15.3	100.0	100.0
9.5	9,500	45.1	1.4	99.6	100.0
6.3	6,300	36.4	0.1	88.4	100.0
4.75	4,750	31.6	0.0	82.2	100.0
3.35	3,350	26.3	0.0	77.7	100.0
2.63	2,630	21.3	0.0	71.6	100.0
1.7	1,700	18.0	0.0	61.7	100.0
1.4	1,400	16.4	0.0	57.8	100.0
1	1,000	12.9	0.0	49.9	100.0
0.71	710	10.2	0.0	41.2	100.0
0.5	500	8.3	0	30.1	99.1
0.355	355	6.2	0	18.9	93.9
0.25	250	4.8	0	11.9	83.7
0.18	180	4.3	0	8.0	72.5
0.15	150	3.9	0	6.8	66.5
0.125	125	3.6	0	5.9	61.3
0.09	90	3.1	0	4.6	53.2
0.063	63	2.7	0	3.7	45.5
0.045	45	2.3	0	3.0	39.1
-0.045	-45				
Total:					
P80	**[mm]**	34.58	42.75	4.00	0.226
P50	**[mm]**	12.03	26.05	1.00	0.08

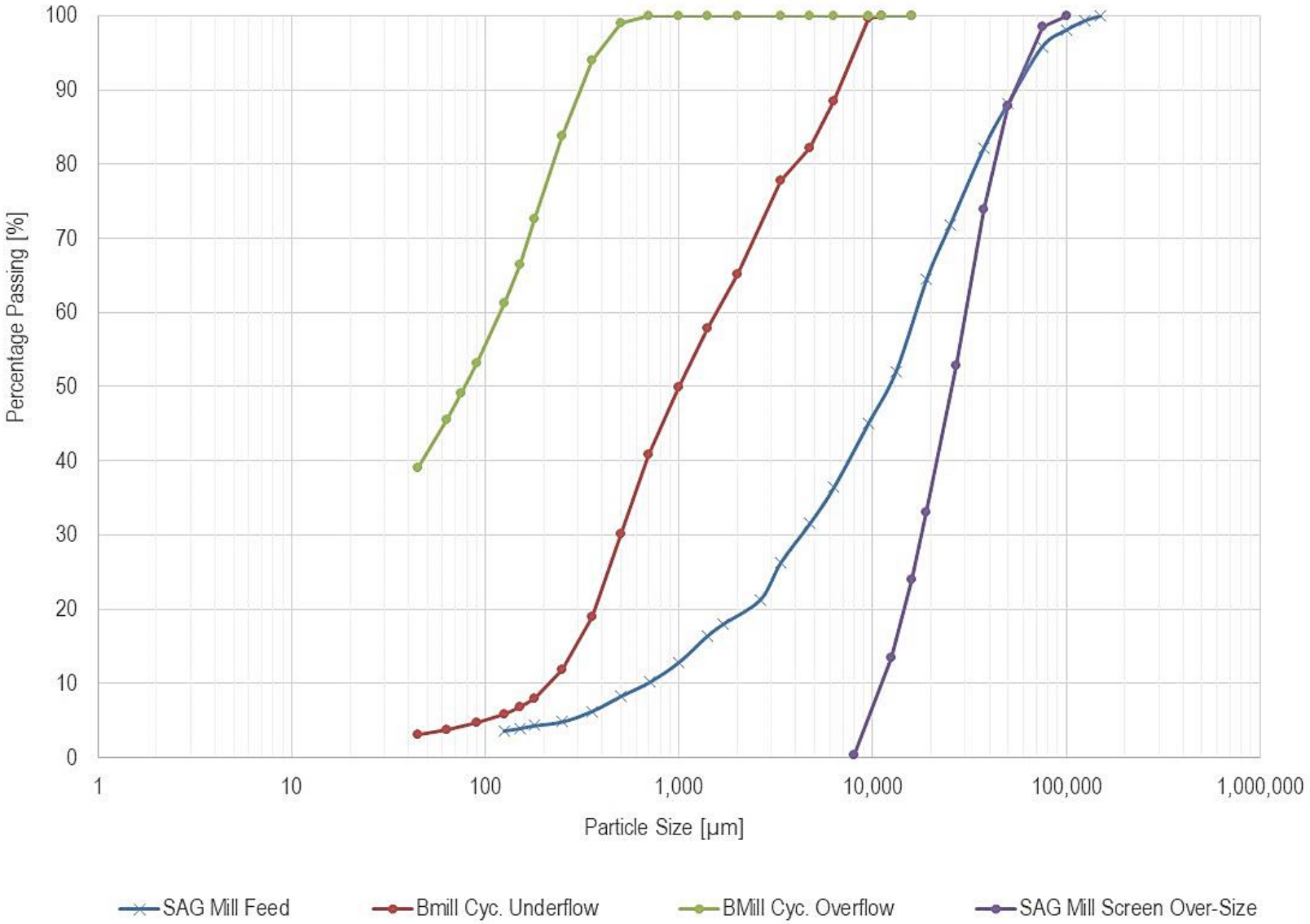

Figure I.1 Size distributions for samples taken March 3rd, 2015

Appendix J Mill Survey Results for Survey Carried Out March 16th, 2016 (survey used for model calibration)

Table J.1 Summary of samples taken March 16th, 2016

Stream	Time & Date	Gross Weight	Packaging weight	Net Sample Weight - Wet	Net Sample Weight - Dry	% Solids	% Moisture
		[kg]	[kg]	[kg]	[kg]		
SAG Mill Feed (S1)	2016-03-16 1039	2,237.0	0.0	2,237.0	2,156.0	96.4	3.6
Pebble Crusher Feed	2016-03-16 1405	335.5	12.0	323.5	319.1	98.6	1.4
SAG Mill Discharge #1/2	2016-03-16 1240 - 1340	30.9	1.1	29.8		0.0	100.0
SAG Mill Discharge #2/2	2016-03-16 1240 - 1340	33.1	1.1	32.0		0.0	100.0
SAG Mill Discharge Total		64.0	2.2	61.8	49.1	79.5	20.5
Ball Mill Discharge	2016-03-16 1240 - 1340	30.9	1.1	29.8	20.1	67.4	32.6
BM Cyclone Underflow	2016-03-16 1240 - 1340	37.3	1.1	36.2	26.8	74.1	25.9
BM Cyclone Overflow	2016-03-16 1240 - 1340	17.7	1.1	16.6	6.1	36.6	63.4
VertiMill Product	2016-03-16 1240 - 1340	34	1.1	32.9	22.3	67.8	32.2
VertiMill Cyclone Underflow	2016-03-16 1240 - 1340	30.4	1.1	29.3	19.9	67.9	32.1
VertiMill Cyclone Overflow	2016-03-16 1240 - 1340	22	1.1	20.9	7.4	35.2	64.8

Table J.2 Size distributions of samples taken March 16th, 2016

Sample:		SAG Mill Feed	*SAG Mill Discharge - from mass balance	SAG Mill Undersize - from mass balance
Particle Size		Cumulative % Passing	Cumulative % Passing	Cumulative % Passing
[mm]	[µm]	[%]		[%]
1,000	1,000,000	100	100	100
849	848,528	100.00	100	100
600	600,000	100.00	100	100
424	424,264	100.00	100	100
300	300,000	100.00	100	100
212	212,132	100.00	100	100
150	150,000	100.00	100	100
125	125,000	99.64	100	100
100	100,000	94.71	100	100
75	75,000	86.54	100	100
63	63,000	81.43	99	100
53	53,000	76.98	99	100
45	45,000	72.85	98	100
37.5	37,500	68.55	97	100
26.5	26,500	59.11	93	100
19	19,000	51.82	89	100
13.2	13,200	43.60	84	100
9.5	9,500	36.68	81	99
6.3	6,300	29.40	75	94
4.75	4,750	26.06	69	87
3.35	3,350	22.32	64	80
2.63	2,630	20.00	60	76
1.7	1,700	16.23	53	66
1.4	1,400	14.82	50	63
1	1,000	12.66	44	56
0.71	710	11.11	40	50
0.5	500	10.01	35	44
0.355	355	8.94	31	39
0.25	250	8.00	27	34
0.18	180	7.16	24	30
0.15	150	6.72	22	28
0.125	125	6.31	21	26
0.09	90	5.62	18	22
0.063	63	5.04	16	20
P80	**[mm]**	59.7	8.82	3.31
P50	**[mm]**	17.6	1.42	0.72

Table J.3 Size distributions of samples taken March 16th, 2016

Sample:		Pebbles	Ball Mill Discharge	Ball Mill Cyclone Underflow	Ball Mill Cyclone Overflow
Particle Size		Cumulative % Passing	Cumulative % Passing	Cumulative % Passing	Cumulative % Passing
[mm]	[µm]	[%]	[%]	[%]	[%]
1,000	1,000,000	100	100	100	100
849	848,528	100	100	100	100
600	600,000	100	100	100	100
424	424,264	100	100	100	100
300	300,000	100	100	100	100
212	212,132	100	100	100	100
150	150,000	100	100	100	100
125	125,000	100	100	100	100
100	100,000	100	100	100	100
75	75,000	99	100	100	100
63	63,000	96	100	100	100
53	53,000	94	100	100	100
45	45,000	89	100	100	100
37.5	37,500	83	100	100	100
26.5	26,500	66	100	100	100
19	19,000	46	100	100	100
13.2	13,200	24	100	100	100
9.5	9,500	10	100	100	100
6.3	6,300	1	99	96	100
4.75	4,750	1	96	91	100
3.35	3,350	0	94	86	100
2.63	2,630	0	91	81	100
1.7	1,700	0	85	72	100
1.4	1,400	0	82	67	100
1	1,000	0	75	58	100
0.71	710	0	66	47	99
0.5	500	0	53	33	95
0.355	355	0	41	23	87
0.25	250	0	33	16	76
0.18	180	0	26	12	65
0.15	150	0	24	11	60
0.125	125	0	21	10	55
0.09	90	0	18	8	47
0.063	63	0	16	7	41
P80	**[mm]**	35.27	1.256	2.505	0.289
P50	**[mm]**	20.46	0.459	0.792	0.102

Table J.4 Size distributions of samples taken March 16th, 2016

Sample:		Vertimill Product	Vertimill Cyclone Underflow	Vertimill Cyclone Overflow
Particle Size		Cumulative % Passing	Cumulative % Passing	Cumulative % Passing
[mm]	[µm]	[%]	[%]	[%]
1,000	1,000,000	100	100	100
849	848,528	100	100	100
600	600,000	100	100	100
424	424,264	100	100	100
300	300,000	100	100	100
212	212,132	100	100	100
150	150,000	100	100	100
125	125,000	100	100	100
100	100,000	100	100	100
75	75,000	100	100	100
63	63,000	100	100	100
53	53,000	100	100	100
45	45,000	100	100	100
37.5	37,500	100	100	100
26.5	26,500	100	100	100
19	19,000	100	100	100
13.2	13,200	100	100	100
9.5	9,500	100	100	100
6.3	6,300	100	100	100
4.75	4,750	100	100	100
3.35	3,350	100	100	100
2.63	2,630	100	100	100
1.7	1,700	100	100	100
1.4	1,400	100	100	100
1	1,000	99	99	100
0.71	710	99	98	100
0.5	500	95	92	100
0.355	355	84	78	99
0.25	250	66	55	95
0.18	180	47	35	87
0.15	150	39	28	80
0.125	125	33	23	73
0.09	90	26	18	62
0.063	63	0	0	0
P80	**[mm]**	0.328	0.378	0.150
P50	**[mm]**	0.191	0.234	-

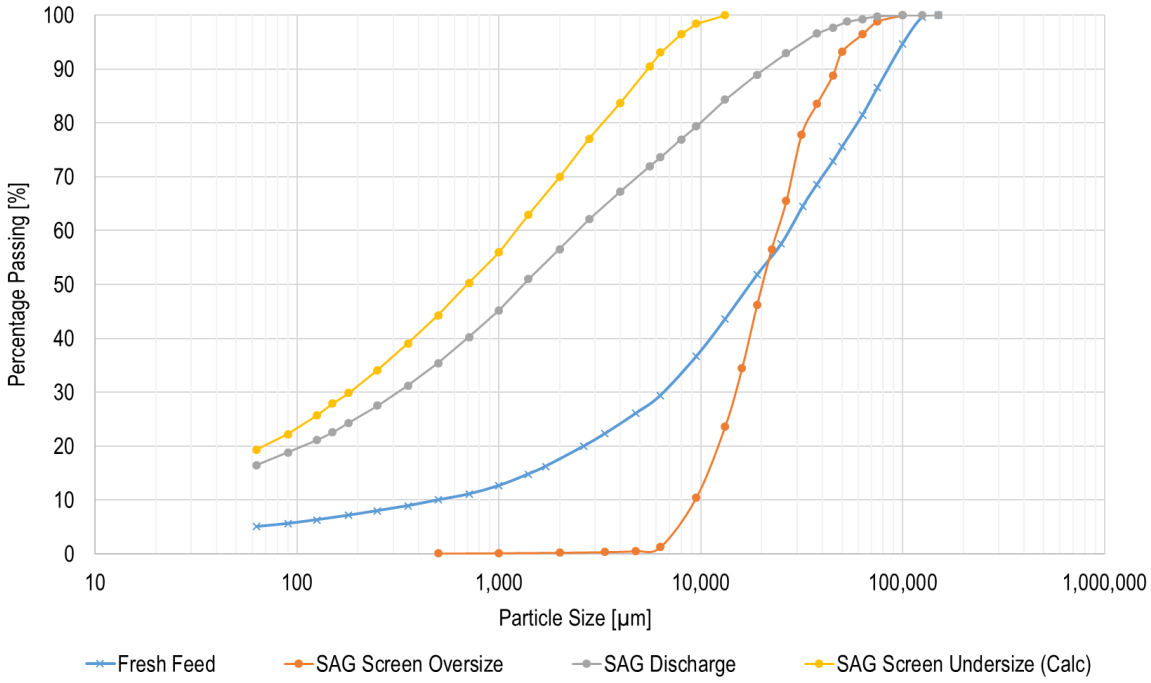

Figure J.1 Size distributions for the SAG mill circuit (March, 2016)

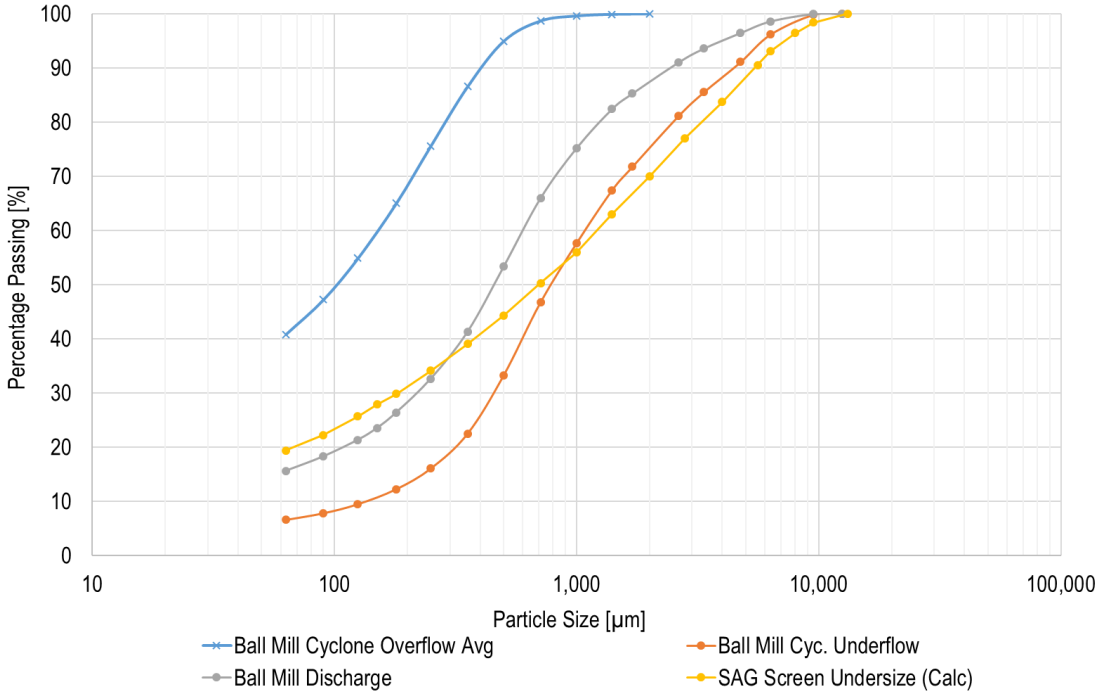

Figure J.2 Size distributions for the SAG mill circuit (March, 2016)

Calculation of SAG Mill Screen Undersize

The SAG mill screen undersize stream could not be sampled directly at New Afton. However, the size distribution could be calculated from either of two mass balances: (1) mass balance around the SAG product screen, and (2) mass balance around the ball mill cyclone.
Both mass balances were used to determine the final SAG screen undersize value.

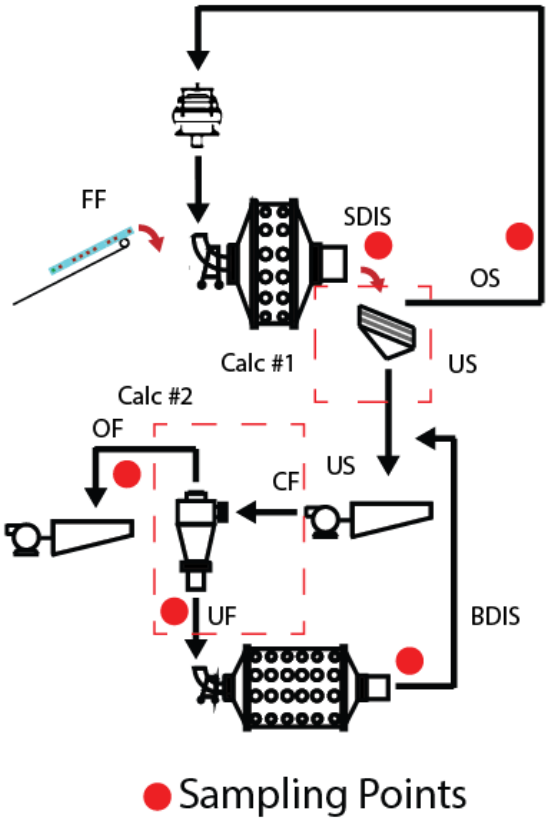

Figure J.3 Mass balances relating to SAG mill screen undersize calculation

Calculation of the two mass balances in Excel provided an average of 3,289 microns (3,115 for method 1 and 3,460 for method 2). In JKSimMet, the mass balance feature was used by weighting each measured value according to the confidence in the measurement method. Lower weighting was assigned to the SAG and ball mill discharge samples than the other streams (eg. cyclone overflow & underflow) which could be cut properly with samplers. Based on the JKSimMet balance calculation, a screen undersize P80 value of 3,311 microns was determined and nominated as the ball mill fresh feed size 80% passing size.

Mass balance #1:

Overall SAG mill discharge (SDIS) size distribution was calculated based on:

1) SAG mill discharge sampled with sampler (49 kg of solids). The sampler opening was about 150 mm in diam.
2) Screen oversize (319 kg of solids) diverted into a bin for collection
3) Dry throughput of fresh feed to mill (percent solids from moisture level of collected+2 tonne sample and wet throughput from belt scale on the mill feed conveyor)
4) Dry throughput of SAG mill screen oversize (wet mtph from belt scale on recirc. conveyor and % solids from moisture level of collected 324 kg wet sample)

For +13.2 mm (effective aperture size of screen) size fractions, the pebble size distribution was used and weighted by tph from belt scale on the recirculation conveyor.
Note: the SAG mill screen uses slotted apertures. Since there was no +13.2 mm material in the cyclone underflow and there was a steep drop at fractions below 13.2 mm in the pebble size distribution, a value of 13.2 mm was nominated as the effective square aperture size

For -13.2 mm size fractions, the sampler size distribution was used and weighted by Fresh Feed tph + oversize tph.

In the next section, capitals refer to solids throughput and lower case refers to percentage passing sieve size x. The following is now available to find the size of the SAG mill screen undersize, us(x):

Table J.5 Outline of measured and calculated streams

Stream	***Solids MTPH***	***% passing of sieve size x***
Fresh Feed	*FF*	*ff(x)*
SAG Mill Discharge	*SDIS*	*sdis(x)*
Screen Oversize	*OS*	*os(x)*
Screen Undersize	*US (equals FF)*	

Mass Balance Equation #1 around screen:

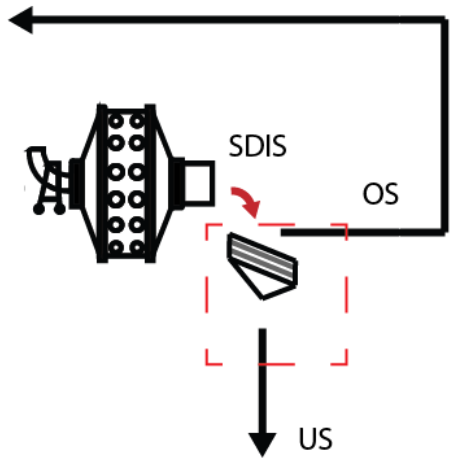

Figure J.4 Mass balance calculation #1 for SAG mill screen undersize

IN = SDIS.sdis(x) = OUT = US.us(x) + OS.os(x), **(J.1)**

Solving for the unknown % passing size x for undersize, us(x):

us(x) = (SDIS.sdis(x) -OS.os(x)) / US note: US = mill fresh feed tph **(J.2)**

Mass balance #2, Around cyclone

The following measurements were referenced:

1) Ball mill discharge sampled with sampler (20 kg solids) and sieved
2) Ball mill cyclone overflow and underflow samples (27 and 6 kg solids weight, respectively)
3) Mill solids fresh feed rate, FF (as in previous calc)
4) Cyclone feed tph measured online (nuclear density gauge and vol. flow rate).

The following is now available to find the size of the **SAG mill screen undersize us(x)**:

Stream	***Solids MTPH***	***% passing of sieve size x***
Fresh feed	FF	ff(x)
Ball Mill Discharge	BDIS	bdis(x)
Cyclone Feed	CF (from DCS)	
Cyclone Underflow	CU (from CF – FF)	cu(x)
Cyclone Overflow	CO (equals FF)	co(x)
Screen Undersize	US (equals FF)	

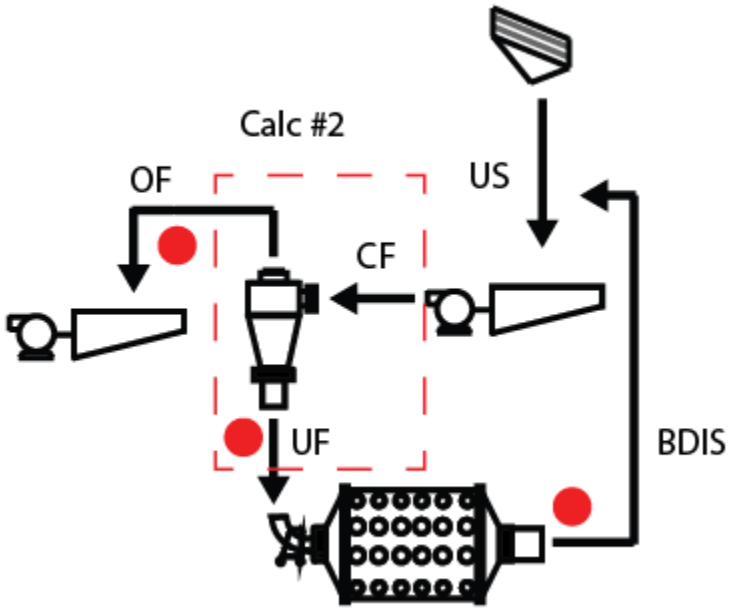

Figure J.5 Mass balance calculation #2 for SAG mill screen undersize

Mass Balance Equation #2 around cyclone:

IN = CF.cf(x) = OUT = OF.of(x) + UF.uf(x) **(J.3)**

Since, CF.cf(x) = BDIS.bdis(x) + US.us(x) **(J.4)**

BDIS.bdis(x) + US.us(x) = OF.of(x) + UF.uf(x) **(J.5)**

Therefore, us(x) = (OF.of(x) + UF.uf(x)-BDIS.bdis(x))/US **(J.6)**

Resulting size distributions for the two separate calculations are shown in Figure J.6.

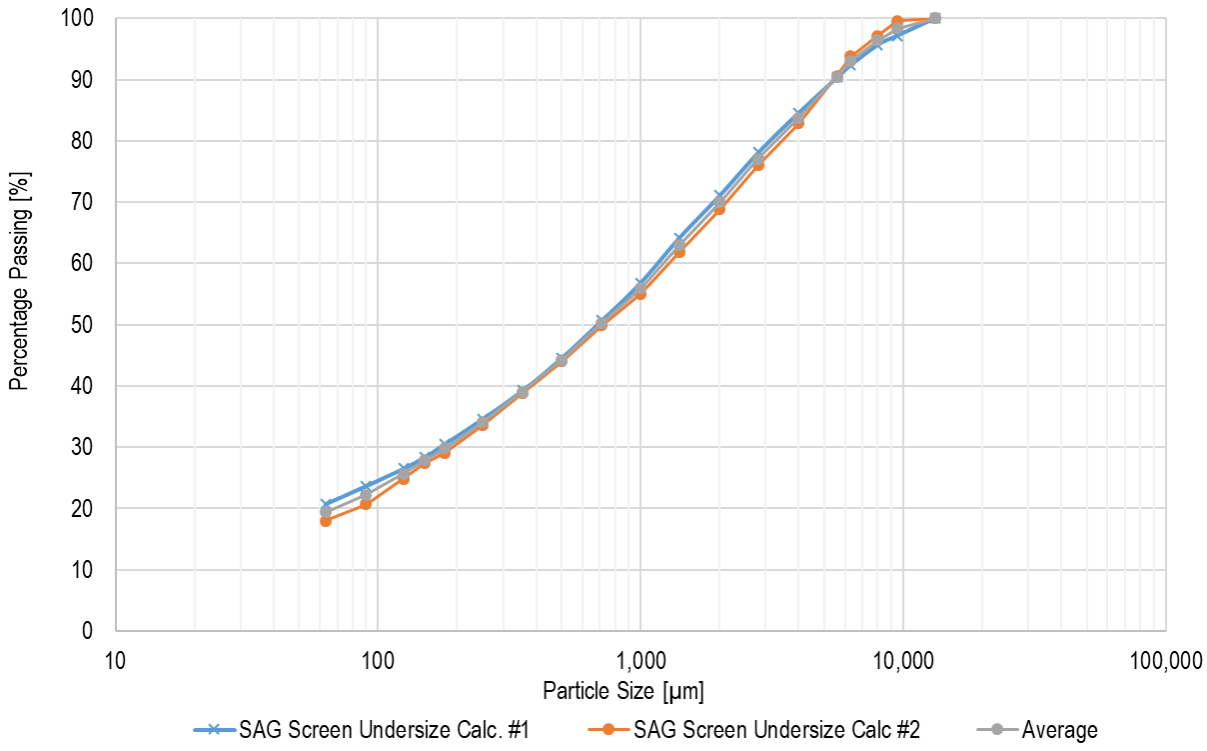

Figure J.6 Size distributions SAG mill screen undersize using calculations methods #1 and #2

Appendix K Sample Preparation Flowsheet for PGNAA Testing

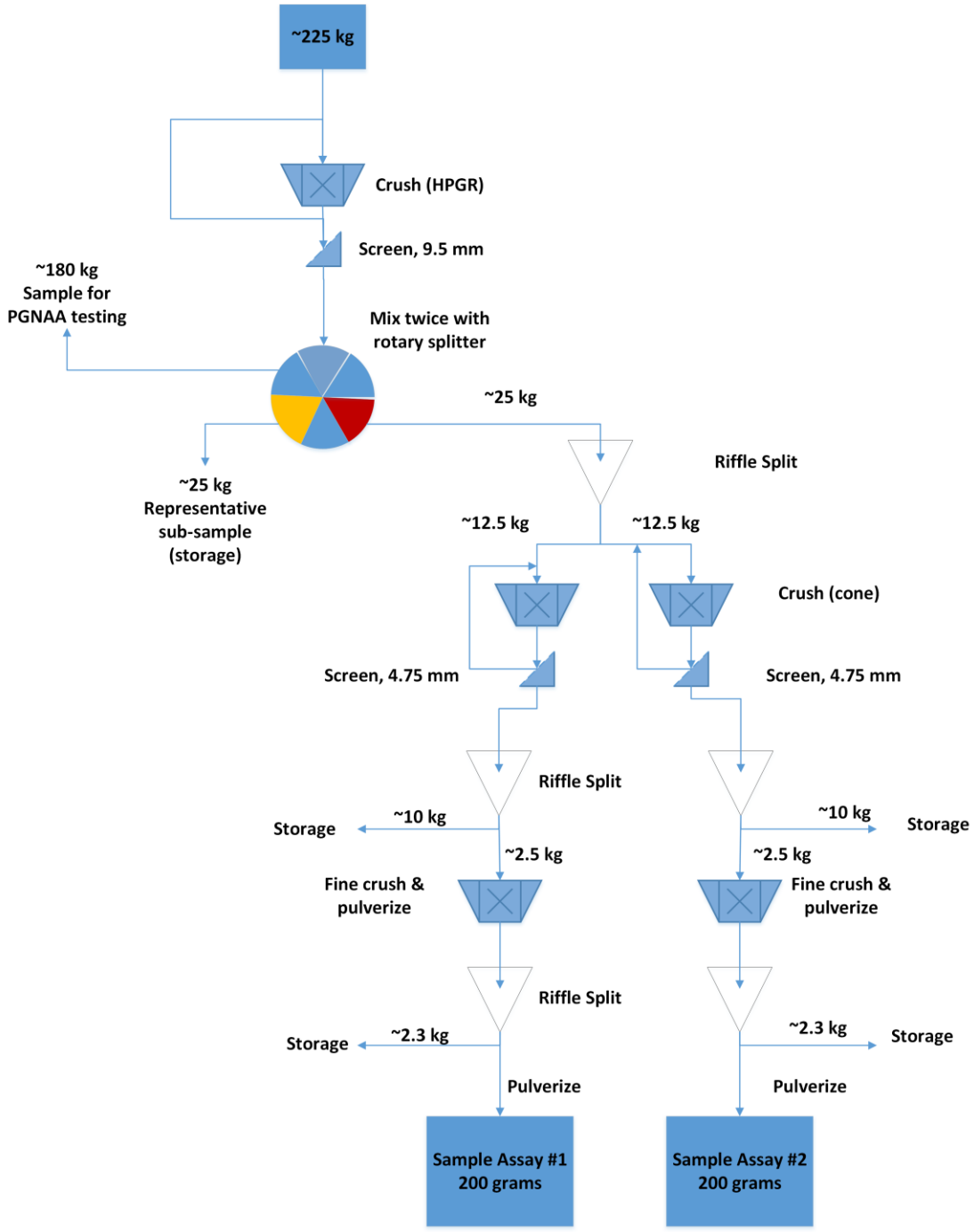

Figure K.1 Sample preparation procedure for sulfide samples (applied to eight of nine samples)

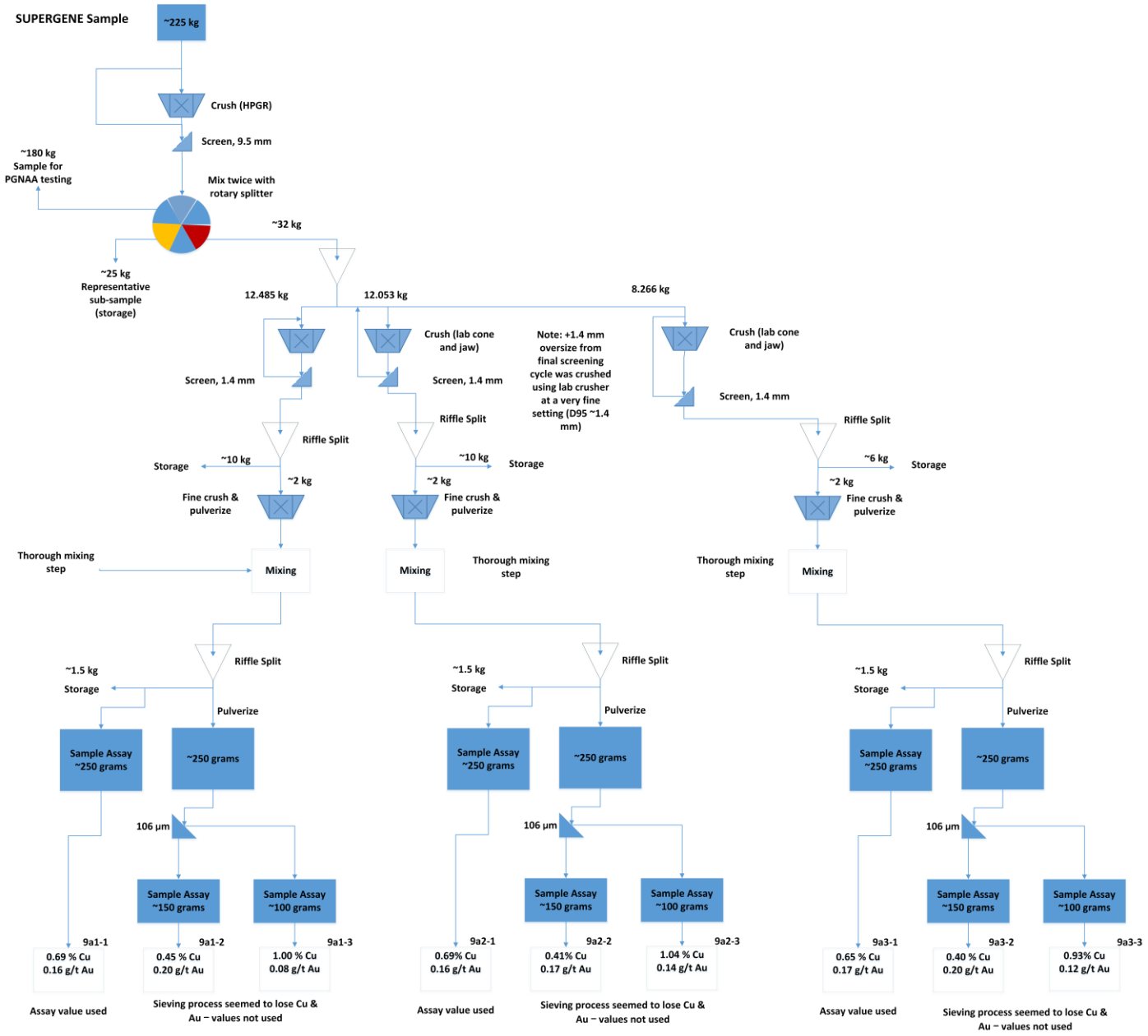

Figure K.2 Sample preparation procedure for oxide sample (applied to one of nine samples)